



**HAL**  
open science

# Hybrid materials based on inorganic glasses doped with organophosphorus molecules for light emitting electrochemical cell applications

Muzhi Cai

► **To cite this version:**

Muzhi Cai. Hybrid materials based on inorganic glasses doped with organophosphorus molecules for light emitting electrochemical cell applications. Organic chemistry. INSA de Rennes, 2019. English. NNT : 2019ISAR0017 . tel-03506238

**HAL Id: tel-03506238**

**<https://theses.hal.science/tel-03506238>**

Submitted on 2 Jan 2022

**HAL** is a multi-disciplinary open access archive for the deposit and dissemination of scientific research documents, whether they are published or not. The documents may come from teaching and research institutions in France or abroad, or from public or private research centers.

L'archive ouverte pluridisciplinaire **HAL**, est destinée au dépôt et à la diffusion de documents scientifiques de niveau recherche, publiés ou non, émanant des établissements d'enseignement et de recherche français ou étrangers, des laboratoires publics ou privés.

# THESE DE DOCTORAT DE

L'INSTITUT NATIONAL DES SCIENCES  
APPLIQUEES RENNES  
COMUE UNIVERSITE BRETAGNE LOIRE

ECOLE DOCTORALE N° 596  
*Matière, Molécules, Matériaux*  
Spécialité : *Sciences de matériaux*

Par

**Muzhi CAI**

**Hybrid materials based on inorganic glasses doped with organophosphorus molecules for light emitting electrochemical cell applications**

Thèse présentée et soutenue à Campus de Beaulieu à Rennes, le 22 November  
Unité de recherche : UMR 6226 Institut des Sciences Chimiques de Rennes  
Thèse N° : 19ISAR 22 / D19 - 22

## Rapporteurs avant soutenance :

Andrea PIARRISTEGUY  
Maître de conférences, Institut Charles Gerhardt Montpellier

Dominique de LIGNY  
Professeur, Friedrich-Alexander Universität Erlangen-Nürnberg

## Composition du Jury :

Andrea PIARRISTEGUY  
Maître de conférences, Institut Charles Gerhardt Montpellier  
Rapporteur  
Dominique de LIGNY  
Professeur, Friedrich-Alexander Universität Erlangen-Nürnberg  
Rapporteur  
Xianghua ZHANG  
Directeur de recherche CNRS - Université de Rennes 1  
Directeur de thèse  
Laurent CALVEZ  
Maître de conférences, Université de Rennes 1  
Co-directeur de thèse  
Junjie ZHANG  
Professeur, China Jiliang University  
Co-superviseur de thèse  
Shiqing XU  
Professeur, China Jiliang University  
Examineur  
Jean ROCHERULLE  
Professeur, Université de Rennes 1  
Examineur



Intitulé de la thèse :

.... Hybrid materials based on inorganic glasses doped with organophosphorus molecules for light emitting electrochemical cell applications.....

**Muzhi CAI**

En partenariat avec :

--	--	--	--	--

*Document protégé par les droits d'auteur*



## Acknowledgement

Time is but a stream. I remember the day I just came to Rennes, and I still remember Prof Xianghua Zhang picked me up at the railway station and drove me to the apartment. In the meanwhile the air is filling with the perfume of promise. I remember the day French football team became the top of the world again (15.07.2018), and not long after that, I broke the anterior cruciate ligament of my left leg when I was playing football. Anyway, there are too many memories, most happy, some sad, which, I think, is “C’est la vie”. Now, I will finish the dissertation soon, and the time to say goodbye is getting closer. Thanks to Rennes.

Concerning the dissertation, I can hardly finish it without the guidance of my committee members, help from my colleague, supporting from my friends and families.

First of all, I would like to give my sincerest gratitude to my supervisors, Xianghua Zhang and Laurent Calvez for their great patience and meticulous guidance throughout my thesis. Every progress of the research is based on their extensive expertise and enthusiasm for science. I also appreciate their care and assistance during my stay in France. I owe additional credit to Laurent for teaching me how to use every device hand by hand and giving me more freedom of the research. He always gives me new ideas and inspirations when I feel confused.

Besides, I have to thank Prof Jean Rocherullé, who is like a supervisor to me, for his guidance, encouragement and earnest attitude towards my thesis. Without his help, I can never finish the work of phosphate glasses. Talking about phosphate glasses, I also appreciate the help and guidance from Ronan Lebullenger.

In addition, I want to thank many of my colleagues who also helped me a lot. Antoine Gautier designs and makes lots of devices for my experiments and shared a “fire disaster” with me. David le Coq teaches me how to manipulate the electrochemical station and the electrochemical knowledge of glass. Michel Cathelinaud teaches me how to measure the ionic conductivity of the films. François Cheviré teaches me how to analyze the XPS spectrum. Without the supporting from Thierry Pain, Thierry Jouan, Albane Bénardais and Adeline Quéant-Hémonin, my experiments would have much more troubles.

Moreover, I would like to thank Muriel Hissler and Pierre-Antoine Bouit from OMC group. They provide us the organophosphorus molecules, and all the organic molecules used in this work are made by them. Without their timely supply, the work would take more time.

During these years in Rennes, Hongli Ma give me a lot of help and support. Especially when I was doing the surgery on my knee, she takes good care of me just like as my mother. I can not say too much thanks to her.

Obviously, without friends or “classmates”, the life is incomplete. I wish to thank Bhuvanesh Srinivasan, Enora Lavanant, Jakub Szlezak, Julie Carcreff, Geoffrey Louvet, Killian Dénoue, Kevin Guy, Guillaume Durand, Yiming Wu, Guangxing Liang, Zhuanghao Zheng, Shuo Chen, Qing Jiao, Yanghai Xu, Dong Fu, Xiaoyang Che, Meng Wei, Donglou Ren and Renguang Ye. In particular, I am grateful that Anna Novikova and Laure Cercueil always organize an activity during the weekends, which brings me a lot of fun.

There is a Chinese proverb, “we should not forget those who dug the well when we drink the water.” I have to thank my master supervisors Prof Shiqing Xu and Prof Junjie Zhang, who help me a lot to get the opportunity to do a Ph.D here. I also wish to thank China scholarship council who grants me study in France.

Last but not the least, I would like to thank my parents, Hongxia Li and Xuanchen Cai, for their spiritual support. Although the distance is too far, they can always cheer me up and warm me up. In particular, I really appreciate the understanding and assistance from my wife Binying Yang, who is a fighter, together with me, resisting the enemy of our love.

# SOMMAIRE

<b>RÉSUMÉ DÉTAILLÉ EN FRANÇAIS.....</b>	<b>I</b>
<b>GENERAL INTRODUCTION .....</b>	<b>1</b>
<b>Chapter I: Light-emitting electrochemical cell .....</b>	<b>5</b>
1. Introduction .....	7
2. Operational Mechanisms for LECs .....	10
2.1 Electrochemical Model (ECM).....	10
2.2 Electrodynamic Model (EDM) .....	11
2.3 Current Consensus Understanding of Operational Mechanism of LECs .....	11
2.4 Transient Phenomena.....	12
2.5 Planar LECs configuration.....	13
2.6 Sandwich LECs configuration .....	17
3. Emitter for LECs .....	18
3.1 Copper(I) complexes.....	19
3.2 Small molecules .....	22
3.3 Quantum dots and perovskite nanoparticles .....	25
4. Electrolyte for LECs.....	26
4.1 Poly (ethylene oxide) based electrolytes (PEO).....	27
4.2 Ionic liquids.....	28
5. Inorganic Glass electrolyte and organophosphorus semiconductor .....	30
5.1 Models of ionic Conduction in Glass.....	31
5.1.1 Strong electrolyte Model.....	32
5.1.2 Weak electrolyte Model .....	33
5.1.3 Martin and Angell revised general model.....	34
5.2 Possible inorganic glass electrolytes for LECs .....	34
5.3 Organophosphorus semiconductor.....	35
6. Conclusions .....	36
<b>REFERENCES .....</b>	<b>38</b>
<b>Chapter II: Hybrid materials based on silicate glasses .....</b>	<b>53</b>
1. Introduction .....	55
2. Experiments.....	57
2.1 Raw Chemicals.....	57
2.2 Sol-gel synthesis methods .....	57
2.2.1 Silica gel.....	57
2.2.2 Lithium modified glass .....	58
2.2.3 OSC doped silica glass.....	59
2.3 Drying procedure .....	60
2.4 Coating method .....	61
2.4.1 Substrate and its clean process.....	61
2.4.2 Spin-coating method .....	61



2.4.3 Drying process .....	61
3. Silica bulk glass .....	62
3.1 Structural evolution during Sol-gel process .....	62
3.2 Preparation of Silica bulk xerogel.....	64
3.3 OPSC doped Silica bulk xerogel.....	66
4. Preparation of silica glass coating .....	68
5. Photoluminescence of the OPSC doped Silica glass.....	71
5.1 Photoluminescence spectrum.....	72
5.2 Luminescent concentrator based on OPSC doped silica coating .....	74
6. Preparation of lithium modified Silica bulk glass and coating .....	74
6.1 Lithium modified silicate glass bulk xerogel.....	74
6.2 Lithium modified silicate glass coating .....	78
7. Conclusion.....	83
REFERENCES .....	85
<b>Chapter III: Hybrid materials based on phosphate glasses .....</b>	<b>89</b>
1. Introduction .....	91
2. Experiments and Measurements.....	95
2.1 Raw chemicals .....	95
2.2 Organophosphorus organic semiconductor.....	95
2.3 Preparation process .....	95
2.3.1 Approach 1:.....	95
2.3.2 Approach 2:.....	97
2.3.3 Working principle of SPS .....	98
3. Analysis of P <sub>2</sub> O <sub>5</sub> – SnO and ZnO-SnO-P <sub>2</sub> O <sub>5</sub> glasses .....	98
4. Analysis of P <sub>2</sub> O <sub>5</sub> – Li <sub>2</sub> O glasses .....	101
4.1 Ionic conductivity.....	102
4.2 DSC analysis.....	104
5. Analysis of Li <sub>2</sub> O-Li <sub>2</sub> SO <sub>4</sub> -P <sub>2</sub> O <sub>5</sub> glasses.....	104
5.1 DSC analysis.....	105
5.2 Ionic conductivity.....	105
5.3 XRD and optical properties of LiS25PM glass.....	106
6. Preparation and analysis of hybrid glasses based on LiS25PM.....	107
6.1 Preparation of hybrid glass.....	107
6.2 Analysis of hybrid glasses.....	109
6.2.1 Photoluminescent and excitation spectra .....	109
6.2.2 Microstructure of the hybrid glass .....	110
6.2.3 Electrochemical properties of the hybrid glass .....	115
7. LEC device based on the hybrid glass .....	118
8. Conclusion.....	118
REFERENCES .....	120
<b>Chapter IV: Luminescence of zinc phosphate glasses .....</b>	<b>123</b>
1. Introduction .....	125
2 Experiments and Chemicals .....	127
2.1 Experiments of phosphate glass containing ANZC .....	127

2.2 Experiments of manganese doped phosphate glass containing ANZC.....	127
3. Results and discussion of ANZC glass .....	128
4. Results and discussion of manganese doped ANZC glass.....	135
5. Conclusions .....	141
REFERENCES.....	142
<b>GENERAL CONCLUSIONS.....</b>	<b>147</b>



# RÉSUMÉ DÉTAILLÉ EN FRANÇAIS

## Introduction

L'éclairage artificiel est l'une des forces motrices les plus importantes de la société moderne. La consommation d'énergie électrique dans le secteur de l'éclairage était d'environ 3500 TWh en 2012, ce qui correspond à une production équivalente de 1900 Mt en CO<sub>2</sub>. Étant donné que nous sommes de plus en plus préoccupés par les économies d'énergie et la réduction des gaz à effet de serre, l'éclairage est l'un des principaux domaines de mise à jour des technologies existantes et la recherche d'illuminants alternatifs efficaces est évidemment un moyen incontournable. D'autre part, l'évolution de la technologie exige des produits inventifs dotés d'architectures de dispositifs avancées. Les dispositifs électroluminescents organiques sont toujours efficaces, minces et flexibles. En outre, ils peuvent même être transparents, ce qui en fait une alternative prometteuse à leurs analogues inorganiques.

En 1953, A. Bernanose et ses collègues ont tout d'abord observé une électroluminescence à partir de matières organiques. Toutefois, les matériaux électroluminescents organiques n'ont fait l'objet d'avancées qu'en 1987 en raison de la nécessité de tensions de commande élevées, ce qui entraîna des rendements énergétiques médiocres. En 1987, Tang et Friend ont inventé les diodes électroluminescentes organiques et polymères (OLEDs), qui permettaient déjà au dispositif de respecter des performances similaires aux tubes fluorescents. Il a également permis de lancer la période actuelle de recherche et développement sur les OLED. Ils ont mis au point une diode à structure bicouche par dépôt en phase vapeur de films minces de semi-conducteurs organiques. Ces électrodes utilisaient une injection de porteur dans les matières organiques relativement efficace. En outre, la structure bicouche a favorisé la recombinaison à l'interface entre les deux films organiques semi-conducteurs afin d'éviter des pertes significatives liées à la trempe par électroluminescence au niveau des électrodes.

Dans un dispositif OLED efficace, il est demandé aux électrons et aux trous de se recombiner dans la majeure partie du semi-conducteur organique, ce qui évite la désactivation par électroluminescence au niveau des électrodes. Pour atteindre cet objectif, l'injection et le transport de porteurs dans les matières organiques doivent être efficaces et équilibrés. L'injection d'électrons dans les semi-conducteurs organiques se produit dans l'orbitale moléculaire la plus basse non occupée (LUMO), tandis que l'injection de trous se produit dans l'orbitale moléculaire la plus haute occupée (HOMO). Cela signifie que pour obtenir des OLED efficaces, une électrode à haute fonction de travail et une basse demandent

respectivement une injection efficace de trous et d'électrons. Ensuite, la mobilité de ces porteurs de charge injectés dépend des différents types de semi-conducteurs. Ce transport de porteurs se produit par des effets tunnels activés thermiquement des porteurs de charges entre des sites localisés dans un paysage énergétique désordonné. Normalement, les films organiques dans les OLED doivent être extrêmement minces (moins de plusieurs centaines de nanomètres) pour obtenir un fonctionnement efficace. L'électroluminescence dans les OLED se produit par la recombinaison d'électrons et de trous pouvant former des paires d'excitons singlets et triplés, qui peuvent être à transition radiale, à transition non radiale ou dissociée. Typiquement, les phonons émis ont une énergie proche de la bande interdite du semi-conducteur organique. Cependant, avec une seule couche organique, les OLED ne peuvent pas atteindre un bon équilibre entre électrons et trous. Par conséquent, une structure bicouche ou plusieurs couches organiques pouvant favoriser l'injection et la mobilité du porteur de charge ont été introduites dans l'OLED pour éviter ces problèmes. En conséquence, les coûts de production des OLED retardent considérablement leur entrée sur le marché à grande échelle pour des applications d'éclairage.

En 1994, Pei et ses collaborateurs ont découvert que les propriétés des OLEDs peuvent être ajustées en mélangeant de fortes concentrations d'ions mobiles avec un polymère conjugué et un électrolyte solide organique. De plus, le comportement de l'appareil ne fonctionne pas comme une diode car il montre une émission en polarisation inverse et que l'intensité de la lumière est similaire pour les deux polarités de polarisation. Ils pensaient que l'oxydation électrochimique et la réduction du polymère conjugué provoquaient l'injection de charges électroniques à partir des électrodes. C'est l'origine du nom des nouveaux dispositifs (cellules électrochimiques électroluminescentes ou LEC). Dans leur travail, la tension d'activation se situe autour de la bande interdite du semi-conducteur polymère conjugué. De plus, cela indique que les matériaux stables à l'air peuvent être utilisés comme électrodes pour un dispositif efficace, malgré la grande barrière d'injection qui en résulte pour l'injection d'électrons. Deux décennies plus tard, de nombreuses alternatives d'émission ont été reportées, notamment les complexes de métaux de transition ionique (iTMC), les petites molécules (SM), les Quantum Dots (QD) et les nanoparticules (NP). Normalement, les exigences de l'émetteur sont un comportement électrochimique réversible et un rendement quantique de photoluminescence élevé à l'état solide. Outre le matériau émetteur, l'électrolyte est également crucial pour la performance des dispositifs LEC. Cependant, bien que de nombreuses recherches se soient concentrées sur les électrolytes pour les polymères contenant du polymère poly (oxyde d'éthylène) (PEO) ou encore les matériaux à base d'oligoéther et les

liquides ioniques, les chercheurs sont toujours à la recherche d'un électrolyte plus idéal pour la fabrication du LEC.

Jusqu'à présent, très peu de travaux sont consacrés à l'étude d'électrolytes inorganiques pour intégration dans un dispositif LEC. Nous nous sommes intéressés dans ce projet à la création de LEC à base d'électrolyte de verre inorganique. En effet, la plupart de ces électrolytes organiques sont dangereux pour l'environnement, comparés à l'électrolyte en verre inorganique, ce qui va à l'encontre du concept de technologie verte. D'autre part, comparés à certains électrolytes organiques, le verre inorganique possède une conductivité ionique comparable, une meilleure stabilité physico-chimique et une meilleure capacité de résistance aux rayons ultraviolets (UV). Il est bien connu que le principal défi de la technologie LEC consiste à réduire la dégradation de l'émetteur organique, ce qui dépend fortement de la stabilité et de la capacité de l'électrolyte à résister aux rayons UV. Par conséquent, la bonne stabilité du verre face aux ultraviolets absorbés empêcheraient la dégradation de l'émetteur organique dans un dispositif LEC. Cependant, la morphologie du mélange molécule organique / électrolyte est également un élément clé d'un dispositif LEC. Ainsi, un émetteur organique qui non seulement possède un rendement quantique de photoluminescence élevé à l'état solide, mais peut également former un bon mélange avec un électrolyte de verre est recherché pour la génération de LEC.

Le nom de phosphore provient du grec ancien phos et phorus, qui signifie respectivement lumière et de portée. Ceci est dû à la forte lumière du phosphore blanc. Cependant, la réactivité et la toxicité élevées de nombreux dérivés contenant du P empêchent son application dans les dispositifs émetteurs. Cette situation a changé une fois que les chimistes ont été capables de stabiliser et de protéger l'atome P, ce qui suggère que des dispositifs opto-électroniques à base de dérivés organophosphorés peuvent être fabriqués. Fait intéressant, bien que les dérivés organophosphorés aient été étudiés pendant des décennies, leur insertion dans des dispositifs n'a que récemment été réalisée. Cependant, à notre connaissance, il existe peu de rapports sur des dispositifs LEC à base de dérivés organophosphorés, encore moins sur des LEC hybrides à base de dérivés organophosphorés et d'électrolyte solide hôte.

L'objectif principal de ce travail est donc de développer un nouveau dispositif LEC à base d'électrolyte de verre inorganique dopé par des molécules organophosphorées. Lors de cette réalisation, la technique classique de fusion-trempe ne peut pas être utilisée. En effet, la température de fusion du verre est toujours beaucoup plus élevée que la température de dégradation de la molécule organique. Des voies alternatives ont ainsi été envisagées.

Dans le premier chapitre, le contexte de l'étude et le mécanisme des dispositifs LEC sont introduits. Le second et le troisième chapitre sont consacrés à l'obtention de LEC par le biais de la synthèse sol-gel et du frittage par Spark Plasma Sintering (SPS), respectivement. Enfin, lors du processus de préparation de LEC par SPS, un phénomène intéressant a été découvert. Une émission bleue à large bande a été observée dans le verre d'oxynitride de phosphate de zinc exempt de terres rares. Le quatrième chapitre est donc consacré à ce phénomène inattendu.

## Chapitre 1

Une cellule électrochimique électroluminescente (LEC) est un dispositif à couches planes, composé d'un semi-conducteur organique électroluminescent (OSC) et d'ions mobiles en tant que matériau actif pris en sandwich entre une anode et une cathode, comme illustré schématiquement à la Fig. 1 (à gauche). Il a été considéré comme l'exemple phare du dispositif d'éclairage à couches minces le plus simple. Parfois, les LEC peuvent également être préparées via une structure plane, comme illustré à la Fig. 1 (à droite).

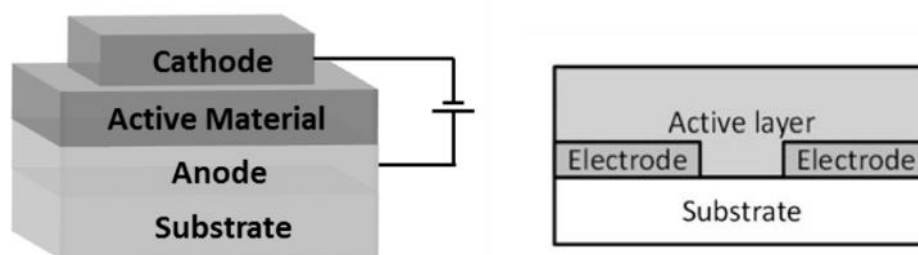


Fig. 1. Structure schématique d'un dispositif à cellules en sandwich (à gauche) et d'un dispositif à cellules planaires (à droite) avec un matériau actif monocouche

Comparé aux OLEDs, une LEC peut fonctionner efficacement à basse tension. La tension d'activation de la cellule se situe autour de la bande interdite du semi-conducteur émetteur. Le tableau 1.1 donne un aperçu général et résume les avantages des LEC.

Tableau 1 Comparaison de différents types de dispositifs électroluminescents organiques, OLED et LEC

Paramètres	OLEDs	LECs	Avantages des LECs
Couches actives	4 ou plus	1 ou 2	Architecture de dispositif simple
Épaisseur typique par couche	60-120 nm	100-500 nm	Des films plus épais promettent des process robustes
Électrodes	Sensible à l'air	Air stable	Les métaux stables à l'air peuvent être utilisés
Conditions d'encapsulation	Haut	faible	Les électrodes stables à l'air promettent un emballage moins exigeant
Traitement des couches organiques	À base de vide	Basé sur la solution	Traitement de préparation rentable
Solvant	n.a.	Bénin	Écologique

Tous ces avantages sont dus aux mécanismes opérationnels uniques des LEC. Un modèle électrochimique (ECM) et un modèle électrodynamique (EDM) ont été proposés pour expliquer le principe de fonctionnement d'une LEC, comme le montre la figure 2. Comme le montre la figure 2 (a), l'ECM suppose que si une tension  $V > E_g/e$  est appliquée sur le dispositif, où  $E_g$  est la bande interdite de l'émetteur et  $e$  est la charge élémentaire, l'injection d'électrons et de trous aux interfaces des électrodes provoquerait un dopage électrochimique de la couche active. De plus, l'injection d'électrons et de trous entraîne respectivement l'oxydation et la réduction du semi-conducteur à l'anode et à la cathode. Le semi-conducteur oxydé et réduit est compensé électrostatiquement par des anions et des cations provenant de l'électrolyte associé, respectivement, ce qui donne des régions dopées de type  $p$  et de type  $n$  dans la masse. L'EDM suppose que le mouvement des ions mobiles provoque la formation de doubles couches électriques minces (EDL : Electric Double Layer) aux interfaces des électrodes en raison de la tension de polarisation appliquée. En conséquence, l'injection de charges au niveau des électrodes s'est produite en raison du grand champ électrique interfacial présenté sur la figure 2 (b).

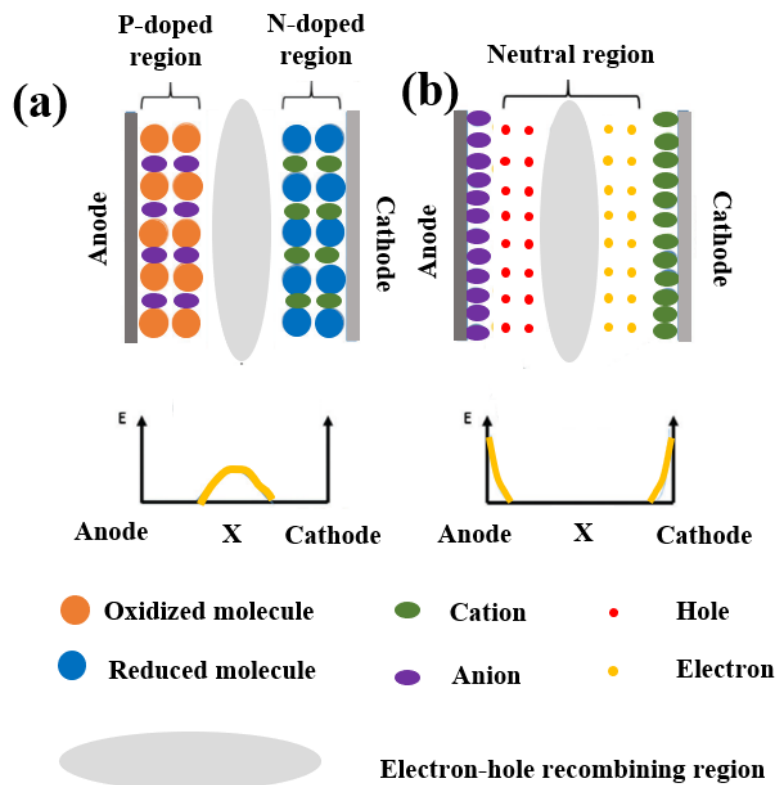


Fig. 2. Modèles électrochimiques (a) et électrodynamiques (b) proposés pour des dispositifs LEC. La distribution spatiale associée du champ électrique est indiquée



La communauté scientifique concernée a mis près de deux décennies à parvenir à un consensus sur le mécanisme des dispositifs des LECs. Ce consensus est que les deux modèles proposés sont les deux régimes du même comportement électrique, aussi les deux modèles sont considérés corrects.

Après avoir compris le mécanisme des LEC, le point clé de celles-ci est la couche d'émetteur constituée d'un mélange d'un émetteur et d'un électrolyte ionique. Les électrolytes en verre inorganique possèdent une fenêtre de stabilité électrochimique plus large, une conductivité ionique élevée, une transmission spectrale étendue et une stabilité mécanique, ce qui est probablement un matériau électrolytique recommandé pour une LEC. Dans ce travail, nous prévoyons d'utiliser deux technologies qui permettent d'éviter les conditions de températures élevées pour préparer le verre hybride organique-inorganique. L'une est la méthode sol-gel, une méthode de chimie douce par voie humide à basse température, et l'autre est le frittage Spark Plasma sintering (SPS), capable de fritter un verre à une température proche de la température de transition vitreuse ( $T_g$ ) du verre.

D'autre part, le semi-conducteur organique recommandé pour le dopage d'électrolytes de verre inorganiques doit présenter un rendement quantique de luminescence élevé à l'état solide, une stabilité chimique élevée et une température de dégradation élevée. Les semi-conducteurs organophosphorés présentent tous ces avantages et seront donc utilisés comme émetteurs lors de nos travaux.

## Chapitre 2

Dans ce chapitre, deux types de molécules OPSC ont été utilisés: OPSCS3 (émission dans le vert) et OPSCTD73 (émission dans le bleu). La structure de l'OPSCS3 et de l'OPSCTD73 est illustrée aux figures 3 (a) et (b), respectivement

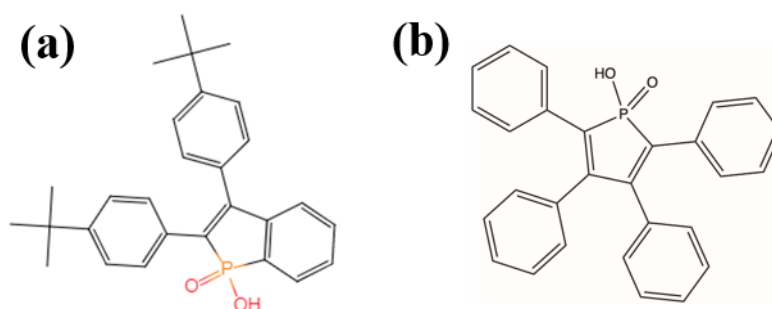


Fig. 3. Structure de l'OPSCTD73 (a) et de l'OPSCS3 (b)

Les xérogels de silice dopés à l'OPCS3 et à l'OPSCTD73 ont été préparés avec succès par la méthode sol-gel. La figure 4 montre les échantillons illuminés par lampe UV. Une forte photoluminescence (PL) a été observée à partir des deux échantillons.

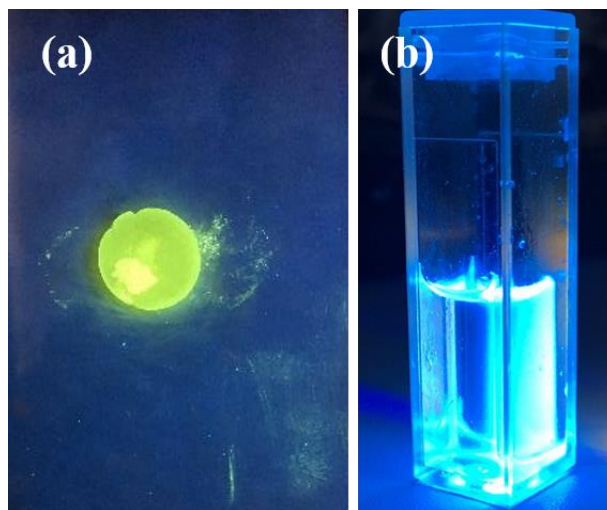


Fig. 4. Xérogel de silice dopée par les molécules OPSCS3 (a) et OPSCTD73 (b) sous lampe UV

Les spectres de photoluminescence des deux échantillons ont été étudiés, comme le montre la figure 5. Les xérogel de silice dopés OPSCS3 et OPSCTD73 montrent un pic d'émission à environ 480 nm et 450 nm, respectivement.

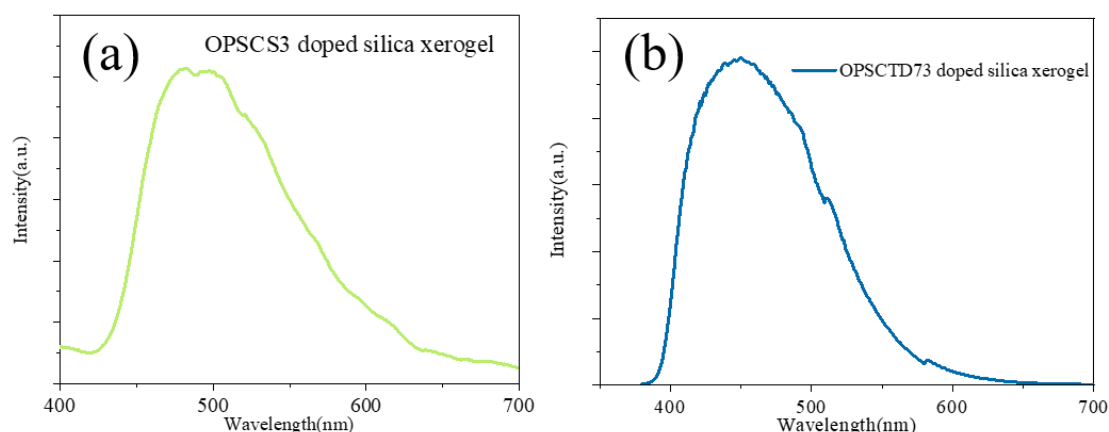


Fig. 5. Spectres de luminescence des xérogel dopes: OPSCS3 (a) and OPSCTD73 (b)

Les xérogels de silice dopés OPSCS3 et OPSCTD73 présentent un “décalage bleu” de 30 nm et 20 nm, respectivement, par rapport à celui des molécules correspondantes dissoutes dans du DCM (dichlorométhane). Ce “virage bleu” peut être dû au changement de l'environnement de coordination de l'OPSC. La structure de l'OPSC aurait donc été modifiée. Le film de silice dopée par l'OPSCTD73 a également été préparé (figure 6). La figure 6 (b) présente la vue au

microscope optique du film de silice dopé montrant une bonne uniformité sous un grossissement x 1000.

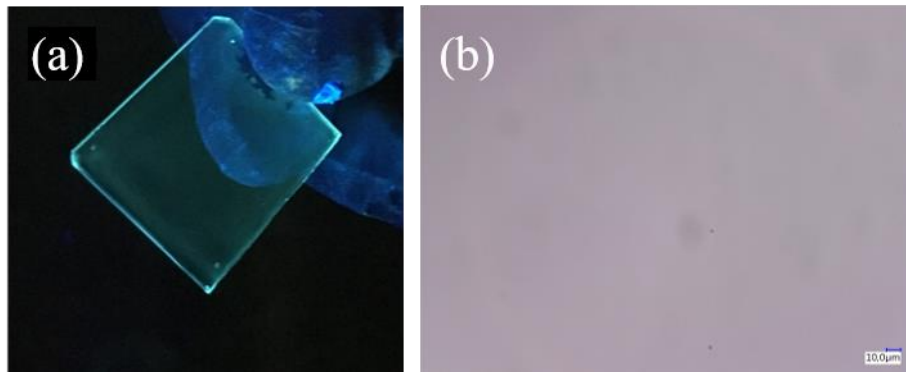


Fig. 6. Photographie du revêtement de silice dopée OPSC7D3 sous lampe UV (a) et sous microscope optique (b) (grossissement x1000)

Une composition à base de 70% molaire de  $\text{SiO}_2$  et 30% de  $\text{Li}_2\text{O}$  a été préparée en utilisant respectivement du  $\text{LiNO}_3$  et du  $\text{LiCl}$  comme précurseurs, comme illustré à la figure 7.



Fig. 7. Photographie du xérogel TEOS- $\text{LiNO}_3$  et TEOS- $\text{LiCl}$

Sur la base de cette solution, des xérogels de silicate de lithium massifs ont été préparés, puis des films ont été réalisés. Cependant, lorsque la concentration de  $\text{Li}_2\text{O}$  est supérieure à 10% en moles, il a été observé que des vides sont générés dans le revêtement, comme présenté sur la figure 8.

Ces vides présents dans le revêtement préparé sont probablement dus à l'échelle de temps courte des processus de dépôt de film menant à une gélification susceptible de se produire par un processus physique. Lorsque la concentration de sels de lithium dépasse un certain point, étant donné que la réaction chimique entre le sel de lithium et le silanol ne se produit pas suffisamment en raison de la courte durée du processus de centrifugation, il existe certains

sels de lithium sous la forme d'origine ( $\text{LiCl}$  ou  $\text{LiNO}_3$ ) dans le revêtement. Et ces sels de lithium sont plus susceptibles de réagir avec l'eau, ce qui provoque l'apparition de vides. Etant donné qu'un grand excès d'eau, correspondant à un rapport molaire eau / TEOS supérieur à 15, a favorisé la formation de métasilicate de lithium, qui favorise la réaction entre le lithium et le silanol, l'ajout excessif d'eau peut être la solution pour supprimer les vides dans le revêtement préparé. Une seconde possibilité, le procédé de dip-coating présente un temps de préparation plus long que celui de spin-coating, le temps de réaction chimique entre le sel de lithium et le silanol est probablement plus long, ce qui permettrait de préparer des films de verre de silicate à teneur élevée en lithium sans vides.

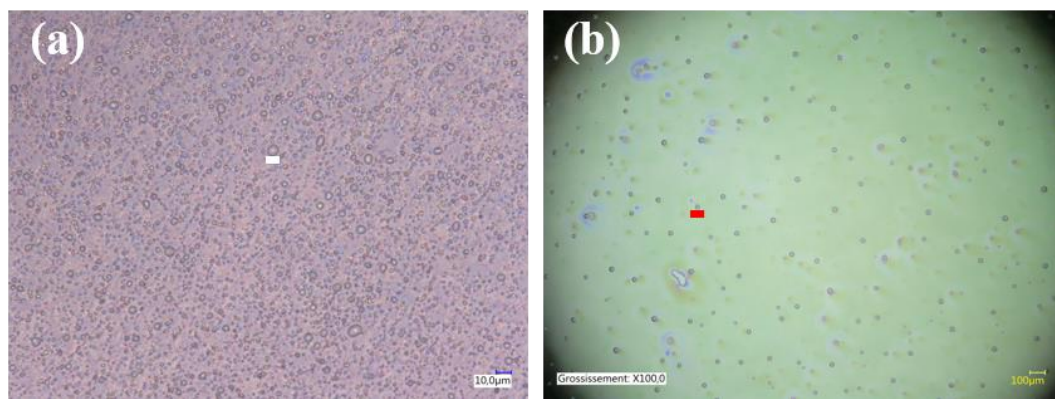


Fig. 8. Revêtement TEOS-C<sub>6</sub>H<sub>5</sub>Li<sub>3</sub>O<sub>7</sub> (a) et TEOS-LiNO<sub>3</sub> (b) au microscope optique (grossissement 300 fois pour (a) et 100 fois pour (b)) trois jours après la préparation des revêtements

Des xérogels de silice massifs et des couches minces de silice présentant une bonne uniformité ont été préparés avec succès. De plus, une forte photoluminescence a été observée à partir du xérogel de silice dopée à l'OPSC ainsi que des couches par illumination sous une lampe UV. Le spectre de photoluminescence a ensuite été étudié et il a été constaté que le pic du spectre de photoluminescence présente un décalage vers les courtes longueurs d'onde par rapport à celui de l'OPSC dilué dans du DCM.

Ainsi, un xérogel de silicate massif à forte teneur en lithium a été préparé en utilisant différents précurseurs de lithium. Ensuite, des films de verre de silicate de lithium correspondants ont été préparés. Cependant, le xérogel de silicate contenant une teneur élevée en lithium a tendance à réagir avec l'eau et quelques vides apparaissent dans le film. Des expériences comparatives ont montré que le temps de vieillissement, les types de précurseurs de lithium et la concentration de lithium peuvent affecter l'apparition des vides dans ces films. Ces vides peuvent être causés par une réaction chimique inadéquate entre le sel de lithium et

le silanol en raison du court laps de temps possible pour les réactions de condensation. Cela indique qu'un ajout d'eau en excès pourrait être une voie envisageable pour supprimer l'apparition de bulles/vides dans le revêtement préparé. Une autre possibilité proposée pour supprimer ces vides consiste à préparer le revêtement de verre de silicate à haute teneur en lithium par dip-coating.

### Chapitre 3

Dans ce chapitre, la molécule OPSCC2 a été utilisée. La structure de l'OPSCC2 est présentée en figure 9. Compte tenu de la température de dégradation des deux molécules, la température de production des verres a été maintenue inférieure ou égale à 300°C.

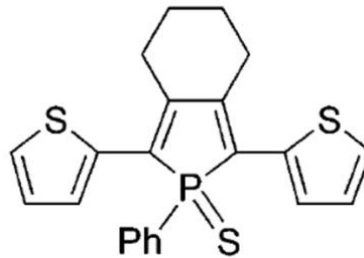


Fig. 9. Structure de OPSCC2

Un verre contenant 25% de  $\text{Li}_2\text{SO}_4$ , 40% de  $\text{Li}_2\text{O}$  et 35% de  $\text{P}_2\text{O}_5$  (LiS25PM) présentant une conductivité ionique supérieure et une faible  $T_g$  a été préparé. La figure 10 présente la courbe DSC et les mesures de conductivités de ce verre. On peut voir que la  $T_g$  du verre LiS25PM est d'environ 297 °C et que la conductivité ionique peut atteindre  $10^{-7}$  S/cm à température ambiante.

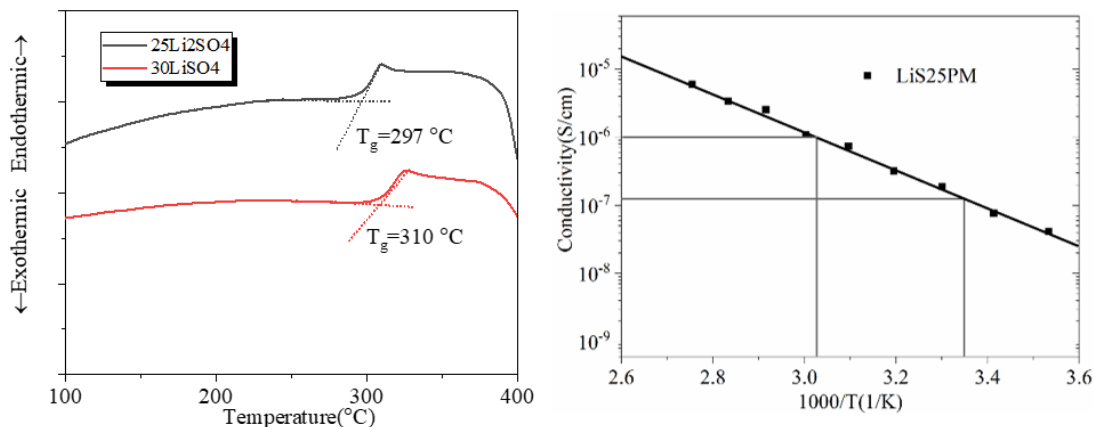


Fig. 10. Courbe DSC des verres de  $\text{Li}_2\text{O}-\text{Li}_2\text{SO}_4-\text{P}_2\text{O}_5$  (à gauche) et diagrammes d'Arrhenius des conductivités en courant continu du verre LiS25PM (à droite)

Sur la base de cette composition de verre contenant 25% de  $\text{Li}_2\text{SO}_4$ , le verre dopé par la molécule OPSCC2 a été préparé avec succès par la méthode de frittage SPS, comme illustré en figure 11. Un échantillon du verre de base (non dopé) a également été préparé par SPS comme échantillon de référence. La Fig. 11 montre que le verre hybride est jaunâtre, couleur similaire à la couleur de la molécule OPSCC2, ceci indique que les molécules sont probablement conservées au cours du processus SPS.



Fig. 11. Photo du verre  $\text{LiS25PS}$  (en haut) et du verre hybride dopé avec l'OPSC (en bas)

Les spectres de photoluminescence et d'excitation (PLE) du verre hybride sont présentés sur la figure 12. L'échantillon hybride a été excité optiquement dans la région des pics d'absorption principaux de l'OSPCC2 (430 nm).

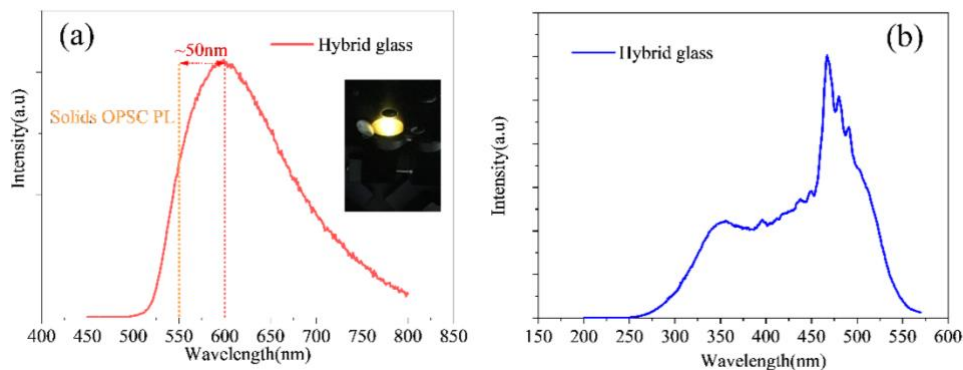


Fig. 12. Spectres PL (a) et PLE (b) du verre hybride

Tout d'abord, une forte PL a été observée à partir du verre hybride montré dans l'encadré de la figure 12 (a) et le pic du spectre PL correspondant est à environ 600 nm. Ceci est une autre preuve convaincante que l'OPSCC2 est conservé pendant le processus de frittage SPS. Comparé à l'émission de l'OPSCC2 solide, un décalage vers le rouge de 50 nm est observé dans l'échantillon du matériau hybride. Cela provient du fait que l'environnement de

coordination est devenu rigide, ce qui a probablement une influence sur le gap HOMO-LUMO de la molécule OPSCC2. Le spectre de PLE avec émission à 600 nm est illustré à la figure 12 (b). Le pic moyen se situe aux alentours de 465 nm, il est également décalé vers le rouge de 30 nm par rapport à celui de l'OPSCC2 solide.

Afin d'examiner la microstructure de la molécule OPSCC2, une observation au microscope électronique à transmission (TEM) a été réalisée. De plus, le TEM est également un moyen envisageable d'étudier la morphologie de l'interface entre l'OPSC et la matrice vitreuse. Les images TEM du verre dopé avec l'OPSCC2 sont présentées en figure 13. La masse atomique de l'OPSCC2 (principalement du carbone) étant beaucoup plus petite que celle de l'hôte du verre (principalement P et O), l'OPSCC2 est claire et la matrice de verre sombre.

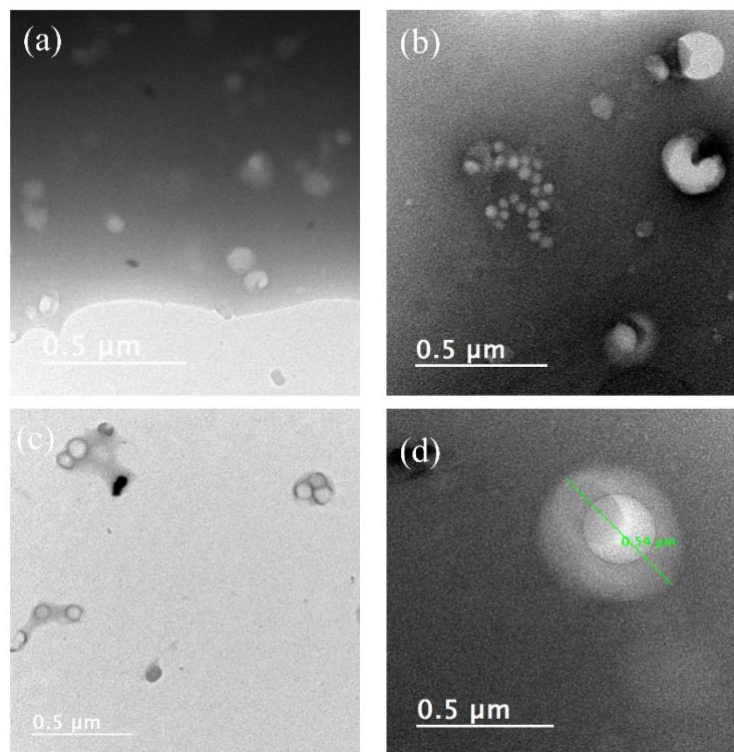


Fig. 13. Images MET des verres hybrides

On peut voir sur la figure 13 (a) que la molécule est en effet distribuée dans la matrice de verre. Cependant, la taille de l'OPSCC2 n'est pas uniforme, de 100 nm à 500 nm, comme indiqué sur la figure 13 (b). Quelques petites pièces de verre hybrides non frittées (inférieures à 500 nm) ont également été observées (figure 13 (c)). La figure montre des nanoparticules dans chaque petit morceau de verre et la taille des nanoparticules OPSCC2 est d'environ 100 nm. La figure 13 (d) montre la plus grande nanoparticule OPSCC2 dans le verre qui a été observée, sa taille est de 540 nm. Aucune structure cristalline n'a été observée par MET.

De plus, une étude RMN du noyau  $^{31}\text{P}$  a été réalisée dans les compositions LiS25PM, le LiS25PS et le verre hybride, les résultats sont présentés à la Fig. 14.

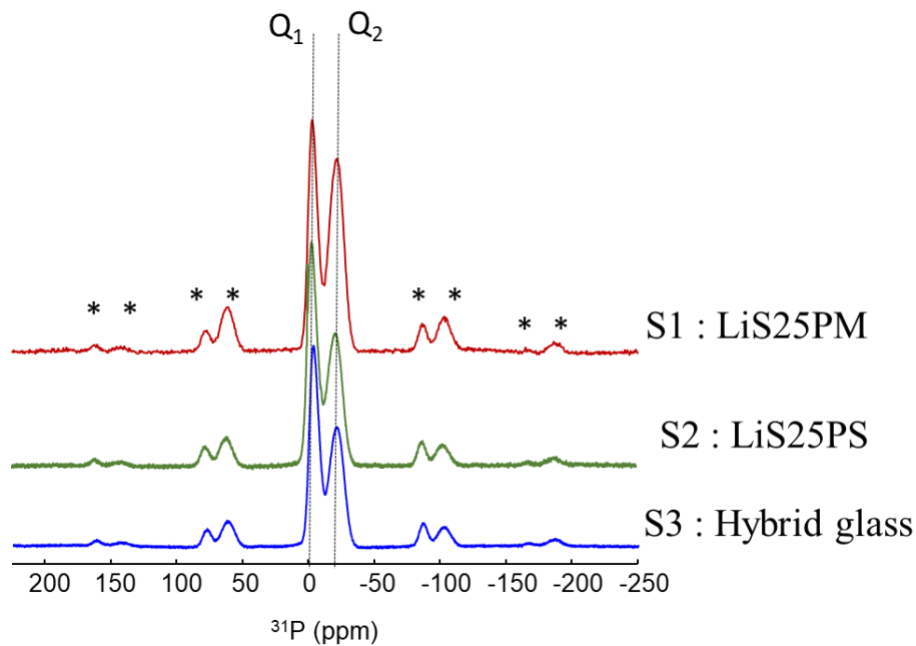


Fig. 14. RMN  $^{31}\text{P}$  de LiS25PM, LiS25PS et du verre hybride

Sur la base des données MET et RMN, il est rationnel de souligner que l'OPSCC2 existe sous forme de nanoparticules amorphes dans la matrice de verre et que la taille moyenne de ces nanoparticules est d'environ 100 nm. Par conséquent, la séparation de phase est conservée à une échelle inférieure au micron, ce qui est bénéfique pour les performances d'un dispositif LEC. En outre, il est raisonnable de souligner qu'il n'y a pas d'accord de liaison entre l'OPSCC2 et le réseau vitreux. Néanmoins, étant donné que l'OPSCC2 existe sous forme de nanoparticules dans la matrice de verre, elles peuvent diminuer le mouvement des ions lithium dans le verre, ce qui peut réduire la conductivité ionique.

La dernière partie est l'étude des propriétés électrochimiques du verre hybride. Tout d'abord, la conductivité ionique du verre hybride a été déterminée par analyse d'impédance complexe (figure 15), les résultats du verre LiS25PS étant donné à titre de référence. Malheureusement, le verre LiS25PS ( $8.1 \times 10^{-8}$  S/cm) et le verre hybride ( $6.1 \times 10^{-8}$  S/cm) ont une conductivité ionique inférieure à celle du LiS25PM ( $10^{-7}$  S/cm), pouvant être causés par des défauts dû au processus de frittage tel que des impuretés, des pores résiduels et des joints de grains.



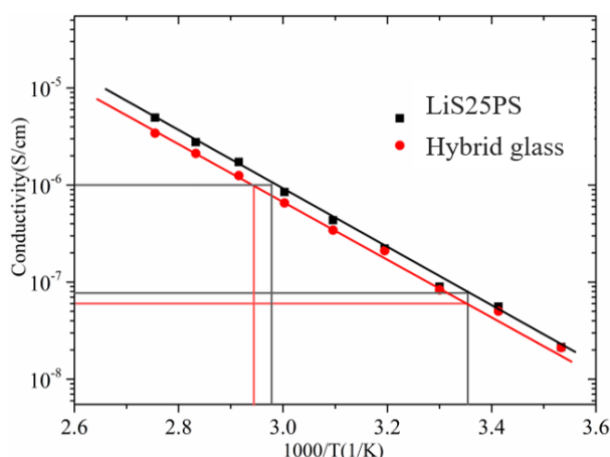


Fig. 15. Diagrammes d'Arrhenius des conductivités en courant continu du LiS25PS et du verre hybride

On peut constater que la conductivité ionique du verre hybride est légèrement inférieure à celle du verre de base LiS25PS. Ceci est cohérent avec de l'effet de «blocage» lié à la présence de molécules OPSCC2. Un matériau monocristallin ou à phase amorphe unique, sans joint de grain, constituerait le support idéal pour une conduction ionique rapide. Par conséquent, la séparation de phase entre la matrice vitreuse et la molécule dans un verre hybride devrait être similaire au comportement des joints de grain rencontré dans des vitrocéramiques.

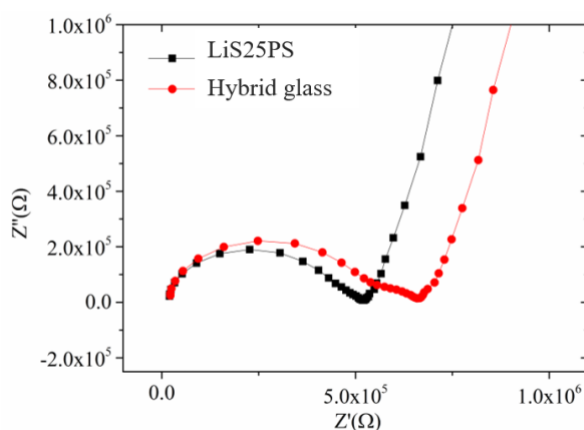


Fig. 16. Parcelles de Nyquist en LiS25PS et verre hybride à 50 ° C

Cette explication est corroborée par les tracés d'impédance complexes du verre LiS25PS et des verres hybrides. La figure 16 montre les courbes d'impédance complexe de LiS25PS et de verre hybride à 50 ° C (dans le but de maintenir une conduction ionique supérieure à  $10^{-7}$  S/cm). Deux demi-cercles, un grand à haute fréquence et un petit à basse fréquence, ont été observés sur les courbes du verre hybride, phénomène non observé sur les autres verres préparés. Ce deuxième demi-cercle est une empreinte typique de la présence de joints de

grain. Bien qu'il n'y ait pas de joints de grain dans la matrice vitreuse, la séparation de phase est probablement à l'origine de la légère diminution de la conductivité ionique. Aussi, même si la conductivité ionique du verre hybride est inférieure à  $10^{-7}$  S/cm à température ambiante, elle peut atteindre  $10^{-6}$  S/cm à environ  $65^{\circ}\text{C}$ , répondant ainsi aux exigences d'un dispositif LEC.

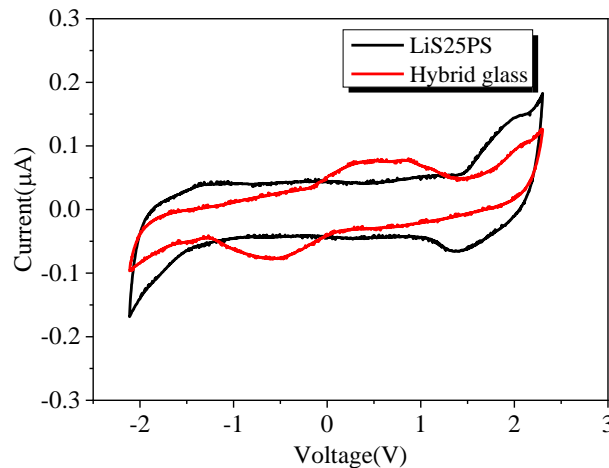


Fig. 17. Mesure de voltamétrie cyclique du verre LiS25PS et de matériau hybride avec une vitesse de balayage de  $0.2 \text{ mV} / \text{S}$  à  $50^{\circ}\text{C}$

Comme mentionné précédemment, le modèle électrochimique suppose que le mécanisme d'une LEC est un processus électrochimique. Par conséquent, un processus de dopage électrochimique de l'OPSCC2 devrait se produire dans le verre hybride. D'autre part, la fenêtre de stabilité électrochimique de l'électrolyte doit être plus large que celle de la molécule. La mesure de voltamétrie cyclique (CV) permet de déterminer la fenêtre de stabilité électrochimique de l'électrolyte de verre ainsi que le processus de dopage électrochimique de l'OPSCC2. Comme le montre la figure 17, des courants anodiques et cathodiques attribuables respectivement à la dissolution de l'or ( $\text{Au} \rightarrow \text{Au}_{3+} + 3\text{e}^{-}$ ) et au dépôt ( $\text{Au}_{3+} + 3\text{e}^{-} \rightarrow \text{Au}$ ) sont observés dans la plage de potentiel de 1,5 à 1,3 V, ce qui indique également une bonne réversibilité. De plus, des courants dus à la décomposition de l'électrolyte sont détectés dans la gamme -2V à 2 V. Dans le verre hybride, outre les pics observés, un couple rédox a été détecté. Ces couples rédox sont liés à la contribution de l'OPSCC2.

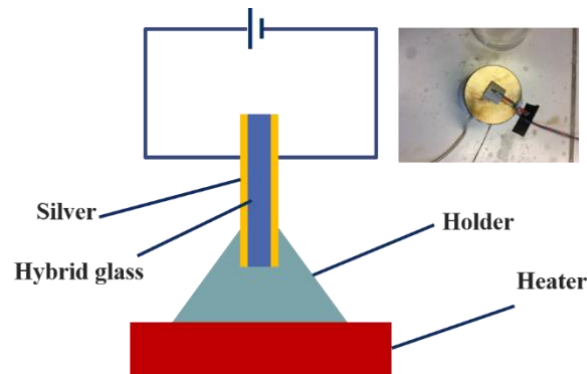


Fig. 18. Schéma de la plateforme pour tester le LEC basé sur le verre hybride

Par la suite, un dispositif LEC basé sur le verre hybride a été fabriqué. L'épaisseur typique du revêtement émetteur d'un LEC est d'environ plusieurs dizaines de microns. Le verre étant fragile, il est très difficile de le polir en dessous de 100 microns. Le verre hybride a été poli à 400 microns pour préparer le dispositif. En raison de l'épaisseur beaucoup plus importante que la normale, un dispositif de chauffage a été utilisé pour augmenter la température du verre dopé afin d'améliorer sa conductivité ionique. Le schéma de la plate-forme expérimentale de test de LEC basé est présenté à la figure 18 et l'encadré montre le dispositif réel. Cependant, nous n'avons pas observé d'électroluminescence à partir du verre hybride même lorsque la température a été augmentée jusqu'à 150 °C.

Plusieurs raisons peuvent expliquer ce résultat:

1. l'épaisseur du verre est encore trop importante;
2. le contact superficiel entre le verre et les électrodes n'est pas parfait;
3. la conductivité ionique est encore trop faible;
4. des impuretés sont introduites par le processus SPS.

Afin de réaliser des LEC, avec des taux de conversion effectifs, ces problèmes devront être résolus dans de futurs travaux.

Pour conclure ce chapitre, nous pouvons mettre en avant le fait qu'une composition de verre au phosphate avec une bonne transmission dans le domaine visible (environ 90%), une faible  $T_g$  (297 °C) et une conductivité ionique relativement élevée ( $10^{-7}$  S/cm) a été obtenue par trempe. Ensuite, sur la base de cette composition de verre, en utilisant un procédé en deux étapes consistant en une trempe et un frittage de poudre par SPS, des verres hybrides dopés à

l'OPSCC2 ont été préparés avec succès. L'observation d'une forte PL du verre hybride montre que l'OPSCC2 n'est pas dégradée au cours du processus de frittage par SPS. Cette constatation est également supportée par les résultats MET. D'après les résultats du MET, la taille de l'OPSCC2 varie de 100 à 500 nm dans le verre dopé. Bien que la morphologie topographique ne puisse pas être mise en évidence par MET, cela suggère que l'échelle de séparation de phase peut atteindre une échelle inférieure au micron. Cela signifie qu'une bonne morphologie peut être obtenue en améliorant les paramètres de mélange. De plus, la conductivité ionique du verre hybride a été déterminée par des tracés d'impédance complexes. Celle-ci peut atteindre  $6.1 \times 10^{-8}$  S/cm et  $10^{-6}$  S/cm à la température ambiante et à 65 °C, respectivement. Enfin, les mesures par voltamétrie cyclique suggèrent qu'un processus de dopage chimique de l'OPSCC2 se produit dans le verre hybride. De plus, la fenêtre de stabilité électrochimique de l'hôte en verre est plus large que celle de l'OPSCC2. Bien qu'aucune électroluminescence du dispositif à base de verre hybride n'ait été observée, sur la base de toutes ces données, il est raisonnable de supposer que ce verre hybride est un bon candidat à utiliser comme matériau émetteur en vue de la réalisation de LEC.

#### Chapitre 4

Au cours du processus de préparation du verre de phosphate pour la préparation de LEC, nous avons observé une luminescence bleue à partir de verres au phosphate et de zinc. Nous avons été intrigué car il existe très peu de travaux sur ce type de verre. Dans ce chapitre, la cause de l'émission dans le verre de zinc amorphe a été étudiée. Après avoir compris la raison de la luminescence bleue, nous avons essayé de trouver une application potentielle à ce verre.

Des verres binaires au phosphate de zinc (40% ZnO - 60% P<sub>2</sub>O<sub>5</sub>) ont été préparés par un procédé classique de fusion-trempe en utilisant un creuset de silice. Des verres constitués de ZnO (99,999%) et de P<sub>2</sub>O<sub>5</sub> (99,99%) sont nommés PO (20g), et les verres obtenus à partir de ZnO (99,999%) et de (NH<sub>4</sub>)<sub>2</sub>HPO<sub>4</sub> (99,99%) sont nommés NHPO (20g). Ensuite, l'un des échantillons NHPO a été placé dans un four tubulaire à travers un flux d'ammoniac à 800 °C pendant 10 h pour obtenir un verre de phosphate de zinc oxynitruré nommé NNHPO. Les verres préparés par P<sub>2</sub>O<sub>5</sub> et les verres dopés au Mn correspondants sont respectivement désignés par PO et PO<sub>x</sub>Mn (x = 0,3, 0,6, 1,0, 1,5, 2,0); le verre préparé par NH<sub>4</sub>H<sub>2</sub>PO<sub>4</sub> et les verres dopés Mn correspondants correspondent respectivement à NHPO et NHPO<sub>x</sub>Mn (x = 0,3, 0,6, 1,0, 1,5, 2,0).

La figure 19 (a) affiche les spectres d'absorption des échantillons préparés. Tout d'abord, on peut voir dans la zone de transparence qu'il n'y a aucun signe de centres de couleur ou d'autres

bandes d'absorption formées par des impuretés. De plus, le pic d'absorption des compositions PO, NHPO et NNHPO est située au-dessous de 300 nm, avec une forte augmentation de l'absorption à 220, 230 et 250 nm. Les décalages du bord d'absorption sont très probablement liés au réarrangement structural du verre. Les échantillons de verre NHPO et NNHPO montrent une large émission autour de 420 nm lorsqu'ils sont excités à 250 nm, les spectres d'excitation de photoluminescence (PLE) et de photoluminescence (PL) sont représentés sur les figures 19 (b) et (c). Les mécanismes proposés correspondants pour les émissions de lumière bleue sont illustrés dans l'encadré de la figure 19 (d). Les émissions violettes et bleues sont attribuées aux transitions des états  $Zn_i$  et  $Zn_i$  étendus à la bande de valence, respectivement. Il convient de noter que la bande d'émission dans le verre NNHPO présente un décalage vers le rouge par rapport à celui du verre NHPO (figure 19 (c)). Un autre comportement typique de la PL des clusters de ZnO amorphes est la courte durée de vie atteignant un niveau de l'ordre de la nanoseconde.

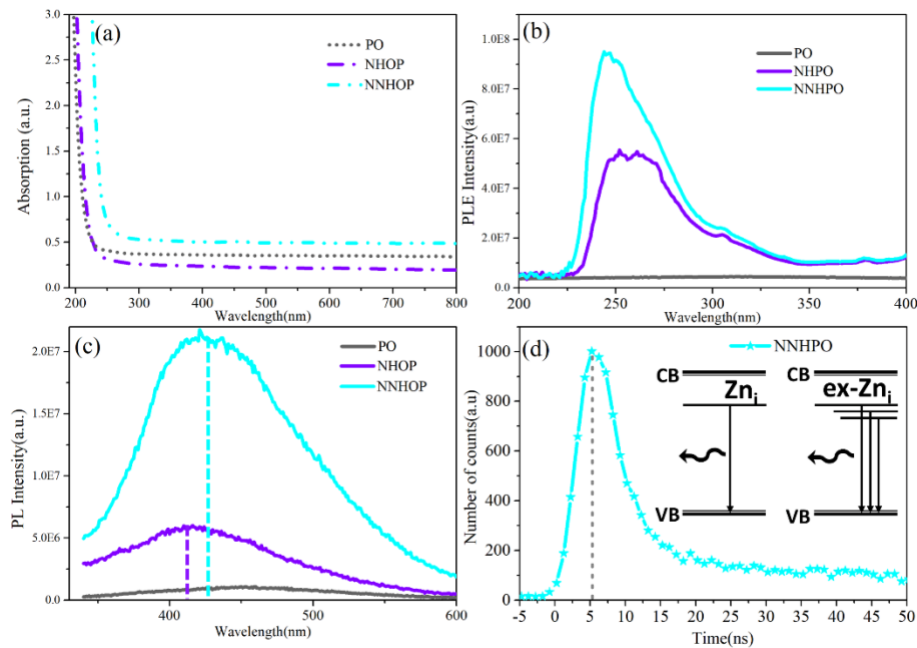


Fig. 19. Spectres d'absorption (a), excitation (b), photoluminescence (c) des échantillons préparés et spectre de décroissance de luminescence (d) du verre NNHPO.

La décroissance de luminescence de NNHPO a été mesurée à 420 nm sous une excitation d'impulsions nanoseconde à 250 nm. L'émission ultra-rapide avec le temps de décroissance a été mesurée comme indiqué sur la figure 19 (d). On peut voir que le temps de décroissance de NNHPO peut atteindre le niveau de la nanoseconde. Sur la base de ces résultats, malgré l'absence de bande d'émission UV intrinsèque évidente, il est possible de souligner que

l'émission bleue dans l'échantillon de verre préparé doit appartenir à une certaine forme de ZnO amorphe.

Pour trouver la raison de l'intensité plus forte et fournir plus d'informations sur la microstructure des échantillons de verre préparés, la microscopie électronique à transmission (MET) a été étudiée et est présentée Fig. 20 et Fig. 20 (a), (b), (c) pour les verres PO, NHPO, NNHPO, respectivement. Comme on peut le voir sur les figures 20 (a)-(c), une certaine agrégation à l'échelle nanométrique s'est formée dans un échantillon NHPO et NNHPO, mais ne s'est pas formée dans le verre PO, ce qui correspond aux propriétés de luminescence des échantillons de verre. Par conséquent, il est raisonnable de souligner que ces agrégations à l'échelle nanométrique sont des clusters de ZnO et que les images MET indiquent à nouveau que ces clusters de ZnO sont amorphes. De plus, la taille ou l'échelle des amas de ZnO à l'échelle nanométrique amorphes (ANZC : Amorphous Nanometric Zinc Cluster) dans NNHPO est plus grande que celles dans NHPO, ce qui expliquerait la forte intensité de l'émission bleue dans NNHPO. Cette ANZC présente la possibilité de former des états Zni plus étendus, ce qui provoquerait le décalage vers le rouge de la bande d'émission de NNHPO.

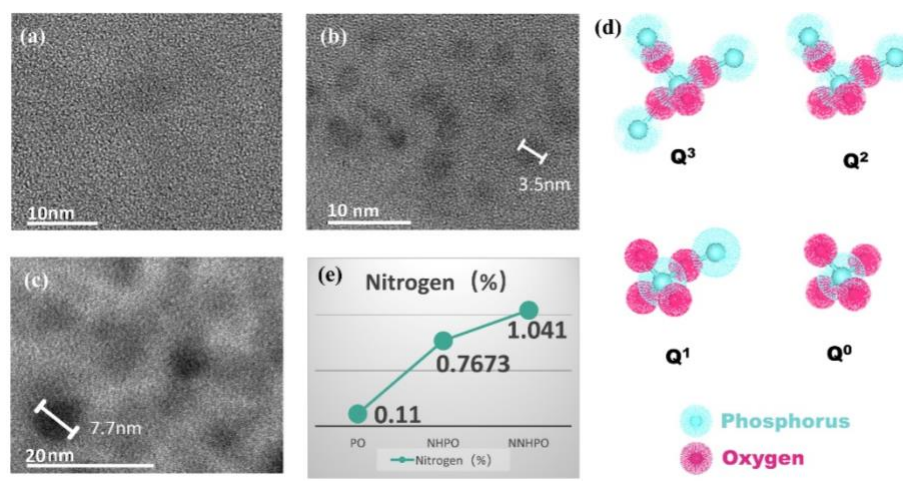


Fig. 20. Image en microscopie électronique à transmission des échantillons PO (a), NHPO (b) et NNHPO (c); (d) unités tétraédriques des phosphates - atomes d'oxygène (rose) reliés à des atomes de phosphore (bleus); e) teneur en azote dans les échantillons de verre préparés (% en poids)

Cependant, la raison pour laquelle les échantillons de verre présentent différents phénomènes ANZC nous intrigue profondément. Les tétraèdres de phosphate ont un, deux, trois oxygènes pontants. Ces unités peuvent être classées en utilisant la terminologie  $Q_i$ , où  $i$  représente le nombre d'atomes d'oxygène pontés par tétraèdre, comme indiqué sur la figure 20 (d). Il a été constaté que l'azote peut être présent sous forme de verre phosphate = N- ou > N-, comme le

montre la figure 21 (a). Le spectre Raman des échantillons préparés présenté à la figure 21 (b)(c) suggère que les contraintes topologiques des verres préparés sont modifiées.

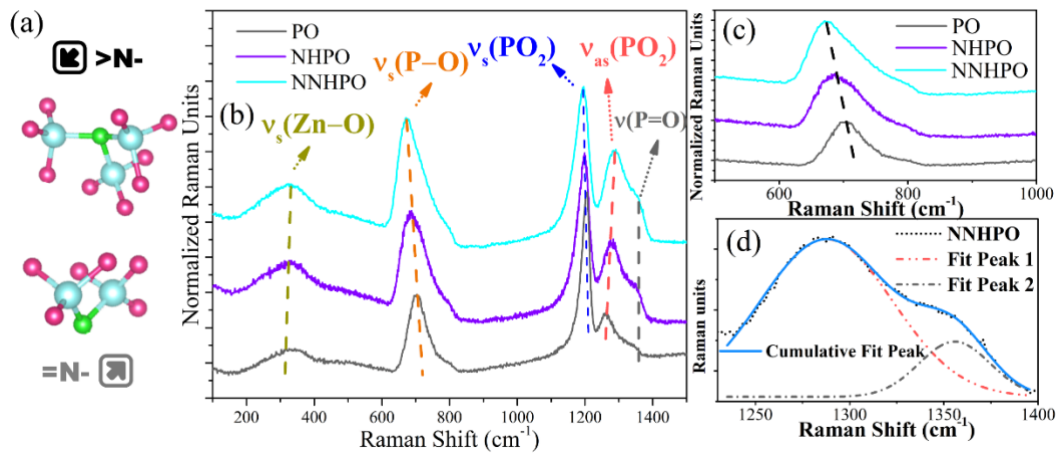


Fig. 21. (a) Schéma des possibilités de liaison de l'azote dans des verres de phosphate; (b) spectres Raman des verres PO, NHPO et NNHPO; (c) le pic  $\nu$  (P-O) des échantillons de PO, NHPO et NNHPO; (d) déconvolution du pic du spectre Raman du verre NNHPO

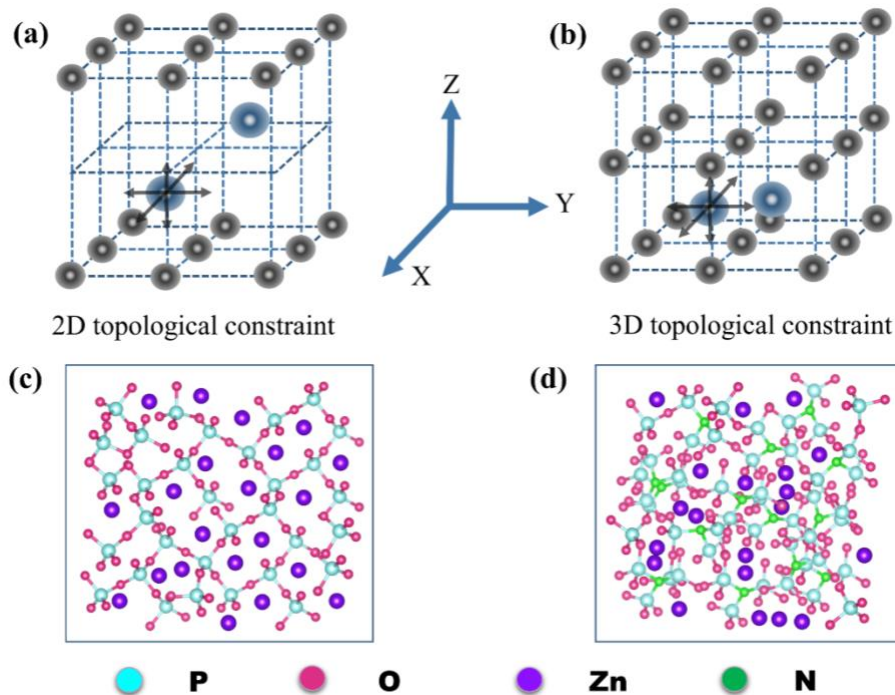


Fig. 22. Illustration schématique montrant le niveau de difficulté de l'évolution des grappes de ZnO dans les sous-réseaux structurés en 2D (a) et en 3D (b). Schéma de la mésosstructure de PO (c) et de NNHPO (d)

La matrice de verre PO se déplace vers une chaîne bidimensionnelle ("type polymère") en 2D et ces chaînes ne présentent pratiquement pas de liaisons croisées. D'après l'illustration schématique des sous-réseaux 2D (figure 22 (a)), on peut voir dans cette configuration topologique que les polyèdres ZnO sont aisément déplaçables dans les directions X et Y et

que la seule contrainte topologique se trouve la direction Z. La figure 22 (c) montre l'illustration schématique de la mésostructure du verre correspondant, des chaînes “semblables à des polymères” sans liaisons croisées. Normalement, une configuration topologique avec une seule contrainte de direction ne tend pas à former une agrégation. Alors que, dans NHPO et NNHPO, la teneur en “oxygène libre” a été réduite en raison de la diminution du nombre de groupes hydroxy et en particulier de l'ajout d'azote. Ceci peut conduire à la séparation de tétraèdres de ZnO du réseau vitreux et le transformer en modificateur de verre sous forme octaédrique. De plus, l'azote modifie également la matrice de verre à partir de chaînes 2D “ressemblant à un polymère” à une structure de cadre tridimensionnelle (3D) en formant des entités  $>N-$  susceptibles de provoquer des réticulations entre chaînes. L'illustration des sous-réseaux présentée à la figure 22 (b) montre que, dans cette configuration, les polyèdres ZnO sont difficiles à déplacer, quelle que soit la direction X, Y ou Z. Le schéma de la mésostructure du verre correspondant comportant des liaisons croisées causées par des entités  $>N-$  est illustré sur la figure 22 (d). Cette configuration 3D avec des contraintes dans 3 directions “expulserait” des polyèdres ZnO, modificateurs de verre, formant ainsi des agrégats de ZnO amorphes. En outre et dans une certaine mesure, plus le niveau d'entités  $>N-$  est grand, plus la structure du verre sera asymétrique et compacte. Par conséquent, il est plus facile de former des ANZC plus étendus dans le NNHPO que dans les NHPO, ce qui illustre une PL plus intense dans les premiers verres cités.

Après avoir compris la formation d'ANZC dans le verre, nous avons souhaité mettre en évidence une application potentielle de ce type de matériau, l'étude s'est portée sur des diodes électroluminescentes blanches (pc-WLED : phosphor-converted white light-emitting diodes). Ces dernières années, l'émergence de recherches sur les verres luminescents émettant de la lumière blanche par émission de terres rares (REF) suggère que ce type de verre luminescent semble être un nouveau matériau compatible pour des applications pc-WLED. Dans ce travail, nous proposons une solution pc-WLED unique à base de ANZC au phosphate de zinc dopé au manganèse. En outre, le verre présentant ce phénomène de luminescence de lumière blanche chaude présente un CRI (Color Rendering Index) élevé et une température de couleur basse, des caractéristiques comparables au phosphore cristallin à haute efficacité lumineuse.

La figure 23 (a) schématise un dispositif pc-WLED basé sur le verre préparé et la figure 23(b) le photoluminescence d'échantillons de verres NHPO dopés  $Mn^{2+}$  excités à 250 nm. La figure 23 (b) montre le PL des échantillons excités à 250 nm. De toute évidence, le transfert d'énergie entre les ions amorphes ZnO et  $Mn^{2+}$  s'est produit.



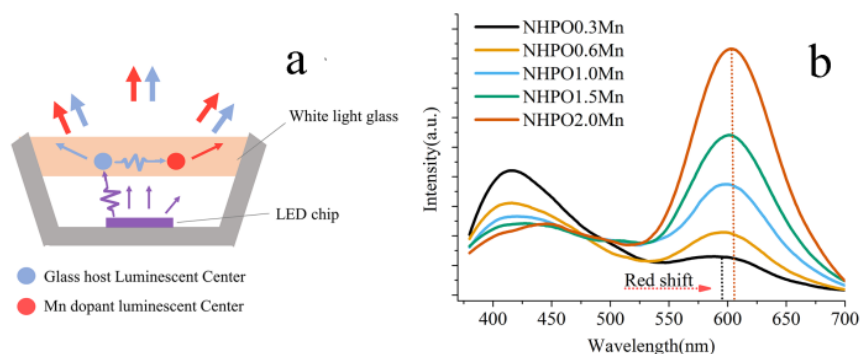


Fig. 23. (a) Schéma d'un dispositif pc-WLED basé sur un verre NHPO dopés  $Mn^{2+}$  et (b) PL d'échantillons de verres NHPO dopés  $Mn^{2+}$  excités à 250 nm.

Les coordonnées chromatiques de la CIE (Commission internationale de l'éclairage) des échantillons de verre  $NHPO_xMn$  ( $x = 0.3, 0.6, 1.0, 1.5$  et  $2.0$ ), calculées sur la base du spectre d'émission correspondant, sont représentées à la Fig. 24. Des détails complémentaires sont présentés dans le tableau 2.

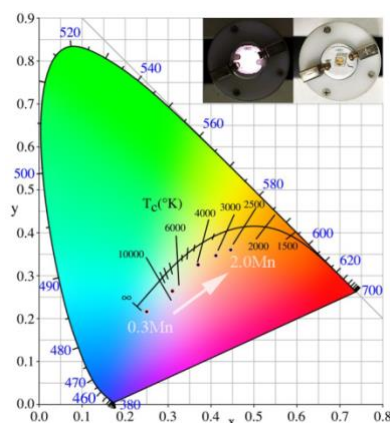


Fig. 24. Diagrammes de chromaticité CIE des échantillons de verres NHPO dopés  $Mn^{2+}$ ; encart: photographie de la WLED réalisée basée sur un échantillon de verre  $NHPO_{1.5}Mn$ , allumée (à gauche) et éteinte (à droite)

Tableau 2. Coordonnées CIE et température de couleur des NHPO dopés  $Mn^{2+}$

Verres	coordonnées CIE		Température de couleur (K)
	X	Y	
NHPO0.3Mn	0.25	0.23	>10000
NHPO0.6Mn	0.31	0.27	8000
NHPO1.0Mn	0.37	0.33	3998
NHPO1.5Mn	0.41	0.35	3000
NHPO2.0Mn	0.44	0.36	2500

L'échantillon  $NHPO_{1.0}Mn$  présente des valeurs CIE de  $x = 0.37$  et  $y = 0.33$ , ce qui correspond à celles attendues pour un matériau émettant de la lumière blanche pure. En outre, il a été constaté que la température de couleur était de 3998 K, valeur attendue pour une source de lumière blanche chaude. De même, une efficacité quantique externe élevée (1%) a

été obtenue. De plus, les WLED encapsulées à base des verres synthétisés ont été préparées. La longueur d'onde d'excitation optimale n'ayant pas été utilisée, des recherches complémentaires devrait permettre d'améliorer ces résultats. Les pc-WLED encapsulés réalisées à partir du verre NHPO1.5Mn ont des valeurs de CIE :  $x = 0.33$ ,  $y = 0.35$ ; TDC avec 5228 K;  $R_a = 86$ . Ces excellentes propriétés rendent ce verre extrêmement prometteur pour la réalisation de WLED à couleur chaude avec l'utilisation d'une LED UV appropriée.

En résumé et à notre connaissance, une émission de bleu aussi intense et ultra-rapide a été observée pour la première fois dans un verre d'oxynitride de phosphate de zinc. Selon le spectre de PL et le spectre de décroissance de la luminescence, l'émission a été attribuée à des amas de ZnO nanométriques amorphes, supposition qui a été validée par des images MET des échantillons de verres préparés. L'intégration de l'azote dans le réseau de verre est la clé pour obtenir ces clusters de ZnO nanométriques amorphes. L'azote module les contraintes topologiques de la matrice de verre de la 2D à la 3D en passant par la réticulation des chaînes de verre via des entités  $>N-$ . Les contraintes topologiques 3D forment des clusters de ZnO nanométriques amorphes plus étendus, qui conduisent à une PL plus forte. Sur la base de ce verre, des verres d'oxynitride de phosphate de zinc dopés au magnésium présentant une lumière blanche chaude sous excitation UV ont été préparés. Parmi ceux-ci, l'échantillon NHPO1.0Mn montre des valeurs de CIE, une température de couleur qui correspondent aux critères recherchés pour un matériau émettant de la lumière blanche pure et chaude.

### **Conclusion générale**

Dans ce travail, notre objectif principal a été de développer un nouveau dispositif LEC basé sur un électrolyte en verre inorganique dopé par un semi-conducteur organophosphoré. Ces matériaux hybrides ne pouvant être synthétisé en utilisant la technique classique de fusion-trempe, les technologies sol-gel et SPS ont été utilisées pour préparer le verre hybride.

Dans le cas du procédé sol-gel, des films de verre de silice dopée par des molécules organophosphorées semi-conductrices ont été préparés avec succès. Cependant, certains vides ont été générés dans les films de verres contenant une teneur élevée en lithium, c'est-à-dire ceux présentant une conductivité ionique souhaitée pour une application LEC. Les raisons probables de la génération de ces vides ont été identifiées et des travaux seront effectués pour réaliser des améliorations.

Dans le cas de la technologie SPS, le verre hybride a été également été préparé avec succès. Les propriétés optiques, la microstructure et les propriétés électrochimiques du verre hybride ont été étudiées. Les résultats montrent que ce verre hybride peut être utilisé dans un dispositif

LEC, qui a ainsi été préparé. Cependant, aucune électroluminescence n'a été observée à partir de l'échantillon de verre hybride. Cela peut être dû aux raisons suivantes: 1. l'épaisseur du verre est encore trop grande; 2. le contact superficiel entre le verre et les électrodes n'est pas optimal; 3. la conductivité ionique est encore trop faible; 4. des impuretés sont introduites lors du processus SPS. Ces problèmes devront être réglés pour pouvoir observer une luminescence à partir des dispositifs réalisés.

Au cours du processus de préparation de LECs, nous avons observé une luminescence bleue à partir de verres de phosphate contenant du zinc. Nous avons démontré que cette luminescence bleue provient de clusters amorphes de zinc nanométriques dans le verre. L'introduction d'azote module les contraintes topologiques de la matrice vitreuse de la 2D à la 3D en jouant sur la réticulation des chaînes de verre. Les contraintes topologiques 3D forment des clusters nanométriques de ZnO amorphes plus étendues conduisant à une PL plus intense. Finalement, après avoir compris la raison de la luminescence bleue, nous avons préparé avec succès des diodes électroluminescentes blanches à conversion de phosphore à partir des verres de phosphate contenant des clusters nanométriques de ZnO amorphes.

## GENERAL INTRODUCTION

Artificial lighting is one of the most important driving forces of modern society. The consumption of electrical energy in the lighting sector was ca. 3500 TW hour in 2012, which is corresponding to an equivalent CO<sub>2</sub> production of 1900 Mt. Since we become more and more concerned about saving energy and decreasing greenhouse gases, lighting represents one of primary fields to update existing technologies and searching for alternative efficient illuminants is obviously an efficient way. On the other hand, the evolution of technology request inventive products with advanced device architectures. Organic electroluminescent devices are always efficient, thin and flexible. Besides, they can be even transparent, which makes them a promising alternative to their inorganic analogs.

In 1953, A. Bernanose and coworkers firstly reported electroluminescence from organic materials. However, subsequent advancement of organic electroluminescent materials was not obtained until 1987 because of the requirement of high drive voltages, which causes poor power efficiencies. In 1987, Tang and Friend invented organic and polymer light-emitting diodes (OLEDs), which made the device already meet the typical performances of fluorescent tubes. It also started the current period of global OLED research and development. A diode with a bilayer structure by vapor deposition of thin films of organic semiconductors was developed by them. Electrodes with work functions that carrier injection in the organics was relatively efficient was used. Furthermore, the bilayer structure promoted recombination at the interface between the two organic semiconducting films in order to avoid significant losses related to electroluminescence quenching at the electrodes.

In an efficient OLED operation, electrons and holes are requested to recombine in the bulk of the organic semiconductor, which avoids electroluminescence quenching at the electrodes. In order to achieve this target, efficient and balanced carrier injection and transport in the organics is the most primary. Electron injection in organic semiconductors occurs in the lowest unoccupied molecular orbital (LUMO), whereas hole injection occurs in the highest occupied molecular orbital (HOMO). That means, in efficient OLEDs, one high- and one low-work function electrode are ask for efficient hole and electron injection, respectively. Then, the mobility of these injected charge carriers depends on the different types of semiconductor. This transportation of carriers happens through thermally activated tunneling of the charge carriers among localized sites in a disordered energy landscape. Normally, the organic films in OLEDs should be extremely thin (below hundreds of nanometers) to obtain efficient operation. Electroluminescence in OLEDs happens through recombination of electrons and

holes that may form singlet and triplet exciton pairs, which can be transition radiatively, transition non-radiatively, or dissociate. Typically, the emitted phonons are with an energy that is close to the bandgap of the organic semiconductor. However, with only one organic layer, OLEDs can not achieve a good balance between electrons and holes. Therefore, a bilayer or more organic layers which could promote injection and the mobilities of charge carrier was introduced in OLED to avoid these problems. As a result, production costs of OLEDs are considerable delaying their large-scale market entry for lighting applications.

In 1994, Pei and co-workers found that the properties of OLEDs can be drastically adjusted by blending high concentrations of mobile ions with a conjugated polymer and an organic solid electrolyte. Besides, the behavior of the device does not work like a diode because it shows emission in reverse bias and the light intensity is similar for both bias polarities. They thought the electrochemical oxidation and reduction of the conjugated polymer cause the injection of electronic charges from the electrodes. This is the origin of the name of the new devices (light-emitting electrochemical cells or LECs). In their work, the turn-on voltage is around the bandgap of the conjugated polymer semiconductor. Moreover, it indicates that air stable materials can be the electrodes of the efficient device, despite the consequent large injection barrier for electron injection. Two decades later, a lot of emitting alternatives have been reported including ionic transition metal complex (iTMC), small molecule (SM), quantum-dot (QD) and nanoparticle (NP). Normally, the emitter requirements are a reversible electrochemical behavior and a high photoluminescence quantum yield in solid-state. On the other hand, besides the emitter material, the electrolyte is also crucial for the performance of LEC devices. However, although there are many researches focused on electrolytes for LEC containing polymer poly (ethylene oxide) (PEO), oligoether-based material and ionic liquids, the researchers are still seeking a more ideal electrolyte for making LEC.

Up to now, there are very few works focused on inorganic electrolyte for a LEC device. As glass researchers, we are intrigued by the promise of making a LEC based on inorganic glass electrolyte. On one hand, most of those organic electrolytes are environmentally hazardous compared with inorganic glass electrolyte, which side against the concept of green technology. On the other hand, compared to some organic electrolytes, inorganic glass possesses comparative ionic conductivity, better physical chemistry stability and better ultraviolet (UV) prevention ability. It is well known that the main challenge for LEC technology is to lower the degradation of the organic emitter, which deeply depends on the stability and UV prevention ability of the blend electrolyte. Therefore, the good stability and ultraviolet prevention ability of glass would prevent the degradation of organic emitter in a LEC. However, the

morphology of the blend of organic molecule and electrolyte is a key point of a LEC device too. Thus, an organic emitter which not only possesses high photoluminescence quantum yield in solid-state, but also can form a good blend with glass electrolyte is seeking for a LEC based on glass electrolyte.

The name of phosphorus is originated from ancient greek phos and phorus, which means light and bringing, respectively. This is because of the strong light of white phosphorus. However, the high reactivity and toxicity of many P containing derivatives prevent its application in emitting devices. This situation changes after that chemists are able to stabilize and protect the P-atom, which suggests the organophosphorus derivatives based opto-electronic devices can be made. Interestingly, while the organophosphorus derivatives have been investigated for decades, their insertion into devices has been recently achieved. However, to our best knowledge, there is few reports on the LEC based on organophosphorus derivatives, let alone the LEC based on organophosphorus derivatives doped glass electrolyte host.

The main objective of this work is to develop a new LEC device based on organophosphorus doped inorganic glass electrolyte, which cannot be synthesized by using classic melt-quenching technique. That because the melting temperature of glass is always much higher than the degradation temperature of organic molecule. In first chapter, the background and mechanism of LEC were introduced. Thus, the second and third chapter is devoted to obtain the LEC through Sol-gel and spark plasm sintering (SPS), respectively. Moreover, during the process of preparing the LEC by SPS, an interesting phenomenon was found. A broadband blue emission was observed in rare-earth free zinc phosphate oxynitride glass. The fourth chapter is focus on this interesting phenomenon.



## **Chapter I: Light-emitting electrochemical cell**





## 1. Introduction

The light-emitting electrochemical cell (LEC) is a planar layered device, which is comprised of an electroluminescent organic semiconductor (OSC) and mobile ions as the active material sandwiched between an anode and a cathode, as depicted schematically in Fig. 1.1(left). It has been considered as the leading example of the simplest thin-film lighting device. Sometimes, LEC also can be prepared through a planar structure as shown in Fig. 1.1(right). Typically, both the active-material and electrode layers can be very thin (around 100 nm), so a substrate to provide mechanical robustness to the layers is needed. Moreover, since the emission is generated within the active layer, one electrode (may contain substrate) of the device needs to be transparent, whereas the other electrode commonly is reflective in order to get efficient lighting.

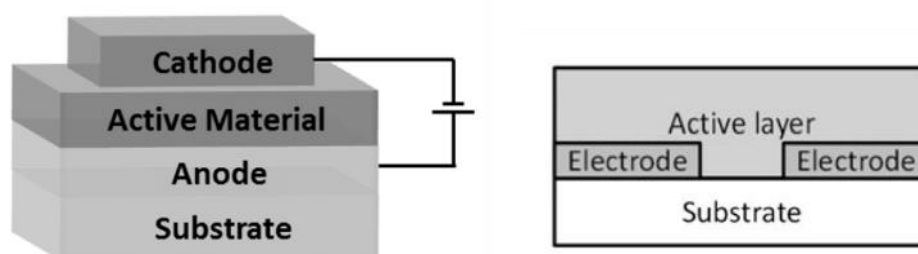


Fig. 1.1. The schematic structure of a sandwich-cell device(left) and a planar-cell device(right) with a single-layer active material

Interestingly, unlike a diode, although different work function electrodes were used, the device does not block current in reverse bias. This behavior is illustrated in the current-voltage characteristic shown in Fig. 1.2.

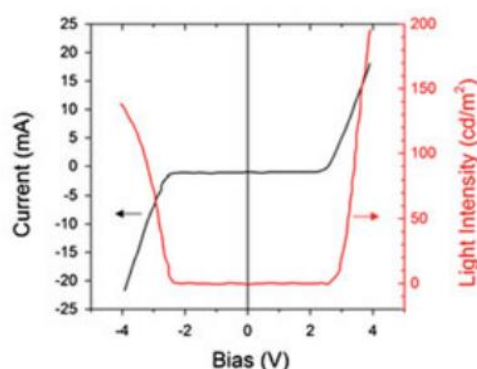


Fig. 1.2. Current-voltage-luminescence characteristic of a typical LEC

The light intensity is similar for both bias polarities, showing that the device possesses the same efficiency in both forward and reverse bias conditions, despite the presence of large injection barriers for at least one of the biasing conditions. At the same time, compare to

OLEDs, a LEC can operate efficiently at low voltages. The turn-on voltage of the cell is found to be around the bandgap of the emitting semiconductor.

The first LEC device was invented by Pei and coworkers, who used a conjugated polymer (CP) as the OSC and a solid polymer electrolyte, poly(ethylene oxide) (PEO), as the source of mobile ions in their pioneering study published in 1995<sup>1</sup>. At nearly the same time Lee et al. showed a LEC with efficient electroluminescence based on an ionic transition-metal complex (iTMC) sandwiched in between two electrodes<sup>2</sup>. They used a tris-ruthenium(II) sodium salt with a bandgap of roughly 2.6 eV and the corresponding light-voltage and current-voltage curves and structure of iTMC is shown in Fig. 1.3 and the inset, respectively. Moreover, the combined use of ions and organic semiconductors in LECs is not limited to these materials. These will be detailed in section 1.3 and 1.4.

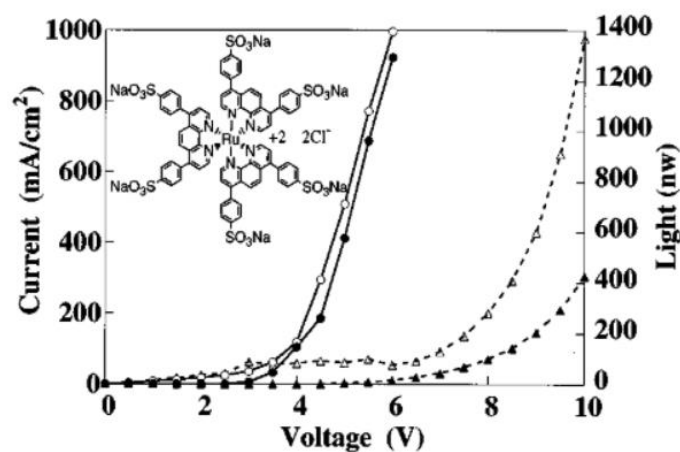


Fig. 1.3. Right current (open symbols) and luminance (closed symbols) characteristics of iTMC-based LECs, in which the iTMC layer is formed by spin-coating (circles) and self-assembly (triangles)<sup>2</sup>

The applications benefit from large-area fabrication such as lighting and signage was thought to be the most promising field for LECs. However, the longer turn on time limits LEC use for further application in high-end displays<sup>3</sup>. This is because, compare to OLEDs, LECs always show a longer turn-on times ranging from milliseconds to hours depending on the ionic conductivity of the light-emitting layer. Besides turn on time, Stephan van Reenen et al. reviewed the figures of merit of LEC performance as follows<sup>4</sup>:

1. The turn-on time ( $t_{on}$ ), which is defined by the time from switch-on of the cell by application of a bias voltage to the luminance reaching a certain predefined level.
2. The luminance ( $cd/m^2$ ), a measure of the brightness of the LEC, shows the amount of luminous power per unit area which is corrected for the wavelength-dependence of the sensitivity of the human eye.

3. The electroluminescent efficiency ( $Eff_{max}$ ), which can be expressed either in lm/W (power efficiency) or cd/A (efficacy) where  $1 \text{ lm} = 1 \text{ cd} \cdot \text{sr}$ .  $Eff_{max}$  describes the conversion efficiency of electronic carriers in photons, which is also corrected by the sensitivity curve of the human eye.

4. External quantum efficiency (EQE), which is the ratio of photons emerging from the device per injected electrons. Another definition is through the equation  $EQE = b\Phi/2n^2$ , where  $b$  is the recombination efficiency (equal to unity for two ohmic contacts),  $\Phi$  is photoluminescence quantum yields, and  $n$  is the refractive index of the glass substrate.

5. The lifetime ( $t_{1/2}$ ), which is defined by the time for the luminance to decay to half-maximum or to below a certain threshold that can depend on the foreseen application.

6. Color coordinates, which can be described by the three colors mapping functions  $x(\lambda)$ ,  $\bar{y}(\lambda)$  and  $\bar{z}(\lambda)$  based on the definition of Commission Internationale de l'Eclairage (CIE), are used to compare color in a standardized way.

Considering the inherent tolerance to layer thickness variations, which will be discussed in the 1.1 sections, LECs highlights the primary advantage: low cost by virtue of facile solution-based fabrication. It should be noted that the total manufacturing costs of an LEC device also contain the cost of materials, substrate, electrodes, and packaging. Regarding further application of LECs in the future, it is important to optimize the key features of LECs as opposed to OLEDs.

Table 1-1 Comparison of different types of organic light-emitting devices, OLEDs and LECs

Parameter	OLEDs	LECs	Benefits of LECs
Active layers	4 or more	1 or 2	Simple device architecture
Typical thickness per layer	60-120 nm	100-500 nm	Thicker films promise robust processes
Electrodes	Air sensitive	Air stable	Air stable metals can be used
Encapsulation requirements	High	Low	Air stable electrodes promise less demanding packaging
Processing of organic layers	Vacuum-based	Solution-based	Cost-efficient preparing processing
Solvent	n.a.	Benign	Environmental friendly

Table 1-1 gives a rough overview and summarizes the advantages of LECs. LECs can not only be made based on conventional substrates like foil and glass, but also can be fabricated on a large range of different kinds of substrates such as fibers, papers, flexible material, and even on complex-shaped surfaces like kitchen forks<sup>7</sup>. It seems that the current industry still put the attention on OLEDs because of their energy efficiency, color quality, and high-contrast ability. A primary advantage of organics is to reduce the cost of the technology, which, however, has not been obtained today. LEC, obviously, is a strong promising device to

reach the target described by Sandström and Edman<sup>7</sup>. They pointed that if LECs are produced with a reasonable luminance of 1000 cd/m<sup>2</sup> in a high-volume roll-to-roll-coating scenario, then the cost per lumen would be roughly 0.0036 €/lm. And this cost would decrease one order of magnitude of the current projected costs for LEDs and OLEDs<sup>7</sup>.

## 2. Operational Mechanisms for LECs

Since the discovery of the LEC concept in 1995,<sup>1,8</sup> several techniques like electrostatic force microscopy (EFM), microcavity effects, scanning Kelvin probe microscopy (SKPM), time-of-flight secondary ion mass spectroscopy (ToF-SIMS), numerical modelling, electrochemical impedance spectroscopy (EIS), optical-beam-induced-current imaging of frozen p–i–n junctions, and current–voltage characteristics have thoughtfully been used for studying the impact of the ions on the device mechanism. <sup>9-53</sup> However, the related scientific community spend nearly 2 decades to reach a consensus about the device mechanism <sup>13,14</sup>.

### 2.1 Electrochemical Model (ECM)

The electrochemical doping model was first reported by Pei et al.<sup>1 24</sup> and later on supported by the work of theoretical calculation by Smith<sup>24</sup> and Manzanares et al. <sup>25</sup>. As shown in Fig 1.4(a), if a voltage that shows  $V > E_g/e$  is applied for the device, where  $E_g$  is the band-gap of the emitter and  $e$  is the elementary charge, injection of electrons and holes at the electrode interfaces would cause an electrochemical doping of the active layer. Moreover, injection of electrons and holes leads, respectively, to the oxidation and reduction of the semiconductor at the anode and the cathode. The oxidized and reduced semiconductor is electrostatically compensated by anions and cations from the related electrolyte, respectively, which results in p-type and n-type doped regions in the bulk. The presence of small and mobile ions keeps the doped regions to be stable, which can control their movement well based on the continuous charge injection. Since the doped regions close to the electrode interfaces, regardless of the work function of the electrodes, it can efficiently assist charge injection. Except the doped region, there is still intrinsic region which called *i*, which is between n and p doped regions. And this region is the place where injected electronic charges recombine. Both the request of time to form the *i* region and its position are decided by the growth and stabilization of the doped regions. Moreover, the characteristic of the electrochemical mechanism is that a large electric field would form in the *i* region and a small electric field also forms in the doped regions, causing the externally applied potential difference drops in the boundary.

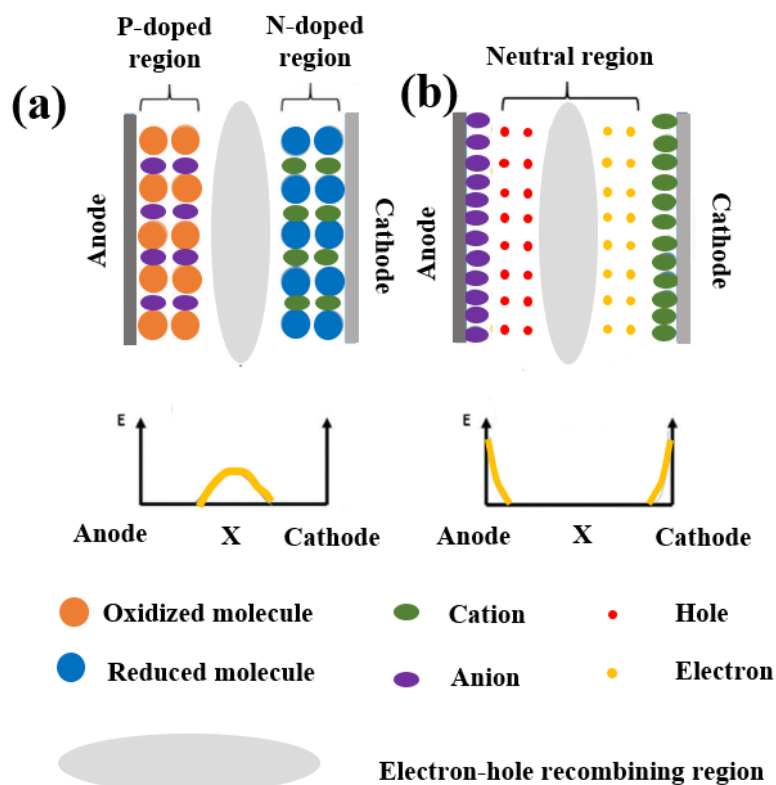


Fig. 1.4. Electrochemical (a) and electrodynamic (b) models proposed for the LEC operation. The associated spatial distribution of the electric field is shown underneath

## 2.2 Electrodynamic Model (EDM)







The electrodynamic mode<sup>9-11</sup> was proposed by Demello and co-workers which was further supported by Slinker and co-workers in 2007 through an EFM technique applied to planar iTMC-based LECs<sup>12</sup>. As shown in Fig. 1.4 (b), due to the applying bias voltage, the movement of the mobile ions cause the formation of thin electric double layers (EDLs) at the electrode interfaces. As a result, the charge injection at the electrodes happened due to the large interfacial electric field. The ions continue to redistribute in the coating until a quasi steady-state is reached, which dissipates the local electric field throughout the coating. This is the characteristic of EDM.

## 2.3 Current Consensus Understanding of Operational Mechanism of LECs

Both of the aforementioned models agree that the presence of ions provides a unique device behavior. However, the only difference is how the carrier injection occurs. In 2007, the groups of Ginger, Kemerink and their co-workers demonstrated that both the fingerprint of ECM and EDM can be achieved by varying the work function of the electrode metal<sup>13</sup>. Actually, systematic experiments<sup>26,53</sup> and numerical modeling<sup>53,54</sup> also have confirmed this

fact. More exactly, the applicability of each model was found to decide by the ability to form Ohmic injecting contacts.

Table 1-2 Overview of the universal operational mechanism of light-emitting electrochemical cells (reproduced from ref 4)

<b>Light-emitting electrochemical cells</b>			
<b>Requirement</b> (depends on applied bias voltage and injection barriers)	0 ohmic contacts	1 ohmic contact	2 ohmic contacts
<b>Operating mechanism</b>	<b>EDM</b>	<b>PECM</b>	<b>ECM</b>
<b>Voltage distribution</b> (back line) and <b>Recombination zone</b> (orange)			
<b>Electron (•), Hole (◦), anion (⊖), cation (⊕) distributions:</b>			

An ohmic contact is a non-rectifying electrical junction: a junction between two conductors that has a linear current–voltage (I-V) curve as with Ohm's law. Low resistance ohmic contacts are used to allow charge to flow easily in both directions between the two conductors, without blocking due to rectification or excess power dissipation due to voltage thresholds. This Ohmic injecting contacts depends on a combination of applied bias voltage and the height of the barriers for carrier injection. If no Ohmic contacts are formed, the LEC shows the EDM behavior; if Ohmic contacts are formed, the LEC shows the ECM behavior. For the Ohmic contacts situation, there actually are two kinds, namely one Ohmic contact (one electrode interface) and two Ohmic contacts (two electrode interfaces). Thus, for only one Ohmic contact, normally only p-type doped regions or n-type doped regions is formed at the anode or the cathode, respectively, which also called preferential ECM (PECM). This consensus model for these LECs based on CP and iTMC emitters has been confirmed by various experimental and numerical studies<sup>1,2,4,11,14,25,26,55</sup>. An overview of this unifying model is shown in Table 1-2.

## 2.4 Transient Phenomena

The ions in the electrolyte of LECs cause operation of these cells extremely time-dependent. Normally, it takes far less than a second to reach quasi-steady state for electronic movement

in organic semiconductors. However, compare to OLEDs, the movement of ions are much slower in LECs since they need to physically move through a solid-state material. Thus, turn-on times in LECs can range from several seconds <sup>1</sup> to several hours, <sup>19</sup> which is decided by the combination of the constituents and the active layer thickness as well as the applied bias voltage.

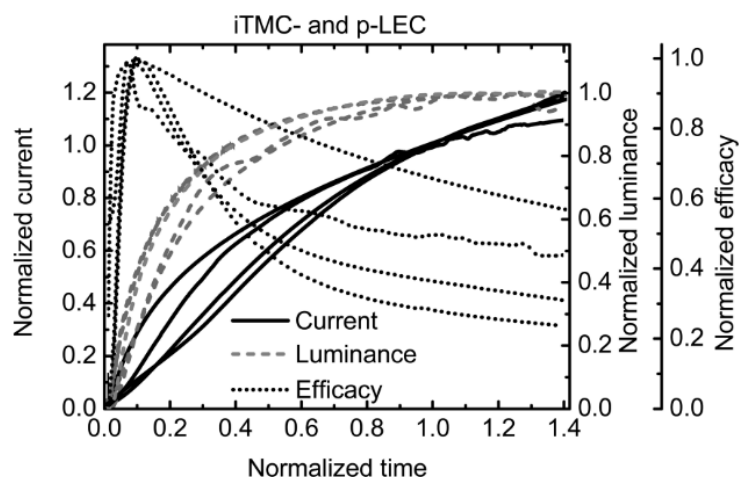


Fig. 1.5. Normalized current, luminance, and efficacy transients of polymer and iTMC-LECs at two temperatures each and biased at 3.5 V <sup>46</sup>

Large quantitative differences are observed in the turn-on transients based on these vast amounts of LECs configurations studies and reports <sup>19,23,46,56-61</sup>. It can be found that the turn-on transients of CP-based LECs in stacked and planar configuration show strong qualitative resemblance with the same architecture iTMC-based LECs. Van Reenen et al. reported the work on the resemblance of two architectures <sup>4</sup>. In this work, the time-dependent current, luminance, and efficacy just after switch-on of freshly prepared CP- and iTMC-based LECs were studied. The result shows that the temperature strongly affects the timescale of turn-on process. This temperature dependence is scaled out through normalizing to the turn-on time. Furthermore, both types of LECs show a universal shape based on normalized current, luminance and efficacy, which is shown in Fig. 1.5. Moreover, the activation energy of the turn-on time and the ionic conductivity measured in the off-state were similar. This indicates that the turn-on of LECs is definitely determined by the ionic conduction.

## 2.5 Planar LECs configuration

Planar LECs configuration has allowed researchers to investigate the active layer through various experimental surface techniques. As shown in Fig. 1.6 (a) and (b), this allowed researchers to study the luminescence including electroluminescence (EL) and photoluminescence (PL) position in LECs. PL studies are always using UV illumination to



excite the semiconductor. It is known, electrochemical doping of semiconductors can quench PL. Therefore, this technique can be used to investigate the dynamic electrochemical doping process in LECs during turn-on<sup>23,55,59,62</sup>. As shown in Fig. 1.6 (a) and (b), as both p- and n-type doping quench the UV-excited PL, the doped regions appear darker than undoped regions. In Fig. 1.6(c)–(e) schematic drawings of the anion and cation concentration distributions in LECs are shown before operation (c), during doping front progression (d), and in steady state (e)<sup>50</sup>. These experiments show that p- and n-type electrochemical doping occurs in the LEC by accelerating doping fronts that move through the active layer, starting from the electrodes, until both meet<sup>63</sup>. The position where the p- and n-type doping fronts meet coincides with the region where light emission takes place as shown in the photograph of 26 s (last one) in Fig. 1.6 (a).

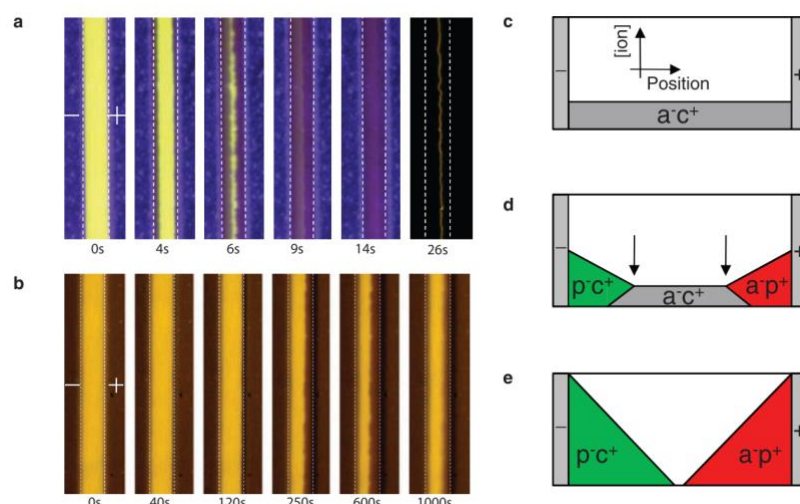


Fig. 1.6. Photographs of planar Au/SY-PPV + PEO + KCF<sub>3</sub>SO<sub>3</sub>/Au LECs with an interelectrode gap of  $\sim 90 \mu\text{m}$  during operation at  $V \text{ bias} = 8 \text{ V}$  and  $T = 333 \text{ K}$ . Two different SY-PPV:PEO:KCF<sub>3</sub>SO<sub>3</sub> weight ratios were used: a) 1:1.35:0.25 – ion-rich and b) 1:1.35:0.06 – ion-poor. c–e) The ionic redistribution and doping process is schematically shown in. a<sup>-</sup> (red area), c<sup>+</sup> (green area), p<sup>-</sup>, and p<sup>+</sup> refer to anions, cations, reduced polymer, and oxidized polymer respectively. In the gray regions, the anion and cation concentrations are equal. The arrows in (d) indicate the position of the doping fronts<sup>4,50</sup>.

The corresponding device current keeps growing during front propagation and after the fronts connect (Fig. 1.7(a)). The continuous electrochemical doping of the doped regions contributes to the increasing current. From the Fig. 1.6 (a) (9s and 14s), it can be found that quenching of PL is enhanced after doping front connection. Other reports have shown that as well, besides this continuation of doping after front connection, the recombination zone can also shift towards the anode or the cathode with time<sup>23,50</sup>. Van Reenen et al. studied the turn-on in planar cells by means of a numerical drift-diffusion model. The transient current (see Fig. 1.7 b) that qualitatively reproduces the experiment can be calculated (Fig. 1.7 a)<sup>62</sup>. The potential

profile evolution in the active layer was studied experimentally by use of scanning Kelvin probe microscopy and numerically, the results are shown in Fig 1.7 c and d, respectively.

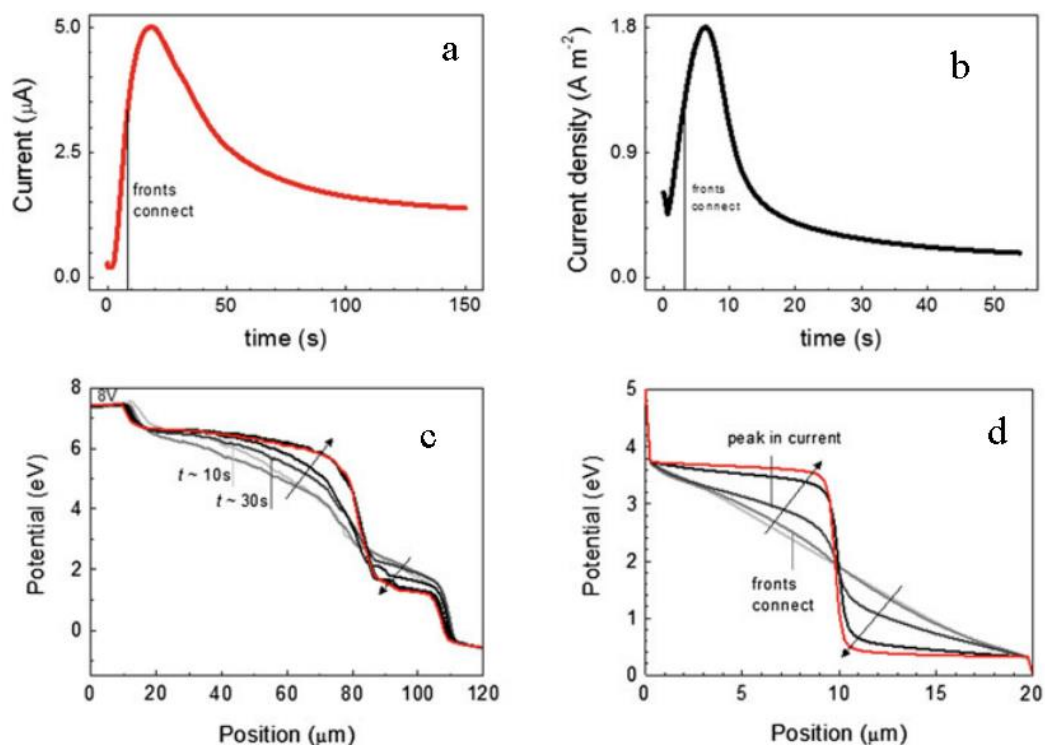


Fig. 1.7. a) Current measured during turn-on of the planar CP-based LEC shown at Fig 1.6a. b) Modeled current in a planar CP-based LEC. c) Experimental potential profile evolution during turn-on of a similar planar CP-based LEC as shown at the Fig 1.6a. d) Modeled potential profile evolution of a planar CP-based LEC<sub>4</sub>

After application of a bias voltage, charges are injected. Electric double layers form at the interfaces, see Fig. 1.7 (c) and (d), enabling carrier injection and consequently n-type and p-type electrochemical doping of the active layer. The p- (a-p<sup>+</sup>) and n-type (c+p<sup>-</sup>) doping fronts propagate towards each other while splitting the available paired ions (a-c<sup>+</sup>) for the doping process (see Fig 1.6 (d)). As shown in Fig. 1.7 (c) (at  $t \sim 10\text{ s}$ ) and (d) (as indicated), the potential is distributed almost evenly across the active layer when the fronts meet. Doping does not stop until all the mobile ions are contributing the electrochemical doping. This is the reason for the continues increasing current. The current gets a highest value in both the model and experiment. During this period, it can be found that the potential change dramatically, which becomes distributed mainly recombination region as shown in Fig. 1.7 (c) (at  $t \sim 30\text{ s}$ ) and (d) (as indicated). The model displays that, meantime, the recombination zone becomes depleted of ions. Thus, the recombination zone becomes intrinsic, i.e., undoped, and therefore has a lower conductivity. Compare to the high conductivity in the chemical doped regions, this lower conductivity of the recombination zone requires a larger field to have current conservation across the device. In Fig. 1.7 (a) and (b), the drop of the current is because the voltage redistributes around the recombination zone. The interesting properties about carrier

mobilities and local field distributions are always intriguing the researchers, therefore the formation of electrochemically doping front in planar LECs has been a major topic.

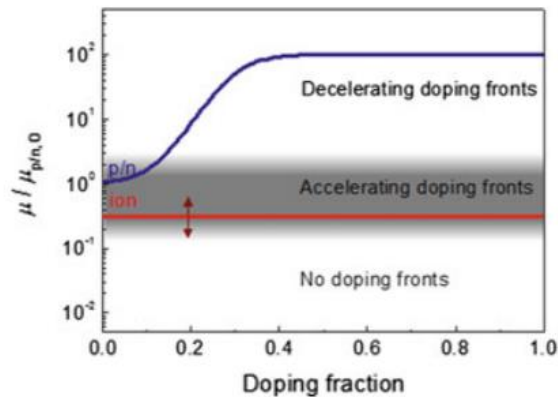


Fig. 1.8. Schematic of the ion mobility criteria with respect to the doping dependent electron and hole mobility (blue line) that result in the formation of accelerating doping fronts in LECs during switch-on <sup>62</sup>

Several experimental studies<sup>64-66</sup> have been performed on these fronts as well as analytical <sup>47</sup> <sup>67</sup> and numerical modeling <sup>68</sup>. Robinson and co-workers developed an analytical model that predicts the position of the doping fronts and the resultant switch-on time <sup>62</sup>. In ref <sup>62</sup>, S. van Reenen et al. shows that accelerating doping fronts are only formed in case a doping dependent  $\mu_{p/n}$  is chosen in addition to  $\mu_{ion}$  being approximately equal to  $\mu_{p/n}$  in the undoped state ( $\mu_{p/n,0}$ ), where  $\mu_{p/n}$  and  $\mu_{ion}$  represents a factor of doping density dependency of the electron/hole mobility and ion mobility, respectively, which is detailed in the reference <sup>62</sup>, the schematic is shown in Fig. 1.8.

In the electrochemically doped systems, compare to the mobility enhanced by field effect, the mobility enhanced by the doping density is stronger <sup>47</sup>. It seems that doping sites can act like a charge traps at low doping densities, which causes a low mobility in weakly doped semiconductors <sup>69</sup>. At higher doping densities, neighboring doping sites are so close to move even without the additional energy to escape the energetically favorable trap <sup>47,69</sup>. That is the reason for the enhanced mobility of the carriers in highly doped system. Both doping fronts are unstable with small perturbations and different outcomes at the nonlinear stage, as shown in Figs 1.9(a), (b), (c). This makes another typical feature of doping fronts in planar LECs, the formation of some peaks similar to “fingers”. An example of this is shown in Fig. 1.9(d). Moreover, a higher applied voltage would increase the instability <sup>70</sup>. In order to further know this behavior, Bychkov et al. work on various numerical modeling studies on the propagation of doping front <sup>22,71</sup>.

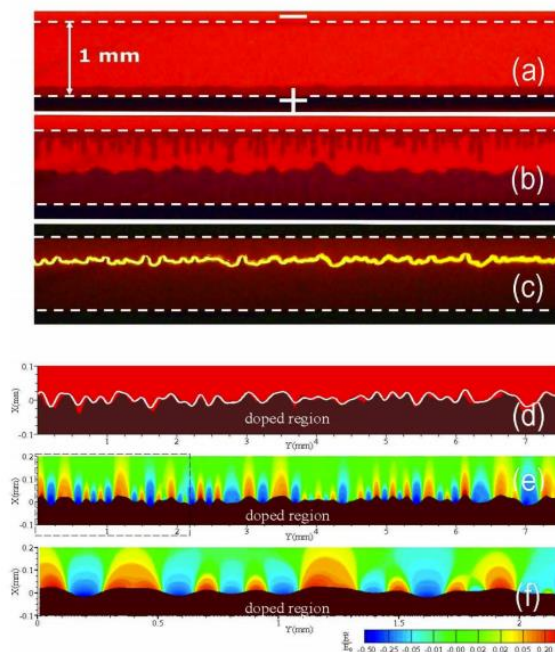


Fig. 1.9. Experimental photos of the doping fronts demonstrate development of the instability at the initial stage (a),  $t = 46$  s, at the developed stage (b),  $t = 80$  s, and the dynamic p-n junction (c),  $t > 170$  s. Plot (d) compares the p-front shapes obtained in the simulations (white curve) and experiments (shading) at 70 s. Plots (e), (f) show relative increase of the electric field in the undoped region obtained numerically for the whole front squeezed along Y-axis, (e), and for the selected part with equal scales, (f).<sup>69</sup>

It was found that the local electric field at the apexes of the doping front is relatively high (Fig. 1.9 (e), (f)), which accelerates the doping front propagation locally. This leads to an enhancement of the finger shape and this process explains the instability at the doping fronts and allowed the researchers to model a similarly shaped doping front.

## 2.6 Sandwich LECs configuration

Similar to in planar LECs configuration, the ions transport also dominates the turn-on time in stacked LECs configuration. Van Reenen et al. study these transients by a calculated model<sup>57</sup>. They tried to use the determined ion mobility and density simulate the turn-on transient of the same CP-based LEC based on the experimental data of the ion conductivity using electrochemical impedance spectroscopy,<sup>57</sup> which is display in Fig. 1.10 dashed line. It was found the timescale of the simulated transient is different from the experiment. The modeled turn time is shorter than that of experiments, however, which can be explained by the binding energy between the ions.<sup>25</sup> (see Fig. 1.10 solid line).

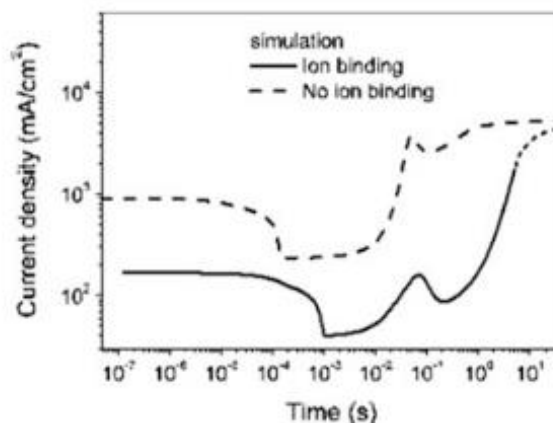


Fig. 1.10. Modeled current transient of a LEC biased at 3.5 V with (straight line) and without (dashed line) binding energy between anions and cations.<sup>4</sup>

### 3. Emitter for LECs

Most of the aforementioned breakthroughs in LECs have been achieved using CP and iTMC emitters. Some typical CP and iTMC emitters are shown in Fig. 1.11 and Fig. 1.12, respectively. CP consist in a polymeric structure where monomers are pi-conjugated system such as PPV (PolyPhenylene Vynylene, Fig. 1.11). This polymer display fluorescence around 554 nm.

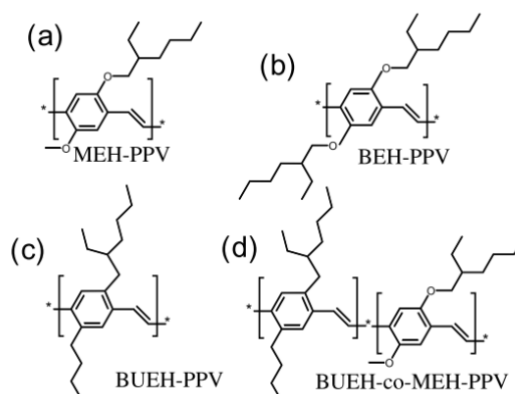


Fig. 1.11. Chemical structures of some typical conjugated polymers

Another strategy consists in using triplet emitters based on transition metal complexes (Ru complexes, Ir complexes etc, Fig. 1.12) featuring bipyridine or phenylpyridine based ligands. These compounds have been widely used in the context of OLEDs. Tuning metal center and ligands allow tuning the emission wavelength from blue to red. However, a limitation of photoluminescence features was found based on only these materials. For example, there are just a few examples of blue, red and infra-red emitting LECs based on these materials.<sup>72-79</sup> Therefore, the researchers in LECs field has started to carry out the other library of emitters for LECs – i.e., copper(I) complexes, small molecules (SMs), quantum dots (QDs), and nanoparticles (NPs).

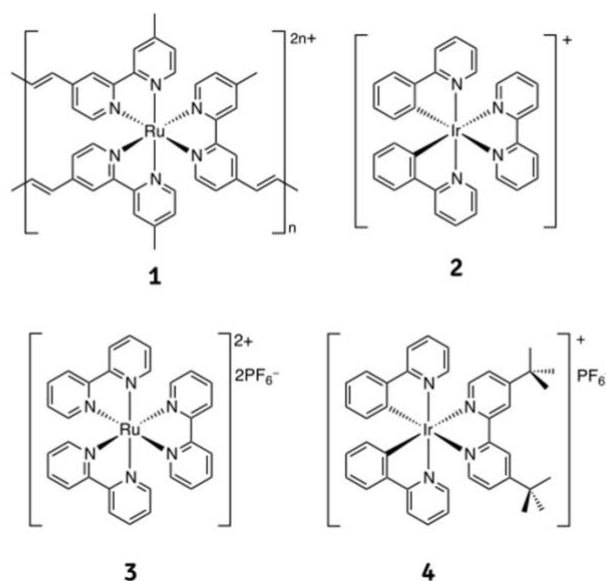


Fig. 1.12. Chemical structures of the iTMCs. Compound 1 is the first iTMC used for LECs: poly-[Ru(vbpy)<sub>3</sub>]<sup>2n+</sup>, vbpy=4-vinyl-4'-methyl-2,2'-bipyridine; Compound 2 is the archetypal complex of the largest class of Ir(III)-iTMCs used in LECs: [Ir(ppy)<sub>2</sub>(bpy)]<sup>+</sup> in which ppy is 2-phenylpyridine and bpy is 2,2'-bipyridine; Compound 3 is [Ru(bpy)<sub>3</sub>][PF<sub>6</sub>]<sub>2</sub>; Compound 4 is [Ir(ppy)<sub>2</sub>(dtb-bpy)][PF<sub>6</sub>].

### 3.1 Copper(I) complexes

Since the abundance, low cost, well-known chemistry, and high photo-luminescence features, copper(I) complexes have intrigued the researchers. In 1978, McMillin and co-workers found heteroleptic copper(I) complexes containing N- and P-coordinating ligands.<sup>80,81</sup> Not long after that, Nishikawa's group attributed the photoluminescence mechanism to efficient thermally activated delayed fluorescence (TADF) process.<sup>82</sup> Briefly, compounds with a small energy gap between the singlet and triplet excited states can emit a delayed fluorescence emission that is thermally promoted. This means it is possible to form a triplet excited state upon electro-hole recombination in fluorescent materials. It indicates that these fluorescent emitters can be highly efficient like phosphorescence emitters. However, they were not reported being used in thin-film lighting devices until recent days.<sup>83-85</sup> D. Costa et al. detailly reviews the state-of-the-art LECs based on copper(I) complexes in ref<sup>86</sup>. Here, we make a brief introduction. The chemical structures of the different families of compounds are provided in Fig. 1.13-17 (reproduced from ref<sup>54</sup>), the most relevant figures-of-merit of the devices were summarized in ref<sup>54</sup>.

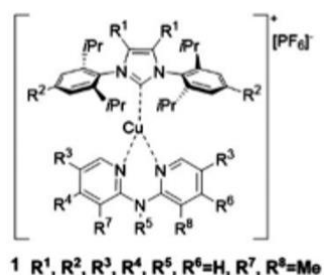


Fig. 1.13. Chemical structures of the copper(I) complexes 1.

As shown in Fig. 1.13, complex **1** is the NHC-copper(I) dipyridylamine complex, which was the first blue-emitting LEC obtained by D. Costa et al in 2016<sup>87</sup>. They noted that the complexes have a TADF emission mechanism. This complex is the most promising blue-emitting copper(I) complexes in the work:  $\lambda_{em} = 458$  nm;  $\phi = 0.86$ , which were applied into LECs. LECs with the ITO/PEDOT:PSS/**1** (100 nm)/Al architecture were investigated based on I–V–L assays and different pulsed current densities. However, a strong luminance decay was observed since the repetitive I–V–L experiments lead the device unstable. The authors think this is because the electrochemical behavior of this family of complexes is not satisfying. Even then, the luminance level and the efficiency are comparative to most of the blue-emitting LECs based on iridium (III) complexes.<sup>88-91</sup>

Compounds **2** and **3** in Fig 1.14 are the heteroleptic copper(I) complexes, which were discovered by Wang and Armaroli's groups in 2006.<sup>92,93</sup> The thin films based on these compounds showed a broad emission peaked at 520 nm with a  $\phi$  value of 0.70.

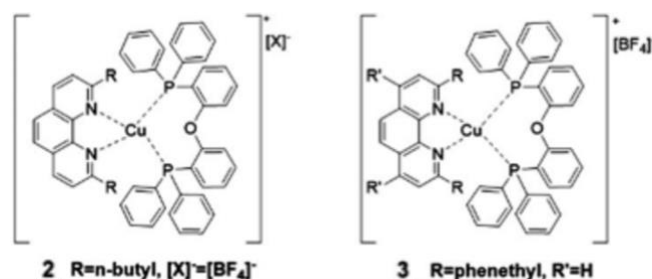


Fig. 1.14. Chemical structures of the copper(I) complexes 2-3.

Compounds **4** and **5** are yellow-emitting copper(I) complexes which were discovered by Bolink, Constable, Housecroft and co-workers in 2014, as shown in Fig. 1.15. In the compounds, P∧P was POP and N∧N were different bipyridine derivatives bearing methyl groups at the positions 6 and 6'.<sup>94</sup> The LEC devices with the composition complex **4** and **5**:[EMIM][PF6] in a molar ratio 1 : 1 shows the  $\phi$  values of 0.01 and 0.05, respectively.

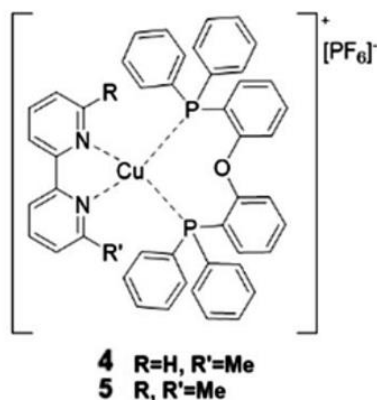


Fig. 1.15. Chemical structures of the copper(I) complexes 4-5.

More recently, compounds **6**, **7**, **8** and **9** were proposed by Costa and co-workers by modifying bpy at the 4 and 4' positions with MeO, Me, H, NO<sub>2</sub>, respectively, which enhance the device performance.<sup>95</sup> These compound shows the emission peaked at 548 nm (**6**), 570 nm (**7**) and 600 nm (**8**, **9**), respectively. Besides, the  $\phi$  values of LEC devices based on these complexes were enhanced up to 0.19.

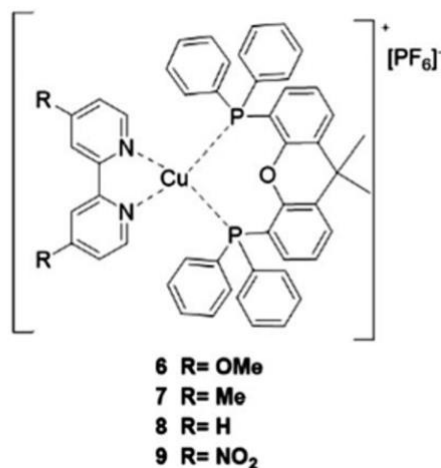


Fig. 1.16. Chemical structures of the copper(I) complexes 6-9.

On the one hand, De Cola, Bruggeller, and co-workers reported a study on a yellow emitting dinuclear copper(I) complex based on a rigid tetraphosphine bridge and 2,9-dimethyl-1,10-phenanthroline (**10**) – Fig. 1.17.<sup>94</sup> These complexes showed a yellowish green emission (550 nm) with a  $\phi$  value of 0.49.

The first example of an orange-emitting LEC was prepared in 2005, at almost the same time, the first LEC based on copper(I) complexes was reported.<sup>96</sup> As shown in Fig. 1.17, a yellow-emitting ( $\lambda_{em} = 570$  nm) dinuclear copper(I) complex (**11**) was prepared by Teng, Fu, and co-



workers<sup>97</sup>. I–V–L assays showed a low turn-on voltage of around 2 V with a maximum efficiency of 0.16 cd A<sup>-1</sup> at 12 V for the LEC device based on these complexes.

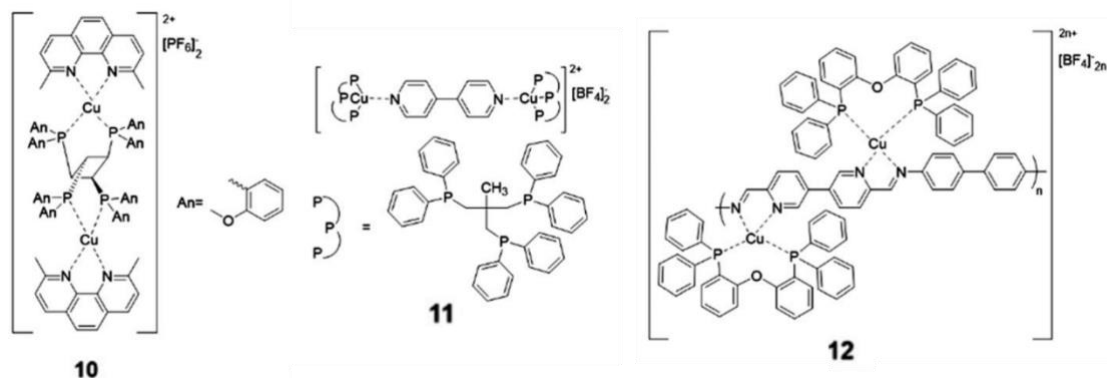


Fig. 1.17. Chemical structures of the copper(I) complexes 10-12.

After that, Friend and co-workers reported the first LECs based on a copper(I) complex polymer (**12**) – Fig. 1.17.<sup>98</sup> The corresponding LEC device emitted a broad spectrum with an infrared light (800 nm) at a low applied voltage of 8 V. In very recently, Housecroft, Sessolo, Ortí and co-workers investigated the synthesis and characterization of five [Cu(P<sup>^</sup>P)(N<sup>^</sup>N)][PF<sub>6</sub>] complexes<sup>99</sup>, which can emit from 522 - 589 nm. In particular, luminances as high as 370 cd m<sup>-2</sup> were obtained for the complex [Cu(*t*Bu<sub>2</sub>xantphos)(6,6'-Me<sub>2</sub>bpy)][PF<sub>6</sub>](**13**), which correspond to an efficiency of 3.7 cd A<sup>-1</sup>, as shown in Fig. 1.18.

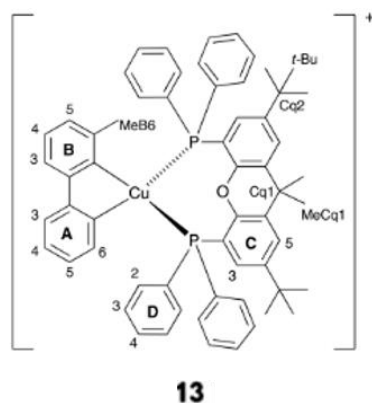


Fig. 1.18. Structures of the copper(I) complexes 13

However, it suggests the copper(I) complexes could easily be degraded during device operation conditions, for example, high applied bias. Thus, optimized synthesis protocols and a proper ligand design can strongly help to improve the device performance<sup>86</sup>.

### 3.2 Small molecules

The advantages of SMs for LECs are: their wide variety using easy-to-functionalized structural scaffolds; their emission covering the whole visible range with high quantum efficiency ( $\phi$ ) values; their stable electrochemical and thermal stabilities; their easy

processability and high stability in solution; and their good carrier mobilities. Actually, SMs can meet most general requirements for LECs, which will be discussed in this section. The chemical structures of some SMs are provided in Fig. 1.19–21 (reproduced from ref 54).

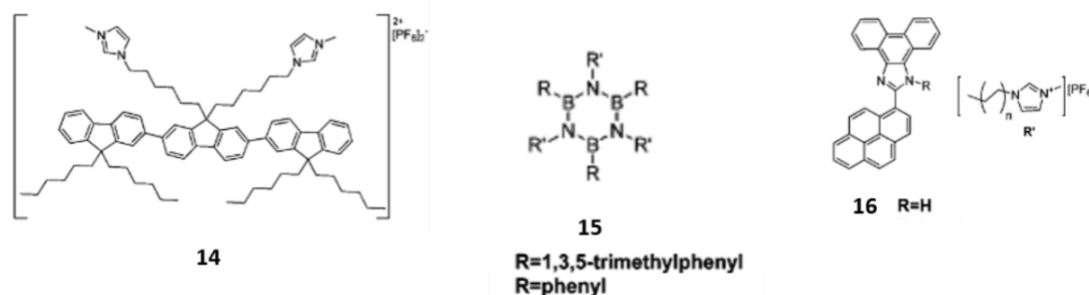


Fig. 1.19. Chemical structures of the SMs 14-16.

The first blue-emitting LEC based on SMs was reported by Chen and co-workers in 2011, and the SMs is based on 2,7-substituted fluorene core, as shown in Fig. 1.19.<sup>100</sup> They select the compound **14** is because it possesses a peak at 393 nm blue emission band; reversible electrochemical behavior and good carrier mobilities, which are the typically features of terfluorene derivatives.<sup>101</sup> The LEC device with a architecture of ITO/PEDOT:PSS/**27**:IL(200 nm)/Al showed an EQE of 1.04% and a luminous power efficiency of 0.63 lmW<sup>-1</sup> under a constant bias of 3.2–3.4 V.

In 2013, Kervyn and co-workers reported another family of blue-emitting SMs based on borazine derivatives.<sup>102</sup> This compound (**15**) shows photoluminescence emission maximum centered in the UV-region ( $\lambda_{em} = 300\text{--}375$  nm) with  $\phi$  values of 6–7%. Besides, the phenanthroimidazole derivatives, which also can emit blue emission was provided in 2015 by Choe's group, as shown in Fig. 1.19.<sup>103,104</sup> The authors tried a neutral compound with a structure containing a phenanthroimidazole moiety linked to a pyrene unit (**16**).<sup>103</sup> The emission of solid-state compound **16** is around 480nm with  $\phi$  value of 0.3, thermal stability of up to 430 °C, and only one quasi-reversible oxidation feature. The I–V–L characteristics of this device display a luminance value of 120 cd m<sup>-2</sup> at 10 V under a turn-on voltage of 4.3 V.

In 2013, Edman and co-workers reported a study on SM-based LECs using green- and red-emitting SMs, which are already tested in OLEDs<sup>105,106</sup> including 4-(3,5-di(4-sec-butoxyphenyl)phenyl)-7-(7-(3,6-di(1-naphthyl)-carbazol-9-yl)-9,9-di-n-octylfluoren-2-yl)-2,1,3-benzothiadiazole (**17**) and 4,7-bis(4-(4-sec-butoxyphenyl)-5-(3,5-di(1-naphthyl)phenyl)thiophen-2-yl)-2,1,3-benzothiadiazole (**23**) – Fig. 1.20 and 21.<sup>107</sup> These compounds present emission wavelength peaked at 500 (**17**) and 610 (**23**) nm with  $\phi$  values of 0.62 (**17**) and 0.71 (**23**).

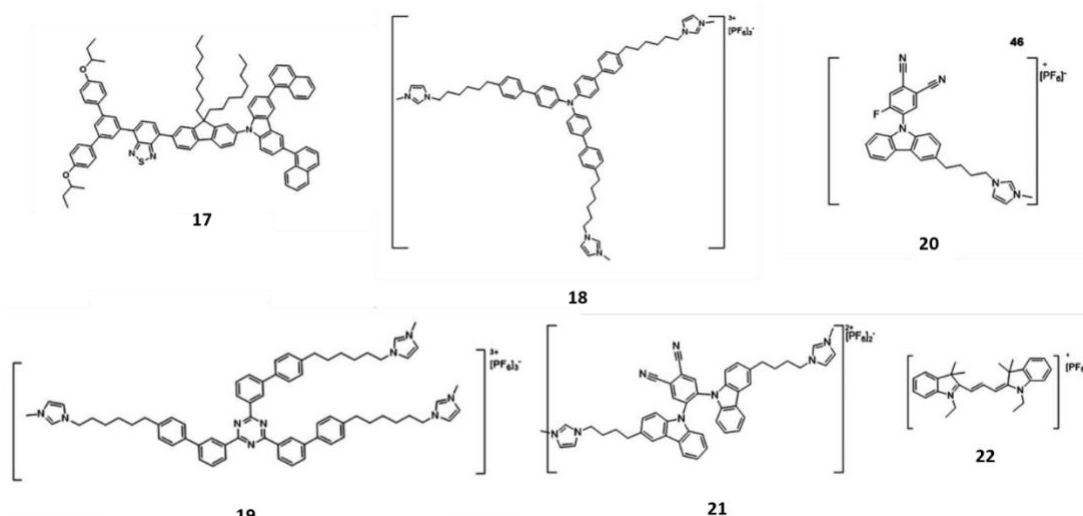


Fig. 1.20 Chemical structures of the SMs 17-22.

At the same year, a SM-LEC based on an active layer containing two ionic SMs with opposite charge transport features was reported by Chen and co-workers.<sup>108</sup> In particular, compound **18** was employed as a hole-transport material and a compound **19** as an electron-transport material, both of which were shown in Fig. 1.20. Upon an applied bias of 3 V, the mixing active layer of **18**: **19** (1:3 mass ratio) displays a green emission located at 550 nm associated with EQE and power efficiency values of 3.04% and 10.29 lm W<sup>-1</sup>, respectively.

At last, the first LECs based on TADF SMs emitters was reported by Zysman-Colman and Bolink groups in 2015.<sup>109</sup> Then, the same authors designed another two ionic TADF SM emitters: compound **20** and **21** based on a previously reported N-carbazoyldicyanobenzene scaffold,<sup>110</sup> as shown in Fig. 1.20. Compound **20** shows an emission centered at around 558 nm with  $\phi$  values of 0.0093 in thin films. Compound **21** shows an emission centered at around 572 nm with  $\phi$  values of 0.21 in thin films. They also designed a LEC using **21** as a host and **22** as a guest that can emit yellow emission.<sup>110</sup> They exhibited a 5-times increase of the luminance (165 cd m<sup>-2</sup>) and EQE (1.90%), however, the device stability was too short (around several seconds).

After that, Edman and co-workers reported a red-emitting SM-based LECs and a green-emitting SM (**23**) mentioned above.<sup>107</sup> Upon being driven at a constant current density of 38.5 mA cm<sup>-2</sup>, the device based on **26** can reach a maximum luminance of 225 cd m<sup>-2</sup> in a few seconds with a stability of around 15 h. The I–V–L characteristics showed a low turn-on voltage at around 4.0 V, reaching a maximum luminance of 750 cd m<sup>-2</sup> and a maximum efficiency of 1.05 cd A<sup>-1</sup>.

In 2013, Chen and co-workers also proposed to design near-infrared emitting dyes using a cationic iridium(III) complex ( $\lambda_{em} = 595$  nm) as a host and two fluorescent ionic cyanines **24** and **25** as a guest, as shown in Fig. 1.21.<sup>111</sup> These devices were driven at a constant voltage of 2.4 V, showing an electroluminescence centered at around 730 and 810 nm, respectively. Furthermore, the EQE values of the devices based on **24** and **25** can reach 0.93 and 1.49% at 2.5 V, respectively.

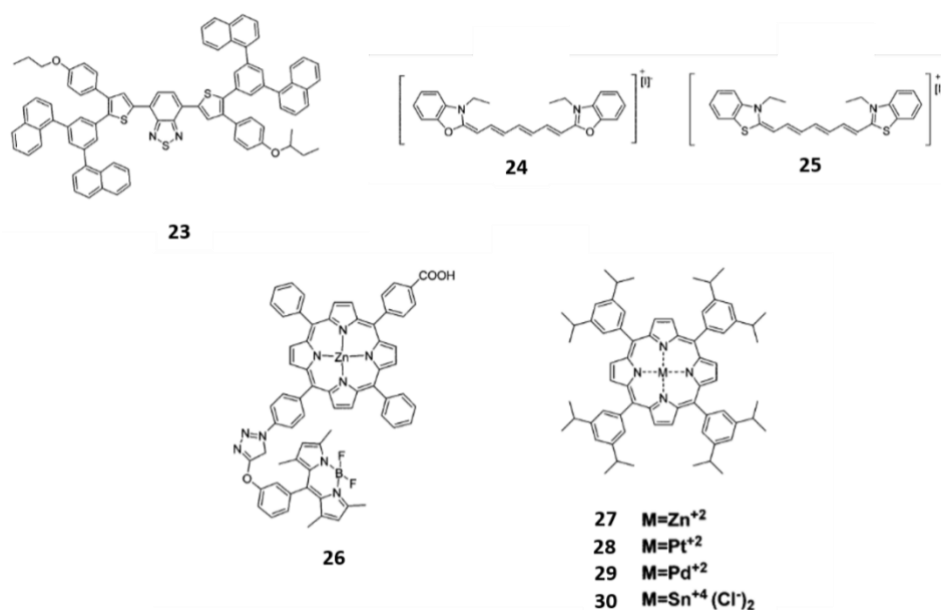


Fig. 1.21. Chemical structures of the SMs 23-30.

In 2016, Costa, Coutsolelos, and co-workers reported another type of red-emitting SMs (porphyrin derivatives) for LECs<sup>112-114</sup> because the photophysical features of porphyrins are easy to be modified through proper molecular design. They used the BODIPY unit acts as a host and the porphyrin unit as a guest, which is “BODIPY-porphyrin dyad (**26**)”.<sup>112</sup> Following this work, the authors used more efficient porphyrins changing the metal core such as Zn<sup>2+</sup>(**27**), Pt<sup>2+</sup>(**28**), Pd<sup>2+</sup>(**29**), and Sn<sup>4+</sup>(**30**) porphyrins as shown in Fig. 1.21.<sup>113</sup> They demonstrated that the metal core is a key aspect to control the nature of the photoluminescence. For example, the  $\lambda_{em}$  of compound **27** is around 600 nm and that of **28** is around 675 nm. The devices with these compounds show the fluorescence: **27**, 600 and 650 nm,  $\phi = 3.8\%$ ; **28**, 675 and 730 nm,  $\phi = 0.095\%$ ; **29**, 565–610 nm and 710 nm,  $\phi = 0.0047$  and 0.0013 for fluorescence and phosphorescence, respectively; **30**, 610 and 665 nm,  $\phi = 1.8$ .

### 3.3 Quantum dots and perovskite nanoparticles

Inorganic colloidal semiconductor nanocrystals such as CdSe/ZnS QDs, have been studied over the last 30 years and have been applied in many applications including displays, lighting

devices, photovoltaics, biological imaging and detection, etc.<sup>115-117</sup> In 2014, Friend and co-workers discovered the hybrid organic–inorganic halide perovskites (PKs).<sup>118</sup> This series of material consists of a distorted Pm3m crystal APbX<sub>3</sub> structure. The X can be Cl, Br, or I that formed the corner-sharing metal halide octahedral, and A can be either an organic compound or an inorganic metal ion. Both compounds are compatible with ionic additives like IP or IL in solution, which is allowed to prepare thin-films by solution-based techniques. Besides, the photoluminescence features of these materials can be easily modified such as emission color and  $f$  values.<sup>115-117,118-122</sup> This has recently intrigued the LEC researchers.

Leger and co-workers firstly reported the QD-based LECs in 2011.<sup>56</sup> In this report, the active layer comprised two QDs: CdSe/ZnS QDs as emitter blended with organic electrolytes. In 2014, Qian and co-workers proposed another approach to design QD-based LECs.<sup>123</sup> In particular, they think the long alkyl chains should act as an insulating barrier for direct charge injection, so they exchanged the organic shell of the QDs by 4-mercaptobenzoic. This improved the miscibility of the QDs with ILs, at the same time, also promoted the charge injection and mobility. Recently, Frohleiks and co-workers reported a new type of hybrid bilayer LEC consisting of top and bottom layers. The top layer is a red-emitting CdSe/CdS QDs ( $\lambda_{em} = 620$  nm) and the bottom layer is a yellow-emitting iTMCs ( $\lambda_{em} = 570$  nm).<sup>124</sup>

In 2015, Costa and co-workers reported the first LECs based on MAPbBr<sub>3</sub> and FAPbBr<sub>3</sub> perovskite NP. The authors not only prepared the LECs based on NPs blended with IP, but also prepared the LECs based on only NPs with similar film thickness. However, the LECs based on only NPs did not show any emission in spite of the similar electrical behavior. After that, Li and co-workers studied LEC devices based on green (MAPbBr<sub>3</sub>;  $\lambda_{em} = 520$  nm), orange (MAPbBr<sub>2</sub>I;  $\lambda_{em} = 593$  nm), and blue (MAPbCl<sub>1.8</sub>Br<sub>1.2</sub>;  $\lambda_{em} = 474$  and 520 nm) PK NPs, which are prepared using a solution of the PbX<sub>2</sub> precursors and MA (500 mg mL<sup>-1</sup>) with a PEO polymer (Mw = 600 000; 16 mg mL<sup>-1</sup>) solution with a mass ratio of 0.5 : 1, 0.75 : 1, and 1 : 1 PEO/PKs.<sup>125</sup> At the same time, the mechanism of bulk perovskite (MAPbI<sub>3-x</sub>Br<sub>x</sub>) was investigated by Zhang and co-workers. They worked on a LEC based on MAPbI<sub>3-x</sub>Br<sub>x</sub> (400 nm) that sandwiched in between two stable electrodes ITO/ PEDOT:PSS(30 nm) and MoO<sub>3</sub>(8 nm)/Au with work functions of 5 and 5.3 eV, respectively.<sup>126</sup>

#### 4. Electrolyte for LECs

As we mentioned above, the enabling characteristic of the LEC, which separates it from the OLED, is the presence of mobile ions, i.e., an electrolyte, in the light-emitting active material.<sup>127-130</sup> The LEC performance is as such intimately dependent on the properties of this

electrolyte. An inadequate electrolyte would cause some drawbacks, such as slow turn-on; poor efficiency; limited stability.<sup>131-134</sup>

#### 4.1 Poly (ethylene oxide) based electrolytes (PEO)

In the first LEC work by Pei et al., the electrolyte consisted of the alkali metal salt  $\text{LiCF}_3\text{SO}_3$  dissolved in the ion-transporting polymer poly(ethylene oxide) (PEO).<sup>1</sup> The PEO possesses good ionic mobility since it solvates the cations and provides ionic transport paths as shown in the left portion of Fig. 1.22.<sup>1</sup> The PEO-based electrolyte was presumably originated from the energy storage field, where a lot of solid-state electrolytes have been extensively investigated since the late 1970s, primarily for use in solid-state Li batteries.<sup>135,136</sup> After many years of researching, although PEO is a decent ion-transporting material for LECs and much of the subsequent LEC research has utilised PEO-based electrolytes, it is not perfect choice. PEO is a semi-crystalline polymer with a melting temperature of 60 °C, and it could form high-melting crystalline complexes in case blend with many salts. This make they tend to be crystallisation at room temperature. Since it has been demonstrated that ion transport almost exclusively takes place in the amorphous PEO regions which is above the glass transition temperature.<sup>137</sup> Thus, such crystallisation would limit the practical operational temperature of the corresponding devices to be above the melting point of the electrolyte, for example, room temperature.<sup>133</sup>

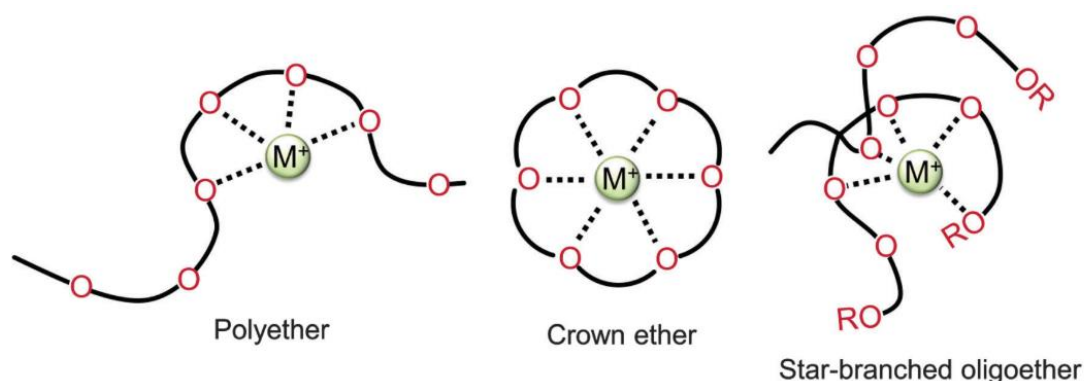


Fig. 1.22 A schematic illustration of the structure and cation coordination of representative ether-based ion transporters. For the star-branched oligoether to the right, R represents the end-group, which can be a hydrogen or a methyl group<sup>138</sup>.

Like the battery, Li-based salts have been the common choice for the salt in PEO-based electrolytes in LECs. This is because the first group of scientists in the LEC field were inspired by the field of Li batteries. However, in several LEC studies, the light-emitting p–n junction will be moved away depending on the observed cations. Normally, it moved away from the cathode and be more centred in case the employ of other cations than  $\text{Li}^+$ . It is desirable since it will effectively eliminate undesirable electrode quenching effects.<sup>54</sup> Among

MClO<sub>4</sub> salts (M = Li, K, Na, Cs, Rb), it is found that, the use of larger cations always led to the light-emitting p–n junction being more centred and more strongly emitting. The work of Shin et al. confirms these findings. The effects of the cation for MCF<sub>3</sub>SO<sub>3</sub> (M = Li, K, Rb) salts was reported and compared to M= Li, a more centred and brighter p–n junction as well as faster turn-on for devices with M=K and Rb were obtained.<sup>133,139</sup> This counterintuitive result maybe can be explained by the fact that the ionic conductivity of PEO:MCF<sub>3</sub>SO<sub>3</sub> electrolytes increases with increasing cation size.<sup>140</sup>

Another way to modulate is the selection of the anion.<sup>141,142</sup> A markedly faster turn-on for sandwich cells was achieved through replacing the CF<sub>3</sub>SO<sub>3</sub> (Tf) anion with a larger N(CF<sub>3</sub>SO<sub>2</sub>)<sub>2</sub> (TFSI) anion in a PEO:LiX electrolyte. A higher ionic conductivity was obtained since the LiTFSI salt was in part developed for suppressing the room temperature crystallinity of the corresponding PEO-based electrolytes.<sup>143</sup> The fastest turn-on was attained by using a combination of both the Tf and the TFSI anions. Besides, it is plausible that this mixed electrolyte featured an even lower degree of crystallinity at room temperature, which is presumably because the combination of two anions kinetically hinder the crystallisation of the electrolyte. However, with these solutions, the long-term stability of the electrolyte is suffered.<sup>132</sup> This can be attributed to the lower cathodic stability of the TFSI anion than the Tf anion, which is implying that the preferred cathodic reaction is reduction of the TFSI anion and not n-type doping of OMC.

## 4.2 Ionic liquids

Ionic liquids (IL) (or ‘molten salts’) are electrolytes with a low melting point (in some cases below room temperature), which can be hydrophobic, highly conductive. The primary advantage of IL is a broad electrochemical stability window.<sup>144</sup> Ionic liquids are a frequent addition to ITMC-LECs to speed up the turn-on kinetics.<sup>145</sup> The first ionic liquids employed in CP-LECs were based on a tetra-alkylammonium cation.<sup>38,146,147</sup> There are also some studies investigated the liquid LECs based on imidazolium<sup>148,149</sup> or phosphonium cations<sup>150,151</sup>. The chemical structures of two investigated ionic liquids with promising properties are presented in Fig. 1.23. Interestingly, several early LEC studies found a severe phase separation occurred between the ionic liquid and the CP, thus the device performance was not impressive.<sup>146,150</sup> However, some success has been attained, the first low-voltage operation of a planar LEC with a mm-sized electrode gap at room temperature was demonstrated by Shin and coworkers. They employ a 1-ethyl-3-methylimidazolium ethylsulfate (EMI-ES) ionic liquid with a

melting temperature below  $-20\text{ }^{\circ}\text{C}$ .<sup>152</sup> Moreover, a long operational lifetime of several days at significant luminance from sandwich-cell LECs, using methyl-trioctylammonium trifluoromethanesulfonate (MATS) as the ionic liquid was reported by Shao et al.<sup>38</sup>

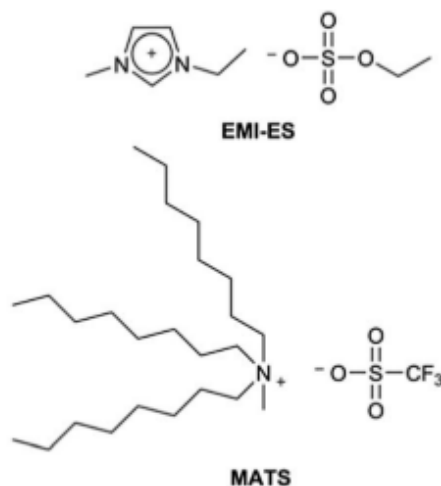


Fig. 1.23 The chemical structure of the ionic liquids 1-ethyl-3-methylimidazolium ethylsulfate (EMI-ES) and methyltrioctylammonium trifluoromethane- sulfonate (MATS).

There are also some reports on linear or non-linear oligoether-based electrolytes<sup>153,154</sup>, which is shown in Fig 1.22 center and right. Besides, developing a multifunctional compound, which simultaneously features electronic conductivity, ionic conductivity, and electroluminescence, is one solution to effectively solve the issues with phase separation. Examples of such compounds are presented in Fig.1.24, and include CPs endowed with ion-transporting side chains in the form of oligoethers (Fig. 1.24 (a))<sup>155-157</sup> or crown ethers <sup>158</sup> (Fig. 1.24 (b)), or the inclusion of an ion-transporting oligoether block within a conjugated main chain for the formation of a block copolymer (Fig. 1.24 (c)).<sup>159,160</sup> However, these groups of compounds have only been explored to a limited extent in LECs. J. Mindemark and L. Edman pointed that most commonly utilised electrolyte groups in LECs – alkali metal salts dissolved in ether-based ion transporters and ionic liquids – are imports from neighbouring scientific fields<sup>138</sup>. And polymerisable electrolytes and mixed ion and electron conductors were to some extent explicitly developed to address LEC-specific issues such as a slow turn-on time and phase separation.

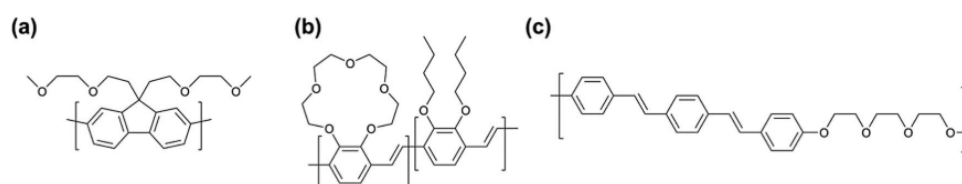


Fig. 1.24 A conjugated polymer endowed with an ion-transporting side chain comprising either an oligoether (a) or a crown ether (b). A block copolymer comprising conjugated and oligoether repeat units (c).



Thus, they also claimed that the efforts dedicated to the design and synthesis of a ‘complete’ electrolyte that considers all of the specific requirements of LECs is rather limited.<sup>138</sup> In order to response their prospect, as glass researchers, we seek a possibility of preparing a inorganic glass host as the electrolyte for a LEC.

### **5. Inorganic Glass electrolyte and organophosphorus semiconductor**

Glass oxide electrolytes, denoted as  $\text{Li}_2\text{O}-\text{MO}_x$  ( $M = \text{Si}, \text{B}, \text{P}, \text{Ge}, \text{etc.}$ ), are typically formed by network-former oxides (e.g.,  $\text{SiO}_2$ ,  $\text{B}_2\text{O}_3$ ,  $\text{P}_2\text{O}_5$ ,  $\text{GeO}_2$ , etc.) and network-modifier oxides ( $\text{Li}_2\text{O}$ ). In 1966, Otto reported glass composition of  $\text{Li}_2\text{O}-\text{SiO}_2-\text{B}_2\text{O}_3$  with high lithium ion conductivity ( $>10^{-4}$  S/cm) at about  $350^\circ\text{C}$  <sup>161</sup>. It was also demonstrating that disorder structure can support fast lithium-ion conduction. Considering some primary advantages of glass oxide electrolytes including isotropic ionic conduction; negligible electronic conductivity; no highly resistive and corrosion-sensitive grain boundaries continuously variable composition; easy of fabrication into complex and thin-walled structures, it would be an ideal electrolyte material if it can reach a high conductivity. Therefore, many researches have been focused on improving the conductivity of the glass. Two strategies have been used in the design of lithium ion conducting electrolytes. One is to use a combination of two anionic species which are known to give increased ionic conductivity and is attributed to the so-called mixed anionic effect <sup>162</sup>. The other strategy is to dissolve a highly ionic conductive lithium salt in a conventional polymeric lithium glass <sup>163</sup>. Moreover, it was also found that mixed glass-former cation glasses are an efficiency way to improve the ionic conductivity <sup>164</sup>. Although the increased conductivity is attributed to a volume increasing effect of the dissolved ionic salt <sup>163</sup>, most oxide glass electrolytes show a low conductivity at room temperature, except some glasses with high  $\text{Li}^+$  ion concentration (containing lithium halogen), which present a relatively high ion conductivity of  $10^{-6}$  S/cm <sup>165</sup>. LiPON (Lithium Phosphorous Oxynitride) amorphous thin-film also has the same level of conductivity <sup>166</sup>. LiPON has been used in thin-film batteries because reducing the electrolyte thickness decreases its resistance. Compare to oxide glasses, a higher ionic conductivity can be obtained in sulfide containing glasses. In the system  $\text{Li}_2\text{S}-\text{P}_2\text{S}_5$ , the glasses containing more than 70 mol%  $\text{Li}_2\text{S}$  have a conductivity of over  $10^{-4}$  S  $\text{cm}^{-1}$  <sup>167</sup>. Moreover, the Arrhenius ionic conductivity of some inorganic crystal and glass with high ionic conductivity are shown in Fig. 1.25. It can be seen that the ionic conductivity of inorganic glass electrolyte is comparable to some organic polymer electrolytes <sup>46</sup>.

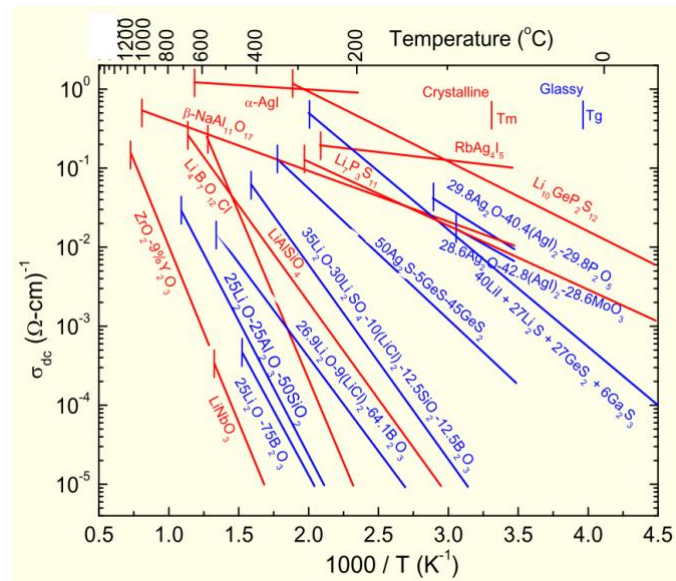


Fig. 1.25. Arrhenius ionic conductivity of some inorganic crystal and glass

Like the polymer electrolyte, both the inorganic crystals and glasses electrolytes were investigated for the lithium battery application. However, the conducting mechanism of each of them is different. Typically, the occurrence of ionic conductivity in crystalline solids is linked to the existence of special structures, “open channels”. For example, in  $\beta$ -alumina, the  $\text{Na}^+$  ion migration is confined to motion in two dimensions in conduction planes located between the close packed spinel blocks <sup>168</sup>. Depending on the details of the structure, crystals can in fact be one-, two- or three-dimensional conductors. Glass lacks long-range order, therefore it lacks the possibility of interconnected “open channels”. The details about the ionic conduction in glass will be discussed in 5.1 section.

### 5.1 Models of ionic Conduction in Glass

The ion transport mechanism is still not clear in glass because of the disorder structure. Although the conduction in glass is viewed from a vacancy defect-type of mechanism, it is different from inorganic crystal since the vacancy concentration in glasses is believed to be significantly larger than in crystals <sup>169</sup>. The binding energies holding the mobile ions in metastable state and the migration energy barriers hindering the mobile ions are considered to be the two main factors for deciding the magnitude of conductivity of the glass. For most glasses, conduction is solely determined by a single ionic species, anionic or cationic.

The conductivity,  $\sigma$ , is expressed as the product of charge carrier, concentration, and mobility as given by the following equation

$$\sigma = neZ\mu \quad (1)$$

where  $eZ$  is the charge of the conducting ion, normally is  $+1$ ,  $\mu$  is the mobility of the conducting ion, and  $n$  is the concentration of the conducting ion. Thus, understanding the two terms  $\mu$  and  $n$  in the equation (1) is the key to model the ionic conductivity in glass. Although several models have been proposed ever, here we briefly introduce two main models: “strong electrolyte” (SE) model and “weak electrolyte” (WE) model that are generally agreed by the researchers. The former supposes that all cations are equally available for conductivity, and the latter supposes that only dissociated cations are available for conduction. The WE model suggests that the activation energy barrier represents the binding energy holding the ions in the metastable state. Once an ion dissociated away from its metastable state, it is thought to face no other energy barriers for moving in the glass. Martin and Angell developed a general model<sup>170</sup>, and in this approach, the two models can be thought of as the two extremes of a more general model where both factors contribute to the conduction energetics in glass. The approach would be introduced after reviewing the SE and WE model.

### 5.1.1 Strong electrolyte Model

In 1954, a calculation of the conduction energetics in an ion-conducting glass was proposed by Anderson and Stuart<sup>171</sup>. In their analysis, the total activation energy  $\Delta E_{act}$ , is the sum of two parts

$$\Delta E_{act} = \Delta E_s + \Delta E_c \quad (2)$$

where  $\Delta E_c$  is the electrostatic binding energy and  $\Delta E_s$  is the strain energy.  $\Delta E_c$  describes the coulombic forces acting on the ion as it moves away from its charge-compensating site, and  $\Delta E_s$  describes the mechanical forces acting on the ion as it dilates the structure sufficiently to allow the ion to move between sites. After several approximations<sup>171,172</sup>, Anderson and Stuart model was revised that

$$\Delta E_c = \frac{\beta Z Z_0 e^2}{\gamma(r + r_0)} \quad (3)$$

$$\Delta E_s = 4\pi G(r - r_d)^2 \lambda \quad (4)$$

where  $\beta$  and  $\gamma$  are parameters, with the latter being set equal to the relative dielectric permittivity,  $\epsilon$ ;  $Z$  and  $r$ , are the charges and radii of the cation, respectively;  $Z_0$  and  $r_0$  are the charges and radii of anion, respectively;  $r_d$  is the "doorway" radius or radius of the network constriction between cation sites; and  $G$  is the shear modulus of the glass.  $\lambda$  is the jump distance between cation sites.

To understand the model better, we introduce a visualization of the energetics of the conduction that provided by Martin and Angell<sup>170</sup>, as shown in Fig. 1.26.  $\Delta E_c$  is treated as the energy holding the target cation in its equilibrium site, which comes from the coulomb forces. Its value is equal to the difference between the coulombic potential energy of the cation when it is midway between the two sites (potential energy maximum) and when it is in its equilibrium position (potential energy minimum).  $\Delta E_s$  is envisioned as an energy barrier in a short-range. If the cation is able to pass to the next site, it needs the energy to "dilate" the glass structure. This energy can be treated as the  $\Delta E_s$ . However, this model ignores that, in high alkali ions situation,  $r$  may be close to  $r_d$ , which means  $\Delta E_s$  is possible to zero that supports WE model.

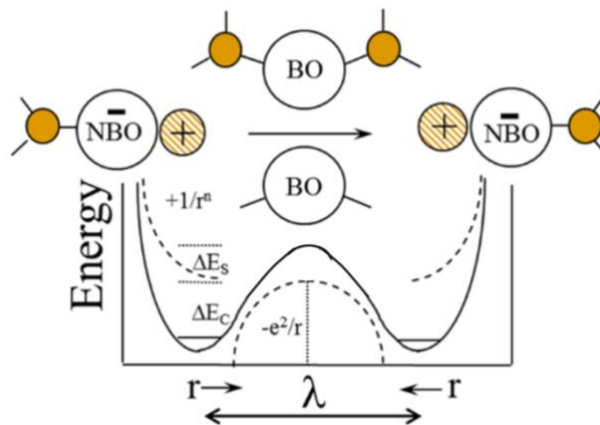


Fig. 1.26. Physical representation of the energetics of ion conduction according to the Anderson and Stuart model by Martin et al<sup>170</sup>

### 5.1.2 Weak electrolyte Model

The weak electrolyte model was developed by Ravaine and Souquet to describe the conduction energetics in glass<sup>173</sup>. They think there are many similarities that exist between aqueous and glassy electrochemistry. In this model, the main energetic barrier for the cation transport in the glass is the dissociation process away from the nonbridging oxygen (or salt anion). Therefore, they suggest that, if a cation has dissociated away from its origin site, the cation enables to migrate before it meets another charge-compensating site. The envisioned dissociation can be occurred by the following reaction:



where  $\text{Na}_2\text{O}$  and  $\text{ONa}^-$  are the undissociated and dissociated cation sites, respectively, and  $\text{Na}^+$  is believed to be the dissociated or "free" cation. Moreover, this approach can be generalized to other dopants.

### 5.1.3 Martin and Angell revised general model

The general model which can reconcile the two models mentioned above was proposed by Martin and Angell<sup>170,174</sup>. They think if  $\Delta E_c$  is larger than  $\Delta E_s$ , the glass is behaving as a weak electrolyte; if the  $\Delta E_s$  is greater than  $\Delta E_c$ , the glass is behaving as a strong electrolyte. They insist that a strain energy barrier is always present in both the SE and WE model. This is because the fact that a cation needs the volume to transport in the glass conducting process.

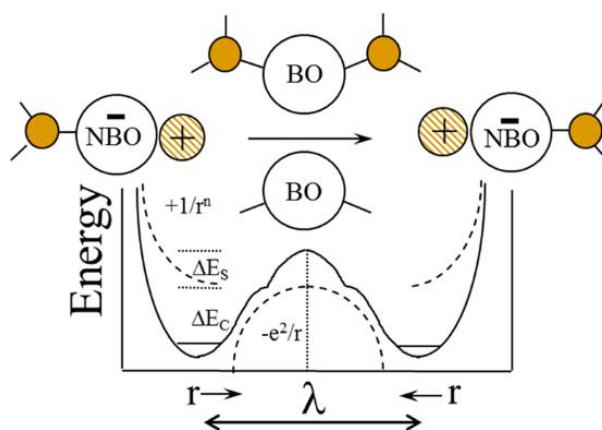


Fig. 1.27. Physical representation of the energetics of ion conduction according to the revised Anderson and Stuart model by Martin et al.<sup>170</sup>

They use the physical representation shown in Fig 1.27 to explain the dissociated and undissociated states in the weak electrolyte model. From the figure, it can be seen that there is a metastable “ridge” at the transition point between the deep potential well of the equilibrium site and the short-range strain energy barrier. This means the availability of “metastable” sites need a higher energy than the bound lowest energy sites. The presence of such intermediate sites would temporarily stabilize or “store” a dissociated cation and make it “available” for ionic conduction.

### 5.2 Possible inorganic glass electrolytes for LECs

From these researches of a desired electrolyte for LECs<sup>138,175</sup>, it is known that a electrolyte with a wider electrochemical stability window, high ionic conductivity, a wide spectral transmission and mechanical stability would be good for a LEC. Inorganic glass electrolytes may meet all these requirements, but this does not mean it is easy to find an appropriate inorganic glass host for the LEC. This is because, contrarily to the organic polymer electrolyte, the inorganic glass electrolytes are always prepared at high temperature. The temperature of the preparing process (900 °C) is much higher than the degradation temperature of the organic molecule (300 °C). This is also one of the primary challenges to prepare the LEC based on an inorganic glass electrolyte. In this work, we plan to use two

technologies that can avoid the high temperature condition to prepare the organic-inorganic hybrid glass. One is the Sol-gel method, a low temperature wet chemistry method, and the other one is spark plasma sintering (SPS) which is able to sinter a glass at the glass transition temperature ( $T_g$ ). Therefore, the glasses electrolytes which can be simply prepared by these two methods will be given the priority in our work. Only based on this term, seeking the higher ionic conductivity of the glass does really make sense. It is known silicate glass have the best mechanical stability among all the kinds of glass, and there are abundant works on the way to prepare silicate glasses by sol-gel. Therefore, using Sol-gel method to prepare the lithium modified silicate glass electrolyte is a reasonable plan.

On the other hand, although SPS technology can agglomerate the glass by sintering at around  $T_g$ , the  $T_g$  of the glass should not be higher than the degradation temperature of the OSC. Therefore, an OSC with higher degradation temperature is also desired for a LEC based on inorganic glass electrolyte, which will be discussed later. This also means glasses with low  $T_g$  and relative higher ionic conductivity would be the promising material. Sulfide glasses seem to be a good choice since it not only has a higher ionic conductivity than oxide glass, but also has a low  $T_g$ . However, the bad spectral transmission in visible light hinder it becoming an appropriate electrolyte for LEC applications. Then, phosphate glasses come into our view since it has a lower  $T_g$  than silicate and borate glass, comparable ionic conductivity and are fully transparent in the visible range.

### **5.3 Organophosphorus semiconductor**

The system based on phosphorus was unlike the other five-membered heterocyclic systems based on such as nitrogen, sulfur, or oxygen, which have been known for more than 130 years and have been studied for decades. Phosphorus was discovered<sup>176</sup> 60 years ago and has been incorporated into  $\pi$ -conjugated systems only since the 90s.<sup>177</sup> The phosphole exhibits unique properties different from the other five-membered heterocyclic members making it an interesting building block for the construction of p-systems having specific properties.<sup>178</sup> For example, phospholes (containing one phosphorus atom) possess unique favorable properties that have several applications in organic electronic materials; (i) phospholes are weakly aromatic favoring the electronic delocalization in extended p-conjugated systems, (ii) substituents of the phosphole can influence the aromaticity of the phosphole and have an effect on the properties of the p-system, especially those directly linked to the phosphorus atom; (iii) phospholes contain a reactive phosphorus atom, which may tune the

physicochemical properties and (iv) the pyramidal shape of the P-atom affords steric hindrance that prevents  $\pi$ -stacking in the solid state and thus promotes solid-state emission.<sup>179</sup> Moreover, many organophosphorus derivatives have been inserted into electronic devices.

The organophosphorus semiconductor used in this work have the desired advantages for doping in the inorganic glass electrolyte including high quantum efficiency in solid state, high chemical stability and high degradation temperature. And the details will be discussed in the corresponding chapter. All these organophosphorus molecules used in this work come from the Phosphorus & Molecular Materials research group, which is under the direction of Prof. Muriel Hissler, belonging Organometallics: Materials & Catalysis research team of Institut des Sciences Chimiques de Rennes (UMR CNRS 6226).

## 6. Conclusions

The researchers around the world did a lot work to understand the complicated device physics of LECs. The carrier injection in the emitter layer is mainly determined by the injection barrier and the applied bias voltage. And the carrier injection plays a key role in the operation of LECs. The electrochemical model is preferred the operational mechanism of LECs when the carrier injection is not limited. The transient properties of the LEC are also determined by the electrochemical doping process.

Both the traditional emitter such as CP and iTMC and new emitter including copper(I) complexes, SMs, QDs and NPs were brief reviewed. These new emitters significantly enhanced the device performances and enrich the LECs family. However, after two decades of intensive research, the state-of-the-art of LECs indicate that this technology has only achieved a moderate performance compared to that of lighting sources and displays based on the OLED concept. The “short slab” of LEC technology is the electrolyte. The common organic electrolytes have been briefly reviewed. The result shows an ideal electrolyte for a LEC should have wider electrochemical stability window, high ionic conductivity, a wide spectral transmission and mechanical stability. Moreover, the morphology between the electrolyte and OSC is also very important.

Inorganic glass electrolytes have all the advantages required for making ideal electrolytes for a LEC application, however, to our best knowledge, there is few reports on the LEC based on organophosphorus derivatives. As glass researchers, we are curious to know that if the inorganic glass electrolytes can be used in a LEC? So, we thought about the possibilities to prepare a LEC based on the OSC doped inorganic glass. First of all, to successfully prepare

the OSC doped glasses, the OSC should have a high degradation temperature. The organophosphorus semiconductors have not only high degradation temperature, but also high quantum efficiency in solid state and high chemical stability. Thus, it is one ideal OSC for doping in an inorganic glass electrolyte.

Therefore, the main objective of this work was to develop a new LEC device based on organophosphorus doped inorganic glass electrolyte, which cannot be synthesized by using classic melt-quenching technique. That because the melting temperature of glass is always much higher than the degradation temperature of organic molecules. Thus, the challenge was to find the way to blend OSC and inorganic glass host. Fortunately, we found two possible ways to try working out the challenge. And these possible solutions should use the advantages of both the OSC and inorganic glass host, which will be discussed in details in the following chapters.



## REFERENCES

- 1 Pei, Q., Yu, G., Zhang, C., Yang, Y. & Heeger, A. J. Polymer light-emitting electrochemical cells. *Science* **269**, 1086-1088 (1995).
- 2 Lee, J. K., Yoo, D., Handy, E. & Rubner, M. J. A. p. l. Thin film light emitting devices from an electroluminescent ruthenium complex. *Applied physics letters* **69**, 1686-1688 (1996).
- 3 Meier, S. B. *et al.* Light-emitting electrochemical cells: recent progress and future prospects. *Materials Today* **17**, 217-223 (2014).
- 4 van Reenen, S. & Kemerink, M. in *Light-Emitting Electrochemical Cells: Mechanisms and Formal Description*. Chapter 1, 3-45 (2017).
- 5 Asadpoordarvish, A. *et al.* Light-Emitting Paper. *Advanced Functional Materials* **25**, 3238-3245 (2015).
- 6 Sandström, A., Asadpoordarvish, A., Enevold, J. & Edman, L. Spraying Light: Ambient-Air Fabrication of Large-Area Emissive Devices on Complex-Shaped Surfaces. *Advanced Materials* **26**, 4975-4980 (2014).
- 7 Sandström, A. & Edman, L. Towards High-Throughput Coating and Printing of Light-Emitting Electrochemical Cells: A Review and Cost Analysis of Current and Future Methods. *Energy Technology* **3**, 329-339 (2015).
- 8 Pei, Q., Yang, Y., Yu, G., Zhang, C. & Heeger, A. J. Polymer light-emitting electrochemical cells: in situ formation of a light-emitting p-n junction. *Journal of the American Chemical Society* **118**, 3922-3929 (1996).
- 9 Tessler, N., Graham, S. & Friend, R. Ionic space-charge effects in polymer light-emitting diodes. *Physical Review B* **57**, 12951 (1998).
- 10 Demello, J. Interfacial feedback dynamics in polymer light-emitting electrochemical cells. *Physical Review B* **66** (2002).
- 11 Halls, J., Graham, S., Tessler, N. & Friend, R. Electric field distribution in polymer light-emitting electrochemical cells. *Physical review letters* **85**, 421 (2000).
- 12 Slinker, J. D. *et al.* Direct measurement of the electric-field distribution in a light-emitting electrochemical cell. *Nat Mater* **6**, 894-899 (2007).
- 13 Rodovsky, D. B., Reid, O. G., Pingree, L. S. & Ginger, D. S. Concerted emission and local potentiometry of light-emitting electrochemical cells. *J Acs Nano* **4**, 2673-2680 (2010).
- 14 van Reenen, S. *et al.* A unifying model for the operation of light-emitting

- electrochemical cells. *Journal of the American Chemical Society* **132**, 13776-13781 (2010).
- 15 Meier, S. B. *et al.* Dynamic Doping in Planar Ionic Transition Metal Complex-Based Light-Emitting Electrochemical Cells. **23**, 3531-3538 (2013).
- 16 Matyba, P., Maturova, K., Kemerink, M., Robinson, N. D. & Edman, L. J. N. m. The dynamic organic p-n junction. **8**, 672 (2009).
- 17 Toshner, S. B., Zhu, Z., Kosilkin, I. V. & Leger, J. M. Characterization of ion profiles in light-emitting electrochemical cells by secondary ion mass spectrometry. *ACS applied materials interfaces* **4**, 1149-1153 (2012).
- 18 Shoji, T. D., Zhu, Z. & Leger, J. M. Characterizing ion profiles in dynamic junction light-emitting electrochemical cells. *ACS applied materials interfaces* **5**, 11509-11514 (2013).
- 19 van Reenen, S., Janssen, R. A. & Kemerink, M. Dynamic Processes in Sandwich Polymer Light-Emitting Electrochemical Cells. *Advanced Functional Materials* **22**, 4547-4556 (2012).
- 20 Li, Y., Gao, J., Yu, G., Cao, Y. & Heeger, A. J. ac impedance of polymer light-emitting electrochemical cells and light-emitting diodes: A comparative study. *Chemical physics letters* **287**, 83-88 (1998).
- 21 Campbell, I., Smith, D., Neef, C. & Ferraris. Capacitance measurements of junction formation and structure in polymer light-emitting electrochemical cells. *Applied physics letters* **72**, 2565-2567 (1998).
- 22 Munar, A., Sandström, A., Tang, S. & Edman, L. Shedding Light on the Operation of Polymer Light-Emitting Electrochemical Cells Using Impedance Spectroscopy. *Advanced Functional Materials* **22**, 1511-1517 (2012).
- 23 Lenes, M. *et al.* Operating Modes of Sandwiched Light-Emitting Electrochemical Cells. *Advanced Functional Material* **21**, 1581-1586 (2011).
- 24 Smith, D. Steady state model for polymer light-emitting electrochemical cells. *Journal of Applied Physics* **81**, 2869-2880 (1997).
- 25 Manzanares, J. A., Reiss, H. & Heeger, A. J. Polymer light-emitting electrochemical cells: a theoretical study of junction formation under steady-state conditions. *The Journal of Physical Chemistry B* **102**, 4327-4336 (1998).
- 26 Mills, T. J. & Lonergan, M. C. Charge injection and transport in low-mobility mixed ionic/electronic conducting systems: Regimes of behavior and limiting cases. *Physical Review B* **85**, 035203 (2012).

- 27 Hu, Y., Dorin, B., Teng, F. & Gao, J. Mapping the built-in electric field in polymer light-emitting electrochemical cells. *Organic Electronics* **13**, 361-365 (2012).
- 28 AlTal, F. & Gao, J. J. E. A. Charging and discharging of a planar polymer light-emitting electrochemical cell. **220**, 529-535 (2016).
- 29 Wang, T.-W. & Su, H.-C. Extracting evolution of recombination zone position in sandwiched solid-state light-emitting electrochemical cells by employing microcavity effect. *Organic Electronics* **14**, 2269-2277 (2013).
- 30 Lin, G.-R. *et al.* Non-doped solid-state white light-emitting electrochemical cells employing the microcavity effect. *Physical Chemistry Chemical Physics* **17**, 6956-6962 (2015).
- 31 Huang, P.-C., Krucaite, G., Su, H.-C. & Grigalevicius, S. Incorporating a hole-transport material into the emissive layer of solid-state light-emitting electrochemical cells to improve device performance. *Physical Chemistry Chemical Physics* **17**, 17253-17259 (2015).
- 32 Li, X., Gao, J. & Liu, G. Reversible luminance decay in polymer light-emitting electrochemical cells. *Applied Physics Letters* **102**, 101-101 (2013).
- 33 Meier, S. B. *et al.* Dynamic doping and degradation in sandwich-type light-emitting electrochemical cells. *Physical Chemistry Chemical Physics* **14**, 10886-10890 (2012).
- 34 Li, X., AlTal, F., Liu, G. & Gao, J. Long-term, intermittent testing of sandwich polymer light-emitting electrochemical cells. *Applied Physics Letters* **103**, 234-231 (2013).
- 35 AlTal, F. & Gao, J. Long-term testing of polymer light-emitting electrochemical cells: Reversible doping and black spots. *Organic Electronics* **18**, 1-7 (2015).
- 36 Gao, J., Yu, G. & Heeger, A. J. Polymer light-emitting electrochemical cells with frozen pin junction. *Applied physics letters* **71**, 1293-1295 (1997).
- 37 Edman, L., Pauchard, M., Moses, D. & Heeger, A. J. Planar polymer light-emitting device with fast kinetics at a low voltage. *Journal of applied physics* **95**, 4357-4361 (2004).
- 38 Shao, Y., Bazan, G. C. & Heeger, A. J. Long-lifetime polymer light-emitting electrochemical cells. *Advanced Materials* **19**, 365-370 (2007).
- 39 AlTal, F. & Gao, J. High resolution scanning optical imaging of a frozen polymer pn junction. *Journal of Applied Physics* **120**, 115501 (2016).
- 40 Jafari, M. J., Liu, J., Engquist, I. & Ederth, T. Time-Resolved Chemical Mapping in

- Light-Emitting Electrochemical Cells. *ACS applied materials interfaces* **9**, 2747-2757 (2017).
- 41 Jenatsch, S. *et al.* Doping Evolution and Junction Formation in Stacked Cyanine Dye Light-Emitting Electrochemical Cells. **8**, 6554-6562 (2016).
- 42 Lin, K.-Y. *et al.* Influence of Lithium Additives in Small Molecule Light-Emitting Electrochemical Cells. *ACS applied materials interfaces* **8**, 16776-16782 (2016).
- 43 Bastatas, L. D. *et al.* Discerning the impact of a lithium salt additive in thin-film light-emitting electrochemical cells with electrochemical impedance spectroscopy. *Langmuir* **32**, 9468-9474 (2016).
- 44 Puscher, B. M., Aygueler, M. F., Docampo, P. & Costa, R. D. Unveiling the dynamic processes in hybrid lead bromide perovskite nanoparticle thin film devices. *Advanced Energy Materials* **7**, 1602283 (2017).
- 45 Meier, S. B., Hartmann, D., Winnacker, A. & Sarfert, W. The dynamic behavior of thin-film ionic transition metal complex-based light-emitting electrochemical cells. *Journal of Applied Physics* **116**, 104504 (2014).
- 46 van Reenen, S., Akatsuka, T., Tordera, D., Kemerink, M. & Bolink, H. J. Universal transients in polymer and ionic transition metal complex light-emitting electrochemical cells. *Journal of the American Chemical Society* **135**, 886-891 (2013).
- 47 Robinson, N. D., Shin, J.-H., Berggren, M. & Edman, L. Doping front propagation in light-emitting electrochemical cells. *Physical Review B* **74**, 155210 (2006).
- 48 Leger, J., Carter, S. & Ruhstaller, B. Recombination profiles in poly [2-methoxy-5-(2-ethylhexyloxy)-1, 4-phenylenevinylene] light-emitting electrochemical cells. *Journal of applied physics* **98**, 124907 (2005).
- 49 Pingree, L. S., Rodovsky, D. B., Coffey, D. C., Bartholomew, G. P. & Ginger, D. S. Scanning kelvin probe imaging of the potential profiles in fixed and dynamic planar LECs. *Journal of the American Chemical Society* **129**, 15903-15910 (2007).
- 50 Van Reenen, S. *et al.* Salt Concentration Effects in Planar Light-Emitting Electrochemical Cells. *Advanced Functional Materials* **21**, 1795-1802 (2011).
- 51 Li, X., Gao, J. & Liu, G. Thickness dependent device characteristics of sandwich polymer light-emitting electrochemical cell. *Organic Electronics* **14**, 1441-1446 (2013).
- 52 Jhang, Y.-P. *et al.* Improving device efficiencies of solid-state white light-emitting electrochemical cells by adjusting the emissive-layer thickness. *Organic Electronics*

- 14**, 2424-2430 (2013).
- 53 Malliaras, G. G. *et al.* Operating mechanism of light-emitting electrochemical cells. *Nature materials* **7**, 168 (2008).
- 54 Gao, J. & Dane, J. Visualization of electrochemical doping and light-emitting junction formation in conjugated polymer films. *Applied Physics Letters* **84**, 2778-2780 (2004).
- 55 Matyba, P., Maturova, K., Kemerink, M., Robinson, N. D. & Edman, L. The dynamic organic p-n junction. *Nat Mater* **8**, 672-676 (2009).
- 56 Norell Bader, A. J., Ilkevich, A. A., Kosilkin, I. V. & Leger, J. M. Precise color tuning via hybrid light-emitting electrochemical cells. *Nano letters* **11**, 461-465 (2010).
- 57 van Reenen, S., Janssen, R. A. & Kemerink, M. Fundamental Tradeoff between Emission Intensity and Efficiency in Light-Emitting Electrochemical Cells. *Advanced Functional Materials* **25**, 3066-3073 (2015).
- 58 Shin, J. H., Robinson, N. D., Xiao, S. & Edman, L. Polymer Light-Emitting Electrochemical Cells: Doping Concentration, Emission-Zone Position, and Turn-On Time. *Advanced Functional Materials* **17**, 1807-1813 (2007).
- 59 Hu, Y. & Gao, J. Direct Imaging and Probing of the p– n Junction in a Planar Polymer Light-Emitting Electrochemical Cell. *Journal of the American Chemical Society* **133**, 2227-2231 (2011).
- 60 Zhang, Y. & Gao, J. Lifetime study of polymer light-emitting electrochemical cells. *Journal of applied physics* **100**, 084501 (2006).
- 61 Lyons, C., Abbas, E., Lee, J.-K. & Rubner, M. Solid-state light-emitting devices based on the trischelated ruthenium (II) complex. 1. Thin film blends with poly (ethylene oxide). *Journal of the American Chemical Society* **120**, 12100-12107 (1998).
- 62 van Reenen, S., Janssen, R. A. J. & Kemerink, M. Doping dynamics in light-emitting electrochemical cells. *Organic Electronics* **12**, 1746-1753 (2011).
- 63 Wågberg, T. *et al.* On the Limited Operational Lifetime of Light-Emitting Electrochemical Cells. *Advanced Materials* **20**, 1744-1749 (2008).
- 64 Gao, J. & Dane, J. Imaging the doping and electroluminescence in extremely large planar polymer light-emitting electrochemical cells. *Journal of applied physics* **98**, 063513 (2005).
- 65 Hohertz, D. & Gao, J. How Electrode Work Function Affects Doping and Electroluminescence of Polymer Light-Emitting Electrochemical Cells. *Advanced Materials* **20**, 3298-3302 (2008).
- 66 Fang, J., Yang, Y. & Edman, L. Understanding the operation of light-emitting

- electrochemical cells. *Applied Physics Letters* **93**, 063503 (2008).
- 67 Robinson, N. D., Fang, J., Matyba, P. & Edman, L. Electrochemical doping during light emission in polymer light-emitting electrochemical cells. *Physical Review B Condensed Matter* **78**, 245202 (2008).
- 68 Modestov, M. *et al.* Model of the electrochemical conversion of an undoped organic semiconductor film to a doped conductor film. *Physical Review B* **81**, 081203 (2010).
- 69 Bychkov, V. *et al.* Speedup of doping fronts in organic semiconductors through plasma instability. *Physical Review Letters* **107**, 016103 (2011).
- 70 Shimotani, H., Diguët, G. & Iwasa, Y. Direct comparison of field-effect and electrochemical doping in regioregular poly(3-hexylthiophene). *Applied Physics Letters* **86**, 022104 (2005).
- 71 Bychkov, V., Jukimenko, O., Modestov, M. & Marklund, M. Nonlinear dynamics of corrugated doping fronts in organic optoelectronic devices. *Physical Review B* **85**, 35-40 (2012).
- 72 Bideh, B. N., Roldán-Carmona, C., Shahroosvand, H. & Nazeeruddin, M. K. Low-voltage, high-brightness and deep-red light-emitting electrochemical cells (LECs) based on new ruthenium (II) phenanthroimidazole complexes. *Dalton Transactions* **45**, 7195-7199 (2016).
- 73 Ross, D. A. *et al.* Luminescent osmium (II) bi-1, 2, 3-triazol-4-yl complexes: Photophysical characterisation and application in light-emitting electrochemical cells. *Dalton Transactions* **45**, 7748-7757 (2016).
- 74 Costa, R. D. *et al.* Efficient deep-red light-emitting electrochemical cells based on a perylenediimide-iridium-complex dyad. *Chemical Communications*, 3886-3888 (2009).
- 75 Rodríguez-Redondo, J. L. *et al.* Red-light-emitting electrochemical cell using a polypyridyl iridium (III) polymer. *Dalton Transactions*, 9787-9793 (2009).
- 76 Breivogel, A. *et al.* Push-Pull Design of Bis (tridentate) Ruthenium (II) Polypyridine Chromophores as Deep Red Light Emitters in Light-Emitting Electrochemical Cells. *European Journal of Inorganic Chemistry* **2014**, 288-295 (2014).
- 77 Constable, E. C. *et al.* Red emitting  $[\text{Ir}(\text{C}^{\wedge}\text{N})_2(\text{N}^{\wedge}\text{N})]_+$  complexes employing bidentate 2, 2': 6', 2''-terpyridine ligands for light-emitting electrochemical cells. *Dalton transactions* **43**, 4653-4667 (2014).
- 78 Bolink, H. J. *et al.* Deep-red-emitting electrochemical cells based on heteroleptic bis-chelated ruthenium(II) complexes. *Inorganic chemistry* **48**, 3907-3909 (2009).

- 79 Costa, R. D. *et al.* A Deep-Red-Emitting Perylenediimide–Iridium-Complex Dyad: Following the Photophysical Deactivation Pathways. *Journal of Physical Chemistry C* **113**, 19292-19297 (2009).
- 80 Buckner, M. T. & McMillin, D. R. Photoluminescence from copper (I) complexes with low-lying metal-to-ligand charge transfer excited states. *Journal of the Chemical Society, Chemical Communications*, **17**,759-761 (1978).
- 81 Rader, R. A. *et al.* Photostudies of 2, 2'-bipyridine bis (triphenylphosphine) copper (1+), 1, 10-phenanthroline bis (triphenylphosphine) copper (1+), and 2, 9-dimethyl-1, 10-phenanthroline bis (triphenylphosphine) copper (1+) in solution and in rigid, low-temperature glasses. Simultaneous multiple emissions from intraligand and charge-transfer states. *Journal of the American Chemical Society* **103**, 5906-5912 (1981).
- 82 ONOUE, Y., HIRAKI, K. & NISHIKAWA, Y. Interactions of solid supports and fluorescent substances in thermally activated delayed fluorescence. *Analytical sciences* **3**, 509-513 (1987).
- 83 Duan, L., Qiao, J., Sun, Y. & Qiu, Y. Strategies to Design Bipolar Small Molecules for OLEDs: Donor-Acceptor Structure and Non-Donor-Acceptor Structure. *Advanced Materials* **23**, 1137-1144 (2011).
- 84 Li, J. *et al.* Highly efficient organic light-emitting diode based on a hidden thermally activated delayed fluorescence channel in a heptazine derivative. *Advanced Materials* **25**, 3319-3323 (2013).
- 85 Zhang, Q. *et al.* Efficient blue organic light-emitting diodes employing thermally activated delayed fluorescence. *Nature Photonics* **8**, 326 (2014).
- 86 Fresta, E. & Costa, R. D. Beyond traditional light-emitting electrochemical cells – a review of new device designs and emitters. *Journal of Materials Chemistry C* **5**, 5643-5675 (2017).
- 87 Elie, M. *et al.* Designing NHC–Copper(I) Dipyridylamine Complexes for Blue Light-Emitting Electrochemical Cells. *ACS applied materials & interfaces* **8**, 14678-14691 (2016).
- 88 Slinker, J. D. *et al.* Electroluminescent devices from ionic transition metal complexes. *Journal of Materials Chemistry* **17**, 2976-2988 (2007).
- 89 Costa, R. D., Ortí, E. & Bolink, H. J. Recent advances in light-emitting electrochemical cells. *Pure and Applied Chemistry* **83**, 2115-2128 (2011).
- 90 Costa, R. D. *et al.* Luminescent ionic transition-metal complexes for light-emitting electrochemical cells. *Angew Chem Int Ed Engl* **51**, 8178-8211 (2012).

- 91 Costa, R. D. *et al.* Stable and Efficient Solid-State Light-Emitting Electrochemical Cells Based on a Series of Hydrophobic Iridium Complexes. *Advanced Energy Materials* **1**, 282-290 (2011).
- 92 Zhang, Q. *et al.* Highly Efficient Electroluminescence from Green-Light-Emitting Electrochemical Cells Based on CuI Complexes. *Advanced functional materials* **16**, 1203-1208 (2006).
- 93 Armaroli, N. *et al.* Highly Luminescent CuI Complexes for Light-Emitting Electrochemical Cells. *Advanced Materials* **18**, 1313-1316 (2006).
- 94 Keller, S. *et al.* [Cu (bpy)(P<sup>^</sup>P)]<sup>+</sup> containing light-emitting electrochemical cells: improving performance through simple substitution. *Dalton transactions* **43**, 16593-16596 (2014).
- 95 Weber, M. D., Viciano-Chumillas, M., Armentano, D., Cano, J. & Costa, R. D.  $\sigma$ -Hammett parameter: a strategy to enhance both photo- and electro-luminescence features of heteroleptic copper(i) complexes. *Dalton Transactions* **46** (2017).
- 96 Wang, Y. M. *et al.* Copper(I) complex employed in organic light-emitting electrochemical cells: Device and spectra shift. *Applied Physics Letters* **87**, 220 (2005).
- 97 Wang, Y.-M. *et al.* Copper (I) complex employed in organic light-emitting electrochemical cells: Device and spectra shift. *Applied Physics Letters* **87**, 233512 (2005).
- 98 Asil, D. *et al.* Temperature- and Voltage-Induced Ligand Rearrangement of a Dynamic Electroluminescent Metallopolymer. *Angewandte Chemie International Edition* **53**, 8388-8391 (2014).
- 99 Brunner, F. *et al.* Phosphane tuning in heteroleptic [Cu(N<sup>^</sup>N)(P<sup>^</sup>P)]<sup>+</sup> complexes for light-emitting electrochemical cells. *Dalton Transactions* **48**, 446-460 (2019).
- 100 Chen, H.-F. *et al.* An ionic terfluorene derivative for saturated deep-blue solid state light-emitting electrochemical cells. *Journal of Materials Chemistry* **21**, 4175-4181(2011).
- 101 Ken-Tsung, W. *et al.* Ter(9,9-diarylfuorene)s: highly efficient blue emitter with promising electrochemical and thermal stability. *Journal of the American Chemical Society* **124**, 11576-11577 (2002).
- 102 Simon, K. *et al.* Polymorphism, fluorescence, and optoelectronic properties of a borazine derivative. *Chemistry - A European Journal* **19**, 7771-7779 (2013).
- 103 Subeesh, M. S., Shanmugasundaram, K., Sunesh, C. D., Won, Y. S. & Choe, Y. Utilization of a phenanthroimidazole based fluorophore in light-emitting



- electrochemical cells. *Journal of Materials Chemistry C* **3**, 4683-4687 (2015).
- 104 Subeesh, M. S., Shanmugasundaram, K., Sunesh, C. D., Nguyen, T. P. & Choe, Y. Phenanthroimidazole Derivative as an Easily Accessible Emitter for Non-Doped Light-Emitting Electrochemical Cells. *The Journal of Physical Chemistry C* **119**, 23676-23684 (2015).
- 105 Yuan, L. *et al.* Asymmetrically 4,7-disubstituted benzothiadiazoles as efficient non-doped solution-processable green fluorescent emitters. *Organic Letters* **11**, 5318-5321 (2009).
- 106 Huang, J. *et al.* Electroluminescence and Laser Emission of Soluble Pure Red Fluorescent Molecular Glasses Based on Dithienylbenzothiadiazole. *Advanced Functional Materials* **19**, 2978-2986 (2010).
- 107 Tang, S., Tan, W. Y., Zhu, X. H. & Edman, L. Small-molecule light-emitting electrochemical cells: evidence for in situ electrochemical doping and functional operation. *Chemical communications* **49**, 4926-4928 (2013).
- 108 Chen, H.-F., Liao, C.-T., Su, H.-C., Yeh, Y.-S. & Wong, K.-T. Highly efficient exciplex emission in solid-state light-emitting electrochemical cells based on mixed ionic hole-transport triarylamine and ionic electron-transport 1,3,5-triazine derivatives. *Journal of Materials Chemistry C* **1**, 4647-4654 (2013).
- 109 Wong, M. Y. *et al.* Light-Emitting Electrochemical Cells and Solution-Processed Organic Light-Emitting Diodes Using Small Molecule Organic Thermally Activated Delayed Fluorescence Emitters. *Chemistry of Materials* **27**, 6535-6542 (2015).
- 110 Uoyama, H., Goushi, K., Shizu, K., Nomura, H. & Adachi, C. Highly efficient organic light-emitting diodes from delayed fluorescence. *Nature* **492(7428)**, 234 (2012)
- 111 Ho, C.-C. *et al.* Phosphorescent sensitized fluorescent solid-state near-infrared light-emitting electrochemical cells. *Physical Chemistry Chemical Physics* **13**, 17729-17736 (2011).
- 112 Weber, M. D. *et al.* Benefits of using BODIPY–porphyrin dyads for developing deep-red lighting sources. *Chemical Communications* **52**, 1602-1605 (2016).
- 113 Weber, K. T. *et al.* Cunning metal core: efficiency/stability dilemma in metallated porphyrin based light-emitting electrochemical cells. *Dalton Transactions* **45**, 13284-13288 (2016).
- 114 Weber, M. D. *et al.* From White to Red: Electric-Field Dependent Chromaticity of Light-Emitting Electrochemical Cells based on Archetypal Porphyrins. *Advanced*

- Functional Materials* **26**, 6737-6750 (2016).
- 115 Shirasaki, Y., Supran, G. J., Bawendi, M. G. & Bulović, V. Emergence of colloidal quantum-dot light-emitting technologies. *Nature Photonics* **7**, 13 (2012).
- 116 Hu, M. Z. & Zhu, T. Semiconductor Nanocrystal Quantum Dot Synthesis Approaches Towards Large-Scale Industrial Production for Energy Applications. *Nanoscale Res Lett* **10**, 469 (2015).
- 117 Frecker, T., Bailey, D., Arzeta-Ferrer, X., McBride, J. & Rosenthal, S. J. Quantum dots and their application in lighting, displays, and biology. *ECS Journal of Solid State Science and Technology* **5**, R3019-R3031 (2016).
- 118 Schmidt, L. C. *et al.* Nontemplate Synthesis of CH<sub>3</sub>NH<sub>3</sub>PbBr<sub>3</sub> Perovskite Nanoparticles. *Journal of the American Chemical Society* **136**, 850-853 (2014).
- 119 Veldhuis, S. A. *et al.* Perovskite Materials for Light-Emitting Diodes and Lasers. *Advanced Materials* **28**, 6804-6834 (2016).
- 120 Reiss, P., Carrière, M., Lincheneau, C., Vaure, L. & Tamang, S. Synthesis of Semiconductor Nanocrystals, Focusing on Nontoxic and Earth-Abundant Materials. *Chemical reviews* **116**, 10731-10819 (2016).
- 121 Park, J., Joo, J., Kwon, S. G., Jang, Y. & Hyeon, T. Synthesis of Monodisperse Spherical Nanocrystals. *Angewandte Chemie International Edition* **46**, 4630-4660 (2007).
- 122 Docampo, P. & Bein, T. A Long-Term View on Perovskite Optoelectronics. *Accounts of Chemical Research* **49**, 339-346 (2016).
- 123 Qian, G. *et al.* Saturated and Multi-Colored Electroluminescence from Quantum Dots Based Light Emitting Electrochemical Cells. *Advanced Functional Materials* **24**, 4484-4490 (2014).
- 124 Frohleiks, J. *et al.* Quantum Dot/Light-Emitting Electrochemical Cell Hybrid Device and Mechanism of Its Operation. *ACS applied materials & interfaces* **8**, 24692-24698 (2016).
- 125 Li, J., Bade, S. G. R., Shan, X. & Yu, Z. Single-Layer Light-Emitting Diodes Using Organometal Halide Perovskite/Poly(ethylene oxide) Composite Thin Films. *Advanced Materials* **27**, 5196-5202 (2015).
- 126 Zhang, H. *et al.* Organic-Inorganic Perovskite Light-Emitting Electrochemical Cells with a Large Capacitance. *Advanced Functional Materials* **25**, 7226-7232 (2015).
- 127 Costa, R. D., Pertegás, A., Ortí, E. & Bolink, H. J. Improving the Turn-On Time of Light-Emitting Electrochemical Cells without Sacrificing their Stability. *Chemistry of*

- Materials* **22** (2010).
- 128 Shen, Y. *et al.* Improving light-emitting electrochemical cells with ionic additives. *Applied Physics Letters* **102** (2013).
- 129 Weber, M. D., Adam, M., Tykwinski, R. R. & Costa, R. D. Controlling the Chromaticity of Small-Molecule Light-Emitting Electrochemical Cells Based on TIPS-Pentacene. *Advanced Functional Materials* **25**, 5066-5074 (2015).
- 130 Aygüler, M. F. *et al.* Light-emitting electrochemical cells based on hybrid lead halide perovskite nanoparticles. *The Journal of Physical Chemistry C* **119**, 12047-12054 (2015).
- 131 Kervella, Y., Armand, M. & Stéphan, O. Organic light-emitting electrochemical cells based on polyfluorene. Investigation of the failure modes. *Journal of The Electrochemical Society* **148**, H155-H160 (2001).
- 132 Edman, L., Moses, D. & Heeger, A. J. Influence of the anion on the kinetics and stability of a light-emitting electrochemical cell. *Synthetic Metals* **138**, 441-446 (2003).
- 133 Shin, J.-H. *et al.* Light emission at 5V from a polymer device with a millimeter-sized interelectrode gap. *Applied Physics Letters* **89**, 013509 (2006).
- 134 Fang, J., Matyba, P., Robinson, N. D. & Edman, L. Identifying and Alleviating Electrochemical Side-Reactions in Light-Emitting Electrochemical Cells. *Journal of the American Chemical Society* **130**, 4562-4568 (2008).
- 135 Armand, M., Chabagno, J. & Duclot, M. Second international meeting on solid electrolytes. *St Andrews, Scotland*, 20-22 (1978).
- 136 Vashishta, P. & Mundy, J. N. *Fast ion transport in solids: electrodes and electrolytes*. (Elsevier North Holland, Inc, 1979).
- 137 Berthier, C. *et al.* Microscopic investigation of ionic conductivity in alkali metal salts-poly(ethylene oxide) adducts. *Solid State Ionics* **11**, 91-95 (1983).
- 138 Mindemark, J. & Edman, L. Illuminating the electrolyte in light-emitting electrochemical cells. *Journal of Materials Chemistry C* **4**, 420-432 (2016).
- 139 Shin, J.-H., Robinson, N. D., Xiao, S. & Edman, L. Polymer Light-Emitting Electrochemical Cells: Doping Concentration, Emission-Zone Position, and Turn-On Time. *Advanced Functional Materials* **17**, 1807-1813 (2007).
- 140 Rietman, E. A., Kaplan, M. L. & Cava, R. J. Alkali metal ion-poly (ethylene oxide) complexes. II. Effect of cation on conductivity. *Solid State Ionics* **25**, 41-44 (1987).
- 141 Kaihovirta, N., Asadpoordarvish, A., Sandström, A. & Edman, L. Doping-Induced Self-Absorption in Light-Emitting Electrochemical Cells. *ACS Photonics* **1**, 182-189

- (2014).
- 142 Kaihovirta, N., Longo, G., Gil-Escrig, L., Bolink, H. J. & Edman, L. Self-absorption in a light-emitting electrochemical cell based on an ionic transition metal complex. *Applied Physics Letters* **106**, 103502 (2015).
- 143 Chandrasekhar, V. in *Blockcopolymers-Polyelectrolytes-Biodegradation* 139-205 (Springer, 1998).
- 144 Galiński, M., Lewandowski, A. & Stępnia, I. Ionic liquids as electrolytes. *Electrochimica Acta* **51**, 5567-5580 (2006).
- 145 Parker, S. T. *et al.* Improved Turn-on Times of Iridium Electroluminescent Devices by Use of Ionic Liquids. *Chemistry of Materials* **17**, 3187-3190 (2005).
- 146 Habrard, F., Ouisse, T. & Stéphan, O. Conjugated Polymer/Molten Salt Blend Optimization. *The Journal of Physical Chemistry B* **110**, 15049-15051 (2006).
- 147 Shin, J.-H., Xiao, S. & Edman, L. Polymer Light-Emitting Electrochemical Cells: The Formation and Effects of Doping-Induced Micro Shorts. *Advanced Functional Materials* **16**, 949-956 (2006).
- 148 Ouisse, T., Stéphan, O., Armand, M. & Leprêtre, J. C. Double-layer formation in organic light-emitting electrochemical cells. *Journal of Applied Physics* **92**, 2795-2802 (2002).
- 149 Yang, C., Sun, Q., Qiao, J. & Li, Y. Ionic Liquid Doped Polymer Light-Emitting Electrochemical Cells. *The Journal of Physical Chemistry B* **107**, 12981-12988 (2003).
- 150 Habrard, F. *et al.* Conjugated polymer/molten salt blends: The relationship between morphology and electrical aging. *Journal of Applied Physics* **96**, 7219-7224 (2004).
- 151 Sakanoue, T. *et al.* Optically pumped amplified spontaneous emission in an ionic liquid-based polymer light-emitting electrochemical cell. *Applied Physics Letters* **100**, 263301 (2012).
- 152 Shin, J.-H. & Edman, L. Light-Emitting Electrochemical Cells with Millimeter-Sized Interelectrode Gap: Low-Voltage Operation at Room Temperature. *Journal of the American Chemical Society* **128**, 15568-15569 (2006).
- 153 Yu, Z. *et al.* Stabilizing the Dynamic p-i-n Junction in Polymer Light-Emitting Electrochemical Cells. *The Journal of Physical Chemistry Letters* **2**, 367-372 (2011).
- 154 Wenzl, F. P. *et al.* Ion dissociation in crown ether based wide band gap LECs. *Synthetic Metals* **121**, 1735-1736 (2001).
- 155 Yang, Y. & Pei, Q. Efficient blue-green and white light-emitting electrochemical cells based on poly[9,9-bis(3,6-dioxaheptyl)-fluorene-2,7-diyl]. *Journal of Applied Physics*

- 81**, 3294-3298 (1997).
- 156 Pei, Q. & Yang. Efficient Photoluminescence and Electroluminescence from a Soluble Polyfluorene. *Journal of the American Chemical Society* **118**, 7416-7417 (1996).
- 157 Morgado, J. *et al.* Light-emitting devices based on a poly(p-phenylene vinylene) derivative with ion-coordinating side groups. *Journal of Applied Physics* **86**, 6392-6395 (1999).
- 158 Morgado, J. *et al.* Luminescence properties of PPV-based copolymers with crown ether substituents. *Synthetic Metals* **111-112**, 449-452 (2000).
- 159 Sun, Q., Wang, H., Yang, C. & Li, Y. Synthesis and electroluminescence of novel copolymers containing crown ether spacers. *Journal of Materials Chemistry* **13**, 800-806 (2003).
- 160 Sun, Q., Yang, C., Wang, H., He, G. & Li, Y. Polymer light-emitting electrochemical cell based on a block copolymer containing tri(ethyleneoxide) spacers. *Polymers for Advanced Technologies* **13**, 663-669 (2002).
- 161 Otto, K. Electrical conductivity of SiO<sub>2</sub>-B<sub>2</sub>O<sub>3</sub> glasses containing lithium or sodium. *Physics and Chemistry of Glasses* **7**, 29 (1966).
- 162 Carette, B., Ribes, M. & Souquet, J. L. The effects of mixed anions in ionic conductive glasses. *Solid State Ionics* **9-10**, 735-737 (1983).
- 163 Button, D. P., Tandon, R. P., Tuller, H. L. & Uhlmann, D. R. Fast Li<sup>+</sup> ion conduction in chloro-borate glasses. *Journal of Non-Crystalline Solids* **42**, 297-306 (1980).
- 164 Zielniok, D., Cramer, C. & Eckert, H. Structure/Property Correlations in Ion-Conducting Mixed-Network Former Glasses: Solid-State NMR Studies of the System Na<sub>2</sub>O– B<sub>2</sub>O<sub>3</sub>– P<sub>2</sub>O<sub>5</sub>. *Chemistry of materials* **19**, 3162-3170 (2007).
- 165 Tatsumisago, M., Nagao, M. & Hayashi, A. Recent development of sulfide solid electrolytes and interfacial modification for all-solid-state rechargeable lithium batteries. *Journal of Asian Ceramic Societies* **1**, 17-25 (2013).
- 166 Yu, X., Bates, J. B., Jellison, G. E. & Hart, F. X. A Stable Thin-Film Lithium Electrolyte: Lithium Phosphorus Oxynitride. *Journal of The Electrochemical Society* **144**, 524-532 (1997).
- 167 Zhang, Z. & Kennedy, J. H. Synthesis and characterization of the B<sub>2</sub>S<sub>3</sub>-Li<sub>2</sub>S, the P<sub>2</sub>S<sub>5</sub>-Li<sub>2</sub>S and the B<sub>2</sub>S<sub>3</sub>-P<sub>2</sub>S<sub>5</sub>-Li<sub>2</sub>S glass systems. *Solid State Ionics* **38**, 217-224 (1990).
- 168 Ingram, M. D. Ionic conductivity and glass structure. *Philosophical Magazine B* **60**, 729-740 (1989).
- 169 Dyre, J. C., Maass, P., Roling, B. & Sidebottom, D. L. Fundamental questions relating

- to ion conduction in disordered solids. *Reports on Progress in Physics* **72**, 046501 (2009).
- 170 Martin, S. W. & Angell, C. Dc and ac conductivity in wide composition range Li<sub>2</sub>O-P<sub>2</sub>O<sub>5</sub> glasses. *Journal of Non-Crystalline Solids* **83**, 185-207 (1986).
- 171 Anderson, O. & Stuart, D. Calculation of activation energy of ionic conductivity in silica glasses by classical methods. *Journal of the American Ceramic Society* **37**, 573-580 (1954).
- 172 McElfresh, D. & Howitt, D. G. Activation enthalpy for diffusion in glass. *Journal of the American Ceramic Society* **69**, C-237-C-238 (1986).
- 173 Ravaine, D. & Souquet, J. A thermodynamic approach to ionic conductivity in oxide glasses—part 2. A statistical model for the variations of the chemical potential of the constituents in binary alkali oxide glasses. *Physics and Chemistry of Glasses* **19**, 115-120 (1978).
- 174 Martin, S. W. Ionic conduction in phosphate glasses. *Journal of the American Ceramic Society* **74**, 1767-1784 (1991).
- 175 Matyba, P., Andersson, M. R. & Edman, L. On the desired properties of a conjugated polymer-electrolyte blend in a light-emitting electrochemical cell. *Organic Electronics* **9**, 699-710 (2008).
- 176 Braye, E. H., Hübel, W. & Caplier, I. New Unsaturated Heterocyclic Systems. I. *Journal of the American Chemical Society* **83**, 4406-4413 (1961).
- 177 Mathey, F. The organic chemistry of phospholes. *Chemical reviews* **88**, 429-453 (1988).
- 178 Schaefer, W., Schweig, A. & Mathey, F. Theory and application of photoelectron spectroscopy. 60. Phospholes. Electronic structure. *Journal of the American Chemical Society* **98**, 407-414 (1976).
- 179 Duffy, M. P., Delaunay, W., Bouit, P. A. & Hissler, M.  $\pi$ -Conjugated phospholes and their incorporation into devices: components with a great deal of potential. *Chemical Society Reviews* **45**, 5296-5310 (2016).



## **Chapter II: Hybrid materials based on silicate glasses**





## 1. Introduction

Silicate glass is developed throughout modern technology. Among all the glass kinds, silicate glass is the “oldest” one. Silicate glasses have many applications in the life including windows, lamps and optical components which be used in a wide of the specialized field such as communication, electronics, laser and composites 1-9.

Numerous works have been carried out to determine the structure of silicate glass using various kinds of technology 1,10-15. Silica glass is the simplest silicate glass, which is the most refractory glass in commercial use. Silica glass is based on the Si-tetrahedra [SiO<sub>4</sub>], which is resulting from the formation of sp<sup>3</sup> hybrid orbitals of Si outer electrons (3s<sup>2</sup>3p<sup>2</sup>). The addition of other oxide modifiers into the silica glass can form other silicate glass. These oxide modifiers can react with the network to break the bonds producing mobile ions and increasing the degrees of freedom of the network. A simple example of this involves the binary lithium silicate glass. Addition of modifier oxide Li<sub>2</sub>O makes Si-O- Li<sup>+</sup> units which reduce the rigidity of the network since Li<sup>+</sup> is mobile, and Si-O- units produce more degrees of freedom available to the network than Si-O-Si bonds.

For a long time, glass was employed an electrical insulator. In 1966, Otto reported glass composition of Li<sub>2</sub>O–SiO<sub>2</sub>–B<sub>2</sub>O<sub>3</sub> with high lithium ion conductivity (>10<sup>-4</sup> S/cm) at about 350 °C, thereby starting the researches of fast lithium ion conduction in the glass. Extensive efforts have been done in order to further increase the conductivity of silicate glass to a practical level for all solid state lithium battery. However, it has to be admitted that silicate glass has a relatively low conductivity for producing batteries (10<sup>-5</sup> S/cm at 423K for the 30Li<sub>2</sub>O-70 SiO<sub>2</sub> glass composition)<sup>16</sup>. Fortunately, this ionic conductivity is high enough to study the possibility of preparing a LEC using such an inorganic glass electrolyte. As we mentioned silicate glasses needs high temperature of the melting before being quenched (usually above 1300 °C). This melting temperature is far higher than the other glass families such as phosphate, fluoride, chalcogenide or metallic glasses. Therefore, it is obviously impossible to use the traditional melt-quenching way to develop an organic semiconductor(OSC) doped silicate glass. To tackle this problem, the sol-gel technology was used to avoid the high temperature process of melt-quenching. Compared to the glass melt-quenching method, the sol–gel process has the advantages of low temperatures and tunable structure that allows controlling over the morphology, porosity, size.

The sol-gel process of silicate glass refers to the controlled hydrolysis and polymerization of a metal alkoxide, generally tetraethyl orthosilicate (TEOS)<sub>3</sub>. The active units that are produced by hydrolysis process grow in size and molecular weight by the condensation and polymerization process. A polymer is a huge molecule which is formed from hundreds or thousands units call monomers that are capable of forming at least two bonds. At some time during the polymerization process, the solution undergo a sol-gel transition, and a stiff gel is formed. The gel is then dried before being heat treated.

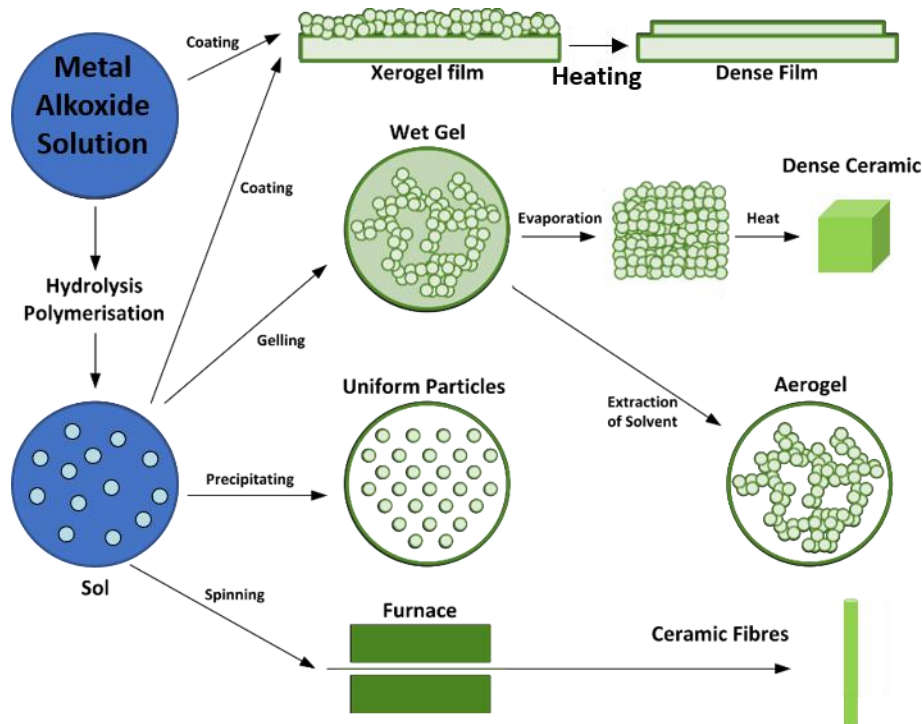


Fig. 2.1. Sol-Gel process technology and chemistry preparation of metal oxides using sol-gel routes proceeds

Depending on the aging time of the solution, different forms of samples can be prepared as shown in Fig 2.1. In this work, we are devoted to use this method to prepare an organophosphorus organic semiconductor (OPSC) doped organic-inorganic hybrid lithium modified silicate glass coating. However, since the presence of alkali in sol-gel solutions not only can encourage polymerization, but also can cause depolymerization, the process of polymerization becomes more complicated after adding alkali ions into the solutions. Therefore, it is rational to formulate the study from preparing silica glass coatings before assembling the lithium modified silicate glass coating. On the other hand, although the underlying physics and chemistry that govern polymer growth and gelation are essentially the same for films as bulk gels, the structural evolution in films are more complicated than that in bulk<sup>17</sup>. Therefore, it is impartial to develop the bulk gel before preparing the coating. Thus,

the systematic schedule of the experiments is shown below for both silica and modified silicate glasses:

#### I. Silica glass

- 1) synthesis of the bulk silica gel;
- 2) synthesis of OPSC doped bulk silica gel;
- 3) preparation of silica coating;
- 4) preparation of OPSC doped silica coating.

#### II. Lithium modified silicate glass:

- 1) synthesis of the bulk lithium modified silicate glass gel;
- 2) preparation of OPSC doped bulk lithium modified silicate glass gel;
- 3). preparation of lithium modified silicate glass coating;
- 4). preparation of OPSC doped lithium modified silicate glass coating.

## 2. Experiments

### 2.1 Raw Chemicals

The following precursors were used without further purification to prepare silica-based sol-gel derived glasses; Tetraethyl orthosilicate ( $C_8H_{20}O_4Si$ , 99+%, Alfa Aesar, US), Lithium hydrate ( $LiOH$ , 99%, Alfa Aesar, US), Lithium chloride ( $LiCl$ , 99%, Alfa Aesar, US), Lithium Nitrate ( $LiNO_3$ , 99.99%, Alfa Aesar, US), Lithium citrate tribasic tetrahydrate ( $C_6H_5Li_3O_7 \cdot 4H_2O$ , 99%, aladdin, China), Ethanol ( $CH_3CH_2OH$ , >99.7%, Sigma-Aldrich, Fr), Acetone ( $CH_3COCH_3$ , >99.5%, Sigma-Aldrich, Fr), Hydrochloric acid ( $HCl$ , ACS reagent 37%, Sigma-Aldrich, Fr),  $H_2O$  (home made deionized water)

### 2.2 Sol-gel synthesis methods

#### 2.2.1 Silica gel

The reaction was initiated by diluting TEOS in ethanol and magnetically stirred for about 10 minutes. Then  $H_2O$  and  $HCl$  were added dropwise into the vessel and mixed by stirring for 2 hours. The schematic of the sol-gel synthesis of silica gel is shown in Fig 2.2.

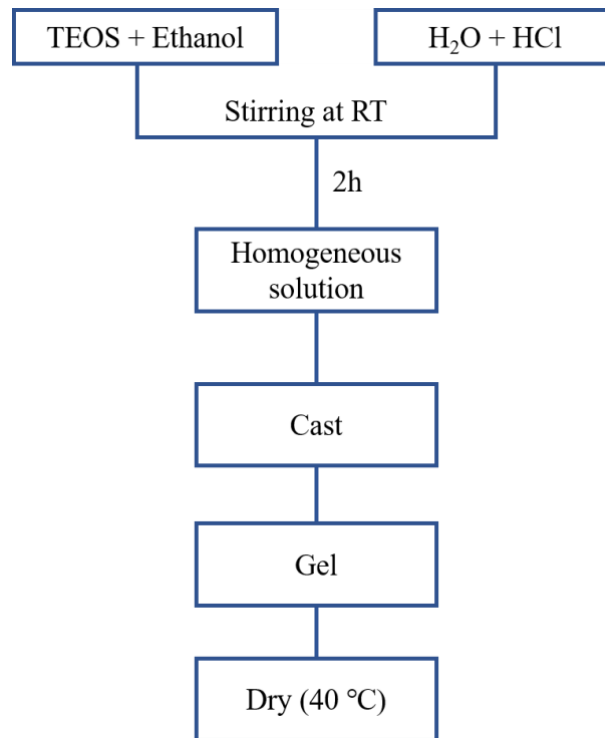


Fig. 2.2. Schematic of the sol-gel synthesis of silica xerogel

### 2.2.2 Lithium modified glass

There are two lithium precursors: LiOH and LiNO<sub>3</sub>. The process is a bit different for both of them.

#### 1. LiOH as precursor:

The reaction was initiated by diluting TEOS in ethanol and magnetically stirred for about 10 minutes. Then H<sub>2</sub>O and LiOH were mixed firstly before being added dropwise into the vessel. Follow that, the solution was mixed by stirring for 2 hours. The schematic of the sol-gel synthesis of silica gel is shown in Fig. 2.3.

#### 2. LiNO<sub>3</sub> as precursor:

The difference from the LiOH as precursor process is that after the H<sub>2</sub>O and LiNO<sub>3</sub> were added into the TEOS solution, the HCl was also added into the solution. In addition, the mixing time increase to 3h. The schematic of the sol-gel synthesis of silica gel is shown in Fig 2.4.

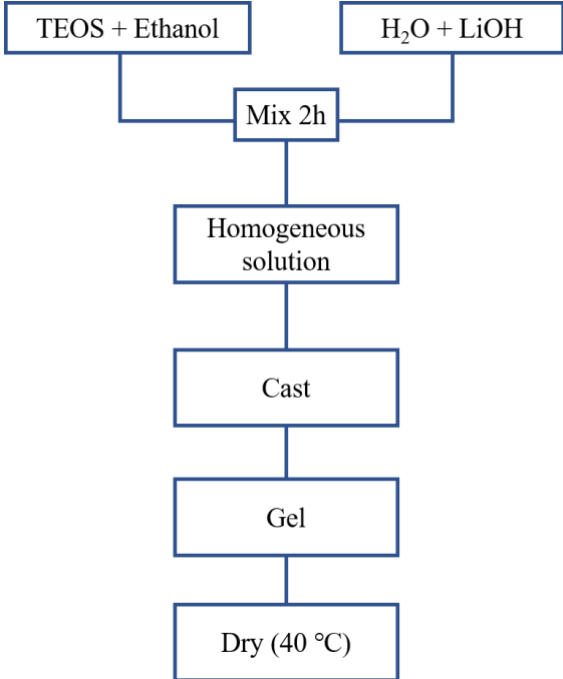


Fig. 2.3. Schematic of the sol-gel synthesis of lithium modified silicate xerogel using LiOH as precursor

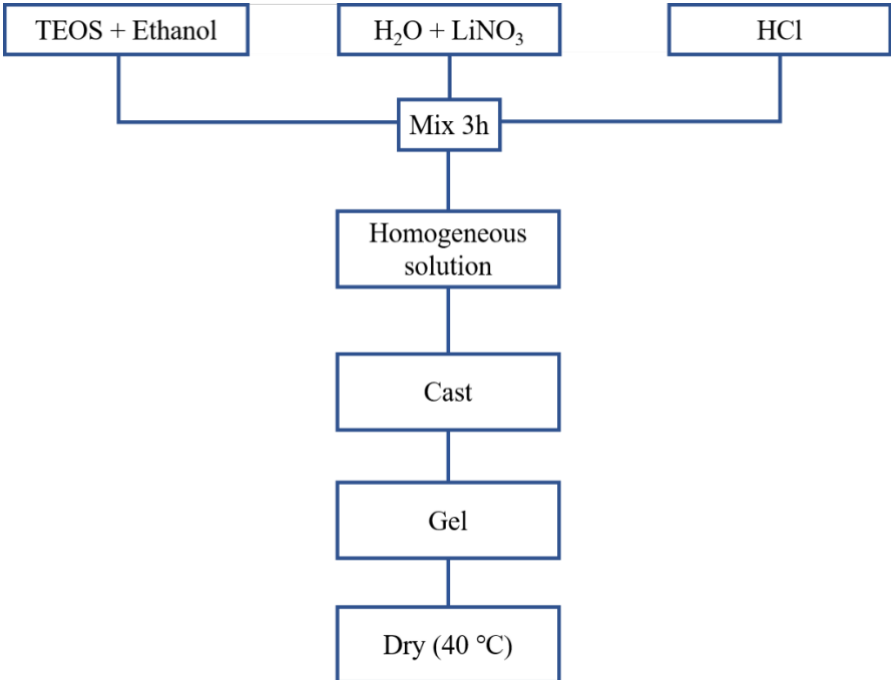


Fig. 2.4. Schematic of the sol-gel synthesis of lithium modified silicate xerogel using LiNO<sub>3</sub> as precursor

**2.2.3 OSC doped silica glass**

This process was initiated by diluting OSC in acetone and ultrasonic vibrated for about 10 min. Then, the next step is similar to the process of silica gel preparation. The complete schematic of the sol-gel synthesis of silica gel is shown in Fig. 2.5.

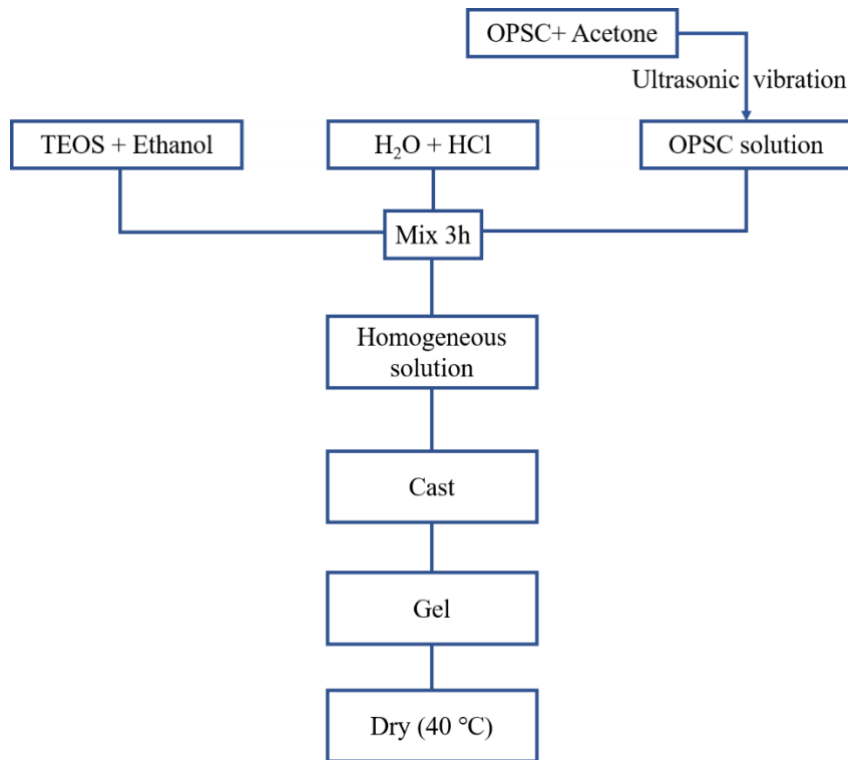


Fig. 2.5. Schematic of the sol-gel synthesis of OPSC doped silica gel

### 2.3 Drying procedure

The obtained homogeneous solutions of both silica and lithium silicate glass were aged at room temperature for three days in glass containers with cast before drying in an oven (EV014-Townson& Mercer, Cheshire, UK). The temperature was then increased gradually ( $0.5\text{ }^{\circ}\text{C s}^{-1}$ ) up to  $60\text{ }^{\circ}\text{C}$  and kept for three days.

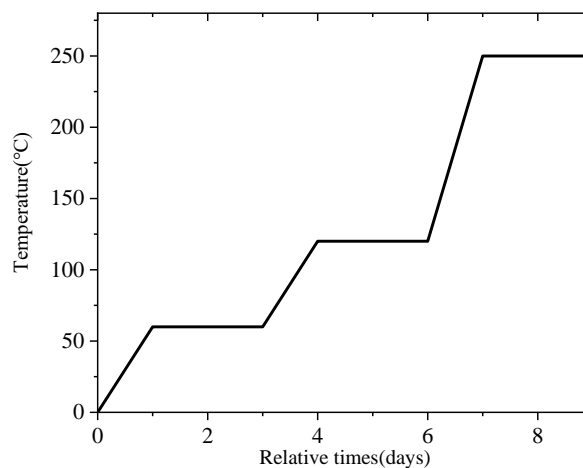


Fig. 2.6. Heat treatment diagram for the sol-gel synthesised silica and lithium modified silicate gel.

Then, the heating was continued at  $120\text{ }^{\circ}\text{C}$  for an additional three days. Finally, the temperature was increased to  $250\text{ }^{\circ}\text{C}$  and kept for three days to remove any remaining solvent and aiming to obtain bulk, amorphous samples 18. After the final heating stage, the oven was

turned off and samples left overnight in the oven to cool down slowly. Fig. 2.6 shows the heat-treatment diagram for the synthesis of silica and lithium modified silicate gel.

## 2.4 Coating method

### 2.4.1 Substrate and its clean process

Silicate glass (K9) substrate (20×20 mm) was used as the substrate. 5 steps have been performed to clean the substrates before preparing the coatings. Firstly, the substrates should be flushed using large amount of deionized water. Secondly, the substrates should be soaked in acetone for 10 min. Thirdly, the substrates should be soaked in ethanol in the beaker put in the ultrasonic cleaners. Fourthly, the substrates should be flushed again using larger amount of deionized water. The last step is put the substrates in a container with the cast to dry in the oven.

### 2.4.2 Spin-coating method

There are four main method to prepare the coating as shown in Fig 2.7. Here, we use the spin way to prepare the coating. The model of the spin-coater is SPIN150 (SPS-Europe, Fr). The coater was put in the dust-free worktable to keep from the dust.

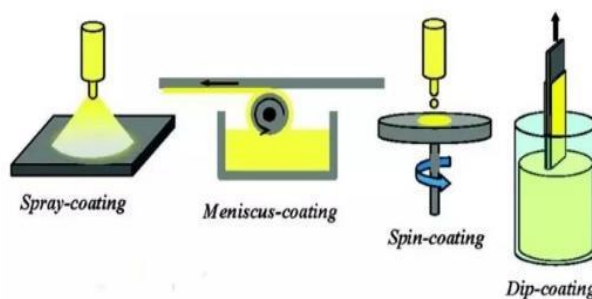


Fig. 2.7. Common methods to prepare coating for sol-gel.

### 2.4.3 Drying process

The obtained coating was put in a container that was placed in an oven at 100 °C for 1 h. Then the sample was put in the furnace, and the temperature was then increased gradually (0.5 °C/s) to 100 °C and kept for 1 h. Following this, a dwell of 3 h at 250 °C was added to remove adsorbed species and organics except OPSC molecules<sup>18</sup>. After the final heating stage, the oven was turned off and samples left overnight in the oven to cool down slowly. Fig 2.8 shows the heat-treatment diagram for the spin-coater synthesized silicate glasses coating.



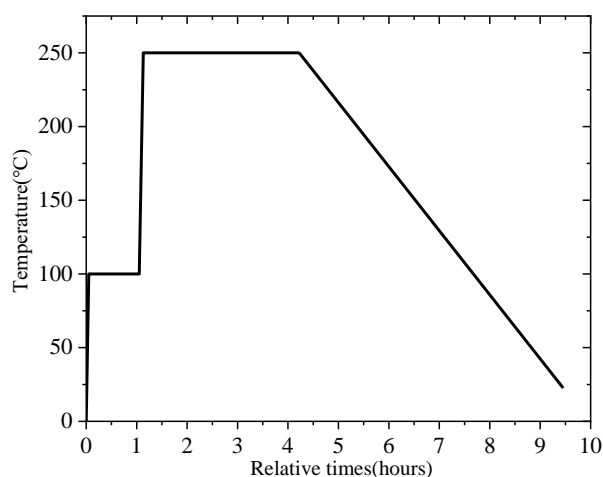
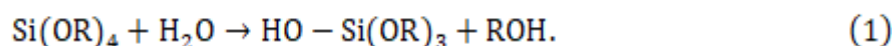


Fig. 2.8. Heat treatment diagram for the sol-gel coating.

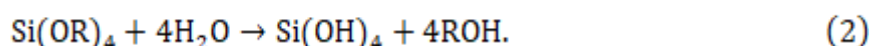
### 3. Silica bulk glass

#### 3.1 Structural evolution during Sol-gel process

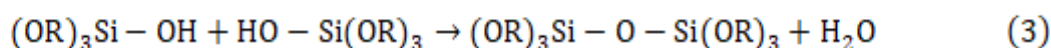
As silicon alkoxides can react rapidly with water, they became popular precursors. The reaction between the precursors and water is called hydrolysis because a hydroxyl ion becomes attached to the metal atom, which can be depicted in the following reaction:



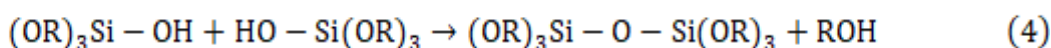
The R represents a proton or other ligand (if R is an alkyl, then OR is an alkoxy group), and ROH is an alcohol; the “-” is used to represent a chemical bond. The redundant amount of water and catalyst makes the hydrolysis go to completion, which means all of the OR groups are replaced by OH



The lack of water and catalyst causes the partial hydrolyzation of the metal,  $\text{Si(OR)}_{4-n}(\text{OH})_n$ . These partially hydrolyzed molecules can also link together in a condensation reaction, such as:



Or



Through definition, condensation liberates a small molecule including water and alcohol. This reaction can also build bigger and bigger silicon-containing molecules by polymerization.

Compare to other transition metals, silicon has a less electropositive property. This makes it less susceptible to nucleophilic attack. Besides, both the coordination number and the

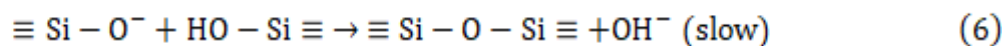
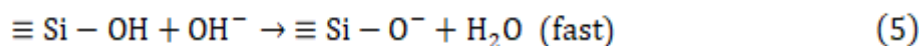
oxidation state of silicon is 4, which makes the coordination expansion does not spontaneously occur with nucleophilic reagents. These factors make both the hydrolysis and condensation process of silicon considerably longer than that of other transition metal systems. Normally, in order to save the time, the catalyst is very important for the polymerization process. Typically, the hydrochloric acid and ammonia water are the most common catalyst through adjusting the pH of the reaction condition.

The polymerization process can be divided into three approximate pH domains:  $\text{pH} < 2$ ,  $2 < \text{pH} < 7$ , and  $\text{pH} > 7$ . pH 2 is the isoelectric point (IEP) of  $\text{SiO}_2$  sol, where the electrical mobility of the silica particles is zero. pH above 7 make the silica particles be ionized so that the particles grow without aggregation or gelation. In addition, the mechanism of the polymerization process between the  $\text{pH} < 2$  and the pH within 2-7 is different.

These three parts are detailed below:

#### 1) Polymerization when pH 2-7

When the  $\text{pH} > \text{IEP}$ , a nucleophilic mechanism occurs. The surface of the silica particles can attract  $\text{OH}^-$ , so the condensation rate is proportional to  $[\text{OH}^-]$  as in the following reaction sequence:



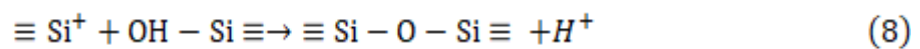
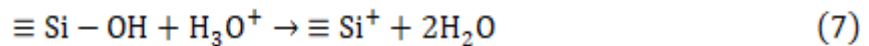
Among all the silicate species, the silanol in the most highly condensed species are the acidic silanol, which is most likely to be deprotonated according to Equation (4). Therefore, the condensation in Equation (5) happens preferentially between more highly condensed species and less highly condensed neutral species, for example, the reaction:  $(\text{OR})_3\text{SiOSiO}^-(\text{OR})_2 + \text{HO} - \text{Si}(\text{OR})_3$  occurs preferentially over  $(\text{OR})_3\text{Si} - \text{O}^- + (\text{OR})_3\text{Si} - \text{OH}$ . This means, the rate of dimerization is low, however, once the  $Q_2^1$  condensed species form, the  $Q_3^2$  or  $(Q_2^1 Q_2^2)$  or  $(Q_1^1 Q_3^3 Q_2^2)$  would fast form. Then, more condensed species will be formed. In  $Q_x^n$  notation, the superscript  $n$  denotes the number of bridging oxygens ( $-\text{OSi}$ ) surrounding the central silicon, and the sum of the subscripts,  $x$ , equals the number of silicons comprising the silicate species. Moreover, since the solubility of silica is low in this pH range, the particle stops growing when the solubility and size-dependence of solubility is greatly reduced, which limits the size of the particle at around 2-4 nm.

#### 2) $\text{pH} > 7$

Above pH 7, it is also nucleophilic mechanism. However, since all the condensed species are in the ionized state and therefore mutually repulsive, which makes the growth of the condensed species depend on the addition of monomers to more highly condensed particles rather than aggregation.

3) pH < 2

When pH < IEP, an electrophilic mechanism takes place. The surface of the silica particles can attract H<sup>+</sup>, so the polymerization rate is proportional to H<sup>+</sup> as in the following reaction sequence:



This mechanism involves an intermediate siliconium ion  $\equiv \text{Si}^+$ . This intermediate  $\equiv \text{Si}^+$  attacks other  $\equiv \text{Si} - \text{OH}$  to form another intermediate  $\equiv \text{Si} - (\text{OH})^+ - \text{Si} \equiv$ , which finally form  $\equiv \text{Si} - \text{O} - \text{Si} \equiv$ , to achieve condensation.

The ratio between H<sub>2</sub>O and Si(OR)<sub>4</sub> (*r*) determines the pattern of the poly-silicate product including fibers, bulk gels, or colloidal particles through controlling the hydrolysis reaction. For TEOS as the alkoxides, when *r* = 4, the TEOS can be totally hydrolysed. Therefore, in the range of *r* < 4, the increase of the value of *r* generally decreases the time of gelation because of promoting hydrolysis, whereas in the range *r* > 4, an increase of the value of *r* generally increases the gelation time because of decreasing concentration of Si-OH. Larger value of *r* causes liquid-liquid immiscibility, therefore, other solvent like alcohol was used to obtain homogenization of the solution.

### 3.2 Preparation of Silica bulk xerogel

In our work, we used the TEOS-H<sub>2</sub>O-C<sub>2</sub>H<sub>5</sub>OH ternary system with HCl as catalyst to prepare the silica bulk xerogel. An addition of C<sub>2</sub>H<sub>5</sub>OH is needed because water and alkoxy silanes are immiscible, a mutual solvent such as alcohol is normally used as a homogenizing agent<sup>19</sup>. Since, water is produced as a by-product of the condensation reaction, *r*, even lower than 4, is theoretically sufficient for complete hydrolysis and condensation to yield anhydrous silica. Moreover, acid-catalyzed hydrolysis process with low H<sub>2</sub>O: Si ratio produces weakly branched “polymeric” sols, whereas base-catalyzed hydrolysis prefer produces highly condensed “particulate” sols<sup>20</sup>. Considering the transport of lithium ions in the material, “polymeric” structure, which is analogous to organic electrolyte, is advisable for our work.

Therefore, in this work, 5 ml solution was prepared with the molar ratio TEOS: H<sub>2</sub>O: C<sub>2</sub>H<sub>5</sub>OH =1:3:4, and the pH is maintained below 2 using 12N HCl. The synthesis process to prepare the sample is shown in Fig 2.2, cast and drying steps were vanished.



Fig. 2.9. Photograph of cracked silica xerogel sample

After the homogeneous solution was prepared, the solution is just put in the ambient atmosphere without any other treatment. Three days later, the gel is formed. Two weeks later, the gel becomes xerogel. Unfortunately, the sample finally cracked as shown in Fig 2.9. This is because the vanished cast step leads the evaporation rate of the solvent is too fast to balance the interfacial residual stress. This problem was solved later by prolonging the drying time using a plastic film, which casts the container as described in the schematic of Fig 2.2, and the sample is shown in Fig 2.10.



Fig. 2.10. Photograph of silica xerogel sample

After the drying process shown in Fig 2.6, the phase and crystalline structure of the silica xerogel were characterized by XRD (D/max 2550 VB/PC Rikagu, Japan). All measurements were carried out at room temperature using Cu  $\alpha$  radiation ( $\lambda=1.54056\text{\AA}$ ). A step size of  $0.02^\circ$  ( $2\theta$ ) was used with a scan speed of  $2^\circ/\text{min}$ . The result is shown in Fig 2.11. There are no obvious crystal peaks, which suggests that the sample is amorphous.

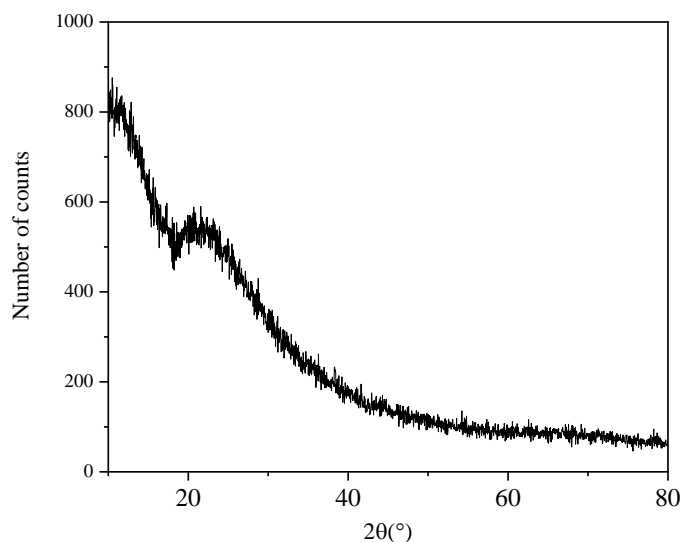


Fig. 2.11. XRD pattern of silica xerogel

### 3.3 OPSC doped Silica bulk xerogel

Based on the silica bulk gel, we investigated the preparation of hybrid gel by introducing organophosphorus organic semiconductor (OPSC). In this work, two kinds of OPSC molecules were used: OPSCS3 (green) and OPSC7D3 (blue). The structure of the OPSC7D3 and OPSCS3 are shown in Fig 2.12 (a) and (b), respectively.

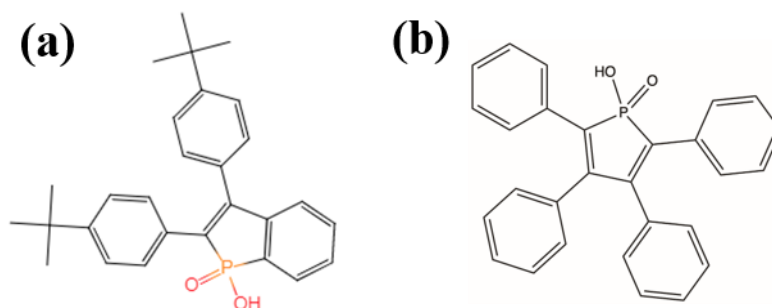


Fig. 2.12. Structure of OPSC7D3 (a) and OPSCS3 (b)

The first experiment consisted in doping the OPSCS3 within silica gel. The process is similar to the classical process of silica gel described before, the only difference remains in the addition of the OPSCS3 molecule into the solution after mixing the precursor. The concentration of OPSCS3 is of 0.06 w%. After doping the OPSCS3, it was found that the OPSCS3 is not soluble in the solution. Some obvious OPSCS3 particles can be observed (Fig. 2.13) by the naked eyes.

Fig 2.13 shows the gel after 7 days and 10 days of preparation. It was found that the bulk xerogel is crack into two pieces.

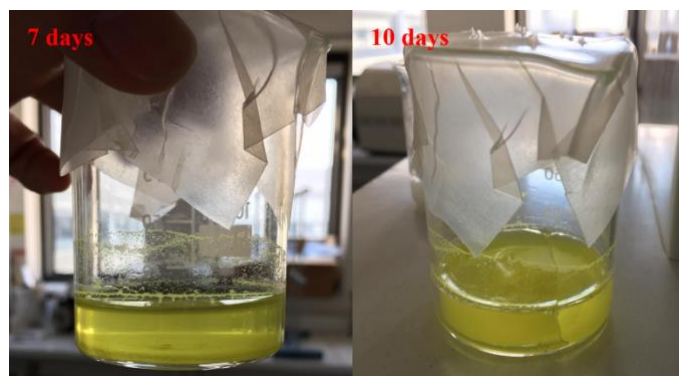


Fig. 2.13. Photograph of OPSCS3 doped silica gel after 7 days and 10 days of preparation

It is probably because the OPSCS3 molecules can not dissolve in the solution of silica gel, they remain as big solid particles within the solution and thus could frustrate the polymerization process in the gel, creating some mechanical constrains. This phenomenon of insolubilization is more obvious after two weeks of drying as shown in Fig 2.14.

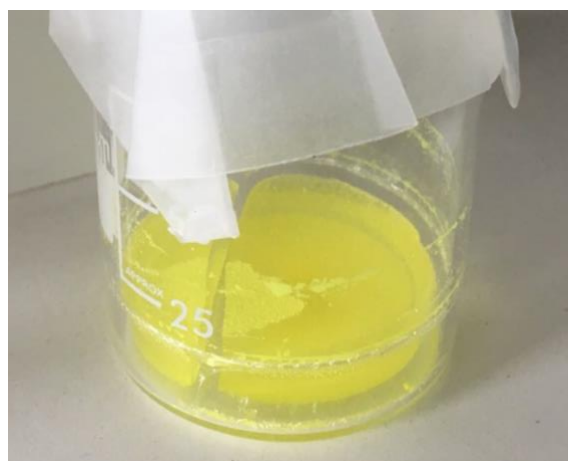


Fig. 2.14. Photograph of OPSCS3 doped silica gel, two weeks after preparation (slow drying)

Therefore, in order to obtain a totally homogeneous solution and crack free bulk gel, a solvent that can dissolve the OPSCS3 must be introduced. Since the OPSCS3 could be dissolved in acetone that would not affect the reactions during the sol-gel process, it is rational to use the mutual solvent to improve the homogeneity of the solution. The corresponding preparation process is already shown in Fig 2.5. Before adding the OPSC molecule into the mixing solution, the OPSC molecule was dissolved into acetone under an ultrasonic vibration process. Through this process, the totally homogeneous gel can be obtained as shown in Fig. 2.15.

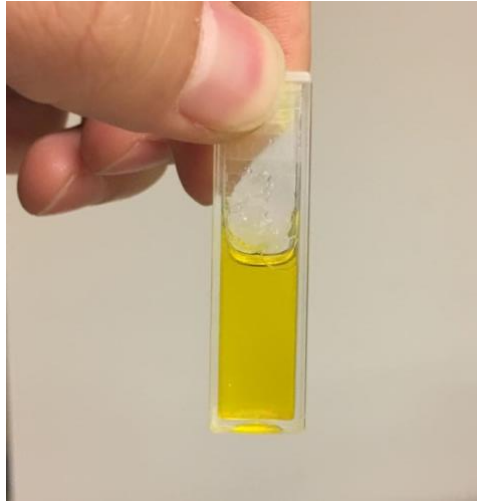


Fig. 2.15. Photograph of OPSCS3 doped silica wet gel with acetone

#### 4. Preparation of silica glass coating

Since LECs are film device, the inorganic glass electrolytes should be prepared in film form. Obviously, preparing the thin film is one of the most important aspects of sol-gel technology. Compare to gelation, the fluid or solution is more appropriate for preparing the films by some low-cost common processes as dipping, spinning, or spraying. These processes only require simple devices than those processes of chemical vapor deposition (CVD), evaporation, or sputtering. Moreover, the microstructure of the deposited film such as pore volume, pore size and surface area can be precisely controlled.

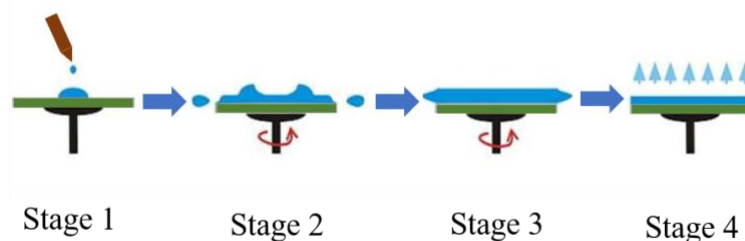


Fig. 2.16. Schematic of four stages of the spin-coating process

In order to prepare thin films, we used the spin coating process. The process of spin coating can be divided into four stages: deposition, spin-up, spin-off, and evaporation, as shown in Fig 2.16 21. An excess of solution is dispensed on the surface in the first stage. In the second stage, the centrifugal force would make the liquid radially flow outward. In the third stage, the excess liquid flows to the boundary. In the last stage, the liquid would be evaporated because of the high rotation speed. Spin coating has one important advantage that a film of solution tends to keep the uniform thickness during the second stage. Moreover, once the film is

uniform, it tends to keep this uniform property. The thickness of an initially uniform film during spin-off is described by the following equation

$$h(t) = \frac{h_0}{\left(1 + \frac{4\rho\omega^2 h_0^2 t}{3\eta}\right)^{\frac{1}{2}}} \quad (9)$$

where  $h_0$  is the initial thickness,  $t$  is the time,  $\omega$  is the angular velocity, and  $\rho$  is the density of the solution. It is known from the Equation (9) that the films tend monotonically toward uniformity by the increasing time.

First experiments of this film preparation were performed on the basic silica glass in order to handle the spin coater equipment and to optimize the parameters of spinning. These first experiments are needed to avoid a waste of organic molecules. The solution composition is the same of the silica xerogel prepared above (TEOS: H<sub>2</sub>O: C<sub>2</sub>H<sub>5</sub>OH = 1:3:4, pH<2). The substrate used for the coating is a silicate glass substrate. The process is shown in Fig 2.17 and the aging time for drying silica glass coating is of 1 h.

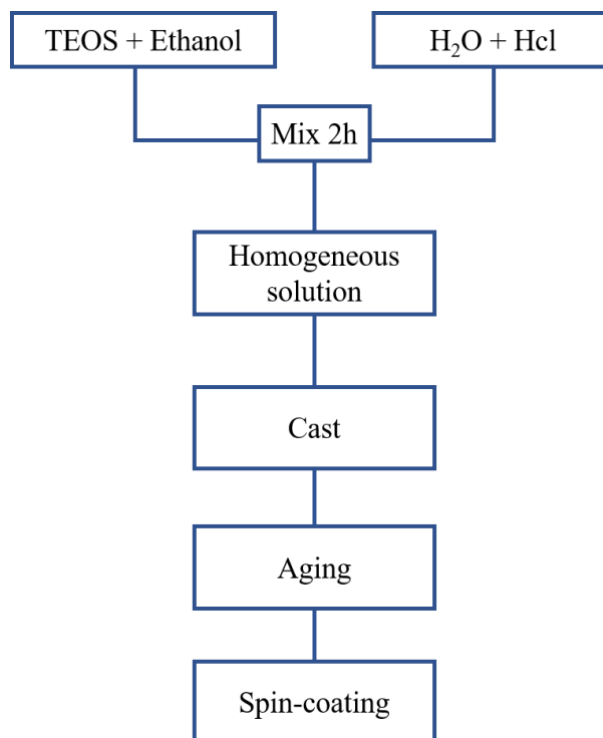


Fig. 2.17. Schematic of the silica spin-coating process

As display in Fig 2.18, the parameters for the spin-coater are: acceleration speed of 500 Rpm/s; rotation speed of 2000 Rpm/s (60s) and 3000 Rpm/s (60s) for first stage and second stage, respectively.



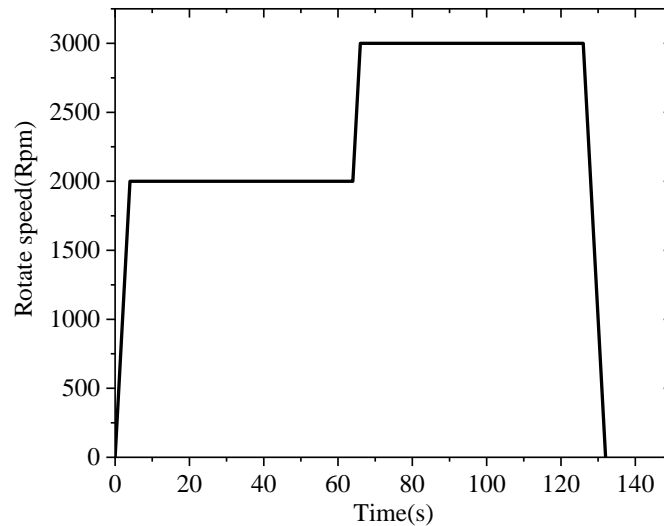


Fig. 2.18. Schematic of the dynamic process of silica spin-coating

A uniform coating on the silicate glass substrate can be obtained after drying process as presented in Fig. 2.19.

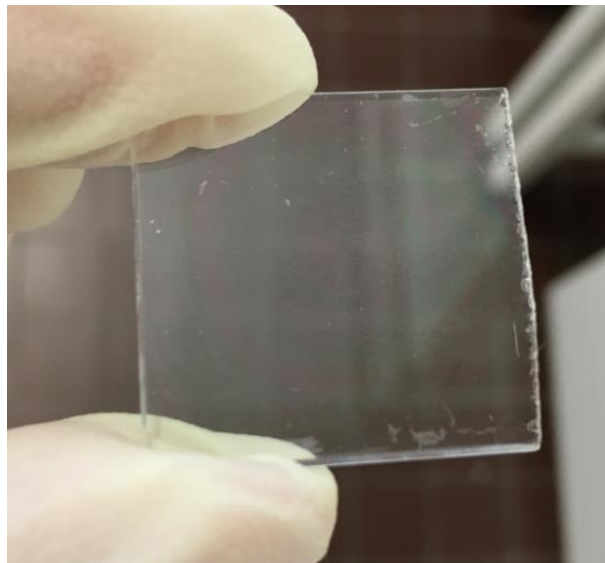


Fig. 2.19. Photograph of the silica coating

Pictures of the coating taken under optical microscope with magnification of 20 times and 1000 times are presented in Fig. 2.20. The photographs of the coating under microscopy were taken by digital microscope VHX-6000 series, Keyence, Japan. It can be seen that the coating has a uniform property even at magnification of 1000 times.

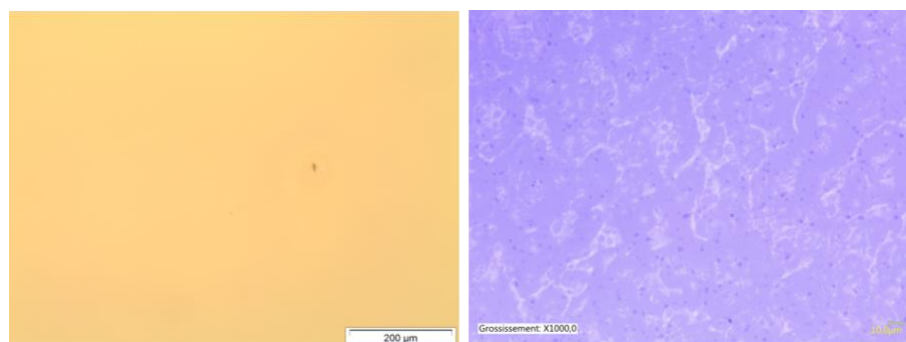


Fig. 2.20. Silica coating under optical microscope, magnification of 10 times (left) and 1000 times (right)

Moreover, OPSC doped silica coatings were also prepared. The preparation of the solution is the same as the OPSC doped silica xerogel (Fig. 2.5). As mentioned above, the lack of the solvent that can dissolve the OPSC induces the phase separation between OPSC and the silica xerogel. This phenomenon is more obvious when the coatings are prepared because of the highest ratio surface /volume. Fig. 2.21 shows the picture of the coating containing OPSCTD73 molecule lighten under UV light without (a) and with acetone (b). It can be seen that the addition of acetone into the solution could strongly improve the uniform continuity of the coating. In addition, luminescence of the OPSCTD73 doped silica coating was observed (Fig. 2.21). This phenomenon will be discussed in detail later in this chapter.

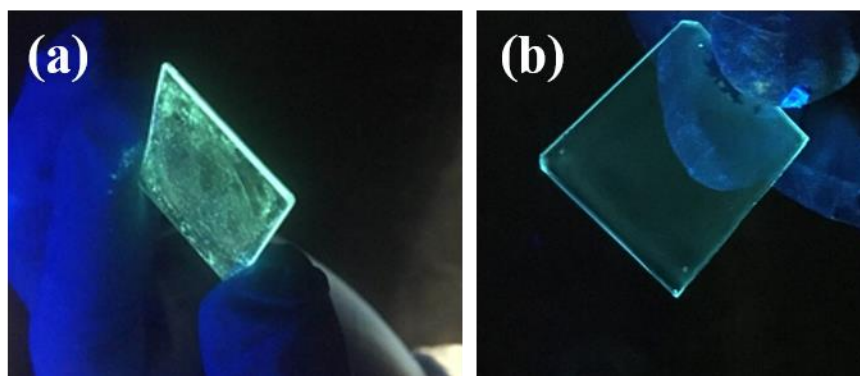


Fig. 2.21. Photograph of the OPSCTD73 doped silica coating onto onto 20x20mm substrates

### 5. Photoluminescence of the OPSC doped Silica glass

When the OPSC doped silica xerogel is obtained as shown in Fig. 2.13 and 2.14, the xerogel became yellow, the color of the OPSCS3 molecule. Unlike to OPSCS3 molecule doped silica xerogel, the OPSCTD73 molecule doped silica xerogel is colorless. However, both OPSCS3 and OPSCTD73 molecules doped silica xerogel has strong luminescence under UV light (365 nm) as shown in Fig. 2.22 (a) and (b), respectively. In order to further understand the

photoluminescence (PL) properties, the photoluminescence spectrum of both samples was investigated.

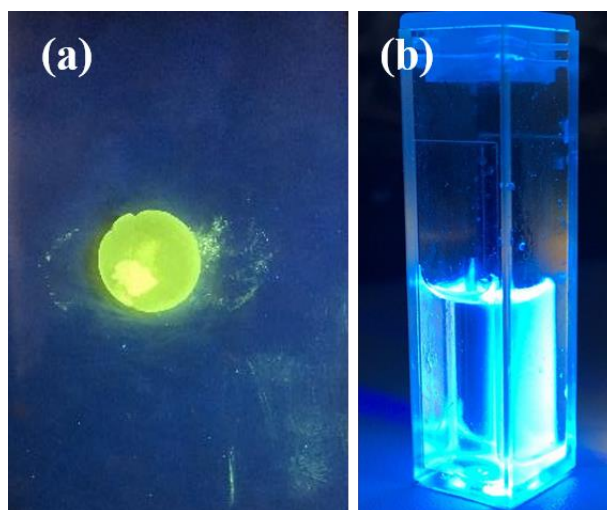


Fig. 2.22. OPSCS3(a) and OPSCTD73(b) doped silica xerogel under UV lamp

### 5.1 Photoluminescence spectrum

Firstly, the absorption and photoluminescence (PL) spectrum of OPSC molecules that are dissolved in diluted  $\text{CH}_2\text{Cl}_2$  solution (DCM) are presented in Fig. 2.33(a) and (b), respectively. They both possess luminescence in the visible range, characteristic of p-conjugated phospholes 22.

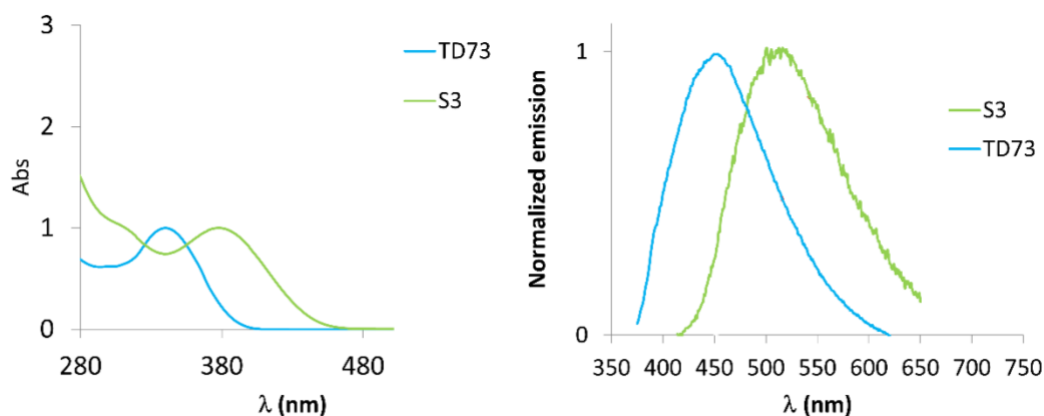


Fig. 2.23. Absorption(left) and emission(right) spectra of OPSC molecules in diluted DCM solutions.

The PL spectrum of OPSCS3 doped silica xerogel was measured 30 days after preparation as shown in Fig. 2.24. The photoluminescence spectra were measured by FLS980 with a 450 W ozone free xenon arc lamp that covers a range of 230 nm to 1000 nm for steady state measurements. The sample was stimulated at 380 nm that is the peak of the absorption spectrum of OPSCS3 dissolved in DCM. From Fig 2.24, it can be seen that the shape of the

spectrum of OPSCS3 doped silica xerogel is similar to that of OPSCC3 dissolved in  $\text{CH}_2\text{Cl}_2$  solution (DCM) as shown in Fig. 2.23 (right). In addition, the OPSCS3 doped silica xerogel shows an emission peak at around 480 nm, which corresponds to a “blue shift” if compared to that of OPSCS3 (510 nm) dissolved in DCM. Similar blue shift was also observed in OPSCD73 doped silica xerogel.

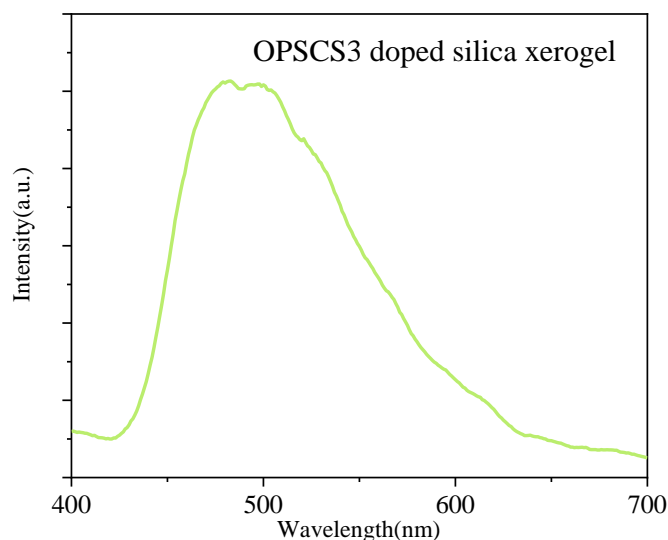


Fig. 2.24. Photoluminescence spectrum of OPSCS3 doped silica xerogel

The PL spectrum of OPSCTD73 doped silica xerogel was measured 30 days after preparation (Fig. 2.25). The sample was excited at 350 nm, wavelength corresponding to the peak of the absorption spectrum of OPSCTD73 dissolved in DCM. The shape of the spectrum of OPSCTD73 doped silica xerogel is similar to that of OPSCTD73 dissolved.

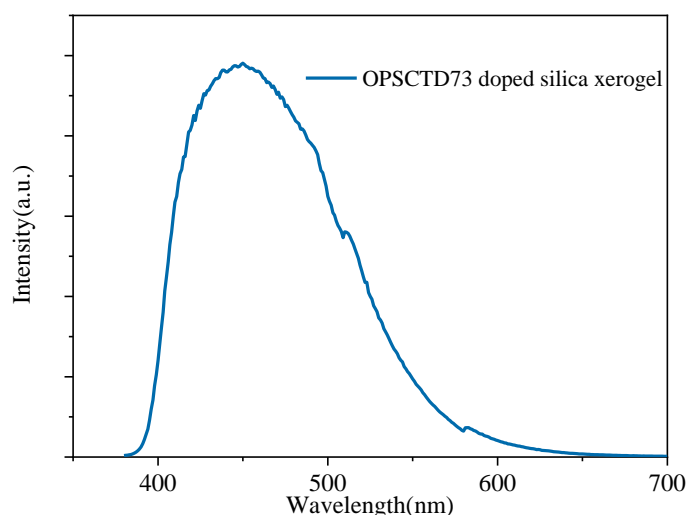


Fig. 2.25. Photoluminescence spectrum of OPSCTD73 doped silica xerogel

in DCM. The OPSCTD73 doped silica xerogel shows the emission peaked at around 450 nm, which also represents a “blue shift” compared to that of OPSCTD73 (470 nm) dissolved in

DCM. Therefore, this “blue shift” may be due to the change of the local environment around the OPSC, thereby the electronic structure of the OPSC has probably changed.

## 5.2 Luminescent concentrator based on OPSC doped silica coating

In addition, the PL was observed from the OPSCD73 doped silica coating as presented in Fig 2.21. From Fig 2.21(b), it is noted that the coating makes the substrate be a luminescent concentrator which emits from the edges of the substrate. The schematic of a luminescent solar concentrator is shown in Fig 2.26 (a). Actually, Fig 2.26 (a) shows the operating principle of a luminescent solar concentrator (LSC) that are devices comprising a transparent matrix embedding optically active centers that absorb the incident radiation, which is re-emitted at a specific wavelength and transferred by total internal reflection to photovoltaic (PV) cells located at the edges of the matrix <sup>23</sup>.

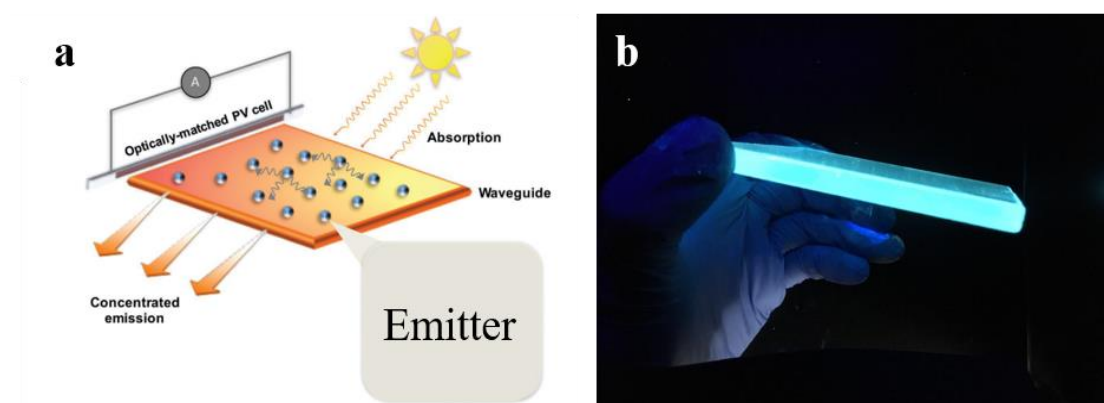


Fig. 2.26. Schematic of a luminescent solar concentrator (a)<sup>15</sup> and picture of OPSCS3 doped silica xerogel under UV lamp (b)

Fig. 2.26 (b) shows the coating on a bigger silicate glass substrate, where this phenomenon is more obviously observed. In reference <sup>24</sup>, the authors point out that “Organic–inorganic hybrids incarcerating trivalent lanthanide ions ( $\text{Ln}_{3+}$ ) are a very promising class of materials for addressing the required challenges in the LSC design to improve solar energy harvesting and, then, PV energy conversion.” Considering the sol-gel method can combine the inorganic part such as  $\text{Ln}_{3+}$  or other quantum dots and the organic emitters, it will be a good choice to prepare the  $\text{Ln}_{3+}$  and OPSC co-doped hybrid coating for LSC.

## 6. Preparation of lithium modified Silica bulk glass and coating

### 6.1 Lithium modified silicate glass bulk xerogel

Alkali silicate glass prepared by conventional melting often present phase separation and crystallize during quenching, which limits their application in the optical and electrical field

that need higher requirement of homogeneity. The sol-gel process for forming alkali silicates has been considered as an alternative way to avoid this problem<sup>18</sup>. However, compare to sodium silicate glass<sup>25-28</sup>, there are very few reports for lithium silicate glass. The first report of lithium silicate glass prepared by sol-gel was reported in 1983.<sup>29</sup> After that, the stability of lithium silicate gels was studied by Schwartz<sup>18</sup>. Study on the conductivity of lithium silicate glass prepared by sol-gel were studies by Klein<sup>30</sup>. Recently, the lithium-silicate sol-gel bioactive glass was reported by L.B. Macon et al.<sup>31</sup>. In these reports, the precursor for lithium is commonly either  $\text{LiNO}_3$  and  $\text{LiOH}$  because of their good solubility in water. Thus, in our work, both the  $\text{LiNO}_3$  and  $\text{LiOH}$  were used as precursors. Moreover, we also studied the behavior of  $\text{LiCl}$  as precursor.



Fig. 2.27. Photograph of TEOS-LiOH wet gel

With  $\text{LiOH}$  as precursor, the  $(100-x)$  % mol  $\text{SiO}_2$  and  $x$  % mol  $\text{Li}_2\text{O}$  ( $x=3,6,8,11$ ) binary glasses were prepared. This synthesis process is performed in a base solution as shown in Fig 2.3. However, the obtained results are a little bit different from the references<sup>29 30</sup>. Fig 2.27 shows the composition based on  $x=3,6,8,11$  (S1-S4) mol %  $\text{Li}_2\text{O}$  after drying 5 days. It can be seen that all the samples were gel, however, a serious phase separation were observed. With a longer mixing time (5h), the phase separation disappears in S1 gel, but the sample is opaque shown in the inset. This result was also found in the dried xerogel of lithium silicate by the work of L.C. KLEIN<sup>30</sup>.

Considering  $\text{LiNO}_3$  as the precursor, the  $(100-x)$  % mol  $\text{SiO}_2$  and  $x$  % mol  $\text{Li}_2\text{O}$  ( $x= 6,8,11$ ) binary glasses were prepared. The main difference consists in the fact that the synthesis process is performed in acidic solution as shown in Fig 2.4. The gels are shown in Fig 2.28 after 5 days of drying. It can be seen that all of the gels are homogeneous and totally transparent, and in this case no obvious phase separation is observed.

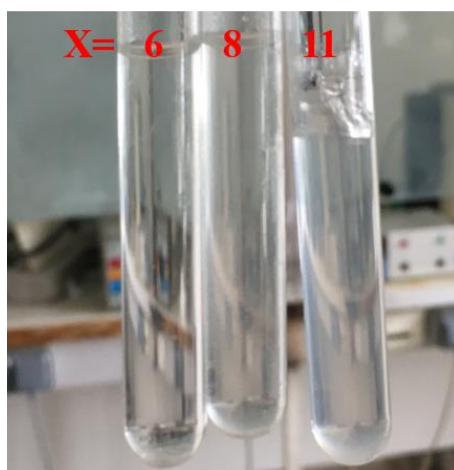


Fig. 2.28. Photograph of TEOS-LiNO<sub>3</sub> wet gel

After the wet gel was heated using the drying process shown in Fig 2.6, xerogel was obtained. Then, XRD experiments were performed. The XRD pattern of X=11 sample is shown in Fig 2.29, it indicates that the sample is amorphous. In fact, the observed peaks belong to the aluminum holder.

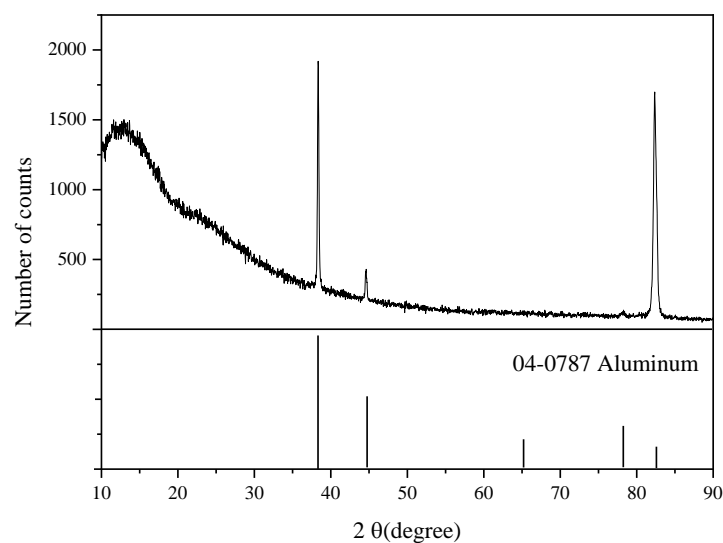


Fig. 2.29. XRD pattern of TEOS-LiNO<sub>3</sub> xerogel

Moreover, since there is no report about preparing the lithium silicate glass using lithium chloride, we also tried to prepare the glass replacing the LiNO<sub>3</sub> by LiCl. When using LiCl, the process is the same as LiNO<sub>3</sub> silicate glass. The solution also becomes a gel after 5 days, and the photo is shown in Fig 2.30.



Fig. 2.30. Photograph of TEOS-LiCl wet gel

It suggests that the lithium silicate gel can also be prepared by lithium chloride. Besides, a bulk lithium silicate xerogel with 6% mol  $\text{Li}_2\text{O}$  using LiCl as precursor was obtained as shown in Fig 2.31.

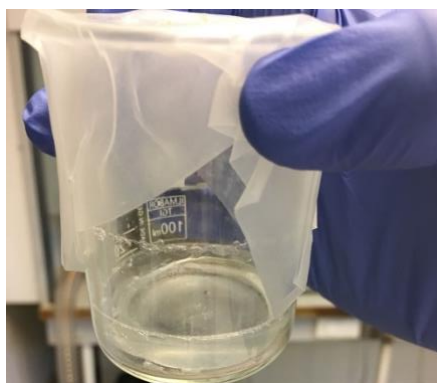


Fig. 2.31. Photograph of TEOS-LiCl xerogel

Although the lithium silicate xerogel were successfully prepared with the precursor  $\text{LiNO}_3$  and LiCl, the concentration of lithium is still low which probably lead to a low ionic conductivity of the glass. Therefore, after having obtained silicate xerogel with relatively low concentration of lithium, we increased the lithium concentration in silicate xerogel to enhance the ionic conductivity.



Fig. 2.32. Photograph of TEOS- $\text{LiNO}_3$  and TEOS-LiCl xerogel



The composition based on 70 % mol SiO<sub>2</sub> and 30 % mol Li<sub>2</sub>O binary lithium silicate xerogel were prepared by using LiNO<sub>3</sub> and LiCl as precursors, respectively, as shown in Fig 2.32. Considering the high lithium content may lead to the appearance of phase separation or crystallization, XRD measurements of both samples were performed after being dried. The result is presented in Fig 2.33. It can be seen that the curves of both samples are similar to that of low lithium content shown in Fig 2.29, which indicates both of the samples are amorphous, the observed peaks still belong to the aluminum holder.

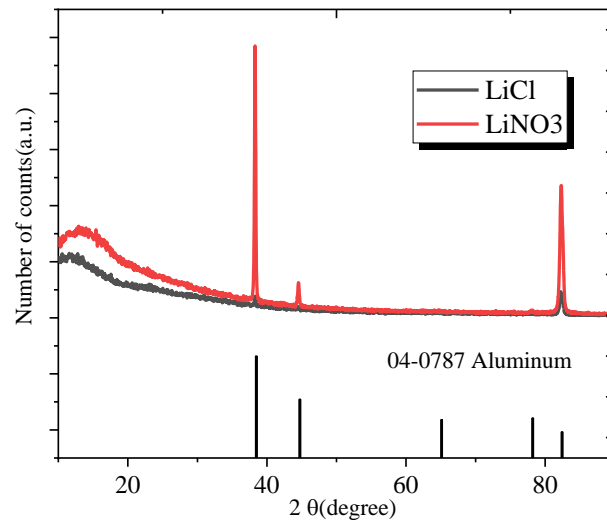


Fig. 2.33. XRD of TEOS-LiNO<sub>3</sub> and TEOS-LiCl xerogel (70 % mol SiO<sub>2</sub> - 30% mol Li<sub>2</sub>O)

However, the silicate xerogel containing higher concentration of lithium react easily with water, especially for LiCl silicate xerogel, leading the bulk to crack and tend to be soluble again. Probably, a more optimized drying process may be the key to solve this problem.

## 6.2 Lithium modified silicate glass coating

Although there are lots of works on silica coating <sup>21,32-35</sup>, there is rather few works on lithium silicate glass coating. In our experiment, the main aim consists in preparing the lithium silicate solution (70% mol SiO<sub>2</sub>-30% mol Li<sub>2</sub>O) using LiCl as precursor. The lithium silicate glass coatings were prepared using the same process and parameters of the silica glass coating presented before. However, it was observed that voids are generated in the coating as displayed in Fig. 2.34. It can be seen that the largest size of the void can reach 120 μm. Since the LEC devices require the emitting layer to be between two electrodes, the emitting layer should enable to prohibit the contact between electrodes. Therefore, the existence of voids within the coating will probably lead to contact between electrodes and thus to short circuit. It is crucial to vanish these voids in the coating.

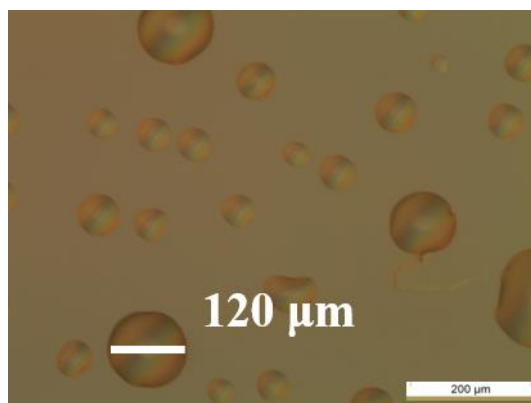


Fig. 2.34. TEOS-LiCl coating under optical microscope (scale)

As mentioned above, the addition of alkali ions in sol-gel solutions lead to the complexification of polymerization process. Considering this key issue, it is not difficult to assume that the appearance of the voids are probably due to the kind of lithium precursor as well as its concentration. Besides, the lithium silicate glass coating was prepared using the same process and parameters of the silica glass coating including the aging time of solution, whereas the assigned aging time of lithium silicate glass solution should be theoretically different from that of silica glass coating because of the more complicated polymerization. It suggests that these voids may also be caused by the incorrect aging time of the lithium silicate solution. Thus, there are three possibilities of the appearance of the voids including 1) aging time of the solution; 2) the concentration of lithium precursor; 3) the kind of the lithium precursor.

Firstly, we investigated the relations between the appearance of voids and the aging time of the solution. The aging time of the solution was investigated using the lithium silicate solution (70% mol  $\text{SiO}_2$  - 30% mol  $\text{Li}_2\text{O}$ ) with LiCl as precursor. The coating was prepared with different aging times of solution of 0.5h, 1h, 6h, 20h, 24h and 48h, respectively. After 48h, the viscosity of the solution was too large to use the spin-coating process. The photo of the coatings under microscopy with 10 times magnification are shown in Fig. 2.35. These photos were taken just after finishing the coating process. It can be seen that, in spite of all the coatings contain voids, the coating prepared after 20h of aging presents less amounts of voids when LiCl is used as precursor. Even if it is noted that the size of the voids is depending of the aging time, however, no obvious trend was found. Since the voids are always present after different aging time of the solution, it is rational to point out that the aging time of the solution is not the main reason for the appearance of these voids.

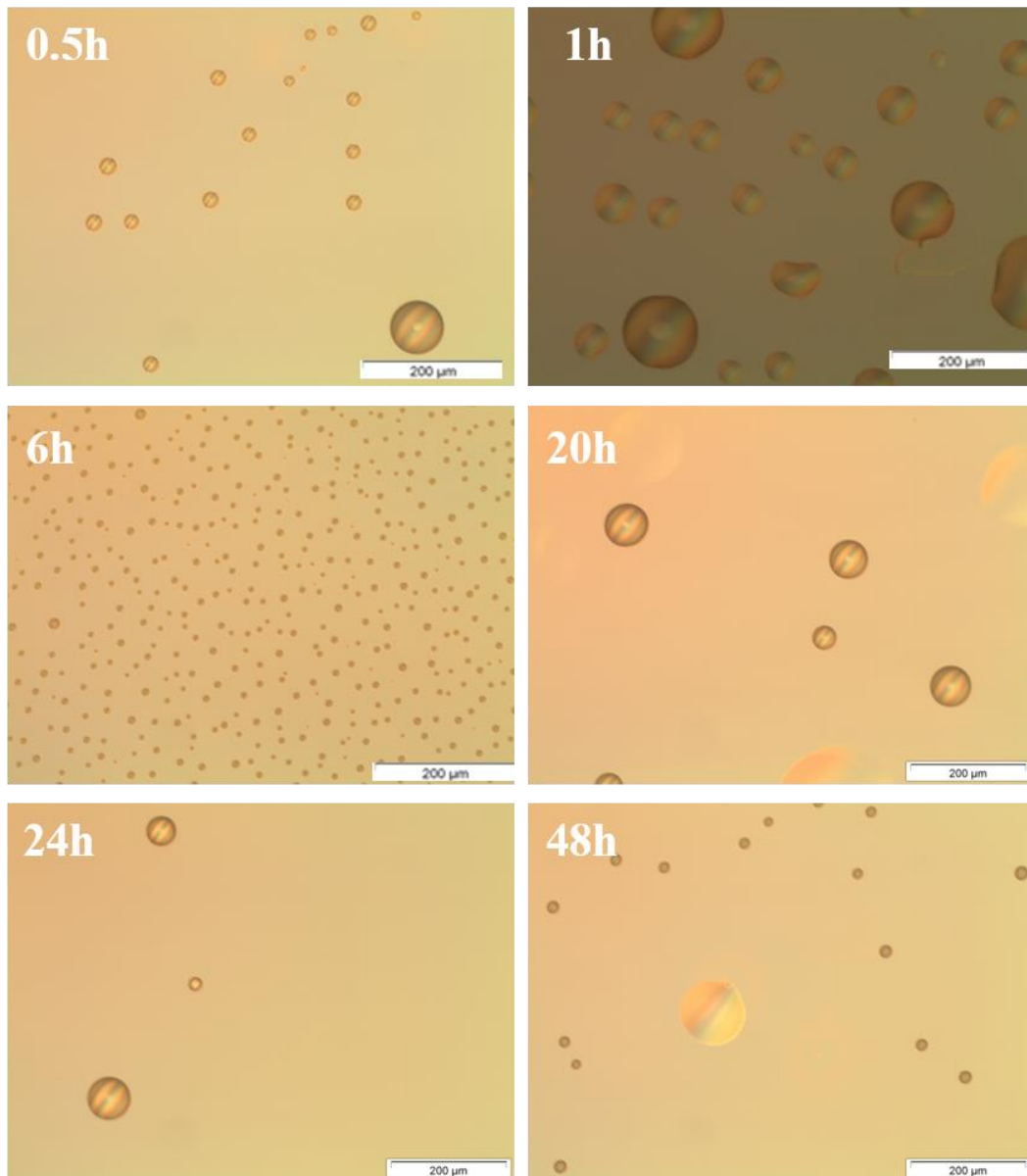


Fig. 2.35 TEOS-LiCl coating under optical microscope after different aging time

Secondly, the concentration of the lithium precursor was investigated. The 70% mol  $\text{SiO}_2$ -30% mol  $\text{Li}_2\text{O}$  and 90% mol  $\text{SiO}_2$ -10% mol  $\text{Li}_2\text{O}$  solutions using  $\text{LiCl}$  as precursor were prepared. The coating based on both solutions were prepared after aging for 1h. The photo of the coatings observed by microscope are shown in Fig. 2.36. Both pictures were taken just after finishing the coating process. It can be seen that no voids are observed from the coating prepared with the solution containing 10% mol of  $\text{Li}_2\text{O}$ . On the contrary, many voids are observed in the other coating. Obviously, the concentration of the lithium precursor largely affects the number and size of voids within the coating.

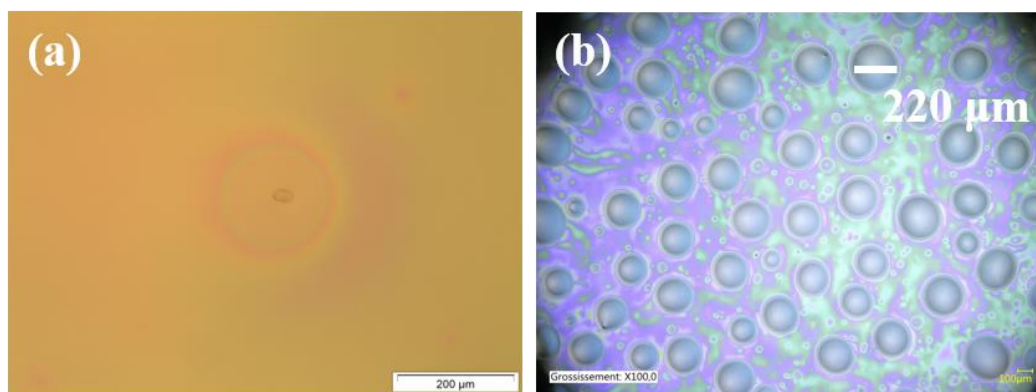


Fig. 2.36 TEOS-LiCl coating of 10% mol Li<sub>2</sub>O (a) and 30% mol Li<sub>2</sub>O under optical microscope (10 times magnification for (a) and 100 times magnification for (b))

Lastly, the nature of the lithium precursor was investigated. Besides the LiCl precursor studied above, the LiNO<sub>3</sub> and C<sub>6</sub>H<sub>5</sub>Li<sub>3</sub>O<sub>7</sub> precursors were used. The 70% mol SiO<sub>2</sub> - 30% mol Li<sub>2</sub>O solution using LiNO<sub>3</sub> and C<sub>6</sub>H<sub>5</sub>Li<sub>3</sub>O<sub>7</sub> as precursor were prepared. The coating based on these two solutions was synthesized after 1h of aging. The pictures of the coatings taken under microscope are shown in Fig. 2.37.

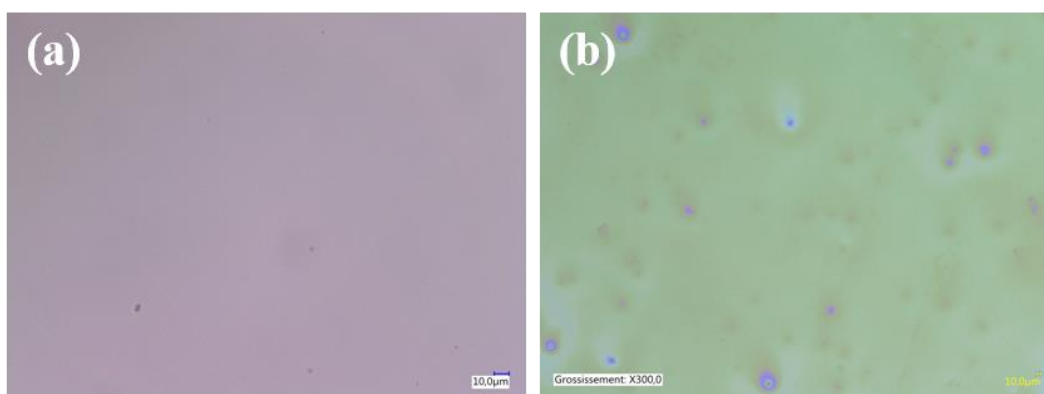


Fig. 2.37 TEOS-C<sub>6</sub>H<sub>5</sub>Li<sub>3</sub>O<sub>7</sub> (a) and TEOS-LiNO<sub>3</sub> (b) coating under optical microscope (300 times magnification) when the coatings were just prepared

Fig. 2.37 (a) shows the coating prepared using the C<sub>6</sub>H<sub>5</sub>Li<sub>3</sub>O<sub>7</sub> as precursor (magnification 300 times). It can be seen that the coating does not present voids, and the black dot in the coating is probably due to the dust. Fig 2.37 (b) shows the coating prepared using the LiNO<sub>3</sub> as precursor (magnification 300 times). Although in this coating, there are lots of dust dots, there are no voids that have been observed before. These results clearly highlight how the kind and content of precursor affect the formation of holes within the thin films.

As mentioned, all these photos were taken just after the coating preparation, however, the voids start to appear after 3 days kept in the air at room temperature, as shown in Fig. 2.38. It can be seen that the size of the voids remains below 10  $\mu\text{m}$ .

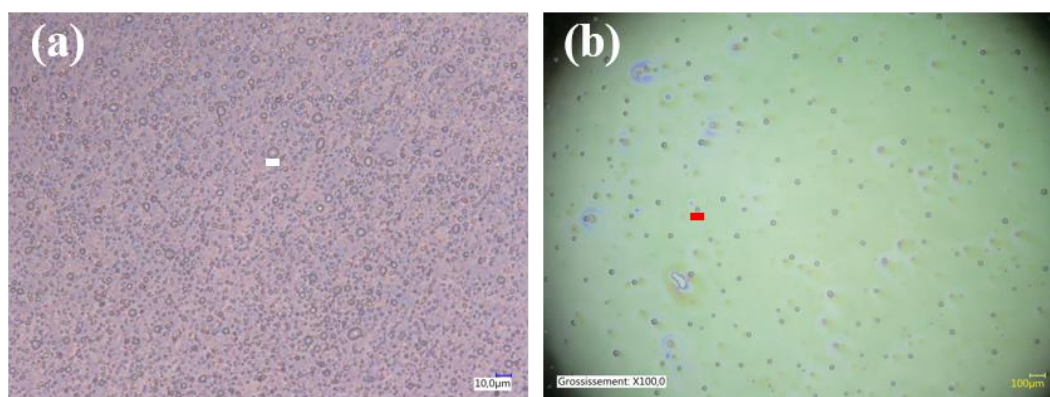


Fig. 2.38 TEOS- $\text{C}_6\text{H}_5\text{Li}_3\text{O}_7$  (a) and TEOS- $\text{LiNO}_3$  (b) coating under optical microscope (300 times magnification for (a) and 100 times for (b)) three days after the coatings were prepared

Normally, in case of bulk gel, a solid-state salt metathesis reaction occurred between lithium salt and the silanol and subsequently diffuses within the bulk silica network <sup>31</sup>, the schematic of which is shown in Fig. 2.39. Although the underlying physics and chemistry that govern polymer growth and gelation are essentially the same for films as bulk gels, their structural evolution is different <sup>36</sup>. In the case of films, because of the short time span for condensation reactions to occur, the competition between evaporation and continuing condensation reactions occurs. Evaporation compacts the structure, whereas condensation reactions stiffen the structure, thereby increasing the resistance to compaction. In addition, the brief duration of the deposition and drying stages of films cause the less crosslinking than bulk gels.

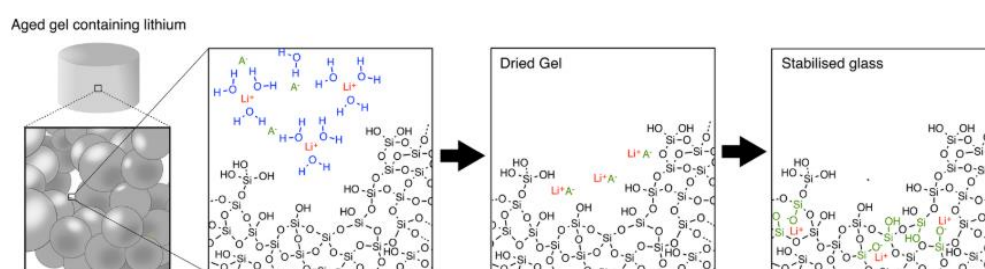


Fig. 2.39 Schematic representing the precipitation of lithium salt within the porous structure of silica gels, subsequently followed by the diffusion of lithium, induced by thermal stabilization, within the silicate networks, decreasing connectivity of the network <sup>31</sup>

Brinker, C. J. et al. point out several consequences of this short timescale of the film deposition processes <sup>36</sup>. One of these consequences is that there is little time available for condensation reactions to occur. Thus, gelation may actually occur by a physical process,

through the concentration dependence of the viscosity, rather than a chemical process. Especially, this physical process tends to be happened in case of the solution consists of complicated entrained condense phases. In fact, these voids presented in the prepared coating in our work are probably due to this reason. When the concentration of lithium salts beyond a certain point, since the chemical reaction between lithium salt and silanol are not sufficiently happen because of the short time of spin process, some lithium salt exists as the origin form (LiCl or LiNO<sub>3</sub>) in the coating. And these lithium salts are more likely to react with water, which cause the appearance of the voids. Thus, the voids were not observed in TEOS-LiCl coating with 10% mol Li<sub>2</sub>O, whereas were observed the TEOS-LiCl coating with 30% mol Li<sub>2</sub>O. In addition, compare to lithium nitrate and citrate, lithium chloride is easier to react with water, which leads the voids appeared immediately in the TEOS-LiCl coating and later in TEOS-LiNO<sub>3</sub> and TEOS- Li<sub>3</sub>C<sub>6</sub>H<sub>5</sub>O<sub>7</sub>. Therefore, controlling the metathesis reaction between lithium salt and silanol is the key to avoid the appearance of voids in the coating. According to Ref 37, a large excess of water, corresponding to a water to TEOS molar ratio above 15, favoured the formation of lithium metasilicate. Thus, the excess addition of water may be the possibility of vanish the voids in the prepared coating. Besides, considering the dip-coating process with a longer preparation time than that of spin-coating, it probably has a longer time for the chemical reaction between lithium salt and silanol, thereby it is possible to prepare the high lithium content silicate glass coating without voids through dip-coating.

## 7. Conclusion

The bulk silica xerogel and silica coating with good uniformity were successfully prepared. In addition, strong photoluminescence was observed from the OPSC doped silica xerogel and coating under UV lamp. The photoluminescence spectrum was also investigated, and it was found that the peak of the photoluminescence spectrum is a bit “blue shift” compared to that of OPSC diluted in DCM.

Based on the silica gel, bulk silicate xerogel with the high lithium content was prepared using different lithium precursor. Then, the corresponding lithium silicate glass coatings were prepared as well. However, the high lithium content silicate xerogel has the tendency of reacting with water and some voids are created within the coating. Through the comparing experiments, it was found that aging time, kinds of lithium precursor and the concentration of lithium can affect the appearance of the voids in the coating. These voids may be caused by the inadequacy of chemical reaction between lithium salt and silanol due to the short time

span for condensation reactions of coating process. It indicates the excess addition of water may be the possibility to vanish the voids in the prepared coating. Another possibility to consider consists in preparing the high lithium content silicate glass coating through dip-coating.

## REFERENCES

- 1 Bansal, N. P. & Doremus, R. H. *Handbook of glass properties*. (Elsevier, 2013).
- 2 Mysen, B. O. & Richet, P. *Silicate glasses and melts*. (Elsevier, 2018).
- 3 Fanderlik, I. *Silica glass and its application*. (Elsevier, 2013).
- 4 Shelby, J. E. *Introduction to glass science and technology*. (Royal Society of Chemistry, 2005).
- 5 Henderson, L. D. *Duchamp in context: Science and technology in the Large Glass and related works*. (Princeton University Press Princeton, 1998).
- 6 Pye, L., Stevens, H. & LaCourse, W. *Introduction to Glass Science. The Vitreous State Plenum Press, New York* (1972).
- 7 Weber, M. Science and technology of laser glass. *Journal of Non-Crystalline Solids* **123**, 208-222 (1990).
- 8 McMillan, P. W. *Glass-ceramics*. (1964).
- 9 Kreidl, N. J. Recent applications of glass science. *Journal of non-crystalline solids* **123**, 377-384 (1990).
- 10 McMillan, P. F. & Piriou, B. Raman spectroscopic studies of silicate and related glass structure: a review. *Bulletin de Mineralogie* **106**, 57-75 (1983).
- 11 Mysen, B. O. & Mysen, B. *Structure and properties of silicate melts*. Vol. 354 (Elsevier Amsterdam, 1988).
- 12 Greaves, G. EXAFS and the structure of glass. *Journal of Non-Crystalline Solids* **71**, 203-217 (1985).
- 13 Jin, W., Vashishta, P., Kalia, R. K. & Rino, J. P. Dynamic structure factor and vibrational properties of SiO<sub>2</sub> glass. *Physical Review B* **48**, 9359-9368 (1993).
- 14 Greaves, G., Fontaine, A., Lagarde, P., Raoux, D. & Gurman, S. Local structure of silicate glasses. *Nature* **293**, 611 (1981).
- 15 Teo, B. K. *EXAFS: basic principles and data analysis*. Vol. 9 (Springer Science & Business Media, 2012).
- 16 Martin, S. W. & Angell, C. Dc and ac conductivity in wide composition range Li<sub>2</sub>O □ P<sub>2</sub>O<sub>5</sub> glasses. *Journal of Non-Crystalline Solids* **83**, 185-207 (1986).
- 17 Brinker, C., Hurd, A., Frye, G., Ward, K. & Ashley, C. Sol-gel thin film formation. *Journal of Non-Crystalline Solids* **121**, 294-302 (1990).
- 18 Schwartz, I., Anderson, P., De Lambilly, H. & Klein, L. Stability of lithium silicate gels. *Journal of non-crystalline solids* **83**, 391-399 (1986).



- 19 Clearfield, A. & Vaughan, P. A. The crystal structure of zirconyl chloride octahydrate and zirconyl bromide octahydrate. *Acta Crystallographica* **9**, 555-558 (1956).
- 20 Freedman, M. L. Polymerization of anions: The hydrolysis of sodium tungstate and of sodium chromate. *Journal of the American Chemical Society* **80**, 2072-2077 (1958).
- 21 Scriven, L. Physics and applications of dip coating and spin coating. *MRS Online Proceedings Library Archive* **121** (1988).
- 22 Duffy, M. P., Delaunay, W., Bouit, P. A. & Hissler, M.  $\pi$ -Conjugated phospholes and their incorporation into devices: components with a great deal of potential. *Chemical Society Reviews* **45**, 5296-5310 (2016).
- 23 McKenna, B. & Evans, R. C. Towards efficient spectral converters through materials design for luminescent solar devices. *Advanced Materials* **29**, 1606491 (2017).
- 24 Correia, S. F. *et al.* Luminescent solar concentrators: challenges for lanthanide-based organic–inorganic hybrid materials. *Journal of Materials Chemistry A* **2**, 5580-5596 (2014).
- 25 Hench, L. L., Prassas, M. & Phalippou, J. Preparation of 33 mol% Na<sub>2</sub>O-67 mol% SiO<sub>2</sub> glass by gel-glass transformation. *Journal of Non-Crystalline Solids* **53**, 183-193 (1982).
- 26 Prassas, M., Phalippou, J. & Hench, L. L. Preparation of xNa<sub>2</sub>O-(1-x) SiO<sub>2</sub> gels for the gel-glass process II. The gel-glass conversion. *Journal of non-crystalline solids* **63**, 375-389 (1984).
- 27 Prassas, M., Phalippou, J., Hench, L. L. & Zarzycki, J. Preparation of xNa<sub>2</sub>O-(1-x) SiO<sub>2</sub> gels for the gel-glass process: I. Atmospheric effect on the structural evolution of the gels. *Journal of Non-Crystalline Solids* **48**, 79-95 (1982).
- 28 Puyané, R., James, P. & Rawson, H. Preparation of silica and soda-silica glasses by the sol-gel process. *Journal of Non-Crystalline Solids* **41**, 105-115 (1980).
- 29 ZJ Huang, T. Y., K. Kamiya and S. Sakka. Effect of Water on the Crystallization of Li<sub>2</sub>O-SiO<sub>2</sub> Glasses and Gels. *Yogyo-Kyokai-Shi* **91**, 215-221 (1983).
- 30 Klein, L. Sol-gel processing of ionic conductors. *Solid State Ionics* **32**, 639-645 (1989).
- 31 Maçon, A. L. *et al.* Lithium-silicate sol–gel bioactive glass and the effect of lithium precursor on structure–property relationships. *Journal of Sol-Gel Science and Technology* **81**, 84-94 (2017).
- 32 Fardad, M., Yeatman, E., Dawnay, E., Green, M. & Horowitz, F. Effects of H<sub>2</sub>O on structure of acid-catalysed SiO<sub>2</sub> sol-gel films. *Journal of Non-Crystalline Solids* **183**, 260-267 (1995).

- 33 Nagayama, H., Honda, H. & Kawahara, H. A new process for silica coating. *Journal of the Electrochemical Society* **135**, 2013-2016 (1988).
- 34 Nisticò, R., Scalarone, D. & Magnacca, G. Sol-gel chemistry, templating and spin-coating deposition: A combined approach to control in a simple way the porosity of inorganic thin films/coatings. *Microporous and Mesoporous Materials* **248**, 18-29 (2017).
- 35 Chou, T. P. *et al.* Organic–inorganic hybrid coatings for corrosion protection. *Journal of Non-Crystalline Solids* **290**, 153-162 (2001).
- 36 Brinker, C. J., Hurd, A. J., Schunk, P. R., Frye, G. C. & Ashley, C. S. Review of sol-gel thin film formation. *Journal of Non-Crystalline Solids* **147-148**, 424-436 (1992).
- 37 Li, P., Ferguson, B. & Francis, L. F. Sol-gel processing of lithium disilicate. *Journal of materials science* **30**, 4076-4086 (1995).



## **Chapter III: Hybrid materials based on phosphate glasses**



## 1. Introduction

Phosphate glass were developed by Schott and co-workers more than 100 years. Subsequent interest in alkaline earth phosphate glasses have never been on wane. More recently, phosphate glasses have been developed for a variety of specialty applications<sup>1,2</sup>. The crystalline and amorphous phosphates are based on the P-tetrahedra, which is resulting from the formation of  $sp^3$  hybrid orbitals by the P outer electrons ( $3s^23p^3$ ). The fifth electron is promoted to a 3d orbital where strong p-bonding molecular orbitals are formed with oxygen 2p electrons. Various phosphate anions are formed based on these tetrahedra link through covalent bridging oxygens. The tetrahedra are specified using the  $Q_i$  terminology<sup>1</sup>, where  $i$  represents the number of bridging oxygens per tetrahedron (shown schematically in Fig. 3.1). The networks of phosphate glasses can be specified by the oxygen-to-phosphorus ratio, which sets the number of tetrahedral linkages, through bridging oxygens, between neighboring P-tetrahedra<sup>3</sup>. Since the depolymerization starts from a network with a threefold linked structural unit, the number of crosslinks is small in phosphate glasses compared with those in silicate glasses of same metal oxide content<sup>4</sup>. On the other hand, a large number of terminal oxygen atoms exist. Thus, a high degree of flexibility remains for the orientation of the  $PO_4$  groups, which also means a lower  $T_g$  of phosphate glass than that of silicate and borate glasses.



Fig. 3.1 Phosphate tetrahedral sites that can exist in phosphate glasses

In addition, phosphate glasses can present some high ionic conductivity<sup>5</sup>.  $xM_2O+(1-x)P_2O_5$  where M is an alkali, silver, or even copper, are the simplest ionically conducting phosphate glasses. Bartholomew was the first to examine the ionic conductivity of these binary alkali phosphate glasses<sup>6</sup>. He investigated the electrical properties of  $xLi_2O-(1-x)P_2O_5$ ,  $xNa_2O-(1-x)P_2O_5$ , and  $xAg_2O-(1-x)P_2O_5$  series with high high-alkali concentration. The work was followed by Doreau et al<sup>7</sup>. They perform a thorough study of the  $xLi_2O-(1-x)P_2O_5$  series and of the ternary series  $Li_2O-P_2O_5-LiCl$  ( $10^{-7}$  S/cm at RT). After that, Pradel et al. used the roller-quenching techniques to expand the normal high-alkali glass-forming range in  $Li_2O-P_2O_5$  glasses from  $x=0.6$  to  $x=0.7$ , which increases the maximum ionic conductivity

obtainable in these glasses ( $3 \times 10^{-7}$  S/cm at RT) <sup>8</sup>. Then, Martin examine glasses down to  $x=0.36$  through preparing these glasses in an anhydrous glove box<sup>5</sup>. However, below this limit, they found the volatilization of  $P_2O_5$  during melting that prevent the formation of a stable liquid phase. The composition dependences of the conductivity and of the activation energy for binary  $Li_2O-P_2O_5$ ,  $Li_2O-B_2O_3$ , and  $Li_2O-SiO_2$  glasses were reviewed by Martin<sup>5</sup>. The silicate glasses have the highest ionic conductivity but phosphate glasses have lowest ionic conductivity, and borate glasses are in the middle. Besides, the activation energy for ionic conduction is the reverse. Martin and Angell thought that this trend order arises from systematically increasing the fraction of alkali-carrying nonbridging oxygens on passing from alkali phosphate to borate and finally to silicate glasses <sup>9</sup>. They think the structure of the glass having the similar composition to the crystal should have similar repeated unit. Therefore, the metaphosphate, metaborate, and metasilicate glasses properties are expected to be dominated by the chain repeat unit which are observed in their crystals. Based on this hypothesis, Martin and Angell explained the trend of ionic conductivity.

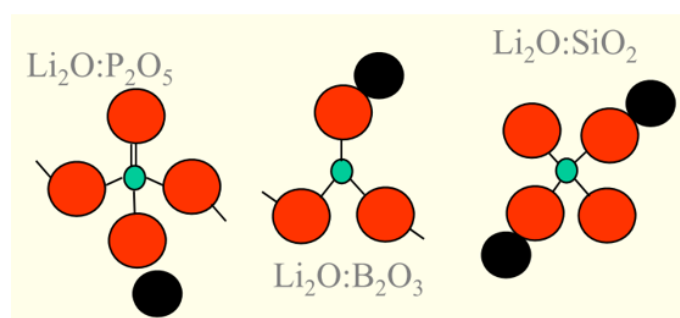


Fig. 3.2 The chain repeat unit of binary phosphate, borate and silicate glass

They observed that the fraction of oxygens possessing a full negative charge increases from 0.25 for  $LiPO_3$  to 0.33 for  $LiBO_2$  to 0.5 for  $Li_2SiO_3$ , and the schematic is shown in Fig. 3.2. They suppose that this is the reason why the phosphate glasses exhibit lower conductivities than the borates and silicates ones (nearly 2 and 3 orders of magnitude, respectively). It is mainly due to the fact that the mobile cation fraction is higher for the borate and silicate glasses than for the phosphate glasses. This higher cation fraction is thought to reduce the activation energy by increasing the overlap of the coulomb energy domes that exist between sites. Here, as the jump distance between sites decreases, the coulombic term acting on the cations becomes less negative before the cation begins to experience the attractive coulombic potential of the next nonbridging oxygen site. They also use this model to explain the rapid decrease of the activation energy for conduction with the increasing alkali oxide fraction in any glass-forming series.

Fortunately, the ternary alkali phosphate glasses have a much better ionic conductivity. In 1972, Malugani et al. found that a glass can be obtained with large amounts of LiX, where X is I-, Br-, and Cl- dissolved into LiPO<sub>3</sub> glass<sup>10</sup>. They found that room-temperature conductivities and activation energies for LiX-LiPO<sub>3</sub> glasses sharply increase and decrease with the addition of LiX, respectively. This is because, based on the weak electrolyte theory, the energy to dissociate the Li<sup>+</sup> cation from a larger and single charged anion (halide) would be less than that for a Li<sup>+</sup> cation linked to a double charged oxygen anion. Besides, the glass compositions outside the glass-forming range are easy to crystallize. Consequently, the conductivity and activation energy decreases and increases, respectively. Martin assumes the relative ordering of the conductivities and activation energies is what would be expected from both the Anderson and Stuart and weak electrolyte models. They think that the LiI-doped glasses exhibit the lowest activation energy because of the largest I- anion, and, therefore, the dissociation energy would be the smallest. They also think LiI would also lead to larger interstitial window radii in the glass matrix, and consequently, a smaller strain energy barrier was obtained as well. They also compared the effect of adding Li<sub>2</sub>O and LiI to LiPO<sub>3</sub><sup>9</sup>. They found that LiI increases the conductivity and decreases the activation energy at a rate faster than does Li<sub>2</sub>O. However, the F- anion behaves very differently from the other halides<sup>11</sup>. Since the F- ion is a strong enough Lewis base, it would form terminal F- groups through attacking the covalently bonded phosphate network (or chain segments). And these terminal F- groups would form high-basicity cation traps which decrease ionic conductivity rather than increase it.

Moreover, it was found that, in the series Li<sub>2</sub>SO<sub>4</sub>-LiPO<sub>3</sub>, additions of Li<sub>2</sub>SO<sub>4</sub> act similarly to additions of LiX and Li<sub>2</sub>O in causing increases in conductivity<sup>12</sup> (10<sup>-6</sup> S/cm at RT). It was also observed that the glass-forming limit occurs around 30 mol% Li<sub>2</sub>SO<sub>4</sub>, which agrees with observations for (LiI)<sub>2</sub>- and Li<sub>2</sub>O-doped glasses.

However, there are very few works on the glass electrolytes for making LEC, let alone integrated report combine a glass host with all the properties including mechanical, optical, electric and electrochemical properties. In this chapter, we discuss the possibility of using a phosphate glass as the electrolyte for LEC applications. There are two main reasons to choose phosphate glass. On one hand, phosphate glasses not only have a high ionic conductivity, but also have a high transparency in the visible range and good chemical durability. On the other hand, phosphate glasses have a relative low T<sub>g</sub> compare to silicate glass or borate glasses. As we mentioned in chapter I, the way to prepare the organic-inorganic hybrid glass is one of the



challenges. In this chapter, we plan to synthesize the organophosphorus organic semiconductor (OPSC) doped organic-inorganic hybrid glass using the spark plasma sintering (SPS) technology that can sinter the glass at its glass transition temperature ( $T_g$ ). The details about the SPS will be presented in the next section. Thus, the low  $T_g$  value of phosphate glass enables their agglomeration by SPS sintering at temperatures below the degradation temperature of OPSC. This technique will allow to homogeneously embedded the molecules within the glass. Moreover, considering the other requirements for a LEC, list of main parameters concerning ideal phosphate glass electrolytes prepared by SPS have been realised: 1) low  $T_g$ ; 2) high ionic conductivity (at least  $10^{-7}$  S/cm at RT); 3) high transmittance at visible light range; and 4) wide electrochemical stability window (ESW).

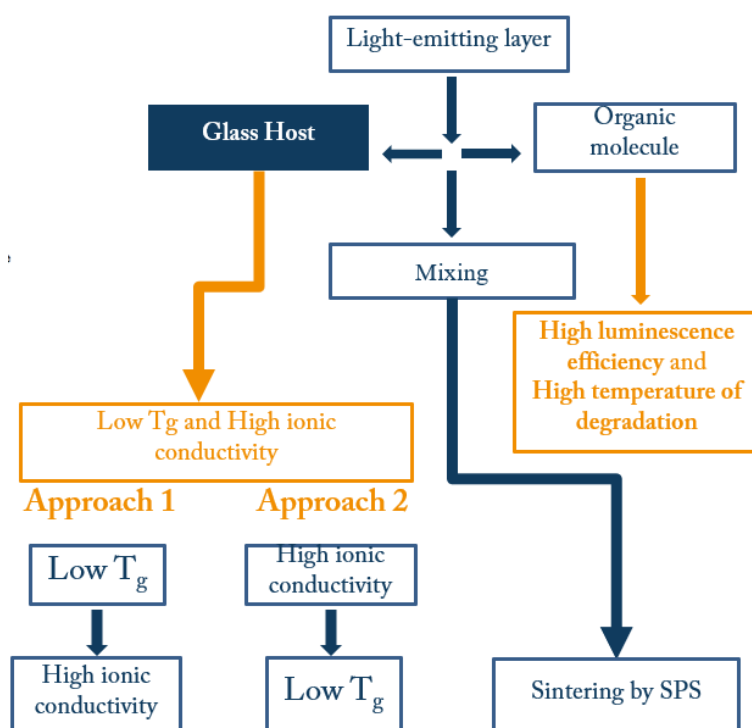


Fig. 3.3 Schematic of preparing hybrid glasses by SPS

Since phosphate glasses always have a high transmittance in the visible light range and a wide electrochemical stability window, the key point concerns the low  $T_g$  of the glass combined to a high ionic conductivity. Then, we proposed two approaches to fulfill these requirements. The approach one is to firstly prepare a glass with low  $T_g$ , and then modify the glass composition (adding alkali salts) to obtain a high ionic conductivity. The approach two is trying to prepare the glass with high ionic conductivity for the first step, then optimize the glass composition to obtain a lower  $T_g$ . The schematic of both process is shown in Fig. 3.3.

## 2. Experiments and Measurements

### 2.1 Raw chemicals

The used raw chemicals are listed in table 3-1.

Table 3-1 The data of raw materials

Chemical formula	Gradient	Producer
$\text{NH}_4\text{H}_2\text{PO}_4$	99.99%	ACROS-ORGANICS Co.Ltd
$\text{Li}_2\text{CO}_3$	99.99%	ACROS-ORGANICS Co.Ltd
$\text{ZnO}$	99.99%	ACROS-ORGANICS Co.Ltd
$\text{SnO}$	99.99%	Alfa Aesar Co.Ltd
$\text{Li}_2\text{SO}_4$	99%	ACROS-ORGANICS Co.Ltd

### 2.2 Organophosphorus organic semiconductor

The organophosphorus organic semiconductor (OPSC) used here is named OPSCC2 and the structure of the molecule is shown in Fig. 3.4. Considering the degradation temperature of both molecules, the temperature of producing the glasses was kept below or equal to 300 °C in this chapter. More details about the OPSCC2 molecule can be found in the Ref 13.

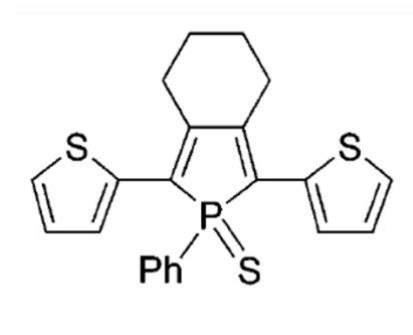


Fig. 3.4 The structure of OPSCC2

### 2.3 Preparation process

#### 2.3.1 Approach 1:

1. The 70%  $\text{P}_2\text{O}_5$  - 30%  $\text{SnO}$  (mol ratio) glass samples were prepared by flame method using  $\text{NH}_4\text{H}_2\text{PO}_4$  and  $\text{SnO}$  as initial raw materials, as shown in Fig 3.5.

2. The glass samples with compositions of 75%  $\text{SnO}$ -25%(30% $\text{ZnO}$ -70%  $\text{P}_2\text{O}_5$ )(ZSP1) and 50% $\text{SnO}$ -50%(30% $\text{ZnO}$ -70% $\text{P}_2\text{O}_5$ )(ZSP2) were prepared by mechanical milling method using  $\text{NH}_4\text{H}_2\text{PO}_4$ ,  $\text{SnO}$  and  $\text{ZnO}$ .



Fig. 3.5 Flame method of preparing glass

Before the mechanical milling process, the glass sample of 30%ZnO-70% P<sub>2</sub>O<sub>5</sub> were prepared by conventional melt-quench method in alumina crucibles in muffle furnace. Batches consisting of ZnO and NH<sub>4</sub>H<sub>2</sub>PO<sub>4</sub> were calcined at 300 °C for 12 h in an ambient atmosphere. Then, the calcined solid melted in air at 1100 °C for 30 min. The glass melt was quenched on a steel plate at room temperature and then annealed at the glass transition temperature, T<sub>g</sub>, for 1 h. The the samples were mechanically grinded to powders as the raw materials for high energy mechanical milling. Mechanical milling is a solid-state process, which uses mechanical energy at about room temperature to induce chemical reaction. Thus, using this equipment the problem of the different melting temperatures is overcome<sup>14</sup>. The mechanical milling instrument used during the preparation is SPEX Mixer 8000D as shown in Fig. 3.6. Tungsten carbide balls of 6 mm diameter and tungsten carbide molds of 45ml were used in this work. The running time of both ZSP1 and ZSP2 is 60h.



Fig. 3.6 Mechanical milling instrument (SPEX Mixer 8000D)

### 2.3.2 Approach 2:

1. Binary alkali phosphate glasses with composition  $x\%Li_2O-(100-x)\%P_2O_5$  ( $x=40, 50, 60$ ) were prepared by conventional melt-quench method in alumina crucibles in muffle furnace. Batches consisting of  $Li_2O$  and  $NH_4H_2PO_4$  were calcined at  $300\text{ }^\circ\text{C}$  for 12 h in an ambient atmosphere. Then, the calcined solid melted in air at  $1000\text{ }^\circ\text{C}$  for 30 min. The glass melt was quenched on a steel plate at room temperature.

2. Ternary alkali phosphate glass with composition  $25\%Li_2SO_4-40\%Li_2O-35\%P_2O_5$  (LiS25PM) and  $30\%Li_2SO_4-35\%Li_2O-35\%P_2O_5$  (LiS30PM) were prepared by the same way of binary alkali phosphate glass. The only difference is the melting temperature is lowered to  $900\text{ }^\circ\text{C}$ .

3. The LiS25PM glass was crushed into powder to be used as raw material for synthesizing OPSC doping hybrid glass by spark plasma sintering (SPS). The powder was weighted (0.5 g) and load into the graphite die of 10 mm diameter using a sheet of Papyex® (flexible graphite sheet) to ensure the release of the solid as well as to protect the diffusion of the graphite component from the mold. Different glass samples were prepared by SPS with different pressures and temperatures. The sintering temperature ranges from  $270\text{ }^\circ\text{C}$  to  $300\text{ }^\circ\text{C}$ . The pressure varies from 3kN to 5kN. The schematic of SPS instrument is shown in Fig 3.7 left. The glasses were named BSPS-temperature-pressure, for example, BSPS3005, which means that blank glass prepared at  $300^\circ\text{C}$  and 5kN. And the schematic of the optimized parameters of SPS process is shown in Fig. 3.7 right.

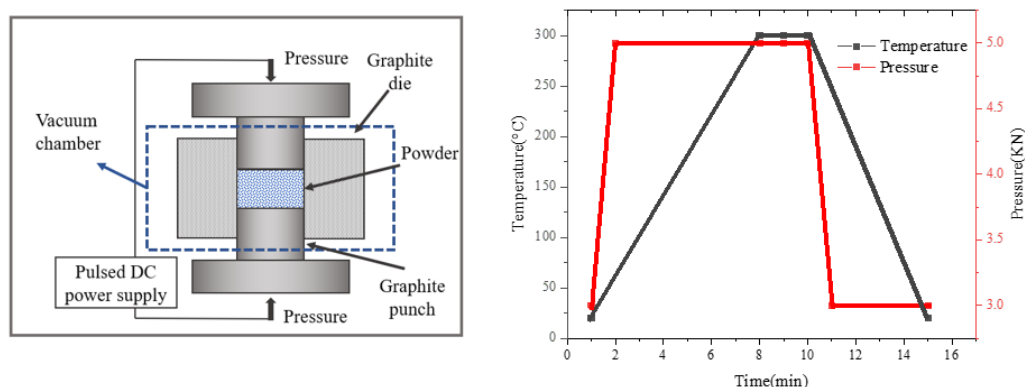


Fig. 3.7 Schematic of SPS instrument(left) and the optimized parameters of SPS process for (right)

4. The OPSC doped glass were prepared based on the optimized parameter ( $300\text{ }^\circ\text{C}$  and 5kN). Firstly, 1 mg OPSC were dissolved in around 5 ml acetone in a beaker, then 0.5 g LiSPM glass powder were added. After that, the beaker was disposed into an ultrasonic apparatus and

processed for 20 minutes at 50 °C. Then, the beaker was put in a hot plate at around 50 °C to dry. After drying, the mixed powder was put in the agate mortar to grind. This is for getting a better homogeneity of the sample. Last step, the powder was loaded into the graphite die to be sintered at 300°C with a pressure of 5kN.

### 2.3.3 Working principle of SPS

Basic SPS configuration is shown in Fig. 3.7 left. The SPS system consists of a hydraulic press with a vertical single pressurization axis. The pressure is transferred via two steel cylinders that are also simultaneously used as electrodes. Besides two graphite punches, there are two graphite spacers as well which were not depicted in the Fig 3.7 left. The two graphite spacers are between upper and lower punch electrodes. The sintered powder is put in the middle of the cylindrical die and pressed using the punches. Electric current formed by the power supply is flowing through graphite punches, the powder inside the cylinder and particularly through graphite die. Therefore, the spacers, die and the punches are made from an electrically conductive material that are able to resist high temperature and pressure, such as graphite and tungsten carbide. The high DC pulse current might create Joule-heating and sparking among the particles of the sintered powder, which leads to the faster heat and mass transfer instantaneously.

This equipment has been used already for molding some exotic glasses such as chalcogenide glasses, which present approximatively the same  $T_g$  as the phosphates glasses we plan to use 15.

### 3. Analysis of $P_2O_5$ – SnO and ZnO-SnO- $P_2O_5$ glasses

Based on our first approach, a glass composition with low  $T_g$  should be prepared. According to a previous works<sup>16</sup>, SnO phosphate glass always has a low  $T_g$ . Therefore, the 30% $P_2O_5$  – 70%SnO (mol ratio) glass was prepared by flame method firstly. However, the glass is not totally amorphous. Phase and crystal structure of the the prepared glasses were characterized by the X-ray diffraction measurements (XRD) (D/max 2550 VB/PC Rikagu, Japanese). All measurements were carried out at room temperature using Cu  $K\alpha$  radiation ( $\lambda=1.54056\text{\AA}$ ). A step size of  $0.02^\circ(2\theta)$  was used with a scan speed of  $2^\circ/\text{min}$ . The XRD patterns of the prepared glass, shown in Fig. 3.8, reveals the presence of several diffraction peaks belonging to the  $SnO_2$  crystalline phase dispersed in a mainly amorphous matrix.

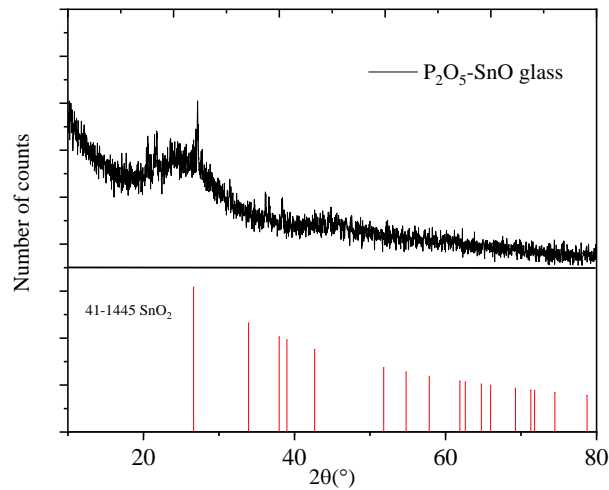


Fig. 3.8 XRD of the prepared 30%P<sub>2</sub>O<sub>5</sub> – 70%SnO glass sample

The  $T_g$  of the glass is higher than that in the report <sup>16,17</sup>. This is due to the formation of Sn<sup>4+</sup>, which is caused by the oxidation reaction of Sn<sup>2+</sup>. In order to obtain a Sn<sup>2+</sup> phosphate glass, the synthesis should be done in an inert glove box by the melting and quenching technique or by using mechanical milling. On the other hand, the addition of ZnO into tin containing phosphate glasses can increase the glass forming ability with only slight increase of the  $T_g$ . Thus, we decided to prepare the ZnO-SnO-P<sub>2</sub>O<sub>5</sub> glass rather than binary SnO phosphate glass. Two glass compositions of 75%SnO-25% (30%ZnO-70% P<sub>2</sub>O<sub>5</sub>) (ZSP1) and 50% SnO-50% (30%ZnO-70% P<sub>2</sub>O<sub>5</sub>) (ZSP2) were prepared by mechanical milling method. Before the mechanical milling process, the 30%ZnO-70% P<sub>2</sub>O<sub>5</sub> glass was prepared by melt-quench technology.

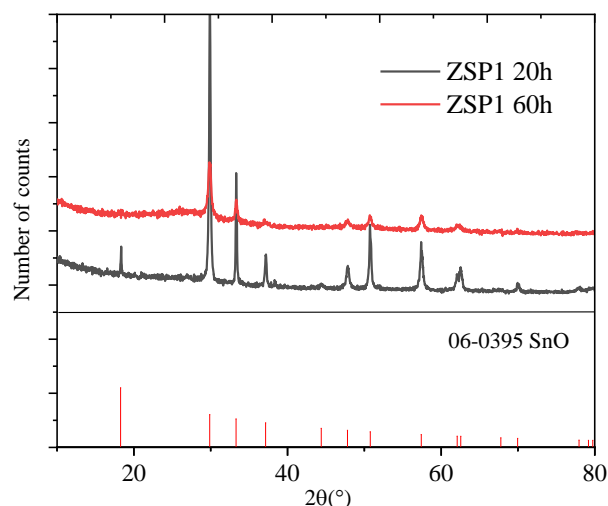


Fig. 3.9 XRD of ZSP1 sample prepared with different time

Fig. 3.9 shows the XRD of ZSP1 prepared after different time (20 h and 60 h) of mechanical milling. It can be seen that, although the composition is not amorphous after milling 60h, the existence of the only one crystalline phase (SnO), suggests that this technology indeed avoid

the formation of  $\text{Sn}^{4+}$ . In addition, a slight signal was observed as well of ZSP1 prepared with 60 h. This indicates that a portion of  $\text{SnO}$  integrates the glass composition after the milling process of 60h. At the same time, a different result concerning the ZSP2 was attained.

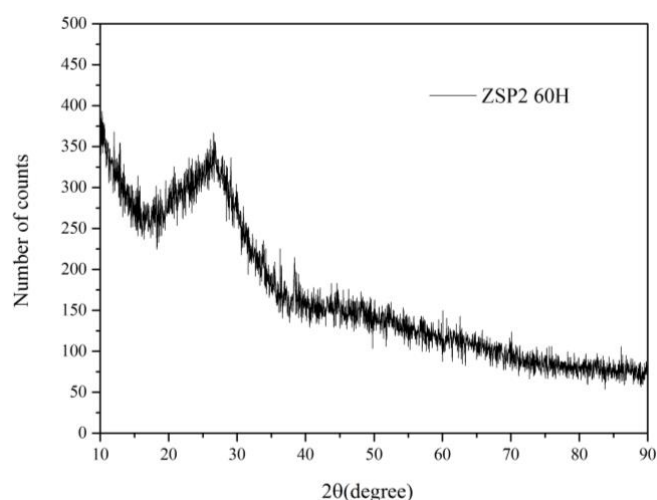


Fig. 3.10 XRD of ZSP2 sample prepared with 60 H

A totally amorphous ZSP2 powder was obtained after 60 h milling process, as observed by the XRD (see Fig 3.10). Then, the  $T_g$  of the prepared ZSP2 was determined by the differential scanning calorimetry (DSC). The DSC scans (TA Instruments SDT 2960) were carried out on a sample contained in a Al pan. Temperature calibration was carried out over a large range employing high-purity materials approved by the Committee on Standardization of the International Confederation for Thermal Analysis (ICTA). The overall accuracy of this measurement is expected to be within  $\pm 1$  K. The  $T_g$  was determined at a heating rate of 20 K/min. As shown in Fig. 3.11, it can be seen that the  $T_g$  of the glass is around 270 °C, which is much lower than the degradation temperature of the OPSCC2.

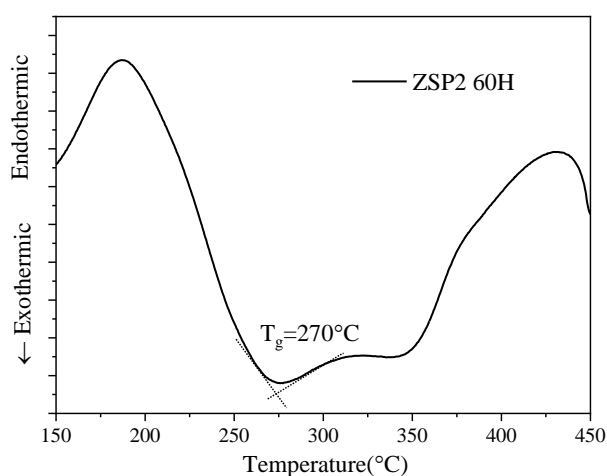


Fig. 3.11 DSC curve of ZSP2 prepared with 60 h

Since it is known that the SnO-ZnO-P<sub>2</sub>O<sub>5</sub> glass have a low conductivity, the task of modifying the glass composition to obtain a higher ionic conductivity should be done next step. Unfortunately, the glass forming ability of alkali containing SnO-ZnO-P<sub>2</sub>O<sub>5</sub> glassy system is really weak, which preventing the integration of alkali halide within the glassy matrix. This means a high ionic conductivity is hardly being achievable. Therefore, this approach was given up.

#### 4. Analysis of P<sub>2</sub>O<sub>5</sub> – Li<sub>2</sub>O glasses

As mentioned above, glasses with high content of alkali generally have a high ionic conductivity. Concerning phosphate glasses, both thermal properties and electric properties of Li metaphosphate glasses have been investigated by Martin<sup>9,18</sup>. The ionic conductivity of various alkali glasses at 150 °C are shown in Fig 3.12. It can be seen that the ionic conductivity of binary Li phosphate glasses increases with the rise of Li content.

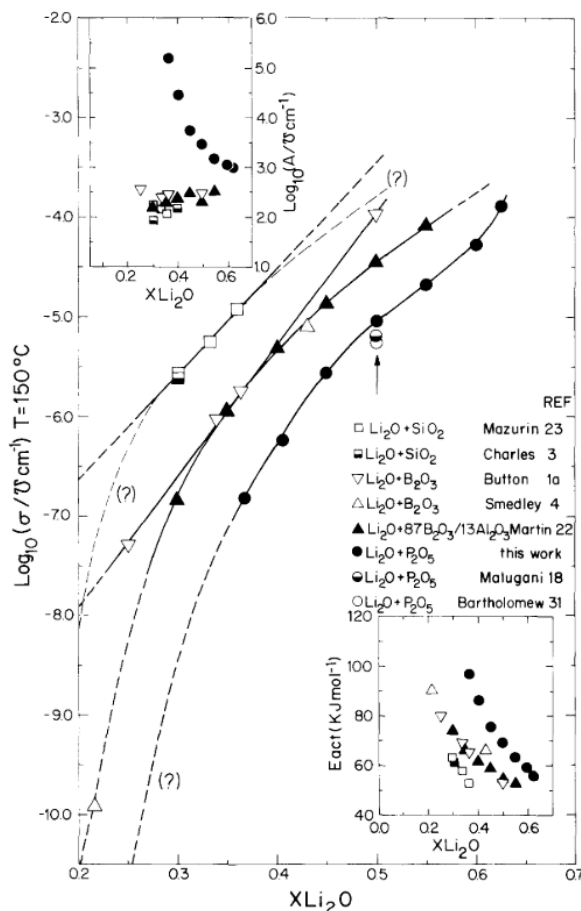


Fig. 3.12 Comparison of conductivities at 150°C for Li glasses in the different systems<sup>9</sup>



#### 4.1 Ionic conductivity

The frequency dependent electrochemical impedance spectroscopy (EIS) of the prepared 60%Li<sub>2</sub>O-40%P<sub>2</sub>O<sub>5</sub> glass at each temperature (Fig. 3.13) is used to assess the experimental DC conductivity  $\sigma_{dc}$  at each temperature  $\theta$ . The electrochemical impedance spectroscopy (EIS) was characterized from the electrochemical station (Autolab PGSTAT302N). Before the measurement, two gold electrodes were made on both the surfaces of the glass sample by the Low Vacuum Coater Leica EM ACE200 during 180 seconds. A stainless-steel plate covered by gold were attached onto both faces of the pellet as working and counter electrodes. The sample was put in a sealed cell with an architecture is presented in Fig. 3.13 left, and the electrochemical station and associated measuring devices is shown in Fig. 3.13 right.

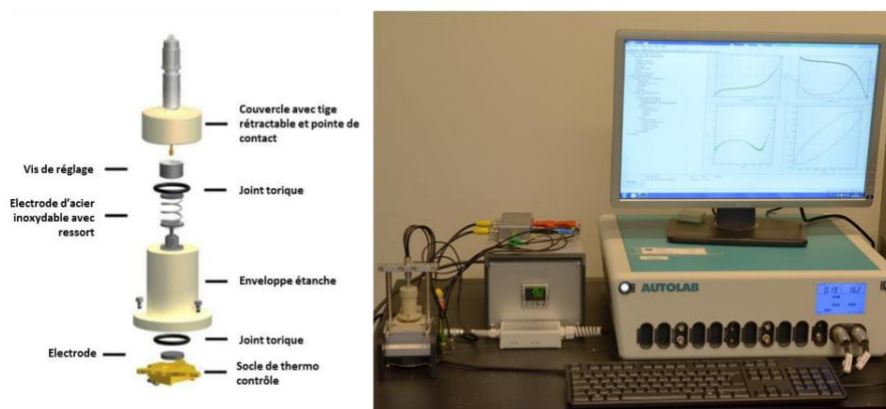


Fig 3.13 Thermo-controlled sealed measuring cell used for EIS characterizations (left) and associated measuring device (right)

As shown in Fig. 3.14 left, typically, for ions transport glass solid electrolyte, a semicircle at high frequency and a low-frequency spike would be observed. The semicircle is attributed to bulk conductivity, whereas the spike is a product of space-charge polarization effects from the accumulation of ions at the electrodes. The conductivity of the prepared Li phosphate glasses were also determined by the frequency dependent complex impedance,  $\hat{Z}(\nu) = Z'(\nu) + iZ''(\nu)$ . The real part of conductivity was calculated according to

$$\sigma'(\nu) = \frac{t}{A} \frac{Z'(\nu)}{[Z'(\nu)]^2 + [Z''(\nu)]^2} \quad (1)$$

where  $t$  is the thickness of the glass and  $A$  is the area of the electrode. Here, since just the DC conductivity was considered, the circuit resistance ( $R$ ) that is equal to the real impedance  $Z'(\nu)$  when the imaginary impedance  $Z''(\nu)$  is at a local minimum at low frequencies (equal to about 0), and the equivalent circuit was depicted in Fig. 3.14 right up. Thus, the Eq (1) is approximately equal to

$$\sigma_{dc} = \frac{t}{RA}, \quad (2)$$

where  $R$  is equal to  $Z'(\nu)$ , and this is shown in Fig. 3.14 right down 9.

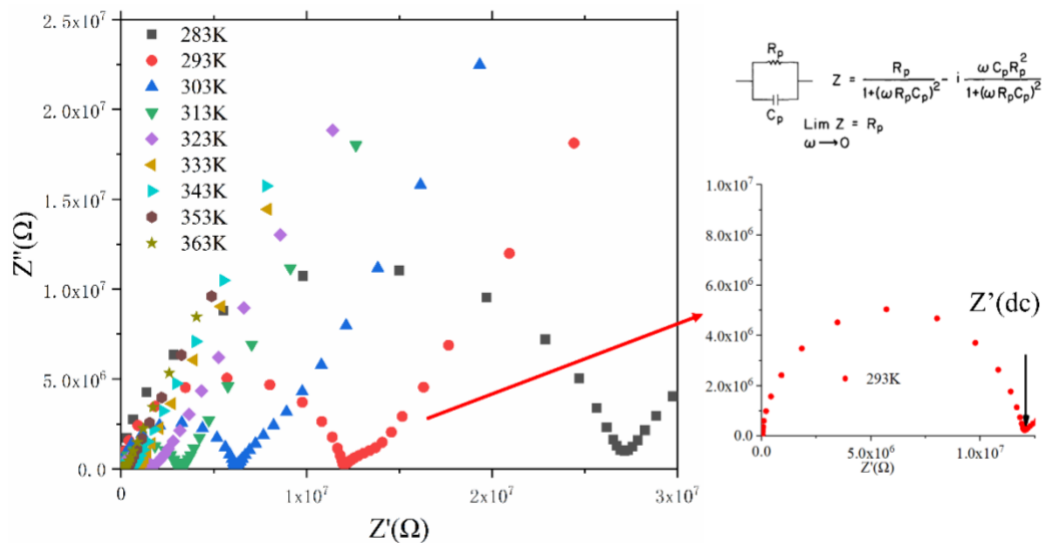


Fig 3.14 Nyquist plots of 60%Li<sub>2</sub>O-40%P<sub>2</sub>O<sub>5</sub> glass at different temperature(left) and at 293 K(right down), a classic equivalent circuit of the ideal solid electrolyte (right up)

Besides, the fitting of the ionic conductivity of the samples also obey well the Arrhenius law:

$$\sigma_{dc} T = A \exp\left(-\frac{E_{act}}{k_B T}\right) \quad (3)$$

which is shown in Fig. 3.15. Here,  $A$  and  $E_{act}$  denote respectively the pre-exponential factor and the activation energy of the dc conductivity, while  $k_B$  is Boltzmann's constant. It can be seen that, the ionic conductivity of the 60%Li<sub>2</sub>O-40%P<sub>2</sub>O<sub>5</sub> glass composition is the highest among the samples. However, it is still a bit below  $10^{-7}$  S/cm at room temperature, which is consistent with the previous report 9.

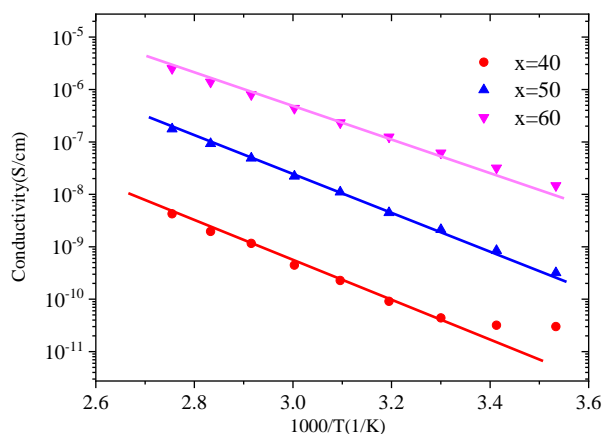


Fig. 3.15 Arrhenius plots of the DC conductivities obtained from the impedance plots of  $X \text{Li}_2\text{O}-(1-X) \text{P}_2\text{O}_5$  glasses,  $X=40,50,60$

#### 4.2 DSC analysis

On one hand, the ionic conductivity of the prepared binary Li phosphate glasses are still lower than  $10^{-7}$  S/cm which was listed as required value, on the other hand, the  $T_g$  of these glasses are higher than  $300^\circ\text{C}$  as shown in Fig. 3.16. The  $T_g$  of all the prepared Li binary phosphate glasses is higher than  $310^\circ\text{C}$ , which is also comparable to the reports <sup>9,18</sup>. Therefore, lithium phosphate glasses can not meet the listed requirements.

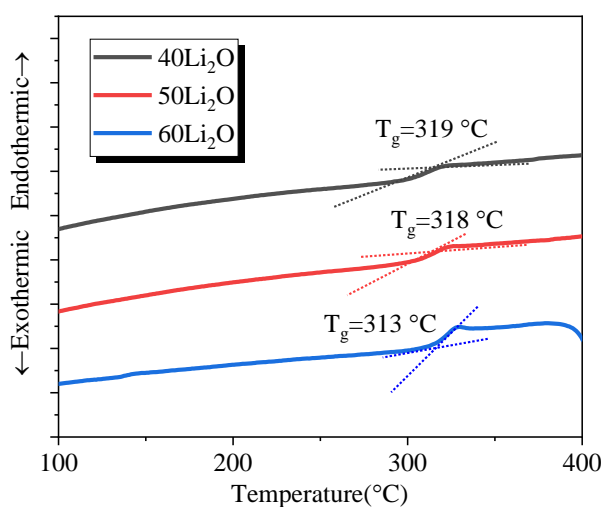


Fig. 3.16 DSC curve of  $X \text{Li}_2\text{O}-(1-X) \text{P}_2\text{O}_5$  glasses,  $X=40,50,60$

#### 5. Analysis of $\text{Li}_2\text{O}-\text{Li}_2\text{SO}_4-\text{P}_2\text{O}_5$ glasses

On one hand, as we mentioned, the addition of  $\text{Li}_2\text{SO}_4$  into binary alkali phosphate glass could effectively increase the ionic conductivity. On the other hand, the addition of S into glass matrix would break the bridging oxygen, which should decrease the  $T_g$  of the glass. Therefore,  $\text{Li}_2\text{O}-\text{Li}_2\text{SO}_4-\text{P}_2\text{O}_5$  glasses were prepared by conventional melt-quenching process.

### 5.1 DSC analysis

According to the previous studies<sup>19,20</sup>, two composition, 25%Li<sub>2</sub>SO<sub>4</sub>-40%Li<sub>2</sub>O-35%P<sub>2</sub>O<sub>5</sub> (LiS25PM) and 30%Li<sub>2</sub>SO<sub>4</sub>-35%Li<sub>2</sub>O-35%P<sub>2</sub>O<sub>5</sub> (LiS30PM), with higher ionic conductivity were prepared. Before we measured the conductivity of the prepared samples, the T<sub>g</sub> of the glasses were measured and illustrated in Fig. 3.17. The T<sub>g</sub> of LiS25PM is below 300 °C meeting the requirement, being below the degradation temperature of the OPSC. However, the T<sub>g</sub> of LiS30PM is higher than that of LiS25PM, which is different from the report<sup>17</sup>. In report<sup>17</sup>, the T<sub>g</sub> of LiS30PM is lower than that of LiS25PM (15 °C). In fact, the similar phenomenon is also observed in binary lithium phosphate glass. It is observed that below 50% Li<sub>2</sub>O segment, the T<sub>g</sub> of the glass decreases with the addition of Li<sub>2</sub>O. However, after that, the T<sub>g</sub> of the glass increase with the addition of Li<sub>2</sub>O.<sup>9</sup>

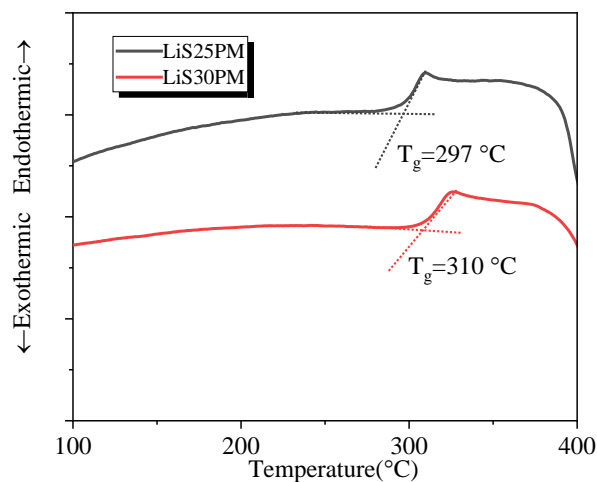


Fig. 3.17 DSC curve of Li<sub>2</sub>O-Li<sub>2</sub>SO<sub>4</sub>-P<sub>2</sub>O<sub>5</sub> glasses

### 5.2 Ionic conductivity

Then, the ionic conductivity of LiS25PM glass sample was determined using complex impedance analysis. The complex impedance plots of LiS25PM at each temperature is shown in Fig. 3.18 (a). The ionic conductivity and Arrhenius fitting are shown in Fig 3.18(b). It can be seen that the ionic conductivity of LiS25PM can reach 10<sup>-7</sup> S/cm at room temperature and reach 10<sup>-6</sup> S/cm at 60 °C.

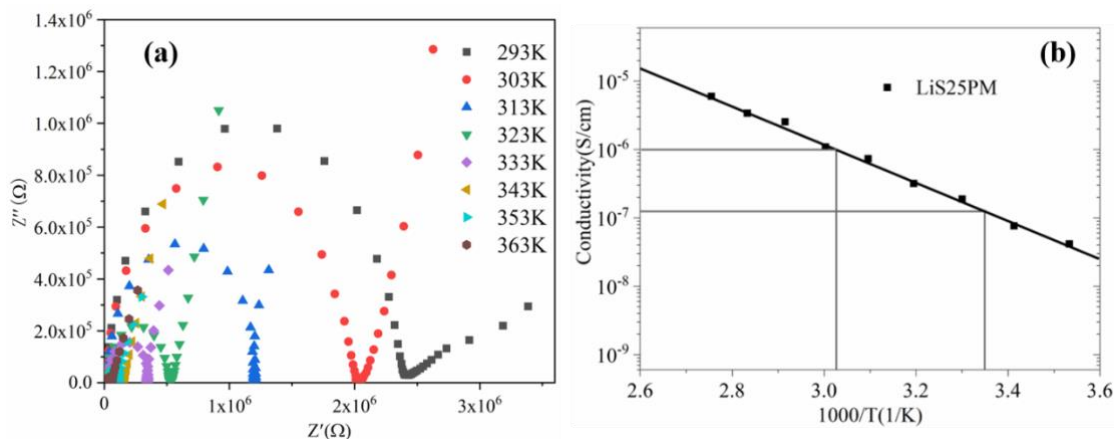


Fig. 3.18 Nyquist plots of LiS25PM glass at different temperature(a) and Arrhenius plots of the dc conductivities of LiS25PM

Compared to the 60%Li<sub>2</sub>O-40%P<sub>2</sub>O<sub>5</sub> glass sample, a slight improvement of the ionic conductivity of LiS25PM was observed as shown in Fig. 3.19. Although it is only a slight improvement, it brings the hope of being a good candidate electrolyte for a LEC (around or beyond  $10^{-7}$  S/cm).

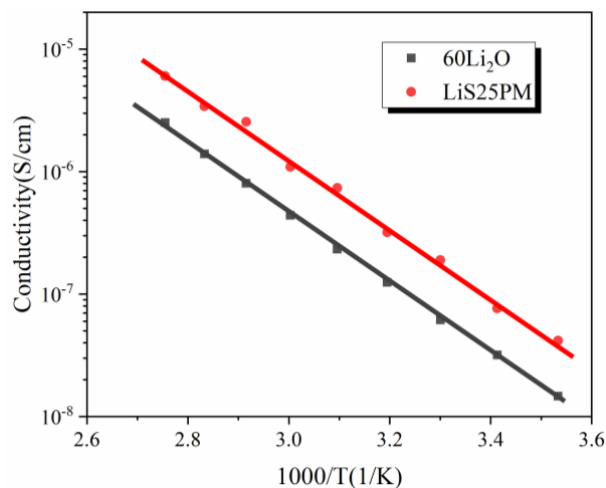


Fig. 3.19 Arrhenius plots of the dc conductivities of 60%Li<sub>2</sub>O-40%P<sub>2</sub>O<sub>5</sub> and LiS25PM glass

### 5.3 XRD and optical properties of LiS25PM glass

As previously observed, both  $T_g$  and ionic conductivity of LiS25PM glass meet the requirement for making efficient electrolytes for LEC application. Since the electrolyte of a LEC should be transparent for the emission of the related OSC. So, the transmittance spectrum of LiS25PM was measured by ultraviolet spectrophotometer ranging from 300 to 1000 nm (Fig. 3.20). It is noticed that the glass is totally transparent in the visible wavelengths. Besides, there is a sharply decrease around 310 nm, which also suggests that the glass could prevent the OPSC from damaging of UV due to the surface absorption.

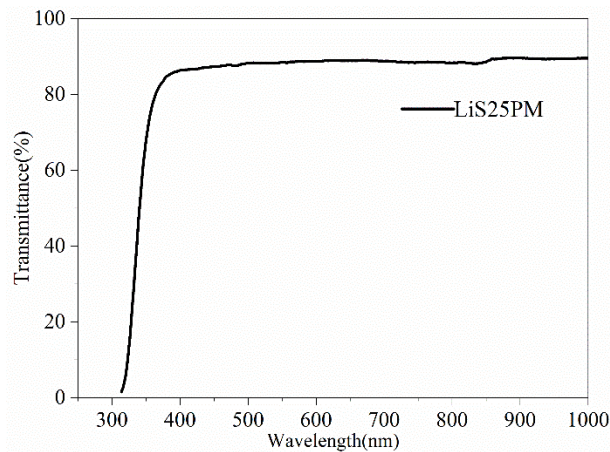


Fig 3.20 The transmittance spectrum of LiS25PM

Because the OPSC will integrate into the glassy matrix, the morphology property between them are important because of its transparency it will be easy to investigate the morphology of the particles if the glass matrix is totally amorphous. However, if some part of the glass are crystalline, then due to scatterings induced by particles, the coordination environment of the OPSC will be much more complicated to identify.

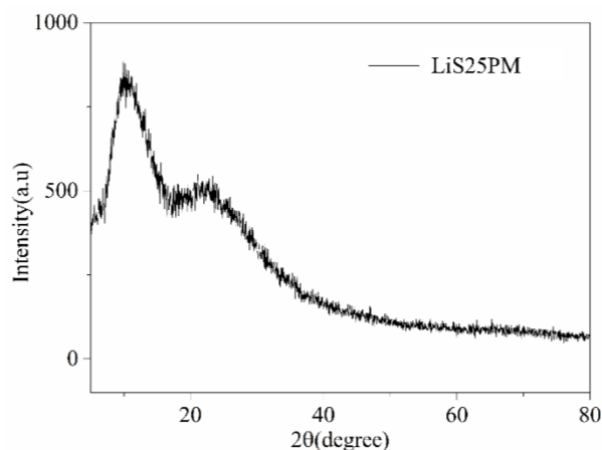


Fig 3.21 XRD pattern of LiS25PM





The XRD pattern of LiS25PM sample is shown in Fig. 3.21. The result shows the LiS25PM glass is totally amorphous. Thus, at present, the LiS25PM glass composition can meet all the requirements that are determined for being an efficient electrolyte for making LEC.

## 6. Preparation and analysis of hybrid glasses based on LiS25PM

### 6.1 Preparation of hybrid glass

The LiS25PM successfully meet all the requirements(wide transparency, low  $T_g$ , high ionic conductivity) and can be easily prepared by melt-quenching technology. The next step consists in preparing the hybrid material based on the LiS25PM glass and OPSC using the

spark plasma sintering (SPS) process. Thus, we should find the best parameters of SPS experiments such as time, temperature and dwell time, to prepare the glass using the powder of LiS25PM as raw material. The digital photos of the samples prepared by SPS with different parameters are shown in Fig 3.22, and the corresponding parameters are presented in the table. As already observed in other papers <sup>21,22</sup>, glasses can be easily sintered close to their glass transition temperature by SPS. The pressure applied is limited to 5kN due to the use of graphite molds of 10 mm diameter.

Temperature(°C)	270	280	290	300
Pressure(KN)	3	3	3	3
Time(min)	3	3	3	3
				





Temperature(°C)	290	290	295	298
Pressure(KN)	4	5	5	5
Time(min)	3	3	3	3
				

Fig. 3.22 Sintering parameters and digital photos of the prepared samples by SPS

It can be seen that the sample prepared at 298°C and 5kN pressure for 3 min has better transmittance property. In fact, the samples prepared at 298-300°C and 5kN pressure for 3 min always present a relatively good transmittance. The transmittance spectra in the range of 380-2000 nm were recorded with a Perkin-Elmer-Lambda 900UV/VIS spectrophotometer. In order to define the samples, the glass prepared by SPS with best transmittance is named as LiS25PS. As predicted, the sample with better transmittance always has a larger density. However, even the sample with the best transmittance prepared by SPS still has a smaller density (2.26 g/cm<sup>3</sup>) than that prepared by melt-quenching (2.34 g/cm<sup>3</sup>). It can be explained by the diffusion of carbon into the glass matrix or small pores inducing scatterings in the short wavelength as shown in Fig. 3.23. Considering that SPS is an efficient way to prepare the

glass, the OPSCC2 doped hybrid glass was prepared using the same parameter the one used to obtain dense LiS25PS.

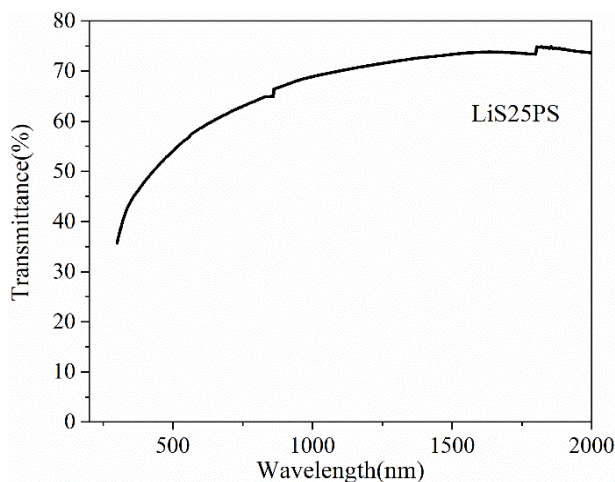


Fig. 3.23 Transmittance spectrum of LiS25PS

## 6.2 Analysis of hybrid glasses

The pictures of LiS25PS and of OPSCC2 doped hybrid glasses are shown in Fig. 3.24. The details of the synthesis process was depicted previously, and the mass of LiS25PS glass powder and the doping concentration of OPSCC2 is 0.5g and 1000 ppm, respectively. The hybrid glass is yellowish, which is similar to the OPSCC2 indicating that the molecules is probably conserved during the SPS process.



Fig. 3.24 Pictures of LiS25PS (up) and of OPSC doped hybrid glass(down)

### 6.2.1 Photoluminescent and excitation spectra

Photoluminescence spectra, including excitation (PLE) and emission spectra (PL) of the hybrid glass were measured by FLS980 (Edinburgh Instruments Ltd. England) fluorescence spectrometer at room temperature. The FLS980 comes standard with a 450 W ozone free



xenon arc lamp that covers a range from 230 nm to 1000 nm for steady state measurements. The PL and PLE spectra of the hybrid glass are shown in Fig. 3.25. The hybrid sample were optically excited in the region of the main absorption peaks of OSPCC2 (430 nm). Firstly, a strong PL was observed from the hybrid glass shown in the inset of Fig 3.25(a) and the peak of the corresponding PL spectrum is at around 600 nm. This is another strong evidence that the OPSCC2 is conserved during the SPS process. Compare to the emission of solid OPSCC2, a red-shift of 50 nm is observed in the hybrid glass sample. This is because the local environment around OPSCC2 changed, which probably influence the HOMO-LUMO of OPSCC2. The PLE spectrum with emission at 600nm is shown in Fig. 3.25(b), the mid-peak is around 465 nm , which is also red-shifted of 30nm compared to that of solid OPSCC2.

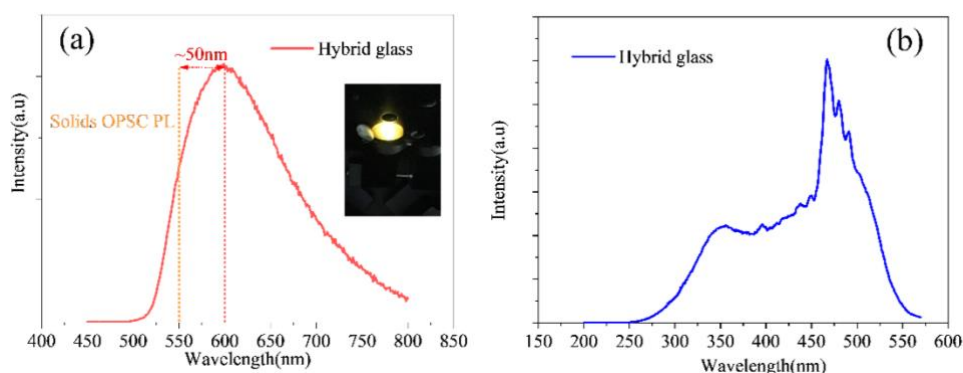


Fig. 3.25 PL (a) and PLE (b) spectra of the hybrid glass

### 6.2.2 Microstructure of the hybrid glass

In order to study the microstructure of the OPSCC2 molecule, a transmission electron microscope (TEM, JEOL JEM 2100F) was executed. Moreover, TEM is also a feasible way to investigate the interface morphology between OPSC and glass matrix. The TEM pictures of OPSCC2 doped glass are shown in Fig. 3.25. Since the atomic mass of the OPSCC2 (mainly carbon) is much lower than the glass host (mainly P and O), the OPSCC2 is bright and the glass matrix is dark. The detailed microstructures and chemical compositions of the samples were observed by transferring onto a copper grid for characterization. It can be seen from Fig. 3.26 (a) that the molecule is indeed distributed in the glass matrix. However, the size of the OPSCC2 is not unify, from 100 nm to 500 nm, as shown in Fig. 3.26(b).

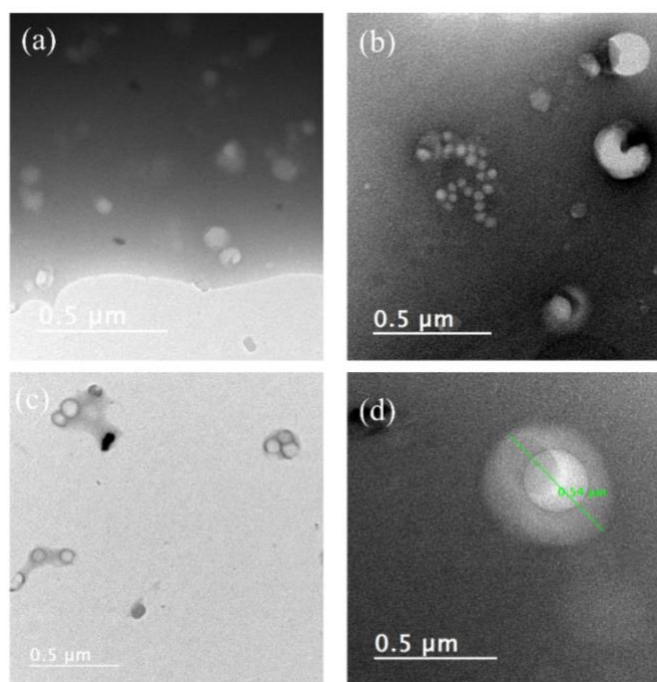


Fig. 3.26 TEM images of the hybrid glass

Some small hybrid glass pieces (below 500 nm) were also observed (Fig. 3.26(c)). From the figure, nanoparticles can be seen in each small glass piece, and the size of the OPSCC2 nanoparticles are all around 100 nm. Fig. 3.26(d) displays the biggest OPSCC2 nanoparticle in the glass host that have been observed during the measurement, and the size is of 540 nm.

In order to confirm that the observation of bright nanoparticle is indeed the OPSCC2, TEM images of the LiS25PS glass (without OPSCC2) was also obtained (Fig. 3.27). No bright nanoparticles were observed in the LiS25PS glass sample, whereas the dark glass matrix is similar to the hybrid glass sample. It is worthy noting that all these observed bright nanoparticles are not the ones which are formed in the glass after the SPS process, which is consistent with the result of XRD measurement of the hybrid glass (Fig. 3.28).

It can be seen that the hybrid glass is totally amorphous since the OPSCC2 does not have a crystalline structure. Thus, it is reasonable to think that these bright nanoparticles are OPSCC2. Moreover, as observed, although TEM can not directly evidences the topography morphology of the hybrid glass, it suggests the hybrid glass exhibits a minor phase separation on a sub-micron scale <sup>23</sup>.

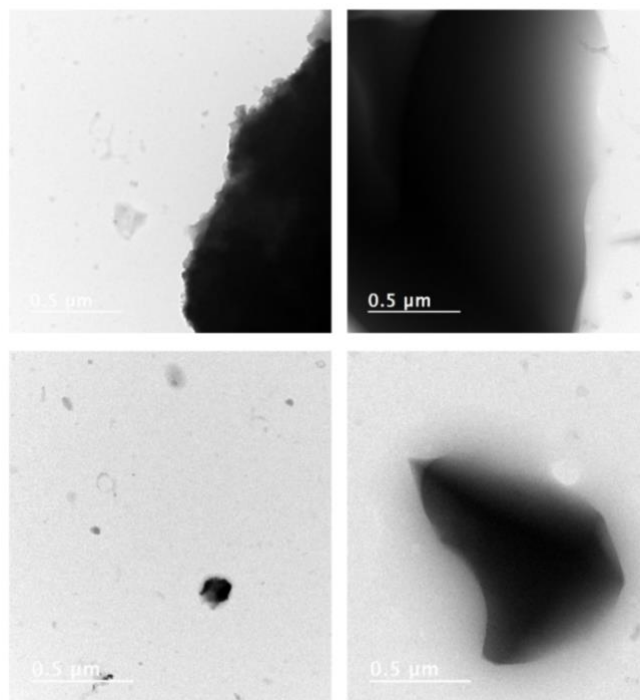


Fig. 3.27 TEM images of the LiS25PS glass

Thus, a better morphology of the hybrid glass can be obtained after the implementation of a better doping homogeneity.

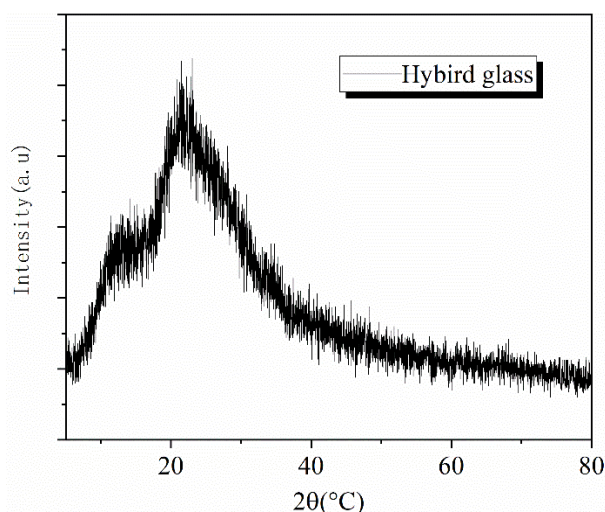


Fig. 3.28 XRD of the hybrid glass

Moreover, the NMR study of the  $^{31}\text{P}$  nucleus has been performed in the LiS25PM, LiS25PS and hybrid glass, the results are presented in Fig. 3.29. All solid-state NMR experiments were performed using a Bruker 600 Avance III spectrometer (14T) using a Bruker triple-gamma 2.5 mm probe head operating at Larmor frequency of 242 MHz for  $^{31}\text{P}$ . Magic Angle Spinning frequency was set to 20 kHz.  $^{31}\text{P}$  NMR spectra were acquired using a single pulse sequence. The pulse length was set to 1.5 μs corresponding to a 90° flip angle with a

repetition delay set to 30 s.  $^{31}\text{P}$  chemical shifts were referenced relative to the 85%  $\text{H}_3\text{PO}_4$  solution. Spectra were fitted using dmfit software. The  $^{31}\text{P}$  resonances and related parameters have been identified and all the chemical shifts are listed in Table 3-2. Only two  $^{31}\text{P}$  resonances are observed. By comparing to the literature <sup>17,24,25</sup>, these resonances are associated with  $^{31}\text{P}$  in metaphosphate (chemical shift around -22 ppm) and pyrophosphate (chemical shift around -3 ppm).

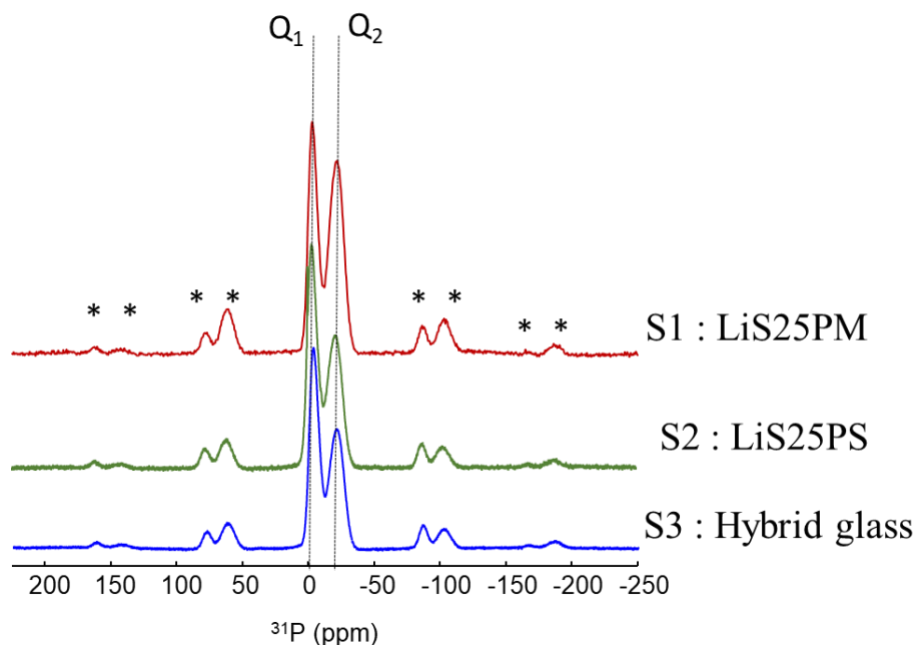


Fig. 3.29  $^{31}\text{P}$  NMR of LiS25PM, LiS25PS and the hybrid glass

The relative intensities of the two resonances measured by the areas under the peaks are also listed in Table 3-2.

Table 3-2  $^{31}\text{P}$  chemical shifts of LiS25PM, LiS25PS and the hybrid glass and the relative proportions of  $\text{Q}_1$  and  $\text{Q}_2$  species as determined by  $^{31}\text{P}$  NMR

Sample		$\delta_{\text{iso}}$ (ppm)	FWHM (Hz)	$\delta_{\text{CSA}}$ (ppm)	$\eta_{\text{CSA}}$	I(%)
LiS25PM	$\text{Q}_1$	-3.4	2000	98	0.2	38
	$\text{Q}_2$	-21	3200	-125	0.6	62
LiS25PS	$\text{Q}_1$	-3.2	2100	89	0.3	46
	$\text{Q}_2$	-20.2	3300	-117	0.9	54
Hybrid	$\text{Q}_1$	-3.3	2000	94	0.2	47
	$\text{Q}_2$	-20.2	3200	-124	0.5	53

Typically, polyphosphate glasses ( $P_2O_5 < 50\%$ ) have networks based on  $Q_2$  chains terminated by  $Q_1$  tetrahedra. The average chain length becomes progressively shorter as the  $[O]/[P]$  ratio increases. In these  $^{31}P$  NMR spectra, there are two resonances observed at a chemical shift of -3 ppm and -20 ppm, respectively. The chemical shift of -3 ppm and -20 ppm contribute to  $Q_1$  and  $Q_2$  species, respectively<sup>17,26,27</sup>. As expected, no peaks of  $Q_3$  species (chemical shift of -50 ppm) were observed. In between metaphosphate ( $P_2O_5=50\%$ ) and pyrophosphate ( $P_2O_5=67\%$ ) boundaries, the fraction of  $Q_1$  and  $Q_2$  tetrahedra can be given by 1:

$$f(Q^1) = 2x - 1/(1 - x) \quad (4)$$

$$f(Q^2) = 2 - 3x/(1 - x). \quad (5)$$

Where  $x$  is the mole ratio of lithium modifiers here. Thus, the fraction of  $Q_1$  and  $Q_2$  of all the prepared glasses should be around 0.85 and 0.15, respectively. However, according to the NMR data, the fraction of  $Q_1$  and  $Q_2$  is 38 and 62 for LiS25PM, respectively; 46 and 54 for LiS25PS, respectively; 47 and 53 for the hybrid glass, respectively. This is because the  $Li_2SO_4$  raw material introduces S into the glass matrix, which decrease the  $[O]/[P]$  ratio leading to the decrease of  $Q_1$ .

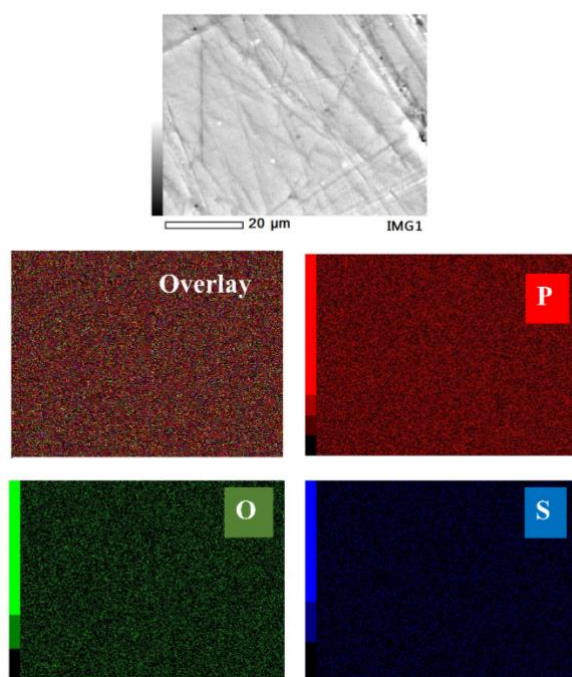


Fig. 3.30 SEM image of LiS25PM and the corresponding EDX analysis mapping images of P, O, S in the glass. SEM images and Energy Dispersive Spectrometer (EDS) elemental mappings of the LiS25PM was obtained with a JEOL JSM-7100F. Before the measurement, the gold deposition was made on the surface of the samples. This gold deposition is prepared by the

Low Vacuum Coater Leica EM ACE200 with 60 seconds. As shown in Fig 3.30, it can be seen that distribution of all the elements is homogeneous.

One can notice that the ratio between  $Q_1$  and  $Q_2$  species is directly affected by the synthesis process, passing from 38/62 for an “usual” melted and quenched process (LiS25PM) to 46/54 for SPS (LiS25PS and hybrid glass). It evidences that the glassy network is less polymerized after SPS glasses. Moreover, the linewidth is similar for the 3 samples ( $Q_1$ : about 2kHz and  $Q_2$ : about 3.2 KHz). That indicates that the local disorder is not impacted by the synthesis route or the presence of the molecule. Chemical shift tensor presents approximatively the same values for the 3 samples ( $\delta_{iso}$ ,  $\delta_{CSA}$  and  $\eta_{CSA}$  are quite similar for LiS25PM, LiS25PS and hybrid glass). So, the chemical environment is not affected by the synthesis process or by the presence of the OPSCC2.

Therefore, based on all these data, several conclusions about the microstructure of hybrid glasses can be obtained. Firstly, the OPSCC2 exists as amorphous nanoparticle in the glass matrix and the average size of these nanoparticles is around 100 nm. Therefore, the phase separation is on a sub-micron scale, which is beneficial to the performance of a LEC device<sup>23,28,29</sup>. In addition, it is reasonable to point out that there are no bonding arrangements between OPSCC2 and glass network. Since the OPSCC2 exists as nanoparticles in the glass matrix, they can decrease the movement of lithium ions in the glass, which may decrease the ionic conductivity.

### **6.2.3 Electrochemical properties of the hybrid glass**

In addition to the PL property and microstructure of the hybrid glass which have been investigated and discussed before, the last but not least task is the electrochemical characterization of the hybrid glass, which plays the crucial role for a LEC.

#### **6.2.3.1 Ionic conductivity**

First of all, the ionic conductivity of the hybrid glass was determined by the complex impedance analysis and the corresponding Arrhenius plots was fitted as shown in Fig. 3.31, LiS25PS is shown as a reference. Unfortunately, both LiS25PS ( $8.1 \times 10^{-8}$  S/cm) and hybrid glass ( $6.1 \times 10^{-8}$  S/cm) with a lower ionic conductivity than LiS25PM ( $10^{-7}$  S/cm), which may be caused by defects due to the sintering process such as impurities, residual pores and grain boundaries.

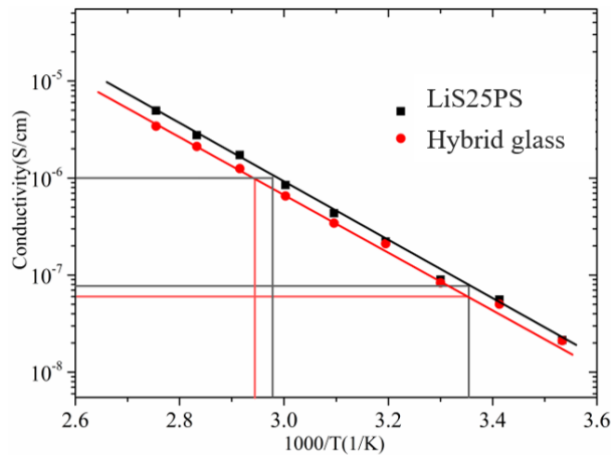


Fig. 3.31 Arrhenius plots of the dc conductivities of LiS25PS and hybrid glass

It can be seen that the ionic conductivity of the hybrid glass is slightly lower than that of LiS25PS. This is consistent with the inference of “blocking” effect of OPSCC2 we discussed above. In fact, a single crystal or single amorphous phase material, without grain boundary, is the ideal medium for fast ionic conduction. Therefore the phase separation between the glassy matrix and OPSCC2 in the hybrid glass is expected to be similar to the grain boundary behaviour in the glass-ceramics <sup>30,31</sup>.

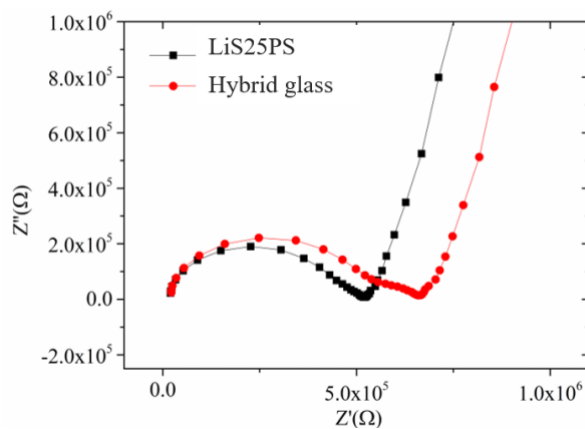


Fig. 3.32 Nyquist plots of LiS25PS and hybrid glass at 50 °C

This explanation is supported by the complex impedance plots of the LiS25PS glass and hybrid glasses. The complex impedance plots of LiS25PS and hybrid glass at 50 °C (keep the ionic above  $10^{-7}$  S/cm) is shown in Fig. 3.32. Two semi-circle, a big one at high frequency and a small one at low frequency, were observed in the case of hybrid glass, which is not observed from other prepared glasses. According to other reports <sup>30,31</sup>, this second semi-circle is a typical fingerprint of the grain boundary. Although there is no grain boundary in the glass matrix, the phase separation is probably causing the slight decrease of the ionic conductivity.

In spite of the ionic conductivity of the hybrid glass is below  $10^{-7}$  S/cm at room temperature, it can reach  $10^{-6}$  S/cm at around 65 °C meeting the requirement of a LEC device.

### 6.2.3.2 Cyclic voltammetry

As mentioned previously, the electrochemical model assumes that the mechanism of a LEC is a electrochemical process. Therefore, an electrochemical doping process of the OPSCC2 is expected to occur in the hybrid glass. On the other hand, the electrochemical stability window of the electrolyte need to be wider than that of OPSCC2. Cyclic voltammetry (CV) measurement is used to determine the electrochemical stability window of the glass electrolyte as well as the electrochemical doping process of the OPSCC2. The cyclic voltammetry was undertaken using a chemical station (Autolab PGSTAT302N) at a scanning rate of 0.2 mV/s between -2.1 and 2.3 V. The other processes is similar to that of EIS measurement. As shown in Fig. 3.33, visible anodic and cathodic current respectively attributable to gold dissolution ( $\text{Au} \rightarrow \text{Au}^{3+} + 3\text{e}^-$ ) and deposition ( $\text{Au}^{3+} + 3\text{e}^- \rightarrow \text{Au}$ ) are observed in the potential range from 1.5 to 1.3 V, which also shows a good reversibility. In addition, current due to electrolyte decomposition is detected in -2 and 2 V. In hybrid glass, besides the observed peaks, a redox couple were observed. These redox couple were contributed to the OPSCC2. Although the oxidation peak ( $E_{\text{pa}}$ ) and reduction peak ( $E_{\text{pc}}$ ) of the OPSCC2 have been measured in  $\text{CH}_2\text{Cl}_2$ , referenced to Fc/Fc<sup>+</sup> half cell 13, it can not make a simple comparison here since the measurement condition is different.

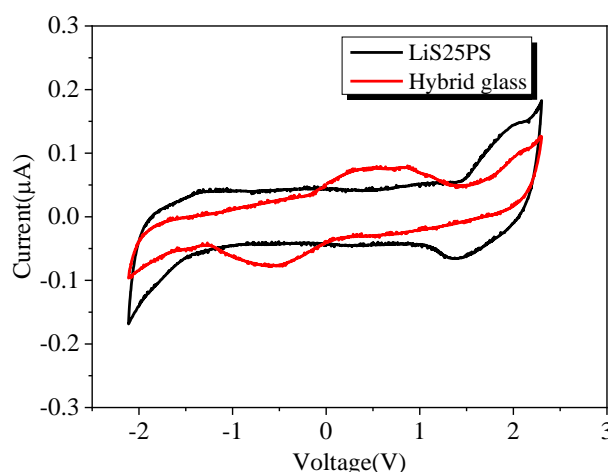


Fig. 3.33 Cyclic voltammetry measurement of LiS25PS and hybrid glass with a scanning rate of 0.2 mV/S at 50 °C

Therefore, more experiments need to be done to confirm the redox peaks belonging OPSCC2. If it is, that means a chemical doping process can be obtained in the OPSCC2 doped hybrid



glass as well as a wider electrochemical stability window than the OPSCC2, which is an ideal emitting material for a LEC.

### 7. LEC device based on the hybrid glass

Further more, a LEC device based on the hybrid glass was made. The typical thickness of the emitting coating of a LEC is around several tens of microns <sup>28,32</sup>. Since the glass is fragile, it is very difficult to polish it below 100 microns. The hybrid glass was polished down to 400 microns to prepare the device. Because of the much larger thickness, a heating device was used to increase the temperature of the hybrid glass sample to improve the ionic conductivity. The schematic of the experimental platform to test the LEC based on the hybrid glass is shown in Fig. 3.34, and the inset shows the real devices. However, we failed to observe the electroluminescence from the hybrid glass even when the temperature was increased up to 150 °C. Several possible reasons can explain this result: 1. the glass thickness is still too large; 2. the surface contact between glass and electrodes are not perfect; 3. the ionic conductivity is still too low; 4. impurities are introduced by SPS process. In the next step, all of these possible problems would be tackled to test the electroluminescence of the hybrid glass.

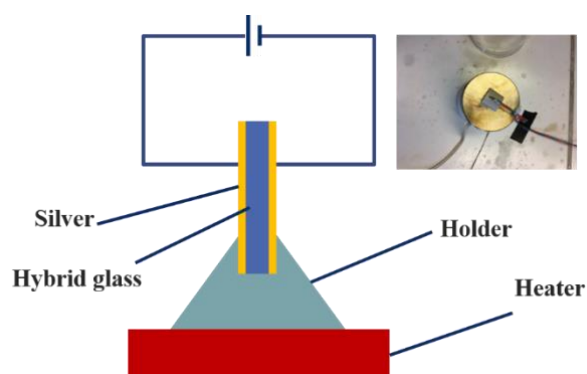


Fig. 3.34 Schematic of the platform to test the LEC based on the hybrid glass

### 8. Conclusion

A phosphate glass composition with good transmittance in the visible range (around 90%), low  $T_g$  (297 °C) and relatively high ionic conductivity ( $10^{-7}$  S/cm) was obtained by melt-quenching. Then, based on this glass composition, by using a two-step method consisting of melt-quenching and subsequent SPS process, the OPSCC2 doped hybrid glasses have been prepared successfully. The observation of the strong PL of the hybrid glass evidences that the OPSCC2 is not degraded during the SPS process. This contestation is also supported by the TEM results which underlines the presence of OPSCC2 nanoparticles in the hybrid glass, with a size ranging from 100 to 500 nm. Although the topographical morphology can not be

evidenced by TEM, it suggests that the phase separation scale can reach sub-micron scale. This means a good morphology can be obtained through improving the parameters of mixing. In addition, the ionic conductivity of the hybrid glass was determined by EIS. It can reach  $6.1 \times 10^{-8}$  S/cm and  $10^{-6}$  S/cm at room temperature and 65 °C, respectively. Lastly, the CV measurement suggests that chemical doping process of OPSCC2 occurs in the hybrid glass. Moreover, the electrochemical stability window of the glass host is wider than that of OPSCC2. However, in order to confirm this result, more experiments and analysis should be done. Although no electroluminescence of the hybrid glass based device was observed, based on all these data, it is reasonable to point out that this hybrid glass is a good candidate to be used as the emitting material for LEC application.

## REFERENCES

- 1 Brow, R. K. the structure of simple phosphate glasses. *Journal of Non-Crystalline Solids* **263**, 1-28 (2000).
- 2 Kirkpatrick, R. J. & Brow, R. K. Nuclear magnetic resonance investigation of the structures of phosphate and phosphate-containing glasses: a review. *Solid state nuclear magnetic resonance* **5**, 9-21 (1995).
- 3 Van Wazer, J. R. Phosphorus and its Compounds. (1958).
- 4 Hoppe, U. A structural model for phosphate glasses. *Journal of Non-Crystalline Solids* **195**, 138-147 (1996).
- 5 Martin, S. W. Ionic conduction in phosphate glasses. *Journal of the American Ceramic Society* **74**, 1767-1784 (1991).
- 6 Bartholomew, R. F. Electrical properties of phosphate glasses. *Journal of Non-Crystalline Solids* **12**, 321-332 (1973).
- 7 Doreau, M., El Anouar, A. A. & Robert, G. Domaine vitreux, structure et conductivite electrique des verres du systeme LiCl/1b Li<sub>2</sub>O/1b P<sub>2</sub>O<sub>5</sub>. *Materials Research Bulletin* **15**, 285-294 (1980).
- 8 Pradel, A., Pagnier, T. & Ribes, M. Effect of rapid quenching on electrical properties of lithium conductive glasses. *Solid State Ionics* **17**, 147-154 (1985).
- 9 Martin, S. W. & Angell, C. Dc and ac conductivity in wide composition range Li<sub>2</sub>O - P<sub>2</sub>O<sub>5</sub> glasses. *Journal of Non-Crystalline Solids* **83**, 185-207 (1986).
- 10 Robert, G., Malugani, J. & Saida, A. Fast ionic silver and lithium conduction in glasses. *Solid State Ionics* **3**, 311-315 (1981).
- 11 Martin, S. Review of the structures of phosphate glasses. *ChemInform* **22**, (1991).
- 12 Malugani, J. & Robert, G. Conductivite ionique dans les verres LiPO<sub>3</sub>Lix (X= I, Br, Cl). *Materials Research Bulletin* **14**, 1075-1081 (1979).
- 13 Fave, C. *et al.* First examples of organophosphorus-containing materials for light-emitting diodes. *Journal of the American Chemical Society* **125**, 9254-9255 (2003).
- 14 Fecht, H., Hellstern, E., Fu, Z. & Johnson, W. Nanocrystalline metals prepared by high-energy ball milling. *Metallurgical Transactions A* **21**, 2333 (1990).
- 15 Hubert, M., Petracovschi, E., Zhang, X. H. & Calvez, L. Synthesis of Germanium–Gallium–Tellurium (Ge–Ga–Te) Ceramics by Ball-Milling and Sintering. *Journal of the American Ceramic Society* **96**, 1444-1449 (2013).
- 16 Lim, J. W., Yung, S. W. & Brow, R. K. Properties and structure of binary tin

- phosphate glasses. *Journal of Non-Crystalline Solids* **357**, 2690-2694 (2011).
- 17 Morena R. Phosphate glasses as alternatives to Pb-based sealing frits. *Journal of non-crystalline solids* **263**, 382-387 (2000)
- 18 Martin, S. W. & Angell, C. A. Glass formation and transition temperatures in sodium and lithium borate and aluminoborate melts up to 72 mol.% alkali. *Journal of non-crystalline solids* **66**, 429-442 (1984).
- 19 Ganguli, M. & Rao, K. Studies of ternary  $\text{Li}_2\text{SO}_4\text{-Li}_2\text{O-P}_2\text{O}_5$  glasses. *Journal of non-crystalline solids* **243**, 251-267 (1999).
- 20 Ganguli, M., Bhat, M. H. & Rao, K. Lithium ion transport in  $\text{Li}_2\text{SO}_4\text{-Li}_2\text{O-P}_2\text{O}_5$  glasses. *Solid state ionics* **122**, 23-33 (1999).
- 21 Hubert, M. *et al.* An innovative approach to develop highly performant chalcogenide glasses and glass-ceramics transparent in the infrared range. *Optics express* **19**, 23513-23522 (2011).
- 22 Delaizir, G. *et al.* Investigation of the Mechanisms Involved in the Sintering of Chalcogenide Glasses and the Preparation of Glass-Ceramics by Spark Plasma Sintering. *Journal of the American Ceramic Society* **95**, 2211-2217 (2012).
- 23 Matyba, P., Andersson, M. R. & Edman, L. On the desired properties of a conjugated polymer-electrolyte blend in a light-emitting electrochemical cell. *Organic Electronics* **9**, 699-710 (2008).
- 24 Brow, R. K., Kirkpatrick, R. J. & Turner, G. L. The short range structure of sodium phosphate glasses I. MAS NMR studies. *Journal of Non-crystalline solids* **116**, 39-45 (1990).
- 25 Müller-Warmuth, W. & Eckert, H. Nuclear magnetic resonance and Mössbauer spectroscopy of glasses. *Physics Reports* **88**, 91-149 (1982).
- 26 Brow, R. K., Phifer, C. C., Turner, G. L. & Kirkpatrick, R. J. Cation effects on  $^{31}\text{P}$  MAS NMR chemical shifts of metaphosphate glasses. *Journal of the American Ceramic Society* **74**, 1287-1290 (1991).
- 27 Losso, P. *et al.*  $^{31}\text{P}$  NMR investigations of binary alkaline earth phosphate glasses of ultra phosphate composition. *Journal of non-crystalline solids* **143**, 265-273 (1992).
- 28 Mindemark, J. & Edman, L. Illuminating the electrolyte in light-emitting electrochemical cells. *Journal of Materials Chemistry C* **4**, 420-432 (2016).
- 29 Tang, S. & Edman, L. Quest for an Appropriate Electrolyte for High-Performance Light-Emitting Electrochemical Cells. *The Journal of Physical Chemistry Letters* **1**, 2727-2732 (2010).

- 30 Fu, J. Superionic conductivity of glass-ceramics in the system  $\text{Li}_2\text{O}-\text{Al}_2\text{O}_3-\text{TiO}_2-\text{P}_2\text{O}_5$ . *Solid State Ionics* **96**, 195-200 (1997).
- 31 van Dijk, T. & Burggraaf, A. J. Grain boundary effects on ionic conductivity in ceramic  $\text{Gd}_x\text{Zr}_{1-x}\text{O}_{2-(x/2)}$  solid solutions. *physica status solidi (a)* **63**, 229-240 (1981).
- 32 Pei, Q., Yu, G., Zhang, C., Yang, Y. & Heeger, A. J. Polymer light-emitting electrochemical cells. *Science* **269**, 1086-1088 (1995).

## **Chapter IV: Luminescence of zinc phosphate glasses**



## 1. Introduction

During the process of preparing phosphate glass for making LECs, blue luminescence was observed from the tin and zinc oxide phosphate glass excited under 256 nm UV lamp, mainly due to the contribution of SnO luminescence centers <sup>1</sup>. However, a blue luminescence was also observed in the entirely amorphous zinc binary phosphate glasses in our work, which intrigues us since there are very few works reported on it. Fortunately, the similar blue photoluminescence (PL) was observed in some totally amorphous zinc multicomponent silicate glasses <sup>2-4</sup>.

Normally, embedding ZnO nanocrystals in a glass matrix can help to stabilize their luminescence properties largely influenced by the surface-interface of the nanoparticles <sup>5</sup>, so ZnO glass-ceramics have been extensively investigated <sup>6,7</sup>. However, it is worthwhile mentioning that besides ZnO glass-ceramic, quite a few amorphous zinc glasses also have PL that is different from that of ZnO crystals or nanoparticles <sup>2</sup>. The PL of amorphous zinc glasses always shows stronger UV but weaker visible emission, which was considered interesting to be used in short wavelength opto-electrical devices <sup>8</sup>. According to these researches <sup>2-4</sup> of amorphous zinc multicomponent silicate glasses, the luminescence is probably due to amorphous ZnO in the glass matrix, which is consistent with the results obtained from our experiments. However, most of these investigations solely pertain to the PL study and are restricted to some settled multicomponent silicate glasses <sup>2-4</sup>. Because of the complicated bonding arrangements in multicomponents glass system, it is hard to thoroughly study the cause of the emission, therefore, so far little is known about the cause of the emission in amorphous zinc glasses.

Compared to multicomponents glass system, binary phosphate glass system has a simpler structure facilitating the study of the causes of the emission. Therefore, in this work, we also seek to remedy the problem by analyzing both PL and structure properties of the glass. The preliminary hypothesis is that the emission is caused by amorphous nanoscale ZnO clusters (ANZC) which are formed after engineering the topological features of the glass matrix. It is hoped that this research will contribute to a deeper understanding of the formation of ANZC in glass.

Moreover, after understanding the formation of ANZC within glass, we devoted to preparing a phosphor-converted white light-emitting diode (pc-WLEDs) based on this glass. WLEDs based solid-state lighting system is rapidly replacing incandescent and fluorescent light sources, both in general lighting and display backlights, because of their high luminous



efficiency, environmental friendliness, and long lifetime.<sup>9-12</sup> Phosphor-converted white light-emitting diodes (pc-WLEDs) are emerging as an indispensable solid-state light source due to their unique properties including but not limited to energy savings, environment-friendliness, small volume, and long persistence.<sup>10,13,14</sup> Until now, major challenges in pc-WLEDs have been to achieve a high luminous efficiency, high chromatic stability, brilliant color-rendering index (CRI), and price competitiveness against fluorescent lamps, which rely critically on the phosphor properties.<sup>15-18</sup> While the field of luminescent materials for solid-state lighting has seen a tremendous increase in the past two decades, the most common way to generate white light is the combination of blue LED chips with yellow-emitting phosphor materials.<sup>19</sup> However, the difference between individual degradation rates of chips and phosphors coated on chips would cause a chromatic aberration and a poor white light performance.<sup>20</sup> Fortunately, luminescent glass is a rational solution, and among various kinds of pc-WLEDs, luminescent glasses possess some obvious advantages:<sup>10,21</sup> homogeneous light-emitting; simpler manufacture procedure; lower production cost; better thermal stability and epoxy resin free in assembly process.

White light-emitting glass was developed by Zhang et al. in 1991<sup>22</sup> for the first time, it intrigues many researchers in the past three decades.<sup>21,23-25</sup> Most of these researches focus on trivalent rare earth ions (REI) doped glass, however, the narrow and sharp emission of REI, which is due to its 4f-4f transition that is hardly affected by the surrounding coordination, makes the related white light-emitting devices possess a lower color rendering. In recent years, the emergence of researches of white light-emitting from rare earth free (REF) luminescent glass suggests that this kind of luminescent glass seems to be a novel pc-WLEDs material.<sup>1,20,26</sup> This is because the REF luminescent glass not only shows white light emission comparable to the crystalline phosphor, but also shows a broader emission band which could improve the color rendering property of the luminescent glass.<sup>1</sup> For example, Chen et al. investigated the Cu/Mn co-doped white light glass;<sup>26</sup> Masai et al. discovered the Mn/Sn co-doped white light glass.<sup>1</sup> However, the former work failed to obtain warm WLED glass (low color temperature); the latter work has not yet clarified the mechanism of the light observed in the glass. Last but not least, neither of them clarified the mechanism of the emission from  $Mn^{2+}$  ions of the glasses in detail.

In this work, we propose a unique pc-WLEDs based on manganese single doped zinc phosphate containing ANZC. Besides, for the first time, we try investigating the mechanism of the emission from  $Mn^{2+}$  ions based on static luminescence analysis through  $Mn^{3+}$  as an “energy acquisition probe”. The energy transfer process between the glass host and  $Mn^{2+}$  ions

in the prepared glass is demonstrated as well. Moreover, the prepared novel warm white light luminescent glass displays a high CRI; low color temperature; comparable to the crystalline phosphor of luminous efficacy. Considering the advantages of luminescent glass mentioned above, the prepared white light glass presents a substantial advance towards tackling the major challenges in pc-WLEDs field.

## **2 Experiments and Chemicals**

### **2.1 Experiments of phosphate glass containing ANZC**

The binary zinc phosphate glasses (40% ZnO-60% P<sub>2</sub>O<sub>5</sub>) were prepared by a conventional melt-quenching method using a silica crucible. Batches consisting of ZnO (99.999%) and P<sub>2</sub>O<sub>5</sub> (99.99%) are donated as PO (20g), and batches consisting of ZnO (99.999%) and (NH<sub>4</sub>)<sub>2</sub>HPO<sub>4</sub> (99.99%) are donated as NHPO (20g). All batches were initially calcined at 800 °C for 3 h in an ambient atmosphere. The calcined solid was then melted at 1000 °C for 60 min in an ambient atmosphere. The glass melt was quenched on a stainless plate maintained at room temperature. Then one of NHPO sample was put into a tube furnace through an ammonia flow at 800 °C for 10h to obtain oxyntride zinc phosphate glass donated as NNHPO. The samples were then mechanically polished to produce a mirror surface and cut into 10\*10\*1 mm wafer.

### **2.2 Experiments of manganese doped phosphate glass containing ANZC**

Phosphate glasses with composition 40ZnO-60P<sub>2</sub>O<sub>5</sub> (mol%) were produced by mixing different inorganic precursors. P<sub>2</sub>O<sub>5</sub> (99.99%, metal basis) or NH<sub>4</sub>H<sub>2</sub>PO<sub>4</sub> (99.99%, metal basis), and ZnO (99.99%, metal basis) were mixed during 30min at room temperature and heated to 450 °C in an alumina crucible in air. The material was maintained at this temperature for 1 h to decompose the phosphorus pentoxide leading to the release of ammonia and water. The material was then heated to temperatures in the range of 1000 °C, and kept at these temperatures for 1 h, for the liquid homogenization. The mixing and heating steps were similar for all glasses, and the melting temperature and time for homogenization were the same. The liquid was stirred, and cast in a heated aluminum mold. Glasses were then annealed at 490 °C for 2 h, and finally cooled to room temperature using the furnace thermal inertia. Glasses were doped with 0.3, 0.6, 1.0, 1.5 and 2 mol% of MnO (99.99%, metal basis). If P<sub>2</sub>O<sub>5</sub> is used as precursor, the atmosphere is oxidative. If NH<sub>4</sub>H<sub>2</sub>PO<sub>4</sub> is used as precursor, the atmosphere will be reductive. The decomposition of NH<sub>4</sub>H<sub>2</sub>PO<sub>4</sub> evolves ammonia and

hydrogen which are responsible for the reductive atmosphere. The glasses prepared by  $P_2O_5$  and the corresponding Mn doped ones are indicated as PO and  $PO_xMn$  ( $x=0.3, 0.6, 1.0, 1.5, 2.0$ ), respectively; the glass prepared by  $NH_4H_2PO_4$  and the corresponding Mn doped ones correspond to NHPO and  $NHPO_xMn$  ( $x=0.3, 0.6, 1.0, 1.5, 2.0$ ), respectively. All samples were cut and polished into  $10 \times 10 \times 2$  mm for further measurements.

### 2.3 Measurements

Phase and crystal structure of the prepared glasses were characterized by the X-ray diffraction measurements (XRD) (D/max 2550 VB/PC Rikagu, Japanese). All measurements carried out at room temperature using Cu  $K\alpha$  radiation ( $\lambda=1.54056\text{\AA}$ ). A step size of  $0.02^\circ(2\theta)$  was used with a scan speed of  $2^\circ/\text{min}$ . The detailed microstructures and chemical compositions were measured by transmission electron microscope (TEM, JEOL JEM 2100F). The obtained samples were transferred onto copper grid for TEM characterization. The photoluminescent (PL) and photoluminescent excitation (PLE) spectra were collected by a high resolution spectrofluorometer (Fluorolog 3-211, Horiba Jobin Yvon Inc., Edison, NJ) using a 450 W Xe-lamp as the excitation source. The color rendering index of glasses was measured in an integrating sphere with a high sensitive spectrometer (Nova, Idea Optics Instruments). Finally, in order to determine the valence state of Mn ions in the host glass, electron paramagnetic resonance (EPR, Germany Bruker A300-10/20, tested in 100K) and the X-ray photoelectron spectroscopy (XPS, Britain Kratos AXIS Supra) analysis is performed. All the measurements were performed at room temperature.

### 3. Results and discussion of ANZC glass

The XRD results of the prepared samples (Fig. 4.1), suggest that all the prepared samples are amorphous.

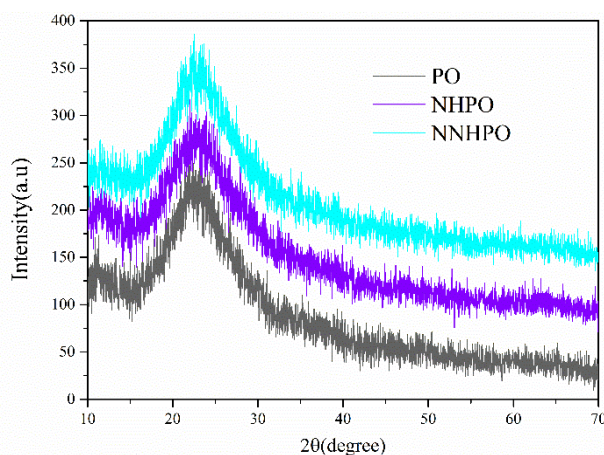


Fig. 4.1. XRD pattern of PO, NHPO and NNHPO samples

Fig. 4.2(a) displays the absorption spectra of the prepared samples. Firstly, it can be seen in the transparency region there is no sign of color centers or other well-shaped absorption bands from impurities. Besides, the absorption edge of PO, NHPO and NNHPO is situated below 300 nm, and with a steep increase of the absorption at 220, 230 and 250 nm.

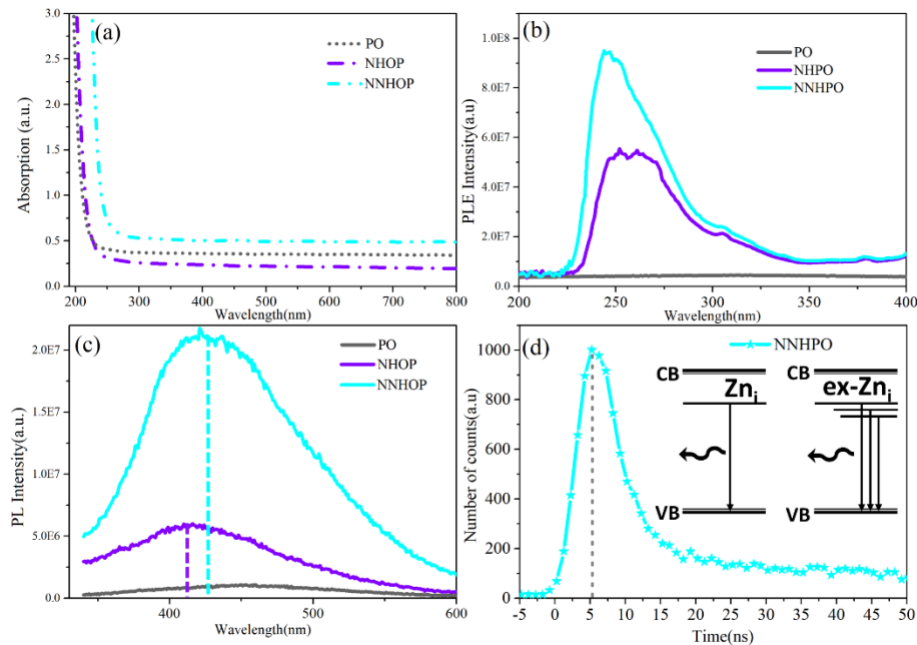


Fig. 4.2. The absorption (a), excitation (b), photoluminescence (c) and spectra of the prepared samples and luminescence decay (d) spectrum of NNHPO

The shifts of the absorption edge are most likely related to the structural rearrangement of the glass. The glass sample NHPO and NNHPO show a broad emission around 420 nm when excited at 250nm, the photoluminescence excitation (PLE) and PL spectra are shown in Fig. 4.1 (b) and (c).

This blue emission was also observed in ZnO nanoshells <sup>27</sup>, ZnO hollow nanoparticles <sup>28</sup> and other emitting amorphous zinc glass <sup>29</sup>. Zeng et al. assigned the violet and blue emission to Zn interstitial-related complex defect ( $Zn_i$ ) in ZnO lattice <sup>30</sup>. The corresponding proposed mechanisms of blue emissions is illustrated in the inset in Fig. 4.2(d). The violet and blue emissions are attributed to the transitions from  $Zn_i$  and extended  $Zn_i$  states to the valence band, respectively. It is worth noting that emission band in NNHPO shows a red shift compare to that in NHPO shown in Fig. 4.2(c). This means more extended  $Zn_i$  states may be formed in NNHPO based on the mechanisms provided above. Fortunately, the results found below suggests that NNHPO does have a higher possibility of forming more considerable extended  $Zn_i$  states than NHPO. On the other hand, another typical behavior of the PL of amorphous ZnO clusters is the short lifetime reaching a nanosecond level <sup>31</sup>. The

photoluminescence decay of NNHPO was measured at 420nm under the nanosecond pulse excitation at 250nm. The superfast emission with the decay time was measured as shown in Fig. 4.2(d). It can be seen that the decay time of NNHPO can reach a nanosecond level. Based on these results, in spite of missing obvious intrinsic UV emission band, it is possible to point out that the blue emission in the prepared glass sample should belong to a certain amorphous ZnO structure. Moreover, the common wide defect-originated emission at 530–600 nm from ZnO is also not obviously observed in the prepared glass samples, which coincides with those reported by Qian et al. 29. The PLE spectrum of NHPO and NNHPO exhibits a peak at about 260 and 246 nm in the deep UV region, which is also similar to that of other emitting amorphous zinc glass 3,4. It is worth noting that NNHPO has a stronger emission than NHPO. To find the reason for the stronger intensity and provide more information about the microstructure of the prepared glass samples, the transmission electron microscopy (TEM) was investigated in Fig. 4.3 and Fig. 4.3(a), (b), (c) displays the TEM images of the PO, NHPO, NNHPO, respectively. As can be seen from Fig. 4.3(a)-(c), some nanoscale aggregation was formed in NHPO and NNHPO sample but was not formed in PO, which is consistent with the luminescence properties of the glass samples. Therefore, it is reasonable to point out that these nanoscale aggregations are ZnO clusters and the TEM images again provide that these ZnO clusters are amorphous. Besides, the size or scale of the ANZC in NNHPO is larger than that of those in NHPO, and this was thought to be the reason for the strong intensity of the blue emission in NNHPO. While, obviously, this more significant ANZC also has a higher possibility of forming more extended  $Zn_i$  states, which causes the red shift of the emission band of NNHPO.

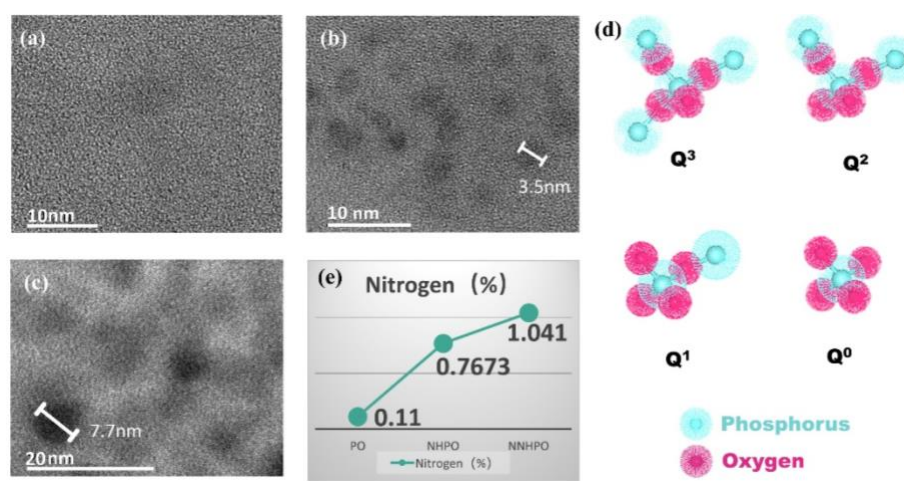


Fig. 4.3. Transmission electron microscopy image of sample PO(a), NHPO(b) and NNHPO(c); (d) phosphate tetrahedral units – oxygen atoms (pink) connected to a phosphorus atoms (blue); (e) nitrogen contents in the prepared glass samples (weight %)

However, the reason why the glass samples have different ANZC phenomena deeply intrigues us. In order to explore this interesting and novel phenomenon, the glass structures must be discussed. The structure of phosphate glasses can be described as a network of phosphate tetrahedra that are linked through covalent bonding of the corner shared oxygen atoms, referred to as bridging oxygen atoms. Oxygen atoms that do not link two phosphate tetrahedra are called non-bridging; the ratio of bridging to non-bridging oxygens depends on the glass composition. Phosphate glasses typically consist of long “polymer like” phosphate chains. The linked phosphate tetrahedra have one, two, three, bridging oxygens. These units can be classified using  $Q_i$  terminology<sup>32</sup>, where  $i$  represents the number of bridging oxygen atoms per tetrahedron, which is shown in Fig. 4.3(d).

The glass transition temperature ( $T_g$ ) is a typical factor of the glass structure, and, normally, the higher  $T_g$ , the more compact is the glass structure. Hence, the glass transition temperature ( $T_g$ ) of the prepared glasses were measured by differential scanning calorimetry (DSC), as shown in Fig. 4.4(a).

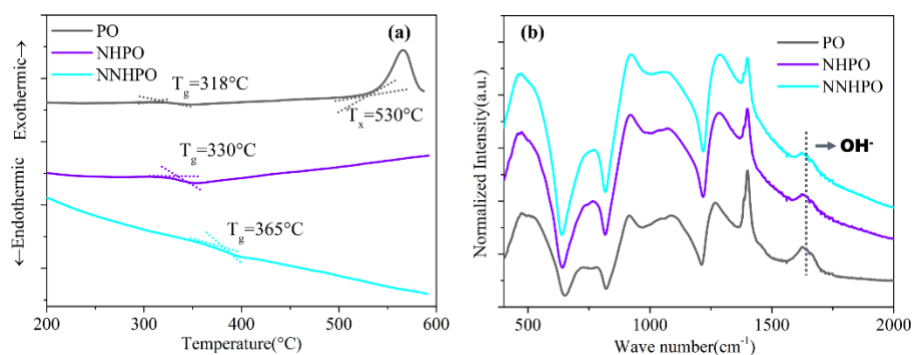
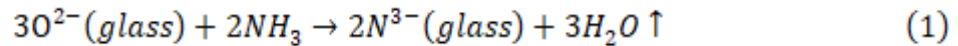


Fig. 4.4. DSC curve (a) and Fourier-Transform Infrared absorbance spectroscopy (b) of the prepared glass samples

It can be seen that the  $T_g$  of PO and NNHPO is the lowest and the highest, respectively. There are two reasons for this. On one hand, hydroxy in glass can depolymerize the phosphate network by forming P-OH bonds and so reducing the  $Q_3$  fraction<sup>33</sup>. From the Fourier-Transform Infrared Spectroscopy (FTIR) shown in Fig 4.4(b), the typical features of the bending vibration of O-H at 1600  $\text{cm}^{-1}$  was observed, and the hydroxy content gradually decreased according to the following sequence PO, NHPO and NNHPO. However, it can be seen that the hydroxy content in NHPO and NNHPO is almost the same but the  $T_g$  of NNHPO is much higher than NHPO. It is also worth noting that the crystallization peak of NHPO and NNHPO disappears between the range of 400-600 °C. Therefore, hydroxy can not be the only interpretation to the increasing  $T_g$  of NNHPO with the nitrogen being the other key reason.

Normally, the nitrogen can be present as  $N^{3-}$  ions which replace the  $O^{2-}$  ions in phosphate melts according to the general reaction 34:



According to this reaction, two  $N^{3-}$  ions replace three  $O^{2-}$  ions and water is a reaction product. From the previous studies 34,35, introducing nitrogen into phosphate glasses network would change some properties of glasses, such as glass transition temperature ( $T_g$ ) and the ability of inhibiting crystallization through compacting and disordering the structure of the glass. On the other hand, the nitrogen content of the prepared glasses was measured by nitrogen elemental analyzer. The results displayed in Fig. 4.3(e) shows that the nitrogen content is clearly related to the increase in  $T_g$  and the ability of inhibiting crystallization. Hence, these findings indicate nitrogen integrates the glass.

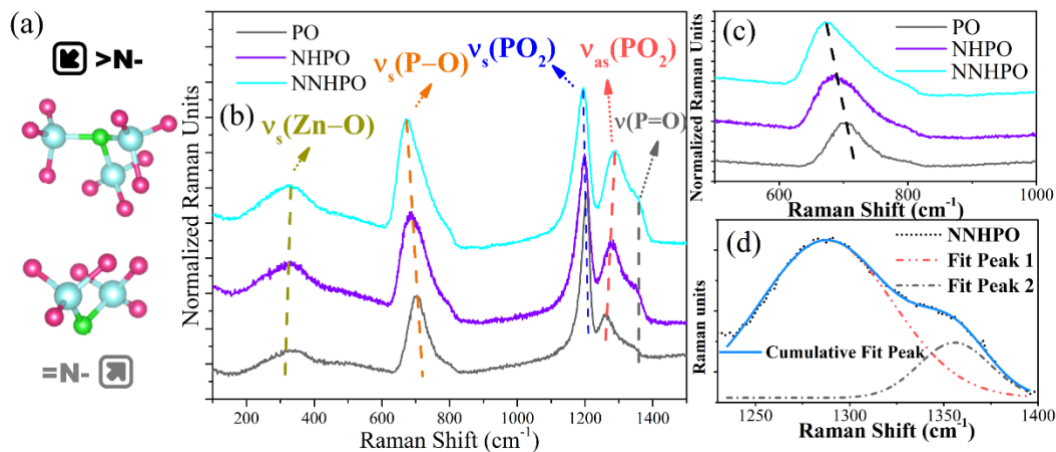


Fig. 4.5 (a) Schematic of the bonding arrangements of nitrogen in phosphate glasses; (b) Raman spectra of PO, NHPO and NNHPO; (c) the peak of  $\nu(P-O)$  of PO, NHPO and NNHPO sample; (d) deconvolution of the raman spectrum peak of NNHPO

Previous work suggests that nitrogen can be present as either  $=N^-$  or  $>N^-$  in phosphate glass, as shown in Fig. 4a 36,37. Normally, nitrogen replaces the BO and NBO at random without preference, and the non-bridging oxygens ( $P-O$ ) associated with the modifying cations remain unchanged, maintaining a concentration sufficient to charge-compensate the modifying cations 34. Raman spectroscopy was used to study the structures of the prepared phosphate glasses. Fig. 4.5(b) shows normalized Raman spectrum of the prepared samples. The large band around  $700\text{ cm}^{-1}$  is attributed to the symmetric stretching mode of bridging oxygen between two  $Q_2$  tetrahedra,  $(POP)_{\text{sym}}$  38. Notably, as shown in Fig. 4.5(c), the peak of NHPO and NNHPO, at  $684$  and  $670\text{ cm}^{-1}$ , respectively, is different from that of PO, at  $705\text{ cm}^{-1}$ . Besides, both the full width at half maximum (FWHM) and cross-section of the peak shows

the trend NNHPO > NHPO > PO. Since the bands near  $650\text{ cm}^{-1}$  can be assigned to  $>N^-$  <sup>34</sup>, it is reasonable to attribute the difference among the  $(PO_2)_{\text{sym}}$  peak of the glass samples to  $>N^-$ , which indicates a good correlation between DSC and nitrogen content analysis. However, from the Raman spectrum, only  $>N^-$  was obviously observed, which means most of the nitrogen in NHPO and NNHPO are present as  $>N^-$ . All the samples show the most intense signal at  $1207\text{ cm}^{-1}$  which is attributed to the symmetric stretching of the P–O non-bridging oxygens on  $Q_2$  phosphate tetrahedra,  $(PO_2)_{\text{sym}}$ . The  $1260\text{ cm}^{-1}$  peak, a shoulder of the  $1207\text{ cm}^{-1}$  peak, corresponds to the asymmetric stretching of P–O non-bridging oxygen atoms,  $(PO_2)_{\text{asym}}$ . It was found that the NNHPO has the highest  $(PO_2)_{\text{asym}}$  peak, which suggests NNHPO has a more asymmetric glass structure. At the same time, it should be pointed out that both NHPO and NNHPO samples have another shoulder at  $1260\text{ cm}^{-1}$  and the peak was decomposed to define the structure. The deconvoluted peak around  $1355\text{ cm}^{-1}$  should belong to vibration of (P=O), which is shown in Fig 4.5(d). It can be explained by the fact that the hydroxy content decreases and the glass has more  $Q_3$  fraction strengthening the glass matrix. It is interesting to notice that the  $330\text{ cm}^{-1}$  peak assigned to  $\nu(\text{Zn-O})$  gradually increases with the more asymmetric and compact glass structure, and this can be explained by the topological constraints theory <sup>39</sup>.

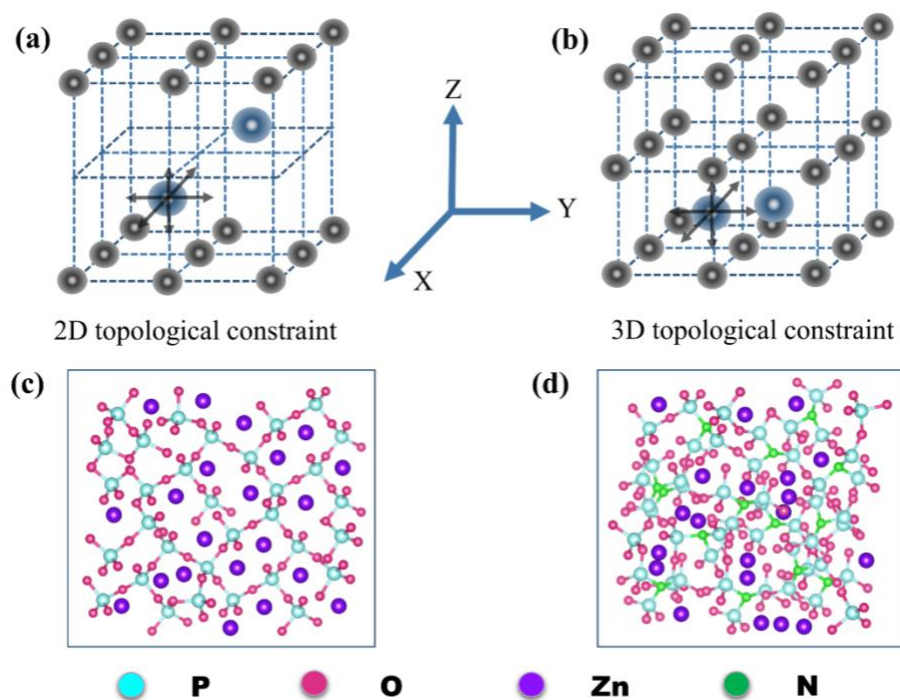


Fig. 4.6. Schematic illustration showing the level of difficulty of clusters evolution of ZnO in 2D(a) and 3D(b) structured sublattices. Schematic of mesostructure of PO(c) and NNHPO(d)

Normally, the phosphate chain and ring anions are linked by bonds between various modifying metal cations and the non-bridging oxygen; these bonds are more ionic in nature.



According to the structural model proposed for ultraphosphate glasses by Hoppe<sup>40</sup>, the bonding arrangements of modifier ions in the ultraphosphate glasses would be dependent on the number of terminal oxygen available to coordinate modifier ions  $R_{v+}$ , where  $v$  is the ion valence. Such cations will have coordination numbers ( $CN_R$ ) similar to those found in appropriate crystalline phases. For glasses with the stoichiometry  $x(R_{2/v}O)(1-x)P_2O_5$ , the number of terminal oxygens per modifying ion is

$$M_{TO} = v(1/x). \quad (2)$$

When  $M_{TO} > CN_R$ , the ions exist as isolated coordination polyhedra within the phosphate network; when  $M_{TO} < CN_R$ , the ions coordination polyhedra exist as bridges between neighboring  $Q_2$  through sharing corners and edges. A number of researchers found the coordination numbers of Zn in ultraphosphate glasses decrease from 6 to 4 for  $x=0.33$  to 0.5, which means ZnO has two bonding arrangements in the prepared glasses ( $M_{TO}=5$ ), namely isolated ZnO tetrahedron within phosphate network and ZnO octahedron as bridges between neighboring  $Q_2$  through sharing corners and edges. In PO, the existence of large amounts of hydroxy groups depolymerize the phosphate network by forming P-OH leading  $Zn^{2+}$  to have more “free oxygen” to form ZnO tetrahedron. Although ZnO tetrahedron can also enter the glass network, the glass matrix of PO moves towards two-dimensional (2D) “polymer like” chain and these chains hardly have cross-links with each other. From the schematic illustration of 2D sublattices shown in Fig 4.6(a), it can be seen in this topological configuration that the ZnO polyhedra are easy to move on the X and Y direction and the only topological constraint is in Z direction. Fig 4.6(c) shows the schematic illustration of the corresponding glass mesostructure, “polymer like” chains without cross-links. Normally, a topological configuration with just one direction constraint is not easy to form an aggregation. While, in NHPO and NNHPO, “free oxygen” content was decreased because of less hydroxy group and especially the adding of nitrogen, which may separate some ZnO tetrahedron from glass network and sever as ZnO octahedron glass modifier. Moreover, the nitrogen also constructs the glass matrix from 2D “polymer like” chains to three-dimensional (3D) framework structure through forming  $>N-$  entities that may cause cross-links between glass chains or layers. The illustration of sublattices shown in Fig 4.6(b) displays that, in this topological configuration, the ZnO polyhedra are hard to move on no matter the X, Y or Z direction. The schematic of the corresponding glass mesostructure with cross-links caused by  $>N-$  entities is shown in Fig 4.6(d). This 3D topological configuration with 3 directions constraints would “extrude” the ZnO polyhedra glass modifier forming ZnO clusters within

limits. Besides, within a certain scope, the greater  $>N-$  level in glass, the more asymmetric and compact the glass structure would be. Therefore, NNHPO is easier to form more extensive ANZC than NHPO, which illustrates the stronger PL in NNHPO.

#### 4. Results and discussion of manganese doped ANZC glass

EPR spectra of Mn doped phosphate glasses (PO2Mn and NHPO2Mn, see in experimental part) are shown in Fig. 4.7(a), revealing the typical fingerprint of  $Mn^{2+}$  which comprises a sextet hyperfine line structure (no resonance was observed in undoped glasses).<sup>41,42</sup> The electronic structure of  $Mn^{2+}$  ( $3d^5$ ) is well known and the Tanabe–Sugano diagrams of a  $d^5$ -electron configuration is shown in Fig 4.7(b). Combining the optical excitation spectra of the zinc phosphate glasses shown in Fig 4.7(c), it can be found that the ground state is  ${}^6A_1(S)$ ; two obvious transitions can readily be identified in the optical excitation spectra of PO glass, peaking at 346 nm and 405 nm, respectively; three obvious transitions can readily be identified in the optical excitation spectra of NHPO glass, peaking at 250 nm, 346 nm, 405 nm, respectively.

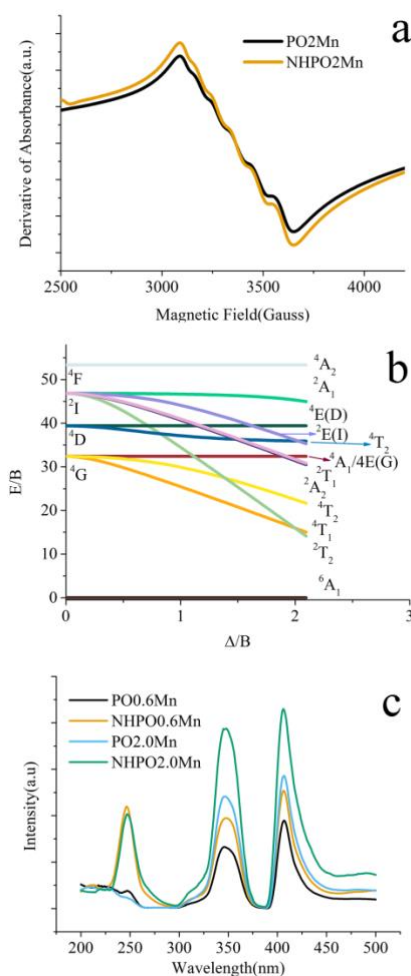


Fig. 4.7. EPR spectra of PO<sub>2</sub>Mn and NHPO<sub>2</sub>Mn glass samples (a), Tanabe–Sugano diagrams for a d<sup>5</sup>-electron configuration (b) and excitation spectra of Mn doped glass samples(c)

The peak of 346 and 405 nm correspond to the transitions  ${}^6A_1(S) \rightarrow {}^4E(D)$  and  ${}^6A_1(S) \rightarrow {}^4A_1(G)$ , respectively; The peak around 250 nm of NHPO<sub>2</sub>Mn is due to the charge transfer which was investigated in previous part. Evaluation of crystal field parameters from the bands in the electronic spectra yields a crystal field parameter  $D_q = 1054 \text{ cm}^{-1}$ , Racah parameter  $B = 775 \text{ cm}^{-1}$  and consequently  $D_q/B = 1.36$ .

Normally, the color of the manganese doped glass is dependent on the valence state of the manganese ions in the glass: pale yellow when Mn<sup>2+</sup> is present and violet when Mn<sup>3+</sup> is present. Noteworthy, with increasing manganese content, the PO samples exhibit increasing violet coloration which indicates that Mn<sup>3+</sup> also exist in the PO glass matrix. In order to confirm this point, the absorption spectra of PO<sub>2</sub>Mn and NHPO<sub>2</sub>Mn were investigated as shown in Fig. 4.8(a). It can be seen that a broad band around 540 nm can be only observed in PO<sub>2</sub>Mn, which corresponds to the  ${}^5E_g \rightarrow {}^5T_{2g}$  transition of Mn<sup>3+</sup>, which has a 3d<sup>4</sup>-electron configuration shown in the inset of Fig 4.8(a). Due to this spin-allowed transition, the intensity of this peak is even stronger than those of Mn<sup>2+</sup> which are spin-forbidden. The XPS spectra illustrated in Fig 4.8(b) again supports this finding. It can be seen that the binding energy value of Mn 2p<sub>3/2</sub> of PO<sub>2</sub>Mn (642.2 eV) is larger than that of NHPO<sub>2</sub>Mn (641.3 eV), which suggests the chemical state of Mn in PO<sub>2</sub>Mn is higher than that in NHPO<sub>2</sub>Mn.<sup>43-45</sup>

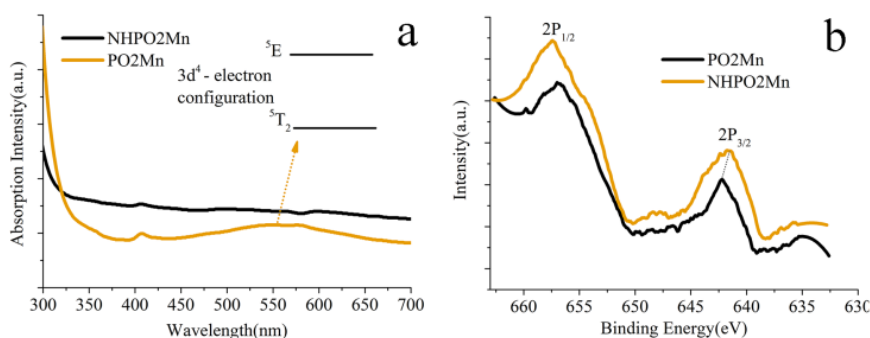


Fig. 4.8. Absorption (a) and XPS (b) spectra of PO<sub>2</sub>Mn and NHPO<sub>2</sub>Mn glass samples

The PL spectrum of Mn<sup>2+</sup> is deemed to be the contribution of two main components: emission from isolated Mn<sup>2+</sup> ions; emission from Mn<sup>2+</sup> ion pairs.<sup>20,46</sup> However, a much debated question is, before concentration quenching, whether the energy migration happened between Mn<sup>2+</sup> and Mn<sup>2+</sup> pairs.<sup>47,48</sup> On one hand, in Ref.47, the nonexponential decay curves of the Mn<sup>2+</sup> in Zn<sub>2</sub>SiO<sub>4</sub>:Mn<sup>2+</sup> were fitted by the Yokota-Tanimoto model for luminescence decay in the presence of diffusion limited energy migration to traps. Good fits were obtained and

information was derived from the fitting parameters. The model describes the luminescence decay of donor ions in the case of (isotropic) diffusion limited energy migration to (deep) traps. The schematic representation of this model is given in Fig. 4.9(e). On the other hand, in Ref. 48, although only the luminescence decay curves of low concentration  $Mn^{2+}$ -doped  $MgAl_2O_4$  was fitted to the exponential model, the authors think the emission comes from the exchange coupling for antiferromagnetic exchange-coupled  $Mn^{2+}$  pairs. This exchange-coupled  $Mn^{2+}$  pairs will form new splitting energy levels which contain one spin-allowed transition. For example, Fig. 4.9 (f) shows the schematic representation of the splitting pattern for a  $Mn^{2+}$  pair with both ions in the ground state and one ion in the excited state, the interaction has been taken as an antiferromagnetic interaction for both the  ${}^6A_1$ - ${}^6A_1$  ground state and the  ${}^6A_1$  -  ${}^4T_1$  excited state. The value of  $J$  is dependent on the distance between ions in the pairs. Emissions originating from the pairs can be attributed to transitions from the lowest excited spin state to different spin components of the ground state. The details were reviewed in Ref. 28. However, due to the intricate coordination environment of  $Mn^{2+}$  pairs, it is too difficult to investigate the model only by dynamic luminescence behavior.<sup>47,48</sup> Here, we try investigating this debated question based on static luminescence analysis through  $Mn^{3+}$  as an “energy acquisition probe”.

Glass samples were optically excited in the region of the main absorption peaks (410nm). The PL spectrum and the corresponding cumulative fit peak of the prepared glass samples are shown in Fig. 4.9 (a)-(c). From Fig. 4.9(a), it can be seen that the emission intensity of NHPO samples is stronger than PO, which can be explained by the concentration of  $Mn^{2+}$  supported by the XPS. The cumulative fitting peaks of NHPO2Mn and PO2Mn are shown in Fig. 4.8(b) and (c). Here, the peak around 575 nm and the peak around 630 nm are attributed to  $Mn^{2+}$  isolate ions and  $Mn^{2+}$  pairs, respectively. It obviously indicates that the emission of  $Mn^{2+}$  pairs is stronger than that of  $Mn^{2+}$  isolate ions in NHPO2Mn. However, it is the opposite in PO2Mn, which means the amount of  $Mn^{2+}$  pairs are less than  $Mn^{2+}$  isolate ions in PO2Mn. This can be explained by the existence of  $Mn^{3+}$  which could inhibit the formation of  $Mn^{2+}$  pairs, the interpretation illustration is shown in Fig. 4.8 (d).

In our experiment, although the crystal field on the position of the energy levels for 3d<sub>5</sub> transition metal  $Mn^{2+}$  is a bit different from that in the previous study,<sup>27,28</sup> the  $Mn^{2+}$  is still in the high spin state which was calculated above that is suitable to the two models. Therefore, the corresponding model can be adopted in our glass samples. Firstly, we suppose the excited donor ions in the case of isotropic diffusion to traps. Then, as an example, the transition process in PO2Mn sample is discussed here. As shown in Fig. 4.8(e), the energy should

diffuse isotropically. Therefore, there are three possible transition traps:  $Mn^{2+}$  isolate ions,  $Mn^{2+}$  pairs and  $Mn^{3+}$  isolate ions. As we mentioned above, the  $Mn^{3+}$  isolate ion has a spin-allowed transition around 540 nm. Considering the emission of  $Mn^{2+}$  isolate ions peaked at 575 nm, the radiative energy transition process between  $Mn^{2+}$  and  $Mn^{3+}$  is hardly possible, which means the only energy transfer process between  $Mn^{2+}$  and  $Mn^{3+}$  is energy diffusion. It suggests that if the donor was trapped by  $Mn^{3+}$ , the emission around 540 nm should be observed and the luminescence decay curve with shorter lifetime should be observed as well. However, as shown in Fig. 4.8 (b) and (c), no obvious emission peak around 540 nm and shorter lifetime is observed from PO2Mn sample. Thus, although the nonexponential decay curves with a good fit was obtained in Ref. 47, the isotropic energy diffusion model is not reliable. In the exchange-coupled model,<sup>28</sup> emissions originating from the pairs can be attributed to transitions from the lowest excited spin state to different spin components of the ground state, which can explain our results very well.

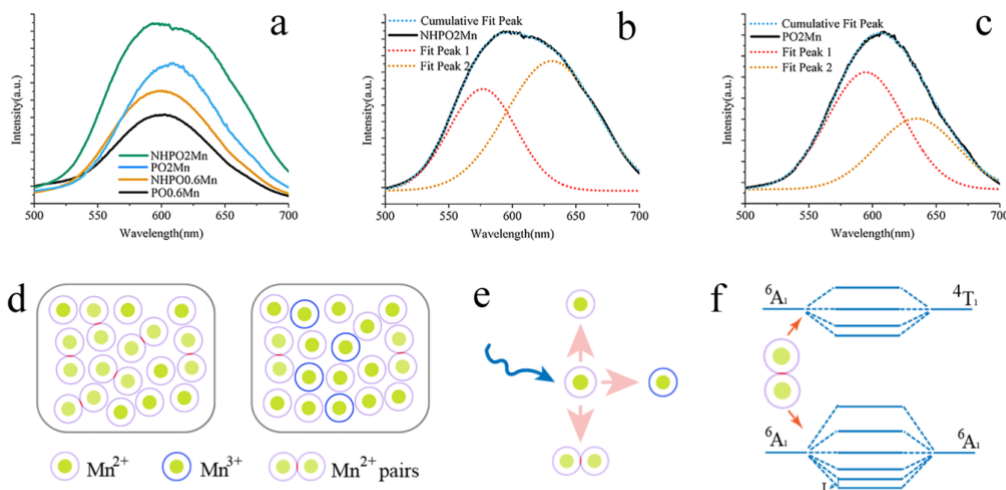


Fig. 4.9. Photoluminescence spectra of Mn doped glass samples excited by 410nm(a); deconvolution of the PL spectrum of NHPO2Mn (b) and PO2Mn (c); (d) schematic illustration of formation of  $Mn^{2+}$  pairs in the glass matrix, energy diffusion model(e) and (f)the splitting for energy levels in  ${}^6A_1 - {}^6A_1$  ground state and  ${}^6A_1 - 4T_1$  state resulting from exchange coupling for antiferromagnetic exchange-coupled  $Mn^{2+}$  pairs

Fig. 4.10 (a) presents a pc-WLED based on the prepared glass and (b) PL of  $Mn^{2+}$  single doped NHPO glass samples excited by 250 nm. From Fig. 4.7(c), it can be seen that the most efficient excitation spectrum is around 410 nm, fortunately, which is exactly the emission wavelength emitted by the zinc phosphate oxynitride glass that was described previously. Therefore, it is possible to prepare a pc-WLED based on the efficient energy transfer process, which schematic of is shown in Fig. 4.10 (a). Fig. 4.10 (b) shows the PL of the samples excited at 250 nm. Obviously, the energy transfer between the amorphous ZnO and  $Mn^{2+}$  ions

occurred. Besides, it can be found that the intensity of the luminescence of Mn increase with the increasing Mn concentration.

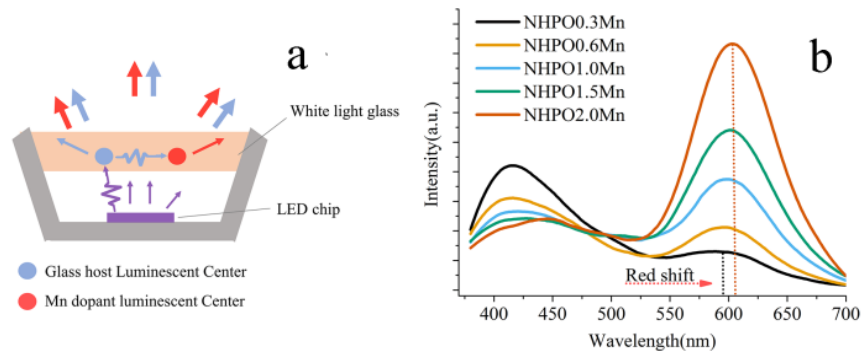


Fig. 4.10. (a) Schematic of a pc-WLED based on the prepared glass and (b) PL of  $Mn^{2+}$  single doped NHPO glass samples excited by 250 nm

On the contrary, the intensity of the blue emission of the glass host decrease with the increasing Mn concentration. This is explained by the fact that, with more  $Mn^{2+}$  ions, the glass host transfer more energy to  $Mn^{2+}$  ions. Furthermore, as shown in Fig. 4.10(b), if spectrum of low  $Mn^{2+}$  concentration are compared to the ones of high  $Mn^{2+}$  concentration, a “red shift” is observed, explained by the increasing amount of  $Mn^{2+}$  pairs discussed above.

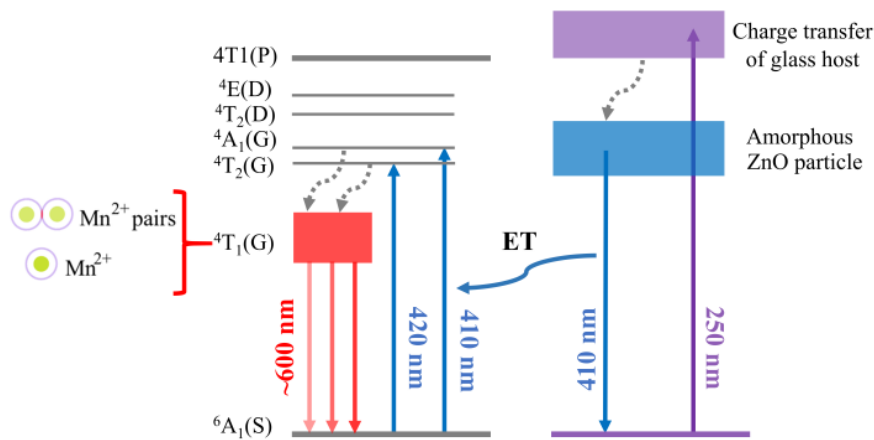


Fig. 4.11. Schematic of brief energy level diagram of  $Mn^{2+}$  single doped NHPO glass samples

The details of the energy transfer process can be described below and the energy transfer diagram is shown in Fig. 4.11. On one hand, energy transfer from glass host to  $Mn^{2+}$  ions can easily occur via the excited state of amorphous ZnO nanoparticle in the glass which is energetically close to the  ${}^4T_2(G)$  and  ${}^4A_1(G)$  level of  $Mn^{2+}$  ions, resulting in populating the  $Mn^{2+}$  excited state  ${}^4T_2(G)$  and  ${}^4A_1(G)$  from the ground state.  $Mn^{2+}$  ions then undergo multiphonon relaxation to the emitting level  ${}^4T_1(G)$  followed by radiative relaxation to the ground state, emitting at 600 nm. As we discussed above, the  $Mn^{2+}$  pairs also contribute to the

emission, so it can be seen from the inset of Fig 4.11, actually, the  $4T_1(G)$  level consists of not only the level of isolate  $Mn^{2+}$  ions, but also the level of exchange-coupled  $Mn^{2+}$  pairs.

Table 4-1. CIE coordinates and color temperature of  $Mn^{2+}$  doped zinc phosphate oxynitride glass

Glass	CIE coordinates		Color temperature(K)
	X	Y	
NHPO0.3Mn	0.25	0.23	>10000
NHPO0.6Mn	0.31	0.27	8000
NHPO1.0Mn	0.37	0.33	3998
NHPO1.5Mn	0.41	0.35	3000
NHPO2.0Mn	0.44	0.36	2500

The CIE (Commission International de l'éclairage) chromaticity coordinates for the prepared glass samples  $NHPO_xMn$  ( $x=0.3, 0.6, 1.0, 1.5$  and  $2.0$ ) which were calculated based on the corresponding emission spectrum are represented in Fig. 4.12. Besides, details and the correlated temperature are listed in Table 4-1.

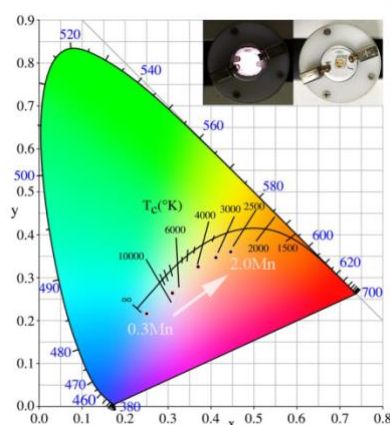


Fig. 4.12. CIE chromaticity diagrams of the  $Mn^{2+}$  single doped NHPO glass samples; inset: the photograph of the encapsulated WLED based on NHPO1.5Mn glass sample, turn on (left) and turn off (right)

The NHPO1.0Mn sample shows CIE values with  $x=0.37$ ,  $y=0.33$ , which is matching to that expected for a pure white light emitting material. Furthermore, the “Color Temperature” was found to be 3998 K, which is expected for a warm white light source. Besides, a high external quantum efficiency (1%) is obtained. Moreover, the encapsulated WLEDs based on the prepared glasses were prepared as well. Although due to the larger excitation wavelength of the violet chip (276 nm) than the best excitation wavelength, the result still deserves expectation. The encapsulated pc-WLED based on NHPO1.5Mn glass presented in the inset of Fig. 4.12 shows: CIE values with  $x=0.33$ ,  $y=0.35$ ; CCT with 5228 K;  $R_a=86$ . These

excellent properties make the prepared glass promising for the warm WLEDs with a proper ultraviolet chip.

## 5. Conclusions

To the best of our knowledge, a strong superfast blue emission was observed in simple zinc phosphate oxynitride glass for the first time. According to the PL and luminescence decay spectrum, the emission was assigned to amorphous nanoscale ZnO clusters which was validated by TEM images in the prepared glass samples. Nitrogen integrating the glass network is the key to obtaining these amorphous nanoscale ZnO clusters. Nitrogen modulates the topological constraints of the glass matrix from 2D to 3D through >N- cross-linking the phosphate glass chains. The 3D topological constraints forms more extensive amorphous nanoscale ZnO clusters, which illustrates a stronger PL.

Based on this glass, the magnesium single doped zinc phosphate oxynitride glasses with warm white light were prepared. EPR and XPS suggest manganese is existence as  $Mn^{2+}/Mn^{3+}$  in PO glasses samples and as single  $Mn^{2+}$  in NHPO glasses. The mechanism of the emission from  $Mn^{2+}$  pairs was investigated based on static luminescence analysis through  $Mn^{3+}$  as a “energy acquisition probe”. The result asserts that the emission comes from the exchange-coupled effect.<sup>48</sup> Among the prepared glasses, the NHPO1.0Mn sample shows CIE values with  $x=0.37$ ,  $y=0.33$ , which is matching to that expected for a pure white light emitting material. Further the “Color Temperature” was found to be 3998 K which is expected for a warm white light source. Moreover, the encapsulated pc-WLED based on 276 nm violet chip shows excellent CIE values with  $x=0.33$ ,  $y=0.35$ ; CCT with 5228 K;  $R_a=86$ . Although the CCT is higher than that of 250 nm excitation, it is deserving expectation that, with a proper violet chip, a pc-WLED with high CRI, low CCT and relative high quantum efficiency can be obtained based on this manganese single doped phosphate glass containing ANZC.



**REFERENCES**

- 1 Masai, H. *et al.* White light emission of Mn-doped SnO-ZnO-P<sub>2</sub>O<sub>5</sub> glass containing no rare earth cation. *Optics letters* **36**, 2868-2870 (2011).
- 2 Luo, Q., Qiao, X., Fan, X. & Zhang, X. Near-infrared emission of Yb<sup>3+</sup> through energy transfer from ZnO to Yb<sup>3+</sup> in glass ceramic containing ZnO nanocrystals. *Optics letters* **36**, 2767-2769 (2011).
- 3 Chen, G. *et al.* Photoluminescent properties of nanocrystallized zinc borosilicate glasses. *Radiation measurements* **38**, 771-774 (2004).
- 4 Nikl, M. *et al.* Photoluminescence of ZnO-aggregates in oxide glasses. *Optical Materials* **29**, 552-555 (2007).
- 5 Zhou, H. *et al.* Behind the weak excitonic emission of ZnO quantum dots: ZnO/Zn(OH)<sub>2</sub> core-shell structure. *Applied physics letters* **80**, 210-212 (2002).
- 6 Alekseeva, I., Dymshits, O., Zhilin, A., Zapalova, S. & Shemchuk, D. Transparent glass-ceramics based on ZnO and ZnO:Co<sup>2+</sup> nanocrystals. *Journal of Optical Technology* **81**, 723-728 (2014).
- 7 Masai, H., Toda, T., Ueno, T., Takahashi, Y. & Fujiwara, T. ZnO glass-ceramics: An alternative way to produce semiconductor materials. *Applied Physics Letters* **94**, 151908 (2009).
- 8 Qian, G. *et al.* Photoluminescent properties and Raman spectra of ZnO-based scintillating glasses. *Journal of Non-Crystalline Solids* **354**, 4626-4629 (2008).
- 9 Xie, R.-J. & Hirosaki, N. Silicon-based oxynitride and nitride phosphors for white LEDs—A review. *Science and technology of Advanced Materials* **8**, 588 (2007).
- 10 Ye, S., Xiao, F., Pan, Y., Ma, Y. & Zhang, Q. Phosphors in phosphor-converted white light-emitting diodes: Recent advances in materials, techniques and properties. *Materials Science and Engineering: R: Reports* **71**, 1-34 (2010).
- 11 Cho, J., Park, J. H., Kim, J. K. & Schubert, E. F. White light-emitting diodes: history, progress, and future. *Laser & photonics reviews* **11**, 1600147 (2017).
- 12 Smet, P. F. & Joos, J. J. White light-emitting diodes: Stabilizing colour and intensity. *Nature materials* **16**, 500 (2017).
- 13 Krames, M. R. *et al.* Status and future of high-power light-emitting diodes for solid-state lighting. *Journal of display technology* **3**, 160-175 (2007).
- 14 Gouveia-Neto, A. *et al.* White light generation by frequency upconversion in Tm<sup>3+</sup>/Ho<sup>3+</sup>/Yb<sup>3+</sup>-codoped fluorolead germanate glass. *Applied Physics Letters* **91**,

- 091114 (2007).
- 15 Argyraki, A., Clemmensen, L. K. H. & Petersen, P. M. Does correlated color temperature affect the ability of humans to identify veins? *J Opt Soc Am A Opt Image Sci Vis* **33**, 141-148 (2017).
  - 16 Daicho, H., Enomoto, K., Sawa, H., Matsuishi, S. & Hosono, H. Improved color uniformity in white light-emitting diodes using newly developed phosphors. *Optics express* **26**, 24784-24791 (2018).
  - 17 Yang, W. J. & Chen, T. M. White-light generation and energy transfer in SrZn<sub>2</sub>(PO<sub>4</sub>)<sub>2</sub>:Eu, Mn phosphor for ultraviolet light-emitting diodes. *Applied Physics Letters* **88**, 2786 (2006).
  - 18 Shimada, J. & Kawakami, Y. Medical lighting composed of LED arrays for surgical operation. *Proceedings of SPIE - The International Society for Optical Engineering* **4278**, 165-172 (2001).
  - 19 Zhu, H. *et al.* Highly efficient non-rare-earth red emitting phosphor for warm white light-emitting diodes. *Nature communications* **5**, 4312 (2014).
  - 20 Ning, D., Mingying, P., Sebastian, K. & Lothar, W. Intense red photoluminescence from Mn<sup>2+</sup>-doped (Na<sup>+</sup>; Zn<sup>2+</sup>) sulfophosphate glasses and glass ceramics as LED converters. *Optics Express* **18**, 2549-2557 (2010).
  - 21 Hai, G., Xiaofeng, W., Jindeng, C. & Fang, L. Ultraviolet light induced white light emission in Ag and Eu<sup>3+</sup> co-doped oxyfluoride glasses. *Optics Express* **18**, 18900-18905 (2010).
  - 22 Heeger, A. J. Light emission from semiconducting polymers: Light-emitting diodes, light-emitting electrochemical cells, lasers and white light for the future. *Solid State Communications* **107**, 673-679 (1998).
  - 23 Jayasimhadri, M. *et al.* White light generation from Dy<sup>3+</sup>-doped ZnO–B<sub>2</sub>O<sub>3</sub>–P<sub>2</sub>O<sub>5</sub> glasses. *Journal of Applied Physics* **106**, 031102 (2009).
  - 24 ANDRADE *et al.* Tunable light emission and similarities with garnet structure of Ce-doped LSCAS glass for white-light devices. *Journal of Alloys & Compounds* **510**, 54-59 (2012).
  - 25 Ye, R. *et al.* Eu<sup>2+</sup> /Dy<sup>3+</sup> co-doped white light emission glass ceramics under UV light excitation. *Journal of Non-Crystalline Solids* **357**, 2282-2285 (2011).
  - 26 Cemmi, A. *et al.* Enhanced and shortened Mn<sup>2+</sup> emissions by Cu<sup>+</sup> co-doping in borosilicate glasses for W-LEDs. *Optical Materials Express* **5**, 51 (2015).
  - 27 Zeng, H., Li, Z., Cai, W. & Liu, P. Strong localization effect in temperature

- dependence of violet-blue emission from ZnO nanoshells. *Journal of Applied Physics* **102**, 104304-104307 (2007).
- 28 Zeng, H. *et al.* ZnO-based hollow nanoparticles by selective etching: elimination and reconstruction of metal-semiconductor interface, improvement of blue emission and photocatalysis. *Acs Nano* **2**, 1661 (2008).
- 29 Qian, G., Liang, X., Bei, J., Yuan, S. & Chen, G. Photoluminescence Properties of Zinc Oxide in Barium and Fluorine Silicate Glasses. *Journal of the American Ceramic Society* **90**, 1255-1257 (2007).
- 30 Zeng, H. *et al.* Blue Luminescence of ZnO Nanoparticles Based on Non-Equilibrium Processes: Defect Origins and Emission Controls. *Advanced Functional Materials* **20**, 561-572 (2010).
- 31 Zou, B. S., Volkov, V. V. & Wang, Z. L. ChemInform Abstract: Optical Properties of Amorphous ZnO, CdO, and PbO Nanoclusters in Solution. *Cheminform* **31**, 3037-3043 (2010).
- 32 Brow, R. K. the structure of simple phosphate glasses. *Journal of Non-Crystalline Solids* **263**, 1-28 (2000).
- 33 Brow, R. K., Tallant, D. R., Hudgens, J. J., Martin, S. W. & Irwin, A. D. The short-range structure of sodium ultraphosphate glasses. *Journal of non-crystalline solids* **177**, 221-228 (1994).
- 34 Bunker, B. C., Tallant, D. R., Balfe, C. A., Kirkpatrick, R. J. & Reidmeyer, M. R. Structure of Phosphorus Oxynitride Glasses. *Journal of the American Ceramic Society* **70**, 675-681 (2010).
- 35 Changwen, W. & Ling, L. Properties and structure of nitrogen-doped phosphate glasses. *Journal of Non-Crystalline Solids* **112**, 296-301 (1989).
- 36 Day, D. E. Structural role of nitrogen in phosphate glasses. *Journal of Non-Crystalline Solids* **112**, 7-14 (1989).
- 37 Reidmeyer, M. R. & Day, D. E. Phosphorus oxynitride glasses. *Journal of Non-Crystalline Solids* **181**, 201-214 (1995).
- 38 Meyer, K. Characterization of the structure of binary zinc ultraphosphate glasses by infrared and Raman spectroscopy. *Journal of Non-Crystalline Solids* **209**, 227-239 (1997).
- 39 Zhou, S. *et al.* Topological Engineering of Glass for Modulating Chemical State of Dopants. *Advanced Materials* **26**, 7966-7972 (2014).
- 40 Hoppe, U. A structural model for phosphate glasses. *Journal of Non-Crystalline Solids*

- 195**, 138-147 (1996).
- 41 Venkatasubbaiah, A., Rao, J. L., Lakshman, S. V. J. & Sreedhar, B. Electron paramagnetic resonance and optical absorption spectra of manganese(II) ions in lead acetate glasses. *Polyhedron* **12**, 1539–1543 (1993).
- 42 Qiu, J. R. *et al.* Space-selective valence state manipulation of transition metal ions inside glasses by a femtosecond laser. *Applied Physics Letters* **79**, 3567-3569 (2001).
- 43 Moses, E. R., A *et al.* XRD and XPS characterization of mixed valence Mn<sub>3</sub>O<sub>4</sub> hausmannite thin films prepared by chemical spray pyrolysis technique. *Applied Surface Science* **256**, 2920-2926 (2010).
- 44 Castro, V. D. & Polzonetti, G. XPS study of MnO oxidation. *Journal of Electron Spectroscopy & Related Phenomena* **48**, 117-123 (1989).
- 45 Beyreuther, E., Thiele, C. & Dörr, K. XPS investigation of Mn valence in lanthanum manganite thin films under variation of oxygen content. *Journal of Virology* **81**, 10123 (2006).
- 46 Ronda, C. R. & Amrein, T. Evidence for exchange-induced luminescence in Zn<sub>2</sub>SiO<sub>4</sub> : Mn. *Journal of Luminescence* **69**, 245-248 (1996).
- 47 Barthou, C., Benoit, J., Benalloul, P. & Morell, A. Mn<sup>2+</sup> concentration effect on the optical properties of Zn<sub>2</sub>SiO<sub>4</sub>: Mn phosphors. *Journal of the Electrochemical Society* **141**, 524-528 (1994).
- 48 Vink, A., De Bruin, M., Roke, S., Peijzel, P. & Meijerink, A. Luminescence of exchange coupled pairs of transition metal ions. *Journal of the Electrochemical Society* **148**, E313-E320 (2001).



## GENERAL CONCLUSIONS

In this work, our main objective is to develop a new LEC device based on organophosphorus semiconductor doped inorganic glass electrolyte, which cannot be synthesized by using classic melt-quenching technique. Thus, sol-gel and SPS technology was used to prepare the organophosphorus doped hybrid glass.

In the case of sol-gel method, the organophosphorus semiconductor doped silica glass coating was successfully prepared. However, some voids were generated in the silicate glass coating containing high lithium content which has the applicable ionic conductivity for a LEC. Fortunately, the probably reason for generation of the voids was found. We will work on vanishing the voids in the silicate glass coating containing high lithium content. After obtaining the silicate glass coating containing high lithium content, the LEC device can be prepared based on this coating.

In the case of SPS technology, the hybrid glass has been successfully prepared. The optical properties, microstructure and electrochemical properties of the hybrid glass were investigated. The results show this hybrid glass can be used in a LEC, and thereby the LEC device based on the hybrid glass was prepared as well. However, no electroluminescence was observed from the hybrid glass sample. This may be due to the reasons as shown below: 1. the glass thickness is still too large; 2. the surface contact between glass and electrodes are not perfect; 3. the ionic conductivity is still too low; 4. impurities are introduced by SPS process. In the next step, all of these possible problems would be tackled to test the electroluminescence of the hybrid glass.

During the process of preparing phosphate glass for LECs, blue luminescence was observed from amorphous zinc binary phosphate glasses in our work. We find that this blue luminescence is from the amorphous nanoscale zinc clusters in the glass. Nitrogen modulates the topological constraints of the glass matrix from 2D to 3D through >N- cross-linking the phosphate glass chains. The 3D topological constraints forms more extensive amorphous nanoscale ZnO clusters, which illustrates a stronger PL. After understanding the reason for the blue luminescence, we prepared the phosphor-converted white light-emitting diodes based on the phosphate glass containing amorphous nanoscale ZnO clusters.



## AVIS DU JURY SUR LA REPRODUCTION DE LA THESE SOUTENUE

**Titre de la thèse:**

Hybrid materials based on inorganic glasses doped with organophosphorus molecules for light emitting electrochemical cell applications

**Nom Prénom de l'auteur : CAI MUZHI**

**Membres du jury :**

- Madame PIARRISTEGUY Andrea
- Monsieur DE LIGNY Dominique
- Monsieur ZHANG Xiang-Hua
- Monsieur XU Shiqing
- Monsieur ZHANG Junjie
- Monsieur ROCHERULLE Jean
- Monsieur CALVEZ Laurent

Président du jury : *Jean ROCHERULLE*

Date de la soutenance : 22 Novembre 2019

Reproduction de la these soutenue

- Thèse pouvant être reproduite en l'état  
 Thèse pouvant être reproduite après corrections suggérées

Fait à Rennes, le 22 Novembre 2019

Le Directeur,

M'hamed DRISSI



Signature du président de jury







**Titre :** Matériaux hybrides verres inorganiques / molécules organiques pour des applications light-emitting electrochemical cells .....

**Mots clés :** luminescence, verre hybride, cellule électrochimique émettant de la lumière, LEC

**Résumé :** La cellule électrochimique électroluminescente (LEC) est un dispositif à couches minces, composé d'un semi-conducteur organique électroluminescent (OSC) et d'ions mobiles en tant que matériau actif intercalé entre une anode et une cathode.

Dans le premier chapitre, le contexte et le mécanisme de la LEC ont été introduits. Dans le deuxième chapitre, nous avons dopé la molécule organophosphorée dans un verre de silicate contenant une teneur élevée en lithium par la méthode sol-gel.

Dans le troisième chapitre, nous avons travaillé à l'obtention d'un verre de phosphate dopé à une molécule organophosphorée avec une conductivité

ionique élevée par frittage Spark Plasma Sintering (SPS). Un verre de phosphate hybride ayant une conductivité ionique d'environ  $10^{-7}$  S / cm a été obtenu et une forte photoluminescence a été observée. En outre, les propriétés électrochimiques ont également été étudiées.

De plus, lors du processus de préparation de la LEC par SPS, un phénomène intéressant a été découvert. Une émission bleue à large bande a été observée dans le verre d'oxynitride de phosphate de zinc exempt de terres rares. Le quatrième chapitre est consacré à ce phénomène.

---

**Title :** Hybrid materials based on inorganic glasses doped with organophosphorus molecules for light-emitting electrochemical cell applications.....

**Keywords :** luminescence, hybrid glass, light-emitting electrochemical cell, LEC

**Abstract:** The light-emitting electrochemical cell (LEC) is a planar layered device, which is comprised of an electroluminescent organic semiconductor (OSC) and mobile ions as the active material sandwiched between an anode and a cathode. Electrolyte is one of the "short slab" of LEC technology.

The main objective of this work is developing a new LEC device based on organophosphorus molecule doped organic-inorganic hybrid glass electrolyte. This hybrid glass cannot be synthesized by using classic melt-quenching technique because the melting temperature of glass is always much higher than the degradation temperature of organic molecule. Thus, in this work, we devote to that how to dope the organophosphorus molecule into the glass with high ionic conductivity.

In first chapter, the background and mechanism of LEC were introduced.

In the second chapter, we attempted to dope the organophosphorus molecule into silicate glass containing high lithium content by sol-gel method.

In third chapter, we are working to obtain organophosphorus molecule doped phosphate glass with high ionic conductivity through spark plasma sintering (SPS). A hybrid phosphate glass with ionic conductivity of around  $10^{-7}$  S/cm was obtained, and strong photoluminescence was observed. Besides, the electrochemical properties were investigated as well.

Moreover, during the process of preparing the LEC by SPS, an interesting phenomenon was found. A broadband blue emission was observed in rare-earth free zinc phosphate oxynitride glass. The fourth chapter is focus on this interesting phenomenon.